Micro-combs: a novel generation of optical sources

Article (Published Version)

Physics Reports 729 (2018) 1–81

Contents lists available at ScienceDirect

Physics Reports

journal homepage: www.elsevier.com/locate/physrep

Micro-combs: A novel generation of optical sources

Alessia Pasquazi [b,a,*], Marco Peccianti [b,a], Luca Razzari [a], David J. Moss [c,a], Stéphane Coen [d], Miro Erkintalo [d], Yanne K. Chembo [e,f], Tobias Hansson [a,g], Stefan Wabnitz [g], Pascal Del'Haye [h], Xiaoxiao Xue [i,j], Andrew M. Weiner [i], Roberto Morandotti [a,k,l,**]

[a] *INRS-EMT, 1650 Blvd. Lionel-Boulet, Varennes, Québec J3X 1S2, Canada*
[b] *Department of Physics and Astronomy, University of Sussex, Brighton BN1 9QH, UK*
[c] *Centre for Microphotonics, Swinburne University of Technology, Hawthorn Victoria, 3122, Australia*
[d] *The Dodd-Walls Centre for Photonic and Quantum Technologies, Department of Physics, The University of Auckland, Auckland 1142, New Zealand*
[e] *FEMTO-ST Institute, Univ. Bourgogne Franche-Comté, CNRS, Optics Department, 15B Avenue des Montboucons, 25030 Besançon cedex, France*
[f] *GeorgiaTech-CNRS Joint International Laboratory [UMI 2958], Atlanta Mirror Site, School of Electrical and Computer Engineering, 777 Atlantic Drive NW, Atlanta, GA 30332, USA*
[g] *Dipartimento di Ingegneria dell'Informazione, Università di Brescia, and INO-CNR, via Branze 38, 25123 Brescia, Italy*
[h] *National Physical Laboratory, Teddington TW11 0LW, UK*
[i] *School of Electrical and Computer Engineering, Purdue University, 465 Northwestern Avenue, West Lafayette, IN 47907-2035, USA*
[j] *Department of Electronic Engineering, Tsinghua University, Beijing 100084, China*
[k] *Institute of Fundamental and Frontier Sciences, University of Electronic Science and Technology of China, Chengdu 610054, China*
[l] *National Research University of Information Technologies, Mechanics and Optics, St Petersburg, Russia*

ARTICLE INFO

Article history:
Accepted 25 August 2017
Available online 12 October 2017
Editor: Donna Strickland

ABSTRACT

The quest towards the integration of ultra-fast, high-precision optical clocks is reflected in the large number of high-impact papers on the topic published in the last few years. This interest has been catalysed by the impact that high-precision optical frequency combs (OFCs) have had on metrology and spectroscopy in the last decade [1–5]. OFCs are often referred to as optical rulers: their spectra consist of a precise sequence of discrete and equally-spaced spectral lines that represent precise marks in frequency. Their importance was recognised worldwide with the 2005 Nobel Prize being awarded to T.W. Hänsch and J. Hall for their breakthrough in OFC science [5]. They demonstrated that a coherent OFC source with a large spectrum – covering at least one octave – can be stabilised with a self-referenced approach, where the frequency and the phase do not vary and are completely determined by the source physical parameters. These fully stabilised OFCs solved the challenge of directly measuring optical frequencies and are now exploited as the most accurate time references available, ready to replace the current standard for time. Very recent advancements in the fabrication technology of optical micro-cavities [6] are contributing to the development of OFC sources. These efforts may open up the way to realise ultra-fast and stable optical clocks and pulsed sources with extremely high repetition-rates, in the form of compact and integrated devices. Indeed, the fabrication of high-quality factor (high-Q) micro-resonators, capable of dramatically amplifying the optical field, can be considered a photonics breakthrough that has boosted not only the scientific investigation of OFC sources [7–13] but also of optical sensors and compact light modulators [6,14].

* Corresponding author at: Department of Physics and Astronomy, University of Sussex, Brighton BN1 9QH, UK.
** Corresponding author at: INRS-EMT, 1650 Blvd. Lionel-Boulet, Varennes, Québec J3X 1S2, Canada.
E-mail addresses: a.pasquazi@sussex.ac.uk (A. Pasquazi), roberto.morandotti@emt.inrs.ca (R. Morandotti).

https://doi.org/10.1016/j.physrep.2017.08.004

In this framework, the demonstration of planar high-Q resonators, compatible with silicon technology [10–14], has opened up a unique opportunity for these devices to provide entirely new capabilities for photonic-integrated technologies. Indeed, it is well acknowledged by the electronics industry that future generations of computer processing chips will inevitably require an extremely high density of copper-based interconnections, significantly increasing the chip power dissipation to beyond practical levels [15–17]; hence, conventional approaches to chip design must undergo radical changes. On-chip optical networks, or optical interconnects, can offer high speed and low energy per-transferred-bit, and micro-resonators are widely seen as a key component to interface the electronic world with photonics.

Many information technology industries have recently focused on the development of integrated ring resonators to be employed for electrically-controlled light modulators [14–17], greatly advancing the maturity of micro-resonator technology as a whole. Recently [11–13], the demonstration of OFC sources in micro-resonators fabricated in electronic (i.e. in complementary metal oxide semiconductor (CMOS)) compatible platforms has given micro-cavities an additional appeal, with the possibility of exploiting them as light sources in microchips. This scenario is creating fierce competition in developing highly efficient OFC generators based on micro-cavities which can radically change the nature of information transport and processing. Even in telecommunications, perhaps a more conventional environment for optical technologies, novel time-division multiplexed optical systems will require extremely stable optical clocks at ultra-high pulse repetition-rates towards the THz scale. Furthermore, arbitrary pulse generators based on OFC [18,19] are seen as one of the most promising solutions for this next generation of high-capacity optical coherent communication systems. This review will summarise the recent exciting achievements in the field of micro-combs, namely optical frequency combs based on high-Q micro-resonators, with a perspective on both the potential of this technology, as well as the open questions and challenges that remain.

Contents

1. Micro-combs: small, efficient and fast sources

Optical frequency combs based on micro-resonators, or micro-combs, represent an exceptionally active field of research that has only developed in the last ten years. This has been motivated by the prospect of creating compact and efficient multi-wavelength sources that are able to replace the very bulky and power-hungry bulk or table-top optical sources, used in many applications, with an ultra-compact and energy-efficient device. This field of research has its roots in the pioneering development of whispering-gallery mode and ring micro-resonators achieved by exploiting different technologies, beginning in the late 1980s and reaching maturity for telecom applications at the turn of the millennium. Section 2 briefly summarises the technology for fabricating optical micro-resonators with a focus on bulk monolithic and integrated technologies. Section 3 introduces the basic mathematical description for micro-resonators, summarising the linear properties of resonant modes and frequencies, and provides the basic principle for the description of frequency comb generation by nonlinear coupling of the resonator modes via the Kerr effect. Here, we also describe the general approach for modelling the process of Kerr micro-comb generation, based on the coupled-model or frequency domain description that was originally applied to comb formation [20–23]. Such an approach has been effectively used by Chembo and co-workers to model double-cascaded comb generation [23].

An important property of optical micro-resonators is their ability to efficiently store and enhance the optical field. For this reason, nonlinear optical phenomena that, typically, require very high-power optical pump sources can be observed in micro-resonators at extremely low powers. This simple scaling was the basis of the breakthrough in 2004 of optical Kerr-based parametric generation, reported by two independent groups [20,21]. Those works opened up intense research on this topic. The first demonstration of large bandwidth optical frequency combs [8] triggered many breakthrough results of wide spectrum generation [24,25] over a range of different spectral regions and with different spectral properties [26,27], achieved in resonators based on a wide range of platforms [13,28]. The first demonstration of optical parametric oscillation (OPO), based on integrated optical platforms, occurred in 2009 by two independent groups [11,12], where micro-comb sources compatible with electronic integrated circuit technology (CMOS) were reported, with the ensuing benefits of increased

manufacturability, reliability, stability, as well as reduced cost, footprint and energy consumption. With these breakthroughs, however, the subsequent question of the quality of the generated combs, particularly with respect to coherence, became a central issue. The first systematic investigation of comb coherence was carried out in 2011 by Ferdous et al. [10] who demonstrated that, while coherent states could be generated by micro-comb sources, not all of the configurations or operating conditions were able to support them. These experiments are reviewed in detail in Section 4.

Very interestingly, the basis of the current theoretical understanding and description of micro-combs can be traced back to the early studies on nonlinear resonators. The famous papers by Ikeda [29,30] were a cornerstone of this original work, showing that the map describing light transmission by nonlinear ring cavities exhibits bi-stability, instabilities and chaos. When including beam diffraction, McLaughlin, Moloney and Newell discovered that Kerr ring cavities could support the stable propagation of solitary waves as fixed points of the map and exhibit a new class of pattern generating modulation instabilities [31,32]. By averaging nonlinear diffractive propagation over the Ikeda map, Lugiato and Lefever [33] have shown that the generation of spatial dissipative structures in nonlinear Kerr ring cavities could be described by the driven and damped nonlinear Schrödinger (NLS) equation, henceforth also known as the Lugiato–Lefever equation (LLE) in nonlinear optics. This equation, which also models charge-density waves in one-dimensional condensates and a plasma driven by a radio-frequency field, has been shown by Kaup and Newell in 1978 [34] and Nozaki and Bekki in 1983 [35,36] to exhibit phase-locked solitary waves and chaos. By neglecting diffraction (e.g. in the case of a single-mode fibre) and including chromatic group velocity dispersion, the LLE was subsequently derived by Haelterman, Trillo and Wabnitz in 1992 to describe temporal modulation instabilities, dissipative structures and solitons in nonlinear Kerr ring cavities [37–39].

Spatial optical patterns [40] and spatial waves phase locking [41] were observed in 1995 and 1997, respectively, in liquid crystal valves with optical feedback, leading to the observation of spatial cavity solitons by Schreiber et al. [42] in 1997 in the same platform. Spatial cavity solitons were also observed in a vertical cavity semiconductor micro-resonator operating slightly below threshold by Barland et al. in 2002 [43]. For a recent review on localised structures, see also [44]. On the other hand, temporal cavity solitons in a Kerr ring fibre cavity were first observed in 2010 by Leo et al. [45]. Since optical micro-resonators are essentially a scaled-down version of fibre-ring cavities, the LLE also provides the foundation for the modelling of optical micro-combs, provided that periodic boundary conditions imposed by the finite cavity length (or circulation time) are explicitly taken into account.

However, earlier theoretical studies of the physics of Kerr micro-comb generation have relied on the coupled-mode or frequency domain description [23], rather than the time-domain approach based on the LLE, which has only been applied in recent years [22,46–48]. These theoretical developments, that are now at the heart of the understanding of optical micro-comb sources, are outlined in detail in Section 5, with an in-depth description of the different observable régimes — both coherent and incoherent.

Section 6 is devoted to the more recent development of the experimental understanding and control of the coherence properties of optical frequency combs. Following the observation of externally injected, stable temporal cavity soliton propagation in fibre-ring cavities [45], two papers on coherent pulse generation appeared on *arXiv* in 2012, respectively by Saha et al. and Herr et al. Saha et al. observed femtosecond pulse train generation associated with parametric comb generation in silicon nitride micro-resonators [49]. Herr et al. demonstrated that temporal solitons could be directly generated from cavity modulation instability in Kerr micro-resonators in a final paper of 2014 [50]. Later, Xue et al. demonstrated that mode-locked dark pulses, showing different features from fibre dark solitons, could also be produced in the normal dispersion region [51]. In parallel to these observations, the group at NIST started to address in detail the properties of coherent states produced in optical micro-resonators, demonstrating that these could be generated and controlled by self-injection and electro-optical modulation [52–55]. Self-injection schemes were also proposed by Matsko and Maleki [56] and by Pasquazi et al. [57] to control the position of the pump resonance [56]. A passive self-starting scheme for producing optical pulses from micro-resonators was developed by Peccianti et al., based on the concept of nesting the micro-cavity in a laser loop in the filter-driven four-wave mixing (FD-FWM) scheme, thus guaranteeing the coherence of the generated pulses [58,59].

These experimental developments are discussed in detail in Section 6, while Section 7 is devoted to proposed applications of micro-combs to metrology, telecommunications and radio-frequency photonics. The application of micro-combs to metrology has been foreseen since the first demonstration of a broadband [8] and octave-spanning comb [24,25], due to the impact that octave-spanning optical frequency combs had on metrology [1–5] and in telecommunications and radio-frequency photonics [60–64]. In contrast, the application of micro-combs to quantum optics, described in Section 8, has only recently attracted the attention of the scientific community, despite the fact that the very first high-Q optical resonators, like microspheres, were developed in order to study quantum electrodynamics (QED) [65]. Micro-resonators now have the potential to provide a new generation of quantum sources.

2. Micro-resonator technologies for micro-combs

Dielectric optical resonators of various shapes and composed of different materials (see Fig. 1) have been exploited for generating micro-combs. Spherical, cylindrical, toroidal and ring geometries have been used, all having the common feature of possessing an exceptionally high-Quality factor (high-Q). Here, we term these types of resonators as whispering-gallery mode (WGM) resonators, following the widely-used definition provided by Ilchenko et al. [66] of *monolithic ring-resonators based on total internal reflection of light*. The development of these devices is closely linked with the history of the many applications of optical resonators that have unfolded over the past thirty years. [6,67,68].

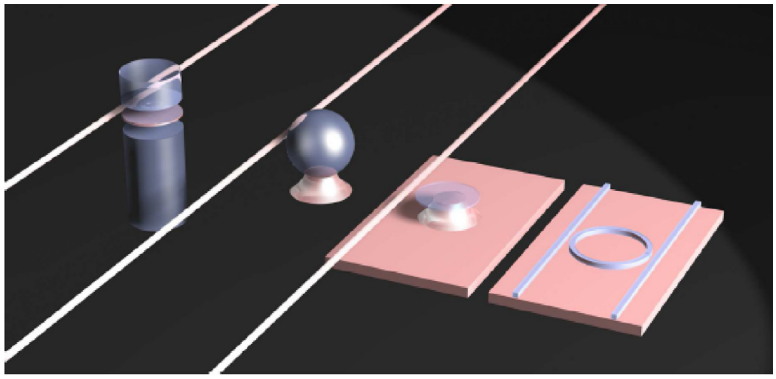

Fig. 1. Micro-combs have been generated by a large class of resonator devices, such as whispering-gallery mode-based bulk toroids, spheres, monolithic toroids and integrated ring-resonators.

The 1980s and 1990s saw the beginning of significant developments in telecommunication-oriented photonics technologies. Many new ideas and concepts were developed over that period in order to enable the practical and cost-effective implementation of photonic telecommunication networks that underpinned the birth of the internet revolution in the 1990s. In this respect, linear passive optical resonators became a key component for the manipulation and filtering of optical signals, an absolutely critical aspect of wavelength division multiplexing (WDM) network technologies [69].

Filters with carefully-tailored complex linear frequency responses, such as add-drop filters, were developed, starting with simple single cavities, such as ring or micro-disc resonators [70]. Although both bulk and integrated technologies have been exploited to achieve a range of linear WDM optical response functions, these designs were particularly amenable to photonic integrated circuit technology [71–73], which was already reaching very sophisticated levels of development [70,74,75].

Technologies capable of achieving very low loss – both intrinsic material absorption and waveguide scattering loss – over large on-chip areas were fundamental in bringing photonic integrated circuits to realisation. Platforms such as silica, silicon nitride and Hydex glass [76–79] were developed with this in mind, which later enabled the fabrication of resonators with extremely high-Q factors, i.e. capable of storing the optical field with very few losses per cycle (see Section 3.2.2).

In parallel with these developments in planar technology, bulk micro-cavities with exceptionally high-Qs were developed in order to address applications in Quantum Electro-Dynamics (QED), sensing and other areas [65,80–82]. Optical micro-spheres were first developed in 1989 by Braginsky, Gorodetsky and Ilchenko [83]. Since then, the technology has evolved rapidly, with optical resonators having Q-factors on the scale of tens of billions [84], limited only by environmental interactions [85]. A variety of different approaches and technologies was developed to realise bulk resonators, from prism-coupled cylinders to fibre-coupled devices, such as planar technology-based micro-toroids [68,86]. More recently, these devices have demonstrated strong potential for biosensing, further driving increased interest and research in high-Q micro-resonators [87].

In this framework, nonlinear optics soon began to play an important role. Micro-resonators, due to their typically small volume, greatly enhance the optical field, thus allowing nonlinear optical behaviour to occur at very low power levels. There were important demonstrations in second-order materials, such as lithium niobate and gallium arsenide, for frequency conversion, as well as for microwave photonic applications [88,89]. The thermo-optic Kerr effect was used for slow optical modulation [90,91], while Raman lasing was demonstrated in a silica sphere in 2002 [7]. Finally, these devices allowed the excitation of the third-order Kerr effect at milliwatt power levels, with all-optical Kerr modulation being reported in silicon ring-resonators in 2004 [92]. In a fundamental breakthrough, critically important for the subsequent work on micro-combs, Kerr optical parametric amplification was first observed in silica toroids in 2004 by Kippenberg et al. and by Savchenkov et al. in calcium fluoride resonators [20,21]. Subsequently, four-wave mixing (FWM) amplification at milliwatt levels was demonstrated in 2008 in integrated ring-resonators [93,94].

In the following sections, we describe the technology for the production of bulk and integrated WGM resonators, while the mathematical modelling is outlined in detail in Section 3.

2.1. Technologies for bulk whispering-gallery mode resonators

Bulk spherical resonators were the first technology developed for micron-scale bulk cavities [65,83] - silica micro-spheres with very high-Q-factors were fabricated using a relatively straightforward technology. A typical approach was to melt the tip of a silica optical fibre. A range of techniques, such as electrical arc heating, a hydrogen flame, or laser re-flow (e.g. with a CO_2 laser), was used to fabricate silica spheres with diameters of hundreds of microns [83,85,95–98]. A spherical shape was obtained due to surface tension, as the melted tip solidified immediately after being removed from the heat source (Fig. 2(a),(b)). The surface obtained with this approach was extremely smooth, strongly suppressing any scattering losses in the micro-cavity, resulting in Q-factors of up to 10^{10} [85,99].

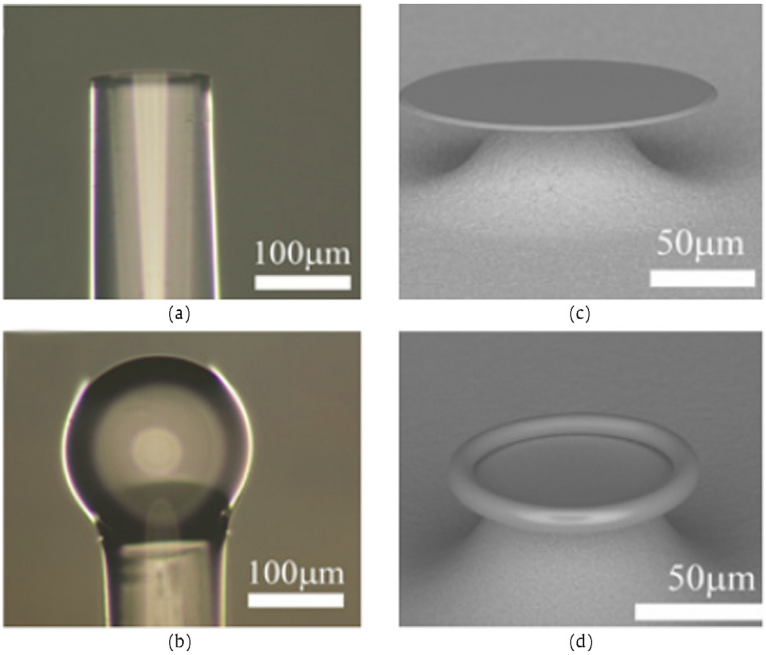

Fig. 2. Examples of silica-based micro-resonators: (a) cleaned and cleaved optical fibre (b) silica micro-sphere; scanning electron micro-graphs of (c) silica micro-disc resonators after under-etching the silicon substrate [95] (d) silica micro-toroid cavity after thermal re-flow. After Ref. [95].

These impressively high-Q-factors were enabled largely by innovative and efficient methods for coupling light into optical fibres, primarily using fibre micro-tapers [100,101]. Although prisms were the first approach used to couple light into micro-spheres [85,99], tapered fibres resulted in a more efficient and controllable coupling [100–103]. High-Q micro-spheres were explored for sensing [96], lasing [7,97,98,104], cavity QED [65,99] and nonlinear Kerr bi-stability [105]. For a recent review on micro-sphere technology, see also [106]. When compared with micro-spheres, micro-toroids and micro-discs have far fewer degenerate modes and so their geometry is preferable in order to control mode crossing — an important parameter in comb formation (see Sections 3.2 and 6.2.1). Several approaches have been explored for developing these geometries.

Resonators with high-Q-factors were obtained in silica glass using melting techniques similar to the fabrication process of silica micro-spheres. This approach was used to achieve the first demonstration of a silicon chip compatible technique for ultra-high-Q-resonators [86,107]. The fabrication started with a lithographic step on a thermally-grown silica layer on a silicon substrate [95], followed by a dry etching step. Circular silica pads were initially defined on the silica layer. The micro-discs were created by under-etching the silicon substrate and then melted by a CO_2 laser using re-flow (Fig. 2(c),(d)). This latter step minimised the surface roughness of the devices, resulting in Q-factors of up to 5×10^8. In contrast to micro-sphere technology, the Q-factor was actually limited by the diffusion of boron from the silicon substrate to the oxide, rather than by roughness [108].

More recently, similar Q-factors have been achieved using laser machining techniques, where micro-rods are defined with a CO_2 laser by shaping and polishing a silica rod [109], as also shown in Fig. 3. Here, the rod is rotated in a spindle, with the laser focused normal to the rod axis. This technique was developed for micro-comb applications and is particularly efficient for achieving a user-defined rod diameter.

Thermal re-flow cannot be used in crystalline materials where grind and polishing approaches, similar to the ones used in lens technology, need to be employed in order to obtain smooth surfaces on a sub-nanometre scale. This approach has allowed the retention of the crystalline material structure and has also been successfully used for the fabrication of resonators made of quadratic nonlinear crystals [88]. These second-order nonlinear resonators have found use as high-efficiency microwave and millimetre-wave electro-optical modulators [89]. Crystals, such as magnesium and calcium fluorides (MgF_2, CaF_2), have been efficiently employed for comb generation, even reaching the mid-infrared (MIR) wavelength range due to their large transparency window. Their fabrication starts from optical windows that are mounted in a rotation spin motor and then ground into a disc resonator [110]. Grinding and polishing steps with abrasive particles of reduced size yield Q-factors to the order of 10^9. Record Q-factors of 10^{11} have been achieved in CaF_2 resonators, with repeated polishing/annealing steps at the last stage [84,110–114]. An example of a magnesium fluoride resonator is shown in Fig. 4.

2.2. CMOS—Compatible integrated micro-resonators

In the last few years a great effort has been devoted to develop a technology for micro-combs in platforms compatible with large-scale integration. Such an achievement would offer enormous benefits in terms of scalability, reduced footprint,

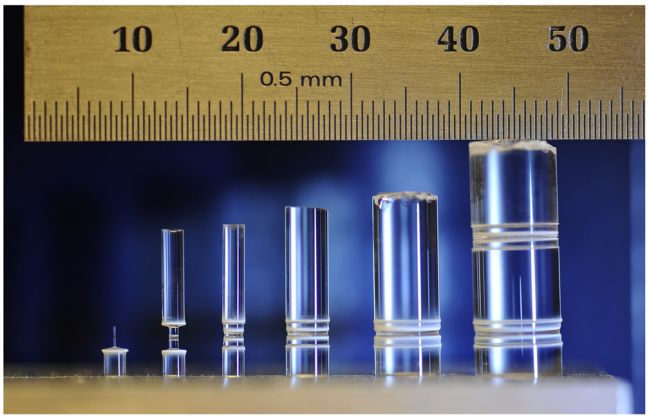

Fig. 3. Laser-machined fused silica micro-rod resonators with diameters ranging from 200 μm to 8 mm. [109].

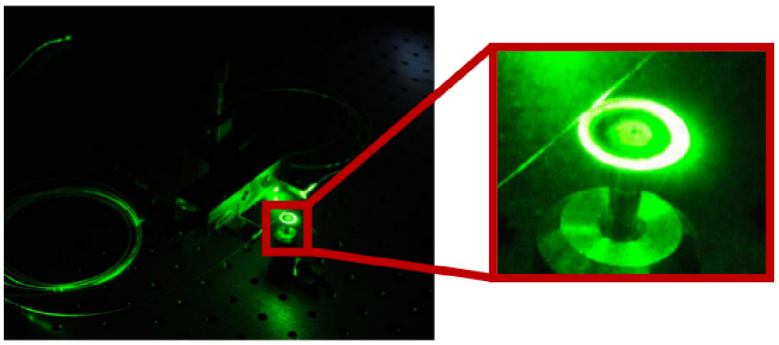

Fig. 4. Examples of a high-Q-resonator manufactured at the FEMTO-ST Institute of Besançon for micro-comb generation: whispering-gallery disc resonator in magnesium fluoride (MgF_2) coupled to green laser light via a tapered fibre waveguide *(photographed by A. Coillet)*.

improved performance and many other advantages, similar to the ones achieved in the electronic computer chip industry. In particular, many information technology industries have recently developed integrated ring resonators to be employed for electrically-controlled light modulators [14–17], advancing the maturity of micro-resonator technology.

Linear photonic technologies based on silicon, particularly in the form of silicon on insulator (SOI), have become a key foundation of the photonic chip industry in the last ten years or so [116], gradually replacing the large interface cards in optical communications networks. These first-generation silicon photonic chips feature highly-sophisticated circuits comprised of splitters, filters, multiplexers and modulators and they offer the substantial benefit of exploiting silicon-integrated circuit technology (Complementary Metal Oxide Semiconductor (CMOS)), although not without challenges [117]. Therefore, SOI would appear to be an attractive platform on which to realise *integrated* micro-combs.

Indeed, even for third-order nonlinear optics - a key ingredient for the generation of optical frequency combs - SOI has been quite successful over the past fifteen years [118]. It offers many attractive features, such as an extremely high Kerr nonlinearity (n_2) which, when combined with the very tight confinement of light within SOI nanowires (due to their extremely high refractive index contrast), has yielded extremely high, nonlinear parameters (γ) of 300,000 W^{-1} km^{-1} - $\gamma = \omega n_2/(c A_{eff})$, where A_{eff} is the effective area of the waveguide, c is the speed of light and ω is the pump frequency.

Many impressive demonstrations in SOI based on nonlinear optics have been reported, such as Raman gain and lasing [119], time lensing [120], slow-light-based signal processing [121], optical regeneration [122], parametric gain [123–127] and even quantum optical applications, such as correlated photon-pair generation [128].

Indeed, SOI has been so successful as a platform for both linear and nonlinear photonics that, were it not for perhaps two main issues, it would now be the sole platform of choice for integrated nonlinear optics. The first issue is its centrosymmetry - thus ruling out any second-order nonlinear optical effects, such as electro-optic modulation functionalities. The second, and, perhaps, far more serious issue is the presence of significant two-photon absorption (TPA) in the telecommunications window near 1550 nm, arising because the indirect bandgap near 1.1 eV is well below the two-photon energy in the telecom band (and, indeed, at all wavelengths shorter than about 2200 nm). While the effect of TPA-generated free carriers can be mitigated - for example by the use of p–i–n junctions to sweep out carriers [129] - the intrinsic nonlinear figure of merit (FOM) (defined as FOM$= n_2/(\beta\lambda)$, where β is the TPA coefficient and λ is the wavelength) of silicon represents a fundamental limitation – being an intrinsic property of the silicon bandstructure – and is only 0.3 near 1550 nm [130–132]. The fact

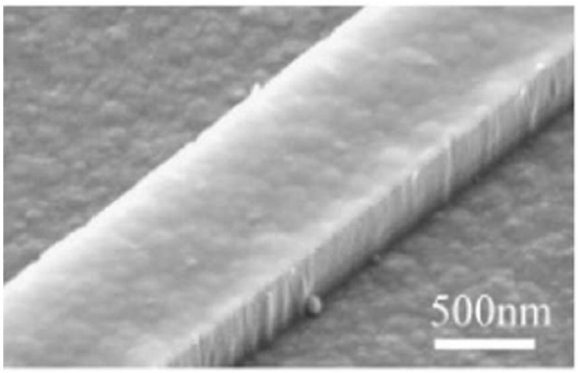

(a)

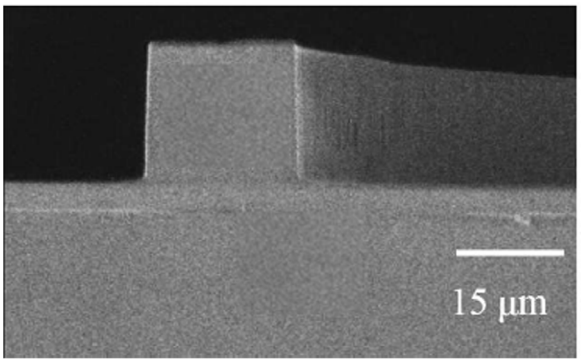

(b)

Fig. 5. Low-loss waveguides in (a) silicon nitride (after [115]) and in (b) Hydex glass (after Ref. [94]).

that, despite its low FOM, many impressive all-optical demonstrations have been made in silicon is a testament to how exceptional its linear and nonlinear optical properties are. The critical impact of the large silicon TPA was illustrated in 2010 by the demonstration of high parametric gain at wavelengths beyond 2 μm [125,126], where TPA vanishes. Indeed, it is likely that silicon will remain a highly attractive platform for nonlinear photonics in the MIR wavelength range (between 2 and 6 μm), where it is transparent to both one and two photon transitions [133] (see Section 6).

For the telecom band, however, the low FOM of silicon has necessitated the development of new CMOS-compatible platforms for nonlinear optics, which have since achieved considerable success. These include silicon nitride (Si_3N_4), silicon oxinitrides (SiO_xN_x) and Hydex glass, which has similar properties to the latter (Fig. 5) [134]. Originally developed for linear optics [78,135], these platforms are particularly promising due to their low linear loss and relatively large nonlinearities compared to typical fibres but, most significantly, with regard to their negligible nonlinear loss at telecommunication wavelengths [136]. In addition, their high-quality CMOS-compatible fabrication processes, high material stability and the ability to engineer dispersion [11] make these platforms highly attractive. Indeed, within a short period of time, significant progress has been made with respect to their nonlinear performance - particularly in the context of optical frequency comb generation in micro-resonators. Since the first demonstration of optical frequency combs in Si_3N_4 and Hydex in 2010 [11,12], this field has proliferated [137]. Extremely wide-band frequency combs [13,24,25], sub-100-GHz combs [138], line-by-line arbitrary optical waveform generation [10], ultra-short pulse generation [49,50,58] and dual-frequency combs [59] have been reported. In addition, optical frequency comb harmonic generation [139] has been observed. These breakthroughs have not been possible in SOI at telecom wavelengths because of its low FOM.

By contrast, only recently has an optical parametric oscillator, or frequency comb source, been directly demonstrated in a silicon ring-resonator [133]. This remarkable achievement was made through the use of three innovative approaches: greatly increasing the Q-factor by using etchless fabrication methods (relying on thermal oxidation) to reduce waveguide roughness (and, hence, loss) [140]; by working at wavelengths beyond 2.2 μm, (the two-photon absorption cut-off wavelength); and, finally, by implementing a p–i–n junction in order to sweep out the free carriers generated by three-photon (and higher order) absorption.

However, whether realised directly in silicon or in these new CMOS-compatible platforms, all approaches based on integrated optics offer substantial benefits over monolithic bulk technologies. Integrated ring-resonators coupled to bus waveguides (either laterally or vertically [71]) can route signals directly on-chip in order to achieve complex functionalities. The low bending loss of high-index contrast waveguides also provides high flexibility in the micro-resonator geometry

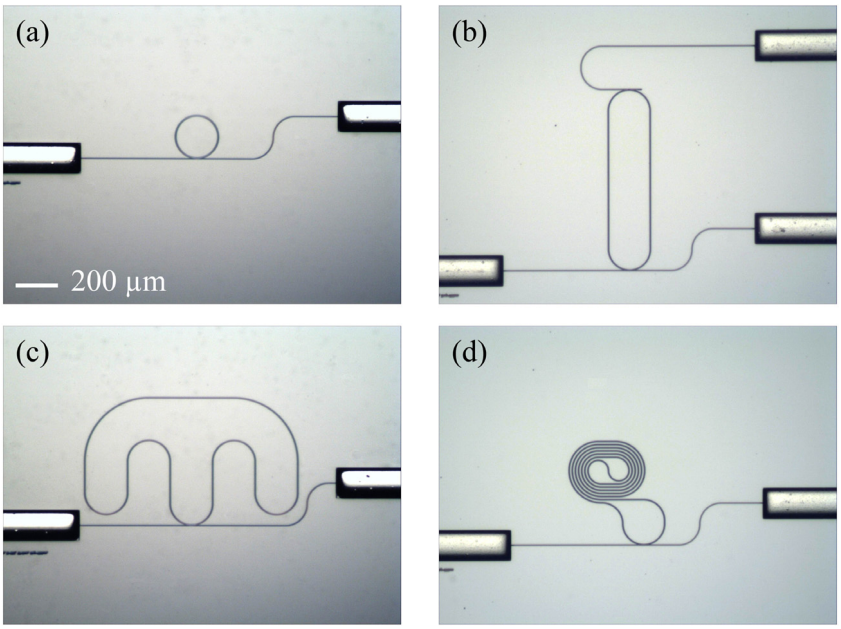

Fig. 6. Silicon nitride micro-resonators, as fabricated by Purdue University, with a free spectral range (FSR) of (a) 231 GHz (b) 75 GHz (c) 37 GHz (d) 25 GHz. The spatial scale reported in panel (a) is the same for all the pictures. Integrated ring-resonators are usually characterised by small footprints, leading to short travelling times and high FSRs of the circular micro-cavity in the order of hundreds of GHz. To decrease such FSRs, different geometries can be used [137].

design. Race-track, spiral or irregular curvilinear shapes can be employed, beyond simple circular rings, to fold the micro-resonator into a very compact footprint (Fig. 6). In turn, the device can be fitted within a typical write-field of an electron beam lithographic writing tool to avoid field-stitching errors. This is especially useful for large micro-resonators that can generate frequency combs with repetition-rates down to tens of GHz in the microwave frequency range. We summarise below the technological development of Si_3N_4 and SiO_xN_x platforms.

Si_3N_4 is a CMOS-compatible insulator used in the computer chip industry that has been exploited as a platform for linear-integrated optics [141] and has only relatively recently been proposed for nonlinear optics [115]. Historically, the challenge for Si_3N_4 optical devices has been to grow low-loss layers thicker than 250 nm, due to tensile film stress, combined with the need to anneal the films at very high temperatures (1100 °C) in order to eliminate residual hydrogen in the films - a source of significant loss in the telecommunications wavelength range (1500 nm). Achieving such thick layers is critical for high-mode confinement and dispersion engineering, which are the key features in designing waveguides for nonlinear applications. Thick ($>$ 500 nm) low-loss Si_3N_4 layers were achieved by plasma-enhanced chemical vapour deposition (PECVD), as well as by low pressure chemical vapour deposition (LPCVD) by Ikeda et al. and Levy et al. [11,115]. The latter approach employed a thermal cycling process that resulted in very thick (700 nm) films that yielded nanowires with very low propagation loss (0.4 dB/cm).

These technological results were instrumental in the first nonlinear optical studies of Si_3N_4 micro-cavities [115], where a nonlinear shifting of the resonances in 700-nm-thick Si_3N_4 ring-resonators was obtained using a continuous-wave (CW) optical pump at a power level of 200 mW. Time-resolved measurements enabled the thermal and Kerr contributions to be separated, resulting in an n_2 that was measured to be a factor of ten greater than that of silica glass. This is consistent with Miller's Rule [142], given the ratio of the linear refractive indices for these two materials. This value has been validated in subsequent studies of nonlinear optics in silicon nitride nanowires and resonators. Parametric gain in Si_3N_4 was first demonstrated in low-loss nanowire-based resonators by centring the pump for the four-wave mixing (FWM) process within the anomalous group velocity dispersion (GVD) régime, near the zero-GVD point [11]. This yielded broad-bandwidth phase matching and, hence, signal amplification, over a wide range of wavelengths. A net gain was achieved in long (6 cm) Si_3N_4 waveguides with a nonlinear parameter γ of 1200 W^{-1} km^{-1} and a zero GVD point near 1560 nm. An on/off signal gain as high as 3.6 dB was observed over a 150 nm bandwidth, representing a net parametric amplification, since the total propagation loss through the waveguides was 3 dB. Intrinsic Q-factors of 7×10^6 have since been achieved in Si_3N_4 rings [143]. Integrated ring-resonators are usually characterised by small footprints, leading to short travelling times and, hence, high free spectral ranges (FSRs) of the circular micro-cavity - in the order of hundreds of GHz. (For the definition of FSR, see Section 3.1.1). For coherent combs (largely discussed in Section 4 and above), where the FSR is equal to the pulse repetition-rate (or possibly a multiple of the FSR), this leads to pulsed optical frequency combs with extremely high repetition-rates that are much higher than what is measurable electronically. To decrease the FSR and repetition-rate in order

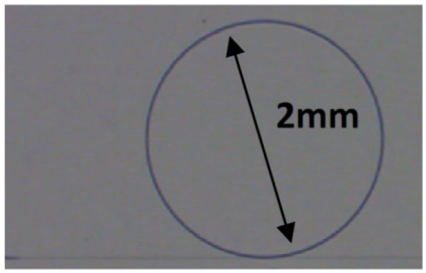

Fig. 7. Planar-integrated ring-resonator in silicon nitride (Si_3N_4), with its tapered coupling waveguide below the resonator, fabricated by the FEMTO-ST Institute (*photographed by R. Salut*).

to bring them within the realm of microwave electronics, different geometries have been proposed [60,137], such as the devices shown in Fig. 6 that were fabricated by Purdue University. Fig. 7 shows a more conventional Si_3N_4 planar resonator, fabricated at the FEMTO-ST Institute, where the small FSR was achieved in a large diameter circular-ring geometry.

Hydex glass was developed [78] as a low-loss CMOS-compatible optical platform, primarily intended for advanced linear filters. Its refractive index range of n = 1.5 to 1.9 is slightly lower than Si_3N_4, being comparable to SiO_xN_x. Therefore, a buried waveguide geometry is typically used, rather than nanowires. Nonetheless, the core–cladding contrast of 0.17 still allows for relatively tight bend radii of 20 μm. Its proprietary composition is primarily aimed at reducing the need for annealing by reducing the presence of N-H bonds - the main source of absorption loss in the telecom band. This platform has resulted in low linear propagation losses of 5–7 dB/metre, allowing for ultra-high-Q-resonators [94].

Fig. 8 shows a Hydex four-port micro-ring resonator with a Q-factor of 1.2 million (corresponding to a mode linewidth of 160 MHz). The waveguides of this resonator possess a high effective-nonlinearity ($\gamma = 220\,\mathrm{W^{-1}\,km^{-1}}$) due to a combination of tight-mode confinement and high intrinsic Kerr nonlinearity (Hydex Kerr coefficient n_2 is five times larger than that of silica glass). Most significantly, the waveguides exhibit both very low linear optical loss and negligible nonlinear optical loss (i.e. two photon absorption (TPA)) for intensities up to 25 GW/cm^2 [136]. The waveguides were engineered to yield small and anomalous dispersion, critical for efficient and wide bandwidth FWM, with zero GVD points being 1600 nm for the transverse electrical (TE) polarisation and 1560 nm for the transverse magnetic (TM) polarisation. All of these factors make this platform particularly attractive for low-power nonlinear optics in the telecom fibre optic C-band (defined between 1530 and 1565 nm).

3. Modelling of optical micro-resonators with coupled-mode theory

Micro-resonator devices come in varying shapes and sizes [6] and rely on the confinement of light inside a small resonance cavity through total internal reflection. The optical modes are commonly known as whispering-gallery modes (WGM), owing to their similarity to the acoustic modes of the curved surfaces that were studied by Lord Rayleigh at the beginning of the 20th century. Strictly speaking, ring-resonators based on optical waveguides are not WGM resonators and can be efficiently modelled as closed-path loop resonators. We will, however, include them in this category for the sake of completeness [66]. We start this section by defining the mathematical model of the electromagnetic field in a generic resonator, including losses, dispersion, nonlinearity and additional coupling structures. We will use a coupled-mode theory approach [70], which will allow the description of the optical field as a superposition of resonator modes with time-varying amplitude. This approach allows for the separation of the dynamics of frequency comb generation from the spatial properties of the resonant modes that depend on the shape, size and materials that make up the micro-resonator device.

The study of the spatial problem will give us an explicit solution for the spatial profiles, i.e. the eigenmodes and, for the resonant frequencies, i.e. eigenfrequencies. These are determined independently from the explicit time dependence of the mode amplitudes. The solution of the spatial problem provides the cavity dispersion and effective mode volume that are the main input parameters of the device for the dynamical problem. The purpose of coupled-mode theory is to build a set of ordinary differential equations that can be used to track the temporal dynamics of each whispering-gallery mode belonging to the Kerr comb [21,23,144] and we refer to this set of equations as the temporal problem. These equations describe the exchange of energy among the modes and their phase evolution and they are usually defined in terms of the complex mode amplitudes. This separation simplifies the analysis and speeds up numerical simulations with respect to the full electromagnetic problem, while simultaneously allowing the influence of different effects to be isolated and considered individually. Once having defined the starting mathematical model (Section 3.1), we will outline the spatial properties of the micro-cavities that are fundamental for obtaining the parameters, e.g. resonance frequencies and mode shapes (Section 3.1.1), necessary to specify and explore the temporal dynamics (Section 3.1.2). Sections 3.2 and 3.3, respectively, outline the general linear and nonlinear temporal problems.

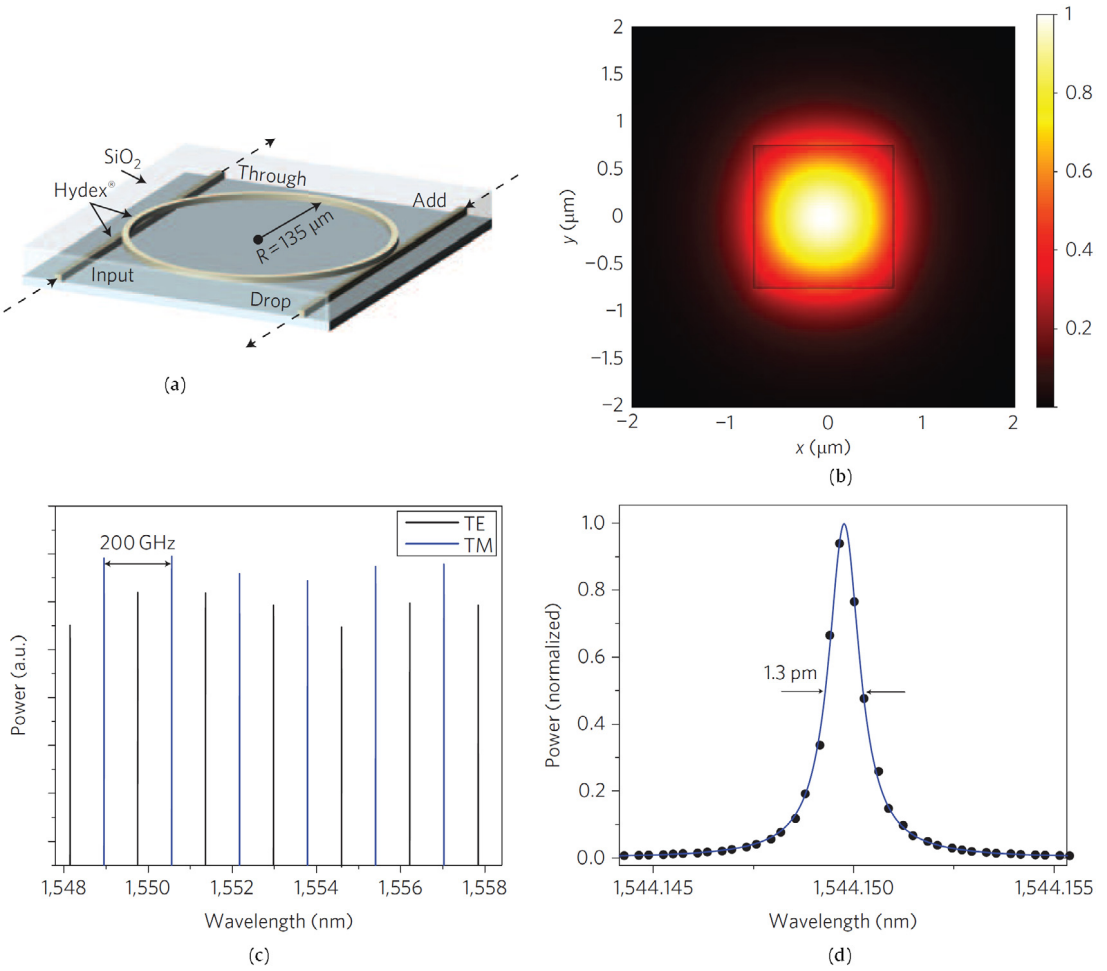

Fig. 8. Four-port Hydex micro-ring resonator (radius: 135 μm, FSR: 200 GHz, Q: 1.2×10^6). (a) Drawing of the four-port device. (b) Transverse mode profile in the waveguide for the fundamental TM mode. (c) Measured resonances in the C-Band for the TE and the TM modes. (d) High-resolution measurement of a single resonance. After Ref. [12].

3.1. Mathematical formulation of the optical field in the resonators

The description of the optical field in the micro-resonator starts with the electromagnetic equations in a dielectric cavity. If the resonator is isotropic, the electric $\mathbf{E}(\mathbf{r}, t)$ and magnetic $\mathbf{H}(\mathbf{r}, t)$ fields obey classical Maxwell equations [70]:

$$\begin{aligned} \nabla \times \mathbf{E}(\mathbf{r}, t) &= -\mu_0 \frac{\partial \mathbf{H}(\mathbf{r}, t)}{\partial t}, \\ \nabla \times \mathbf{H}(\mathbf{r}, t) &= \frac{\partial \mathbf{D}(\mathbf{r}, t)}{\partial t} + \frac{\partial \mathbf{P}^{\Delta}(\mathbf{r}, \mathbf{t})}{\partial t}, \end{aligned} \tag{1}$$

with $\nabla = \hat{\mathbf{x}}\partial/\partial x + \hat{\mathbf{y}}\partial/\partial y + \hat{\mathbf{z}}\partial/\partial z$ and ε_0 and μ_0 vacuum electric and magnetic permittivities. The Fourier transform $\tilde{\mathbf{D}}(\mathbf{r}, \omega)$[1] of the unperturbed linear dielectric displacement $\mathbf{D}(\mathbf{r}, t)$ is related to the electric field through:

$$\tilde{\mathbf{D}}(\mathbf{r}, \omega) = \varepsilon_0 \epsilon(\mathbf{r}, \omega) \tilde{\mathbf{E}}(\mathbf{r}, \omega). \tag{2}$$

[1] The Fourier transform $\tilde{\mathbf{E}}(\mathbf{r}, \omega)$ of the electric field $\mathbf{E}(\mathbf{r}, t)$ is defined as

$$\mathbf{E}(\mathbf{r}, t) = \frac{1}{2\pi} \int \tilde{\mathbf{E}}(\mathbf{r}, \omega) e^{-i\omega t} d\omega.$$

.

The relative permittivity $\epsilon(\mathbf{r}, \omega)$ is space and frequency dependent. Here it is assumed to be real and so it defines the geometry of an ideal lossless resonator. $\mathbf{P}^{\Delta}(\mathbf{r}, t) = \mathbf{P}^{\Delta}_{\mathbf{L}}(\mathbf{r}, t) + \mathbf{P}^{\Delta}_{\mathbf{NL}}(\mathbf{r}, t)$ is a polarisation vector that separately takes into account the linear $\mathbf{P}^{\Delta}_{\mathbf{L}}$ and nonlinear $\mathbf{P}^{\Delta}_{\mathbf{NL}}$ perturbations of the ideal resonator. Material absorption, geometric imperfections of the resonator, as well as coupling devices such as waveguides, fibres or prisms, can be taken into account in an additional dielectric function $\Delta\epsilon(\mathbf{r}, \omega)$, which is generally complex valued:

$$\tilde{\mathbf{P}}^{\Delta}_{\mathbf{L}}(\mathbf{r}, \omega) = \epsilon_0 \Delta\epsilon(\mathbf{r}, \omega)\tilde{\mathbf{E}}(\mathbf{r}, \omega). \tag{3}$$

Nonlinearity can be also taken into account. For the case of a scalar, isotropic and instantaneous Kerr nonlinearity (Raman and Brillouin processes will not be considered here), the complex amplitude of the nonlinear polarisation can be expressed as

$$\mathbf{P}^{\Delta}_{\mathbf{NL}}(\mathbf{r}, t) \approx \frac{3}{4}\varepsilon_0 \chi^{(3)} |\mathbf{E}(\mathbf{r}, t)|^2 \mathbf{E}(\mathbf{r}, t), \tag{4}$$

where we neglect third harmonic generation and negative frequency mixing effects [145].[2] These perturbations do not necessarily have to be small: the spatio-temporal Eq. (1) is, in general, exact and contains all the information about the optical field in the cavity [70,74]. It can be directly simulated using, for example, finite difference time-domain (FDTD) methods [146]. This approach, however, is usually avoided as it can be prohibitively time consuming for realistic frequency comb simulations.

Coupled-mode theory, conversely, is a powerful perturbative approach that is widely used in optics and which allows, in principle, analytic solutions to be obtained. It has been particularly useful for the modelling of optical resonators [70,147]. A specific derivation for micro-combs can also be found in [144]. It starts from the assumption that the electric field can be written as a linear combination of spatial eigenmodes with temporally varying amplitudes.

When $\mathbf{P}^{\Delta} = 0$, Eq. (1) is then linear and represents an ideal and lossless resonator. A generic solution to this problem can be obtained as a superposition of orthogonal eigenmodes. For dielectric resonators, these solutions are of two types: bounded and radiating. Bounded solutions belong to a discrete set labelled by a mode index and have finite and constant energy. They represent the modes confined in the resonator and decay exponentially outside it. Radiating solutions, conversely, belong to a continuous set that does not have a finite energy but instead has a finite power. Being orthogonal, such modes cannot exchange energy or power.

When $\mathbf{P}^{\Delta} \neq 0$, the electromagnetic problem changes, but the generic electromagnetic field can still be described in terms of modes of the ideal resonator under a suitable approximation. Such modes, however, will interact in time and exchange energy. For instance, scattering imperfections of the resonator will allow coupling between the confined and radiating modes, creating an important source of loss of the field stored in the resonator. The nonlinear coupling can transfer energy between different frequencies and is the physical mechanism at the basis of comb formation. The purpose of the coupled-mode theory is then to build a set of ordinary differential equations, one equation for each mode, which can be used to track their temporal dynamics and, in our specific case, to map the formation of a Kerr comb [21,23,144]. Using this approach, the complexity of Eq. (1) can be considerably reduced.

3.1.1. Spatial problem: eigenvalues and eigenmodes

The *spatial problem* aims to describe the electromagnetic field of a linear and lossless resonator defined by the real dispersive dielectric constant $\epsilon(\mathbf{r}, \omega)$. It is given by Eq. (1) for $\mathbf{P}^{\Delta} = 0$. A generic solution to this problem can be written in terms of a superposition of orthogonal eigenmodes, $\mathbf{E}_\ell$ and $\mathbf{H}_\ell$ of absolute frequency ω_ℓ. The theory of the modes in dielectric resonators has been treated by many authors [70]; for a review of whispering-gallery modes see, for example, [68,148]. Each mode satisfies the equations:

$$\begin{aligned} \nabla \times \mathbf{E}_\ell(\mathbf{r}) &= i\omega_\ell \mu_0 \mathbf{H}_\ell(\mathbf{r}), \\ \nabla \times \mathbf{H}_\ell(\mathbf{r}) &= -i\omega_\ell \varepsilon_0 \epsilon(\mathbf{r}, \omega_\ell)\mathbf{E}_\ell(\mathbf{r}), \end{aligned} \tag{5}$$

or, equivalently, the wave equation

$$\nabla \times \nabla \times \mathbf{E}_\ell(\mathbf{r}) - \frac{\omega_\ell^2 \epsilon(\mathbf{r}, \omega_\ell)}{c^2}\mathbf{E}_\ell(\mathbf{r}) = 0. \tag{6}$$

The cavity modes and the corresponding resonance frequencies result from the solution of the eigenmode problem Eq. (5), with the condition that the radiated power, i.e. the Poynting vector, towards infinity is zero [149]. This leads to a quantised mode spectrum where each mode and frequency can be labelled by a set of integer mode numbers represented by ℓ. We

[2] The nonlinear susceptibility is related to the Kerr refractive index as $n_2 = \frac{3}{4}\frac{\chi^{(3)}}{\varepsilon_0 c n_0^2}$, with c the speed of light and n_0 the refractive index at the carrier frequency.

normalise such modes with the following definition

$$\begin{aligned}\mathbf{E}_\ell(\mathbf{r};t) &= \sqrt{\frac{2}{\varepsilon_0 n_\ell^2 V_\ell}} a_\ell \mathbf{e}_\ell(\mathbf{r}) e^{-i\omega_\ell t} \\ \mathbf{H}_\ell(\mathbf{r};t) &= \sqrt{\frac{2}{\mu_0 V_\ell}} a_\ell \mathbf{h}_\ell(\mathbf{r}) e^{-i\omega_\ell t},\end{aligned} \tag{7}$$

where $\mathbf{e}_\ell(\mathbf{r})$ and $\mathbf{h}_\ell(\mathbf{r})$ represent the spatial profiles of the electric and magnetic mode fields, respectively, and they are normalised in such a way that they are dimensionless. They define the mode volume V_ℓ

$$V_\ell = \int_V \|\mathbf{h}_\ell(\mathbf{r})\|^2 dV \approx \int_V \|\mathbf{e}_\ell(\mathbf{r})\|^2 dV\,, \tag{8}$$

which represents the actual space filled by the optical field in the resonator. The integral is calculated over an infinite domain V and can be taken as equal to unity for orthonormal modes. The normalisation of the electric and magnetic fields are related through the impedance $\eta = \sqrt{\mu_0/(\epsilon_0 n_\ell^2)}$, where n_ℓ is an averaged refractive index that is conveniently defined here by

$$n_\ell^2 = \frac{\int_V \epsilon(\mathbf{r})\|\mathbf{e}_\ell(\mathbf{r})\|^2 dV}{\int_V \|\mathbf{e}_\ell(\mathbf{r})\|^2 dV}\,. \tag{9}$$

For travelling guided wave resonators, n_ℓ is the effective refractive index of the guided mode.

With this normalisation, the mode amplitudes a_ℓ can be expressed in $[\sqrt{J}]$, such that they are directly related to the energy-per-frequency of the mode W_ℓ,

$$W_\ell = \frac{1}{2}\int_V \varepsilon_0 \epsilon(\mathbf{r})\|\mathbf{E}_\ell(\mathbf{r})\|^2 dV = \frac{1}{2}\int_V \mu_0 \|\mathbf{H}_\ell(\mathbf{r})\|^2 dV = |a_\ell|^2, \tag{10}$$

where we have taken into account that the magnetic and electric energies of a resonant mode are equal. The total energy confined in the resonator is the superposition of the energies of the individual modes, i.e. $\sum_\ell W_\ell$, because the modes are orthogonal:

$$\int_V \mathbf{h}_m^*(\mathbf{r}) \cdot \mathbf{h}_\ell(\mathbf{r})\, dV = \delta_{\ell,m} V_\ell\,, \tag{11}$$

where $\delta_{\ell,m}$ is the Kronecker delta function, $\delta_{\ell,m} = 1$ for $\ell = m$, $\delta_{\ell,m} = 0$ otherwise. In general, for axially-symmetric resonators with arbitrary form, the spatial problem Eq. (5) must be solved numerically with the help of a mode solver, although approximate analytical solutions can be found for a number of simple geometries. Various commercial mode solvers are available based on, for example, the finite element method (FEM) [150,151].

It is instructive to consider, as a first example, a guided travelling wave resonator, e.g. a ring-shaped resonator or a fibre loop of length L. We consider a single-mode waveguide that has a propagation constant $\beta(\omega) = n_{\text{eff}}\omega/c$, where n_{eff} is the effective refractive index of the waveguide. When travelling in the resonator, the modes need to conserve their phase at every round-trip, this is represented by the condition

$$\beta(\omega_\ell)L = 2\pi\ell. \tag{12}$$

This relation allows us to find the eigenvalues ω_ℓ of the problem. If we neglect the dispersion of the effective refractive index, the resonant frequency scales linearly with the mode number

$$\omega_\ell = \frac{2\pi c}{n_{\text{eff}} L}\ell = 2\pi\ell\Delta F = \ell\Omega_{\text{R}}, \tag{13}$$

where $\Delta F = c/(n_{\text{eff}}L)$ is the free spectral range (FSR) of the cavity and $\Omega_{\text{R}} = 2\pi\Delta F$ the average angular eigenfrequency spacing. The FSR is an important design parameter that defines the round-trip time $t_R = 1/\Delta F$ of the light in the resonator and is commonly in the GHz to THz range for micro-resonators. Usually, micro-cavities are also characterised by the spectral non-equidistance of the resonant frequencies that comes from the frequency variation of the effective refractive index (i.e. dispersion), which will be discussed in Section 3.2.3. WGM resonators are, in general, designed to sustain travelling wave modes and it is possible to obtain a similar expression to Eq. (12) for the FSR of these families of modes. As an instructive example, we discuss the specific case of a spherical resonator in Appendix B and solve the eigenvalue problem.

3.1.2. Temporal problem: formal derivation of the coupled-mode theory

The electromagnetic fields $\mathbf{E}, \mathbf{H}$ form a generic solution of the complete system given by Eq. (1). We will express it in terms of resonator eigenmodes $\mathbf{E}_\ell, \mathbf{H}_\ell$ and start using a form of the reciprocity theorem [149], by combining Eqs. (1), (5) (see Appendix A):

$$\begin{aligned}&\int_V \left[\frac{\partial \mathbf{D}}{\partial t}\cdot\mathbf{E}_\ell^* + i\omega_\ell\varepsilon_0\epsilon(\mathbf{r},\omega_\ell)\mathbf{E}\cdot\mathbf{E}_\ell^*\right]dV + \mu_0\int_V\left[\frac{\partial \mathbf{H}}{\partial t}\cdot\mathbf{H}_\ell^* + i\omega_\ell\mathbf{H}\cdot\mathbf{H}_\ell^*\right]dV \\ &= -\int_V \frac{\partial \mathbf{P}^{\Delta}}{\partial t}\cdot\mathbf{E}_\ell^* dV.\end{aligned} \tag{14}$$

We now have to express the generic solution **E**, **H** as a superposition of resonator modes, each one oscillating at a distinct resonance frequency ω_ℓ. We will eventually develop a model that can take into account the behaviour of the resonator when loaded with a continuous-wave (CW) pump resonantly coupled into one of the micro-cavity modes. For this reason, we will also take into account an external pump field $\mathbf{E_P}$, $\mathbf{H_P}$ that can couple/decouple power into the resonator by a perturbation of the original resonator structure introduced by, for example, a prism or a waveguide. Additional radiating fields are assumed to be orthogonal to the confined resonator modes and are neglected in the analysis. Note also that surface inhomogeneities represent a perturbation of the ideal resonator and so can decouple energy from the resonator modes, transferring power into scattering modes. We define the complex field in time:

$$\begin{aligned}\mathbf{E}(\mathbf{r},t) &= \sum_\ell \mathbf{E}_\ell(\mathbf{r},t) + \mathbf{E_P}(\mathbf{r},t)\\ \mathbf{H}(\mathbf{r},t) &= \sum_\ell \mathbf{H}_\ell(\mathbf{r},t) + \mathbf{H_P}(\mathbf{r},t),\end{aligned} \tag{15}$$

which contains $a_\ell(t)$ that are the complex-valued modal amplitudes, under the assumption that $|a_\ell|^2$ is equal to the energy in the mode ℓ, following the normalisation used in Eq. (7). We make the a priori assumption that $a_\ell(t)$ is a slowly-varying function of time. It is assumed that the amplitude is a constant function of space and that the fast temporal variation corresponding to the eigenfrequency of the mode ω_ℓ can be separated from the slow temporal variation of the mode amplitude $a_\ell(t)$. The field in Eq. (15) can be substituted into the electric displacement Eq. (2) and in Eq. (14). Using the orthogonality of the modes Eq. (11) and Eqs. (8), (10) we obtain[3]

$$\frac{da_\ell(t)}{dt} = -\frac{1}{4}\sqrt{\frac{2}{\varepsilon_0 n_\ell^2 V_\ell}}\int_V \frac{\partial \mathbf{P}^{\Delta}}{\partial t}\cdot \mathbf{e}_\ell^* e^{i\omega_\ell t} dV. \tag{16}$$

With this approach, it is possible to build a set of ordinary differential equations, one equation for every complex modal amplitude. The right-hand side (RHS) term is responsible for the coupling between the different resonator modes and with the external fields. This system represents the temporal problem and gives the dynamic evolution of the energy and phase of each mode. Before going into the dynamic description, including the nonlinear effects, we discuss some basic linear properties of the resonator, starting from the linear dynamic coupling.

3.2. Linear properties of micro-resonators

In this section we will outline some general linear features of micro-resonators. We discuss some fundamental dynamic characteristics and define important quantities, such as the Q-factor and the modal dispersion, and then solve the spatial problem for a specific resonator system in Appendix B.

3.2.1. Linear mode coupling

Considering the slowly-varying envelope approximation and Eqs. (3), (15), for $\mathbf{P}_{\mathbf{NL}}^{\Delta} = 0$, Eq. (16) can be reduced to:

$$\frac{da_\ell(t)}{dt} = \sum_m \Gamma_{\ell,m} a_m(t) e^{i(\omega_\ell-\omega_m)t} + K, \tag{17}$$

where $\Gamma_{\ell,m}$ is the coupling coefficient between the modes:

$$\Gamma_{\ell,m} = \frac{i\omega_m}{2}\int_V \frac{\Delta\epsilon(\mathbf{r},\omega_m)}{n_\ell\, n_m}\mathbf{e}_m\cdot\mathbf{e}_\ell^*\frac{dV}{\sqrt{V_m V_\ell}}. \tag{18}$$

Although the resonator modes are orthogonal, the additional dielectric function $\Delta\epsilon(\mathbf{r},\omega)$ may couple the energies of the different modes. As usual in coupled-mode theory, the exponential function $\exp[i(\omega_\ell-\omega_m)t]$ in Eq. (17) rules out all the terms with a large phase mismatch $\omega_\ell - \omega_m$. Hence, only the modes with $\omega_m \approx \omega_\ell$ can interact. Such modes are called degenerate and these mode crossings can dramatically affect the generation of the micro-combs, as discussed in Section 6.2.1. In many cases, however, mode crossing can be neglected and we will not consider linear coupling between modes of different order

[3] We have approximated

$$\mathbf{D} \approx \sum_\ell \varepsilon_0\epsilon(\mathbf{r},\omega_\ell)\mathbf{E}_\ell(\mathbf{r},t) + \varepsilon_0\epsilon(\mathbf{r},\omega_R)\mathbf{E_P}(\mathbf{r},t)$$

for the slowly-varying complex amplitudes. Practically, we are neglecting the material dispersion inside every cavity mode.

here. $\Gamma_{\ell,\ell} = \Gamma_\ell$ represents the effect of the perturbation on the structure of the mode itself. The imaginary part of Γ_ℓ induces a change in the resonant frequency. We will not explicitly consider this effect here as it may be formally included in the modal dispersion of the resonator. The real part represents loss (gain is excluded, as we consider only passive devices). Material absorption losses can be taken into account via an imaginary dielectric coefficient. These represent the propagation losses of the system and we can put $\Gamma_\ell = 1/\tau_a$ where τ_a is the characteristic decay time of the mode energy.[4]

The variable K depicts the linear coupling of the applied external pump field with the confined modes and can be described in terms of overlapping coefficients similarly to Eq. (18), but it is more instructive to introduce a phenomenological description of this term. The external coupling K which is, in general, achieved through evanescent field coupling from an on-chip waveguide, a tapered fibre or by using prism couplers, can be used to transfer power to the resonator. The energy of the resonator will then increase at the time rate τ_e, which can be formally used to build up the coupling coefficient of the driving field to the resonator. The external coupling will also couple the energy of the resonator into an output optical field that carries energy away from the resonator. From time-reversal properties [70], the decay rate of the energy needs to be the same τ_e. This effectively results in a loss term that can be formally expressed as $a_\ell(t)/\tau_e$, similar to the case of the absorption losses. Notably, surface inhomogeneities of the resonator can also induce coupling between the resonator modes and scattering modes. These losses, characterised by a decay constant τ_s, can be added up with a term $a_\ell(t)/\tau_s$. We can now write the final equation, where we explicitly consider the resonator loaded with a CW pump as:

$$\frac{da_\ell(t)}{dt} = -\frac{1}{\tau}a_\ell(t) + \sqrt{\frac{2}{\tau_e}}E_{in}e^{i(\omega_\ell-\omega_p)t}. \tag{19}$$

Eq. (19) is characterised by several key parameters. The first is the total loss of the modes, which is assumed to be the same (degenerate) for all modes. They are characterised by the loaded time decay $\tau = (\tau_i^{-1} + \tau_e^{-1})^{-1}$, which is composed of the intrinsic and extrinsic losses τ_i and τ_e, respectively. The variable τ_e models the extrinsic losses, which depend on the coupling geometry and are the price to pay for transferring energy to the resonator. The intrinsic losses, $\tau_i = (\tau_s^{-1} + \tau_a^{-1})^{-1}$, conversely depend on the resonator itself. The scattering losses, τ_s, are usually the main limitation [85] and depend on resonator manufacturing and preparation techniques (e.g. polishing or etching). By contrast, the absorption losses τ_a instead represent a fundamental limitation (Rayleigh, Brillouin and Raman scattering that influence the absorption losses have also been studied for crystalline WGM resonators, see [152]). Radiation losses could additionally be taken into account but they vanish exponentially with increasing resonator size and are, therefore, generally negligible for resonators with dimensions larger than a few wavelengths.

The cavity is driven by a CW pump with frequency ω_p and power $|E_{in}|^2$ through the input coupling coefficient $\sqrt{2/\tau_e}$, which only depends on the extrinsic losses τ_e. In the case of a single coupler, the field at the output coupler for every mode is given by

$$E_\ell = E_{in}e^{i(\omega_\ell-\omega_p)t} - \sqrt{\frac{2}{\tau_e}}a_\ell, \tag{20}$$

that is also in $[\sqrt{W}]$. As noted above, a rapidly varying exponential function $\exp[i(\omega_\ell - \omega_p)t]$ cancels the coupling terms. We will consider the case where the pump is resonantly coupled with the mode with index $\ell = \ell_0$, i.e. with $\omega_p = \omega_{\ell_0} + \sigma$, and σ being a small de-tuning. The coupling of the pump to the other modes is assumed to be zero.

3.2.2. Linewidth and quality factor

It is useful to consider the solution to the simple linear equation Eq. (19). It is easy to verify that:

$$a_\ell(t) = \frac{\sqrt{2/\tau_e}}{\frac{1}{\tau} + i(\omega_\ell - \omega_p)}E_{in}e^{i(\omega_\ell-\omega_p)t}. \tag{21}$$

From Eq. (21) we notice that τ defines the acceptance bandwidth of the resonance $\Delta\omega = 2/\tau$, defined as full width at half maximum. The bandwidth of the resonance is typically quite narrow, thus justifying the separation of the mode amplitude from the fast temporal variation of the carrier frequency. The resonator is said to be critically coupled when the internal losses are equal to the coupling losses, i.e. $\tau = \tau_e/2$. Under such conditions, a resonant incident field can be fully absorbed by the resonator [147] and the output field Eq. (20) is zero.

When we turn off the source E_{in}, it is easy to verify that the energy of the mode W_0 decays with a time constant proportional to τ:

$$\frac{d|a_\ell(t)|^2}{dt} = -\frac{2}{\tau}|a_\ell(t)|^2 \text{ or } P_\ell = -\frac{2}{\tau}W_\ell, \tag{22}$$

where P_ℓ represents the power dissipated by the mode.

[4] Losses can be calculated from Eq. (18) by considering an imaginary dielectric perturbation $\Delta\epsilon = i\alpha n_\ell c\omega_\ell^{-1}$, with α the absorption of the material, expressed in $[m^{-1}]$. For a highly-confined mode we have

$$\Gamma_\ell \approx -\frac{\alpha c}{2n_\ell} = \frac{1}{\tau_a}$$

.

We can now define the quality (Q) factor, which is a fundamental figure of merit for micro-resonators and which measures the ability of the resonator to confine light. Operatively, the Q-factor can be defined as the ratio between the linewidth and the resonant frequency. We have

$$Q = \frac{\omega_\ell}{\Delta\omega} = \frac{\tau\omega_\ell}{2} = \frac{W_\ell\omega_\ell}{P_\ell}. \tag{23}$$

Considering that the energy lost per optical cycle is $P_\ell\omega_\ell$, the Q-factor is then the ratio between the stored energy W_ℓ of the mode and the dissipated energy per optical cycle. Ultra-high Q-factors are desired for many applications: Q-factors as high as $Q \approx 10^{11}$ have been demonstrated in crystalline WGM resonators [84], while micro-rings have more modest Q-factors in the order of $Q < 10^7$. Following the distinction between the different sources of loss discussed above, it is common to distinguish between the intrinsic, extrinsic (or coupling) and the loaded (or total) Q-factors, which are directly related to each other by

$$Q_{\text{tot}}^{-1} = Q_{\text{int}}^{-1} + Q_{\text{ext}}^{-1}. \tag{24}$$

It follows from the above relation that the loaded Q-factor is lower than both the intrinsic and extrinsic Q-factors. The optical finesse $\mathcal{F}$ is sometimes used instead of the Q-factor, which is directly related to the FSR $\Delta F = \Omega_{\text{R}}/(2\pi)$:

$$\mathcal{F} = \frac{\Omega_{\text{R}}}{\Delta\omega} \approx \frac{Q}{\ell}, \tag{25}$$

where we used the approximate relation Eq. (13). When the losses of the resonator and, hence, τ are invariant with frequency, $\mathcal{F}$ is independent of the resonance frequency and is rather a property of the resonator, while the Q-factor increases with the order of the resonance frequency.

3.2.3. Cavity dispersion

Cavity dispersion is one of the most important characteristics of a micro-resonator due to its profound influence on the dynamic evolution of different comb states and its importance for the comb bandwidth. We start by considering a travelling wave resonator with propagation constant $\beta(\omega)$ and the resonant condition expressed by Eq. (12), which has a frequency dependence that is generally nonlinear. Formally, we can define an inverse function ζ of the propagation constant β and, in this case, the eigenfrequencies are defined as

$$\omega_\ell = \zeta\left(\frac{2\pi\ell}{L}\right). \tag{26}$$

Let us consider that the eigennumber of the pumped (reference) mode is $\ell = \ell_0$. In the spectral neighbourhood of ℓ_0, the eigenfrequencies of the resonator can be expanded in a Taylor series, as follows:

$$\omega_\ell = \omega_{\ell_0} + \sum_{n=1}^{N} \frac{\zeta_n}{n!}(\ell - \ell_0)^n, \tag{27}$$

where N is the order of truncation for the expansion. The coefficients ζ_n can be related to the Taylor expansion coefficients β_n of the propagation constant $\beta(\omega)$ via the following relation:

$$\zeta_n = \left(\frac{2\pi}{L}\right)^n \frac{d^{n-1}}{d\omega^{n-1}}\left[\frac{\omega - \omega_0}{\beta(\omega) - \beta(\omega_0)}\right]\Bigg|_{\omega=\omega_0} \approx -v_g(\Omega_{\text{R}})^n\beta_n, \tag{28}$$

where $v_g = 1/\beta_1$ is the group velocity. The last equality is exact up to ζ_2. The first Taylor coefficient of the expansion (27) is related to the resonator FSR, $\zeta_1 = \Omega_{\text{R}} = 2\pi\Delta F$. The second Taylor coefficient ζ_2 corresponds to the second-order group velocity dispersion. It is positive for anomalous dispersion and negative for normal dispersion. It should be recalled that ζ_2 generally takes into account two contributions, namely the geometrical dispersion and the material dispersion (either normal or anomalous). The parameters ζ_n for $n \geq 3$ stand for higher-order dispersion terms, which are generally neglected for combs with narrow bandwidths but have to be accounted for when the spectral extension of the comb becomes significantly large, such as in the case of octave-spanning combs. The optical modes and the concomitant resonant frequencies are, in general, determined both by the geometric shape of the cavity and also by the distribution of the refractive index inside and outside the resonator. The dispersion properties stem from the non-equidistance of the cavity modes due to the frequency dependence of the effective refractive index and are of primary importance for frequency comb generation, as dispersion can determine the sideband spacings and the attainable bandwidth of the optical frequency comb. Both the material refractive index dispersion, as well as the geometry of the resonator, contribute to the overall dispersion and this allows, for example, resonators with normal material dispersion to operate in the anomalous dispersion régime through careful design of the device geometry. Engineering the dispersion is of critical importance for many applications where a wideband frequency comb is desired (see Section 5.5).

3.3. Nonlinear properties of micro-resonators

Now that we have discussed in detail the linear properties of the resonator and the spatial problem, we can focus on the dynamics of the nonlinear field inside the resonator. The purpose of the coupled-mode theory is to build a set of ordinary differential equations that can be used to track the temporal dynamics of each whispering-gallery mode belonging to the Kerr comb [21,23,144].

3.3.1. Nonlinear coupling coefficients and mode volume

We start by calculating the nonlinear coupling term in Eq. (16) due to the nonlinear polarisation in Eq. (4). We obtain:

$$-\frac{1}{4}\sqrt{\frac{2}{\varepsilon_0 n_\ell^2 V_\ell}}\int_V \frac{\partial \mathbf{P}_{\mathbf{NL}}^{\Delta}}{\partial t}\cdot \mathbf{e}_\ell^* e^{i\omega_\ell t}dV = \sum_{k,m,q}\Gamma_{\ell,q}^{k,m} a_k(t)a_m(t)a_q^*(t)e^{i(\omega_\ell+\omega_q-\omega_k-\omega_m)t}. \tag{29}$$

The overlap parameter $\Gamma_{\ell,q}^{k,m}$ is an intermodal coupling tensor which weighs the spatial and spectral overlap among the interacting modes:

$$\Gamma_{\ell,q}^{k,m} = i(\omega_k+\omega_m-\omega_q)\frac{3}{4\varepsilon_0}\int_V \frac{\chi^{(3)}(\mathbf{r})\mathbf{e}_k\cdot\mathbf{e}_\ell^*\cdot\mathbf{e}_m\cdot\mathbf{e}_q^*}{n_k n_\ell n_m n_q\sqrt{V_k V_\ell V_m V_q}}dV, \tag{30}$$

where V_ℓ is the mode volume Eq. (8). This expression can be simplified. First of all, the phase mismatch $\omega_\ell+\omega_q-\omega_k-\omega_m$ of the exponential term in Eq. (29) needs to be small for efficient energy exchange between the modes. The nonlinear susceptibility $\chi^{(3)}$ is usually considered constant over the mode volumes and we make the approximation of quasi-degenerate modes in the spatial domain, which is usually the case for modes belonging to the same mode family, so that $\mathbf{e}_\ell \approx \mathbf{e}_{\ell_0}$. For similar reasons, we assume the refractive indices are also degenerate and so we obtain:

$$\Gamma_{\ell_0} = i\omega_\ell\frac{3}{4}\frac{\chi^{(3)}}{\varepsilon_0 n_{\ell_0}^4}\frac{\int_V \left\|\mathbf{e}_{\ell_0}\right\|^4 dV}{\left[\int_V \left\|\mathbf{e}_{\ell_0}\right\|^2 dV\right]^2} = i\omega_\ell\frac{n_2\, c}{n_{\ell_0}^2 V_{\text{eff}}}, \tag{31}$$

where we explicitly take into account the Kerr refractive index $n_2 = 3\chi^{(3)}/(4\varepsilon_0 c n_{\ell_0}^2)$ in $[\text{W}^{-1}\text{m}^2]$. We have additionally removed the dependence on the indices k, m and q.

The effective mode volume of the cavity $V_{\text{eff}} = V_{\ell_0}^2\left[\int_V \left\|\mathbf{e}_{\ell_0}\right\|^4 dV\right]^{-1}$ is an important figure of merit, although it should be noted that other definitions also exist - see, for example [83,107,150]. The effective mode volume is related to the peak strength of the confined field and its significance stems from the fact that a small mode volume decreases the threshold for optical bi-stability and nonlinear wave-mixing processes. A small mode volume can compensate for a weak nonlinearity, as it is inversely accounted for in the nonlinear coupling coefficient Eq. (31). A small mode volume is necessary for providing a large field enhancement. This will ensure high efficiency for nonlinear processes, such as wavelength conversion [153], and a low threshold intensity for processes such as modulational instability and parametric oscillation. Although the effective mode volume can be made smaller by, for example, decreasing the cross section of a micro-ring resonator, it often comes at the expense of increasing the magnitude of the dispersion. Thus, there can be a trade-off between achieving low dispersion and a small mode volume [154].

A similar trade-off for simultaneously achieving high-Q and small mode volume also exists for spherical resonators. The nonlinear interaction efficiency will reach a maximum for an optimal size of the micro-sphere. The efficiency of nonlinear interactions scales as Q^2/V_{eff}, while both the Q-factor and the mode volume typically grow as the size of the resonator is increased.

When considering guided travelling-wave resonators, it is useful to express the coupling coefficient $\Gamma_{\ell,q}^{m,n}$ in terms of the waveguide nonlinear coefficient $\gamma = \omega_{\ell_0} n_2/(cA_{\text{eff}})$, which is expressed in $[\text{W}^{-1}\text{m}^{-1}]$. The variable A_{eff} is the effective nonlinear mode area of the waveguide, analogous to the definition of the effective mode volume. If the length of the travelling-wave resonator is L, the mode volume can be related to the effective mode area as $V_{\text{eff}} = A_{\text{eff}}L$ and, if we neglect the frequency variation, we obtain a nonlinear coupling coefficient:

$$\Gamma_{\ell_0} = i\gamma\frac{c^2}{n_{\ell_0}^2 L} \approx i\gamma\frac{v_g}{t_R}, \tag{32}$$

where $v_g = L/t_R$ is the group velocity and t_R is the round-trip time. The coupling coefficient Γ_{ℓ_0} is expressed in $[J^{-1}s^{-1}]$.

3.4. Coupled-mode theory: the dynamic problem for resonant continuous-wave pumping

The Kerr nonlinearity can transfer energy from the pump to different resonator modes. Note that, generally speaking, such coupled-mode models are restricted to frequency combs involving the modes of the same family in the transverse direction. In that case, the modes can be unambiguously labelled by a single eigennumber ℓ, related to the order of the mode in the azimuthal (or longitudinal) direction [68,106].

We begin by developing a model that can take into account the behaviour of the resonator when loaded with a CW pump resonantly coupled into one of the micro-cavity resonances. We extend the linear system Eq. (19) by including the nonlinear term given by Eq. (29) in Eq. (16), where we will consider the nonlinear coupling coefficient Eq. (32). As in the case of Eq. (19), the cavity is loaded with a CW pump with power $|E_{\rm in}|^2$ resonantly coupled into the mode ℓ_0 with frequency $\omega_{\rm p} = \omega_{\ell_0} + \sigma$, where σ is the laser de-tuning shift. The nondispersive total and coupling losses are τ and $\tau_{\rm e}$, respectively.

$$\begin{aligned}\frac{da_\ell(t)}{dt} &= -\frac{1}{\tau}a_\ell(t) + \delta_{\ell,\ell_0}\sqrt{\frac{2}{\tau_{\rm e}}}E_{\rm in}e^{i(\omega_{\ell_0}-\omega_{\rm p})t} \\ &+ \Gamma_{\ell_0}\sum_{n,q,m}\delta_{\ell+q-m-n,0}a_n(t)a_m(t)a_q^*(t)e^{i(\omega_\ell+\omega_q-\omega_m-\omega_n)t}.\end{aligned} \tag{33}$$

Eq. (33) explicitly depends on time due to the laser de-tuning shift σ and the dispersion shifts generated by the nonlinear phase terms $\omega_\ell + \omega_q - \omega_m - \omega_n$, which are expressed with respect to the non-equidistant frequency grid ω_ℓ.

These explicit time dependencies can be removed by setting the reference frequency to $\omega_{\rm p}$ and by expressing the modal fields with respect to an equidistant (dispersion-less) frequency grid . These transformations mathematically correspond to the substitution:

$$a_\ell = \bar{a}_\ell\ \exp[i(\omega_\ell - \omega_{\rm p} - \zeta_1 l)t] = \bar{a}_\ell\ \exp[i(\omega_\ell - \omega_{\ell_0} - \zeta_1 l - \sigma)t]\,, \tag{34}$$

and, by inserting Eq. (34) into Eq. (33), we find that the dynamics of the new modal fields $\bar{a}_\ell$ are governed by the equation system:

$$\begin{aligned}\frac{d\bar{a}_l(t)}{dt} &= i\sigma\bar{a}_l(t) - i\left[\sum_{n=2}^{N}\frac{\zeta_n}{n!}l^n\right]\bar{a}_l(t) - \frac{1}{\tau}\bar{a}_\ell(t) + \delta_{l,0}\sqrt{\frac{2}{\tau_{\rm e}}}E_{\rm in} \\ &+ \Gamma_{\ell_0}\sum_{n,q,m}\delta_{l+q-m-n,0}\bar{a}_n(t)\bar{a}_m(t)\bar{a}_q^*(t),\end{aligned} \tag{35}$$

which has the mathematical advantage of being autonomous. When recalling that the eigennumber of the pumped mode is ℓ_0 and that the eigenfrequencies of the resonator can be expanded as in Eq. (27), it proves convenient to introduce the reduced eigennumber $l = \ell - \ell_0$, which is such that the pumped mode is $l = 0$, while the side-modes are labelled as $l = \pm1, \pm2$, etc. The dispersion parameters β_n, corresponding to the Taylor series coefficients of the propagation constant $\beta(\omega)$ used in waveguide optics, are linked to the eigenfrequency dispersion terms as in Eq. (28), while the relation of the nonlinear Γ_{ℓ_0} coefficient with the waveguide nonlinearity γ is given by Eq. (32). These terms can be inserted into Eq. (35) to yield

$$\begin{aligned}\frac{d\bar{a}_l(t)}{dt} &= i\sigma\bar{a}_l(t) + iv_g\left[\sum_{n=2}^{N}(\Omega_{\rm R})^n\frac{\beta_n}{n!}l^n\right]\bar{a}_l(t) - \frac{1}{\tau}\bar{a}_\ell(t) + \delta_{l,0}\sqrt{\frac{2}{\tau_{\rm e}}}E_{\rm in} \\ &+ i\gamma\frac{v_g}{t_{\rm R}}\sum_{n,q,m}\delta_{l+q-m-n,0}\bar{a}_n(t)\bar{a}_m(t)\bar{a}_q^*(t).\end{aligned} \tag{36}$$

It is sometimes useful to express the energy coupled in the modes as power per round-trip, using the transformation

$$\mathcal{E}_l = \sqrt{\frac{1}{t_{\rm R}}}\,\bar{a}_l\,. \tag{37}$$

The new equations are explicitly written as

$$\begin{aligned}\frac{d\mathcal{E}_l}{dt} &= -\frac{1}{2}\Delta\omega_{\rm t}\,\mathcal{E}_l + i\sigma\mathcal{E}_l + iv_g\left[\sum_{n=2}^{N}(\Omega_{\rm R})^n\frac{\beta_n}{n!}l^n\right]\mathcal{E}_l \\ &+ iv_g\gamma\sum_{n,q,m}\delta_{l+q-m-n,0}\,\mathcal{E}_n\mathcal{E}_q^*\mathcal{E}_m + \delta_{l,0}\sqrt{\frac{\Delta\omega_{\rm e}}{t_{\rm R}}}\,E_{\rm in}\,,\end{aligned} \tag{38}$$

where we also expressed the losses in terms of linewidths $\Delta\omega_{\rm t} = 2/\tau$ and $\Delta\omega_{\rm e} = 2/\tau_{\rm e}$.

Note that most articles dealing with coupled-mode theory adopt the convention that there is a negative sign in front of the Kerr term [21,23,144]; while most articles related to the spatiotemporal model generally adopt the convention where this sign is positive [22,46,47]. The physical content of the models is identical in both cases and complex conjugation allows one to pass from one convention to the other.

3.5. Optical parametric generation in Kerr resonators

The first important phenomenon to discuss in the context of micro-comb generation is optical parametric oscillation (OPO). The fourth term on the right-hand side of Eq. (38) explicitly shows that the Kerr nonlinearity allows the mixing of

four different photons. In particular, two photons of an optical pump with frequency ω_p can annihilate to generate two photons at signal and idler frequencies ω_s and ω_i, respectively. This process is known as degenerate four-wave mixing but is also referred to as optical parametric oscillation and modulation instability. Because of energy conservation, the pump, signal and idler photons must satisfy the relation:

$$2\omega_p = \omega_s + \omega_i. \tag{39}$$

Thus, the generated signal and idler frequencies appear symmetrically-distributed with respect to the central pump frequency and, therefore, necessarily need to be expressed in terms of symmetrically-distributed frequencies, e.g. $\omega_s = \omega_{+l}$ and $\omega_i = \omega_{-l}$, following the convention defined in the paragraph above. We now focus only on a single pair of signal and idler waves defined by the mode numbers $\pm l$. Below oscillation threshold, with only the pump coupled to the resonator, linearised equations for these two modes can be obtained from Eq. (38), which is reduced to:

$$\begin{aligned}\frac{d\mathcal{E}_{\pm l}}{dt} = &\left(-\frac{1}{2}\Delta\omega_t + i\sigma + iv_g\left[\sum_{n=2}^{N}(\Omega_R)^n\frac{\beta_n}{n!}(\pm l)^n\right]\right)\mathcal{E}_{\pm l}\\ &+ iv_g\gamma\left(2|\mathcal{E}_0|^2\right)\mathcal{E}_{\pm l} + iv_g\gamma\mathcal{E}_0^2\mathcal{E}_{\mp l}^*.\end{aligned} \tag{40}$$

In the first term on the second line of Eqs. (40), we have the cross-phase modulation (XPM) due to the pump. This takes into account that the Kerr effect directly modifies the refractive index experienced by the different modes, with a linear dependence on the mode intensity - the pump intensity being the dominant factor here. Note that the self-phase modulation (SPM) and XPM terms, due to the signal/idler modes, are neglected here as we are focusing on the linearised behaviour below threshold. Moreover, the pump field $\mathcal{E}_0$ is obtained from Eq. (38) by solving the equation for the pump mode with $l = 0$ and retaining the driving laser field E_{in} only. The steady-state pump field has a bi-stable response depending on the de-tuning and the power of the driving field (see Section 5 and Eq. (56) for more details).

The last term, conversely, takes into account the energy exchange between the pump, signal and idler modes. We can see that Eqs. (40) support the trivial solution ($\mathcal{E}_{\pm l} = 0$ for $l \neq 0$). Such a solution is stable for low pump energies. However, when the energy of the pump is high enough, this solution can become unstable and the signal and idler waves will grow at the expense of the pump energy. The incremental rate of gain of the signal and idler frequencies is called parametric gain. From a practical point of view, the parametric gain can be found by studying the linear stability around the equilibrium point ($\mathcal{E}_{\pm l} = 0$). With this analysis, we obtain the growth coefficient κ for a perturbation of the solution (that is the real part of the eigenvalue of the perturbed equation). The overall parametric gain associated with Eqs. (40) is then:

$$\kappa = G - \frac{\Delta\omega_t}{2}, \tag{41}$$

with G being the so-called parametric gain of the nonlinear interaction, which takes into account the energy transfer from the pump to the side-modes:

$$G = \mathrm{Re}\{\sqrt{v_g^2\gamma^2|\mathcal{E}_0|^4 - \Delta\phi^2}\}. \tag{42}$$

A very important parameter in Eq. (42) is the effective phase mismatch $\Delta\phi$ that is given by:

$$\Delta\phi = \sigma + v_g\left[\sum_{n=2}^{N/2}(\Omega_R)^{2n}\frac{\beta_{2n}}{(2n)!}(l)^{2n}\right] + 2v_g\gamma|\mathcal{E}_0|^2. \tag{43}$$

The side-modes of the pump grow when $\kappa > 0$. This condition defines the threshold for oscillation, which can be achieved when the signal and idler modes experience a gain G large enough to overcome the intrinsic loss of the device, expressed by the term $\Delta\omega_t$ in Eq. (41). The square root term in Eq. (42), conversely, is real only when the energy of the pump is large enough to have $v_g\gamma|\mathcal{E}_0|^2 > \Delta\phi$. The phase mismatch term in Eq. (43), which is dependent on the mode number l, controls the bandwidth of parametric gain. Such a parameter depends on the pump intensity in two ways: (i) the gain increases with the square of the pump intensity [155], hence, for higher pump powers, more modes can overcome the threshold for oscillation and (ii) the Kerr effect also directly modifies the refractive index experienced by the different modes (via SPM/XPM), with a linear dependence on the pump intensity. Note also (from Eq. (43)) that the cavity de-tuning σ may compensate for the dispersive mismatch and lead to parametric gain, even in the case of normal dispersion [38,48].

This picture effectively describes some important properties of OPOs, such as threshold and bandwidth, which are dealt with in more detail in Section 4. The complex interaction among the generated frequencies and the coherence properties of the radiation will be discussed in detail in Section 5, as these are better discussed in the context of the alternative time-domain mean-field theory (LLE), which allows for recovering and describing the parametric gain in the frame of the modulation instability picture.

3.6. Thermal effects

To conclude this section, we briefly summarise the thermo-optical effects that can arise in micro-resonator devices, as they have a fundamental role in the control of micro-combs since they effectively modify the refractive index of the resonator as a function of the pump power.

When pumped with laser light, WGM resonators with ultra-high-Q-factors can contain optical fields whose intensities can be higher than 1 GW/cm^2. The volume of the intra-cavity field can therefore be subjected to a strong increase in temperature. Subsequently, the modal volume plays the role of a heat source which diffuses the heat inside the bulk resonator. Finally, the resonator transfers part of this heat to the surroundings. Understanding this phenomenon is essential for many reasons.

Firstly, the refractive index is temperature dependent and so the bulk optical properties, such as the group velocity, are also affected by the intra-cavity field via the induced temperature variation. This effect is essentially restricted to the modal volume. Secondly, as the resonator heats up, it undergoes a thermal dilatation which modifies its main radius. Both effects induce a shift of the free spectral range or, equivalently, of the WGM resonances. These shifts are critical in Kerr comb generation because they modify the de-tuning between the resonance and the laser frequency. The overall frequency shift can be explicitly expressed as

$$\Delta\omega = -\omega_0 \left[\alpha_1 \Delta T_1 + \alpha_2 \Delta T_2\right], \tag{44}$$

where ΔT_1 is the temperature change of the modal volume, ΔT_2 the average temperature shift of the full resonator and $\alpha_{1,2}$ are coefficients enabling the conversion from temperature to frequency shifts.

The two effects highlighted above can be either stochastic or deterministic, depending on the physical origin of the variables ΔT_1 and ΔT_2. Random temperature shifts correspond to fast timescale thermodynamic fluctuations, whereas slow timescale thermal shifts can be considered as deterministic. In the stochastic case, these thermal effects are associated with fundamental fluctuations set by the laws of statistical thermodynamics. In the deterministic case, thermal effects can either induce a desired locking between the laser and the resonance frequencies, or undesired thermo-optical oscillations [156].

3.6.1. Thermal noise

At a constant temperature, bulk WGM resonators host a wide variety of fluctuation and dissipation phenomena related to the thermal equilibrium between the resonator and its environment. These fluctuations are of a statistical nature and they set fundamental levels of the noise floor for any applications of WGM resonators for a given temperature. These fundamental limitations, which have been comprehensively analysed in Refs. [157,158], are briefly outlined here.

Thermo-refractive noise is induced by fluctuations in the refractive index with temperature of the mode volume. This noise contribution, therefore, depends on the volume of the modes under consideration and on the temperature in these mode volumes. The relative variation of the related eigenfrequency fluctuations is

$$\frac{\langle(\Delta\omega)^2\rangle}{\omega^2} = \alpha_n^2 \frac{k_B T_m^2}{C_\mathrm{p} V_m \rho}, \tag{45}$$

where k_B is the Boltzmann constant, T_m is the absolute temperature in the mode volume, $\alpha_n = (1/n)(\partial n/\partial T)$ is the thermo-refractive coefficient, V_m is the mode volume, C_p is the specific heat capacity at constant pressure and ρ is the volumetric mass.

Thermo-elastic noise originates from the elastic fluctuations of the resonator main radius a, which is determined by the temperature-induced fluctuation of the resonator's volume. The relative variance of these eigenfrequency fluctuations is

$$\frac{\langle(\Delta\omega)^2\rangle}{\omega^2} = \alpha_L^2 \frac{k_B T_r^2}{C_\mathrm{p} V_r \rho}, \tag{46}$$

where $\alpha_L = (1/L)(\partial L/\partial T)$ is the linear thermal expansion coefficient, T_r is the resonator temperature and the other parameters are the same as for the case of thermo-refractive noise.

Thermal expansion noise corresponds to the eigenfrequency fluctuation mediated by the volumetric expansion of the resonator. Its relative variance obeys the relation

$$\frac{\langle(\Delta\omega)^2\rangle}{\omega^2} = \beta_T \frac{k_B T_r}{9 V_r}, \tag{47}$$

where $\beta_T = -[(1/V)(\partial V/\partial p)]_T$ is the isothermal compressibility of the resonator host material, V_r is the resonator volume, while the other parameters are defined as in the previous cases.

3.6.2. Thermal locking

The deterministic temperature-induced frequency shifts are linked to the intra-cavity power, that is, to the square modulus of the intra-cavity field. However, such a quantity responds linearly to these frequency shifts. Linking both mechanisms from a mathematical perspective yields an autonomous set of coupled nonlinear equations describing how the intra-cavity field, the mode temperature and the resonator temperature can mutually influence each other.

Depending on the absolute value and the sign of the coefficients α_1 and α_2, thermal-locking phenomena can take place, which may play a favourable role for Kerr comb generation. In that case, as the wavelength of the pump laser is scanned, the intra-cavity power displays an hysteresis-like behaviour with three equilibria. As usual, the intermediate solution in the hysteretic area is unstable, while the extremal ones are stable against small power and/or frequency fluctuations. The uppermost solution is the one that has to be targeted for Kerr comb generation and corresponds to the so-called *thermal self-locked state*, since it guarantees, at the same time, high-power and stability against small perturbations [159]. It is

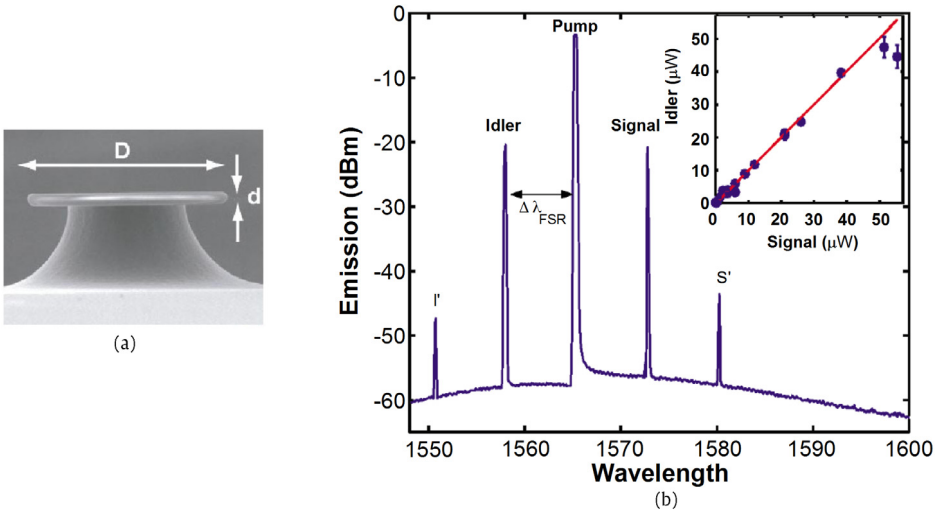

Fig. 9. (a) Scanning Electron Microscopy (SEM) image of a toroidal micro-cavity, indicating the geometry parameters. (b) Parametric oscillation spectrum for a toroidal cavity with $D = 67\ \mu m$ and $d = 3.9\ \mu m$. The inset shows the idler emission power as a function of the signal emission power. After Ref. [20].

noteworthy that, in the most unfavourable configuration and, depending on α_1 and α_2, nonlinear oscillations (stationary or non-stationary) can take place in the WGM resonator instead of thermal locking [160–162]. This latter case is generally incompatible with key applications of Kerr frequency combs but might be useful for other applications, such as thermo-optomechanical oscillators [163].

4. Micro-combs based on optical parametric oscillation

In this section, we review the early experiments on optical parametric oscillation in Kerr micro-resonators. We follow an almost historical perspective, starting from the first demonstration of optical parametric oscillation in micro-resonators [20, 21] and the demonstration of large bandwidth spectral generation [8], which opened up the potential of employing nonlinear micro-cavities as ultra-compact optical frequency comb sources. We identify the first experimental study of the coherence properties of micro-combs by Ferdous et al. [10] as the turning point of these investigations, which subsequently triggered a substantial body of theoretical works.

4.1. First observations: overcoming the optical parametric oscillation threshold

OPO in micro-resonators is based on the optical third-order nonlinearity. As detailed in Section 3.5, the Kerr effect allows the mixing of four different photons. As with optical parametric generation in quadratic materials [155], in third-order OPOs an optical pump with frequency ω_p can be used to generate two twin frequencies in a Kerr resonator, ω_s and ω_i, usually referred to as signal and idler frequencies.

In micro-cavities, the pump is usually coupled into one of the resonances of the device. In order to achieve oscillation, the parametric gain, as defined in Eq. (42), needs to overcome the loss of the device. Therefore, the modes of the resonator that first achieve this condition are the frequencies near the maxima of the parametric gain curves.

Energy conservation imposes the relation in Eq. (39), i.e. $2\omega_p = \omega_s + \omega_i$, and this allows only frequency pairs that are equidistant from the pump frequency ω_p to oscillate. However, there is a complex interplay between this restriction and the micro-resonator FSR which, in general, is not constant even for modes of the same family and order. As discussed in Section 3.5, the dispersion arising from both material properties and from waveguide or geometry induces a progressive shift in the mode resonances from their ideally equally-spaced distribution.

The frequency range where oscillation can take place is, therefore, restricted and defined by the bandwidth of the cavity parametric gain Eq. (41) or, equivalently, cavity modulation instability gain, to be discussed in Section 5.5.1.

Parametric oscillation was reported in micro-resonators for the first time in 2004 by two independent groups [20,21]. Kippenberg, Spillane and Vahala observed this phenomenon in a fibre-coupled toroidal micro-cavity with a quality factor Q of the order of 10^8 (Fig. 9(a)). To overcome the OPO threshold, the silica glass-based monolithic cavities were designed to reduce the modal effective areas which, in turn, increased the parametric gain bandwidth. In this way, the threshold pump power for parametric oscillation could be designed to fall below that for stimulated Raman scattering [155]. Previous designs were dominated by Raman gain [7], since stimulated Raman scattering (SRS) is an intrinsically phase-matched mechanism, thus it does not depend on material dispersion. SRS is particularly important in silica glass, where material dispersion in the near IR is large. Fig. 9(b) shows the parametric oscillation spectrum of a toroidal micro-cavity with principal diameter

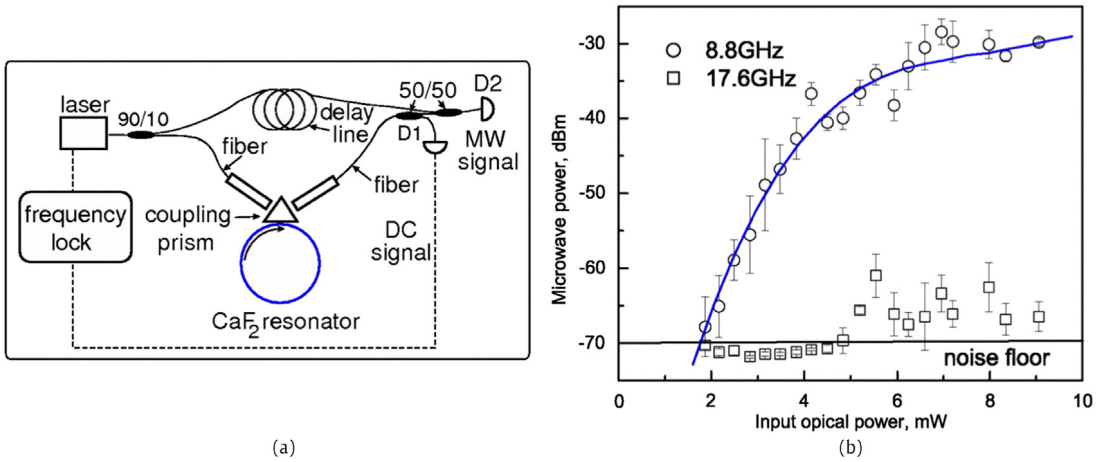

(a) (b)

Fig. 10. (a) Experimental set-up for OPO gneration from Matsko and co-workers. A DC feedback signal is retrieved from a slow photodiode (D1) at the output of the resonator and is used to actively lock the laser output to one resonance of the cavity. The MW beat-note is instead recorded by a fast photodiode (D2). (b) Microwave power versus optical pump power. Circles and squares represent the first and second microwave (MW) harmonics, respectively. After Ref. [21].

$D = 67$ μm and minor diameter $d = 3.9$ μm. The micro-toroid was pumped in the telecommunications window near 1550 nm with a pump power significantly above the OPO threshold. The generation of a signal/idler pair was clearly observed. The distance between the pump and the oscillating signal and idler corresponded to a single FSR (7.6 nm, almost 6 THz). Signal and idler were also found to have identical oscillation thresholds, with an idler-to-signal emission-power ratio close to 1 (see inset of Fig. 9(b)). These results were used as clear evidence of Kerr-induced parametric oscillation. Interestingly, Fig. 9(b) also shows the appearance for high pump powers of secondary peaks (marked as I' and S'), which represent the onset of comb generation by cascaded FWM.

A few months after the report by Kippenberg et al., Savchenkov et al. were also able to overcome the OPO threshold in a prism-coupled calcium fluoride resonator [21], see Fig. 10. The Q-factor of this device significantly exceeded one billion. An interesting experimental set-up, in which the resonator was placed in one arm of a Mach–Zehnder interferometer, allowed the authors to study the OPO behaviour from a different perspective - by measuring the microwave beat-note of the pump, signal and idler waves. Fig. 10(a) shows the retrieved microwave power as a function of the input optical power obtained with the set-up in Fig. 10(b). A clear threshold behaviour could be observed at the frequency corresponding to 1 FSR (8.8 GHz, open circles), revealing parametric oscillation for optical powers above 1 mW. Fig. 10(a) also shows that, for higher pump powers, higher harmonics start to appear (note the open squares show the power of the second microwave harmonic).

This work highlighted two important points: the dimensions of the resonator produced an FSR in the microwave frequency range, while the exceptionally high-Q of the cavities yielded a resonance with a bandwidth in the kilohertz range, which suggested the possibility of using these resonators as a precise frequency reference for the microwave-generated signal, as also discussed by the same authors in [164]. The strong link between micro-comb sources, microwave photonics and comb stabilisation will be discussed in detail in Sections 7.1 and 7.2.

Optical parametric oscillation was also subsequently demonstrated in a silica micro-sphere by Agha et al. [165] (see Fig. 11). This was obtained by selecting the micro-sphere size in order to engineer the overall dispersion of the cavity, thus achieving the desired anomalous dispersion régime. In addition, Raman oscillation was kept below threshold (see inset of Fig. 11) through careful control of the input pump polarisation. The universality of the OPO behaviour in different whispering-gallery mode Kerr resonators, lately investigated theoretically and experimentally by different authors [13,28], was thus already evident in these very early demonstrations.

4.2. Micro-combs breakthrough: large bandwidth generation

The demonstration of large bandwidth parametric conversion can be considered the first breakthrough in the field because it paved the way for the idea that micro-resonators could be used to generate optical frequency combs with extremely low pump powers and with compact designs. The first large bandwidth generation was demonstrated in a silica micro-toroid in 2007 by Del'Haye, Holzwarth, Kippenberg and co-workers [8]. By pumping a 75 μm diameter micro-toroid with a continuous-wave (CW) pump in the telecom band (at 1550 nm), extreme broadband operation was achieved (Fig. 12). The signal and idler sidebands that were initially generated interacted with each other through a complex sequence of cascaded FWM processes that resulted in precisely-spaced, higher order sidebands. Parametric frequency conversion was observed over a wavelength range larger than 490 nm (see inset of Fig. 12), with a total conversion efficiency greater than 20%. Most impressively, these results were obtained by using only modest pump powers, of the order of tens of milliwatts.

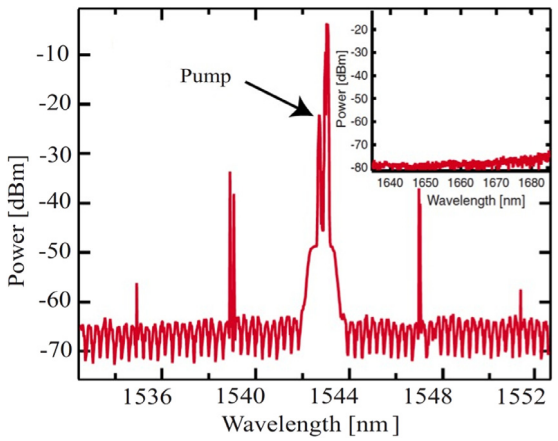

Fig. 11. Parametric oscillation in a 150 μm silica micro-sphere (pump power: 1 mW at 1543 nm). The Raman signal (expected around 1645 nm) is absent, as can be seen in the inset. After Ref. [165].

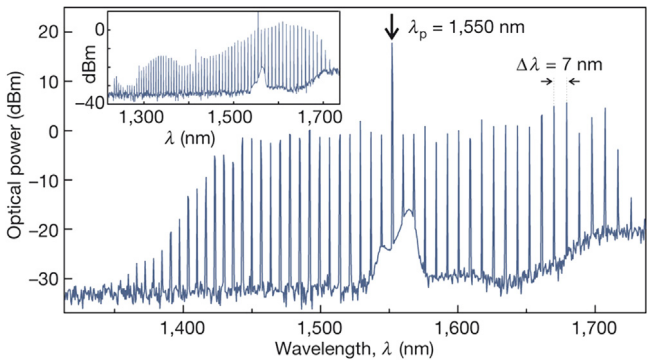

Fig. 12. Parametric frequency conversion observed in a monolithic toroid micro-cavity (pump power: 60 mW at 1550 nm). Inset: broadband emission in a different sample generating more than 70 parametric modes (pump power: 130 mW). After Ref. [8].

By exploiting the same principle, the authors later demonstrated a configuration where the comb signal could be stabilised to a microwave signal [9]. This stabilisation was achieved as a result of important technological advancements in the fabrication of monolithic toroids. In fact, the micro-cavities possessed a diameter (750 μm) large enough to guarantee an FSR below 100 GHz, thus allowing direct detection of the modulated output signal with fast photodiodes. This work was a precursor to the full stabilisation schemes for micro-combs that have been recently employed to target metrological applications. This will be also discussed in Section 7.1.

Broadband parametric conversion in a calcium fluoride resonator (Fig. 13(a)) was also observed by Grudinin and co-workers in 2009. Remarkably, the experiments in [166] report several of the prototypical generation spectra of the micro-combs. Fig. 13(b) shows two examples of broadband parametric conversion in this system, featuring a line spacing corresponding to the cavity FSR. By changing the pump power level and coupling conditions, the authors were also able to excite a different régime in which the line spacing was equal to specific multiples of the FSR (e.g. see Fig. 13(c)). Finally, an intermediate régime could also be observed, showing the simultaneous coexistence of two main line spacings (Fig. 13(d)), thus reporting one of the first observations of the primary/secondary comb formation that was subsequently investigated in detail in Ref. [10] and which we cover in the following paragraphs. During the same period, integrated planar resonators reached technological maturity, allowing for efficient FWM and nonlinear optics generally at milliwatt power levels, which was demonstrated by Ikeda et al. in silicon nitride [115] and Ferrera et al. in Hydex glass [94]. Both materials are compatible with standard silicon technology and do not suffer from two-photon absorption or the ensuing free-carrier absorption which are known to affect silicon at telecom wavelengths, as was discussed in Section 2.2.

These results served as the foundation for the subsequent demonstration of a large bandwidth OPO in integrated planar microstructures for both platforms [11,12].

Levy et al. [11] employed a silicon nitride (Si_3N_4) two-port micro-ring resonator geometry (i.e. a planar ring cavity coupled to a single bus waveguide) as the basis for the OPO. The resonator had a radius of 58 μm, a Q-factor of 500,000, an FSR of 403 GHz and an anomalous group velocity dispersion (GVD) for $\lambda < \lambda_0 = 1610$ nm (λ_0 being the zero-GVD point). A key technological improvement in this work dealt with employing a novel fabrication technique (relying on a thermal cycling

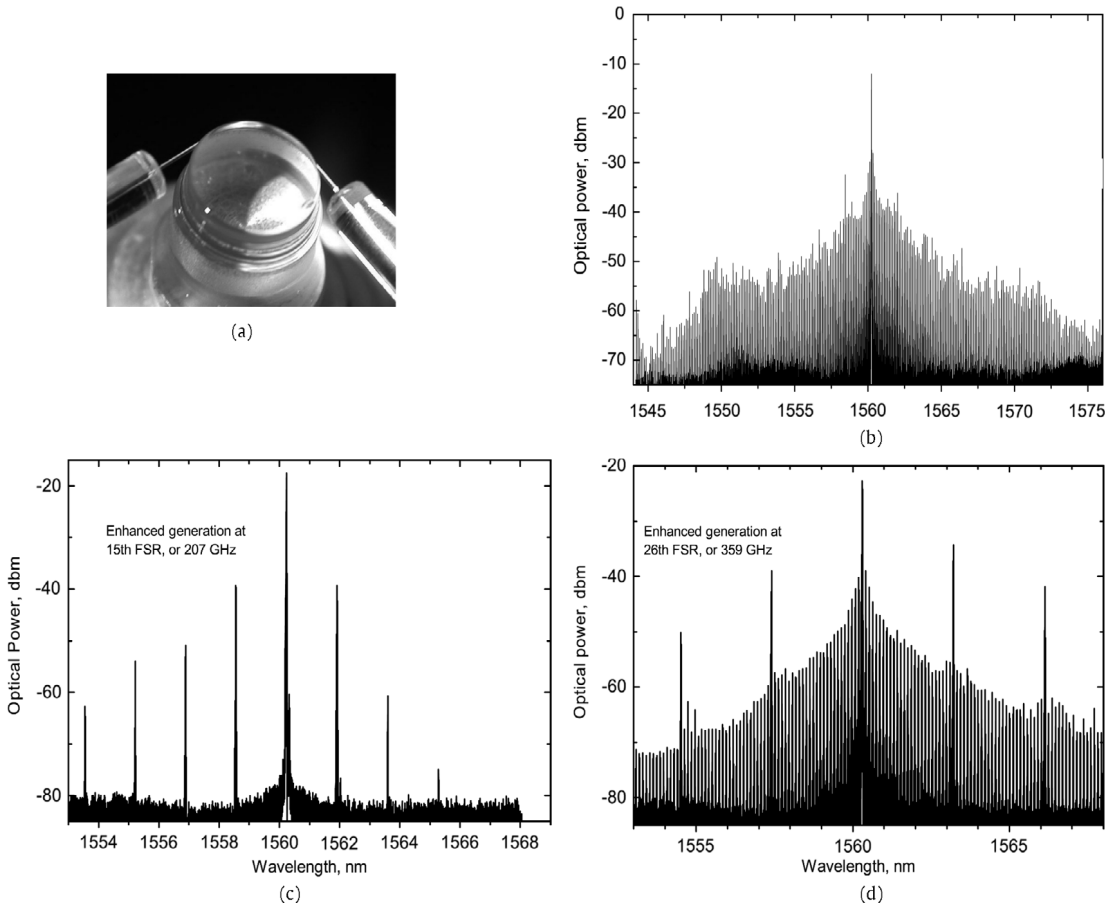

Fig. 13. (a) Calcium fluoride resonator with two fibre couplers. (b) Broadband parametric conversion in a 4.85 mm diameter resonator, featuring a line spacing of 13.81 GHz—1 FSR (pump power: 25 mW at 1560 nm). (c) Parametric conversion with line spacing of 207 GHz (15 FSR). (d) Mixed régime. Besides components spaced by the cavity FSR, selectively enhanced generation is observed at 26 cavity FSRs. (c, d) recall the spectral features of the Type I, Type II comb operation. After Ref. [166].

process) that allowed for thicker, low-loss (Si_3N_4) films. This, in turn, guaranteed a significant reduction in the effective modal area of the Si_3N_4 waveguides and allowed for a fine tailoring of waveguide dispersion, in turn enabling the engineering of the phase-matching requirements underpinning the FWM processes (see also Section 2.2). Fig. 14(a) shows the output spectrum measured for a pump power of 310 mW at 1557.8 nm. Eighty-seven new frequencies, spaced by one FSR, were generated between 1450 and 1750 nm. Similar results were also obtained with a smaller ring (with radius of 20 μm), featuring a Q-factor of 100,000 and an FSR of 1.17 THz.

Razzari et al. [12] observed parametric oscillation in a planar-integrated four-port micro-ring resonator fabricated in a Hydex glass platform. Hydex waveguides are low loss, with a reasonably high nonlinearity and are CMOS compatible, primarily because films deposited at low temperatures can be used to prepare low-loss guiding structures without the need for high-temperature annealing. Parametric oscillation was obtained for pump powers above 54 mW at 1544.15 nm (see Fig. 14(b)), i.e. in the anomalous dispersion region (occurring for wavelengths $<$ 1560 nm in these waveguides). Fig. 14(b), (c) show the evolution of the generated spectral components as a function of the pump power. Interestingly, in this case a different régime of OPO operation was observed to that reported by Levy et al.; in fact, the generated OPO spectral lines did not uniformly cover all the resonances of the micro-ring but were, instead, spaced by 32 FSRs. The behaviour was attributed to the spectral shape of the parametric gain in the system, which was estimated to peak at around 1590 nm (Stokes side). Considering the micro-ring characteristics and pump power, this was in agreement with the wavelength of the first oscillating mode visible in Fig. 14(b). The observed OPO started oscillating at the micro-cavity resonances nearest to the parametric gain maxima. Once oscillation occurred, an increase in pump power further amplified the oscillating modes and initiated a process of cascaded FWM that generated a series of wavelengths at multiples of the initial spacing. This behaviour is reminiscent of the régime of cavity modulation instability observed for negative cavity de-tuning that is discussed in Section 5.5.1.

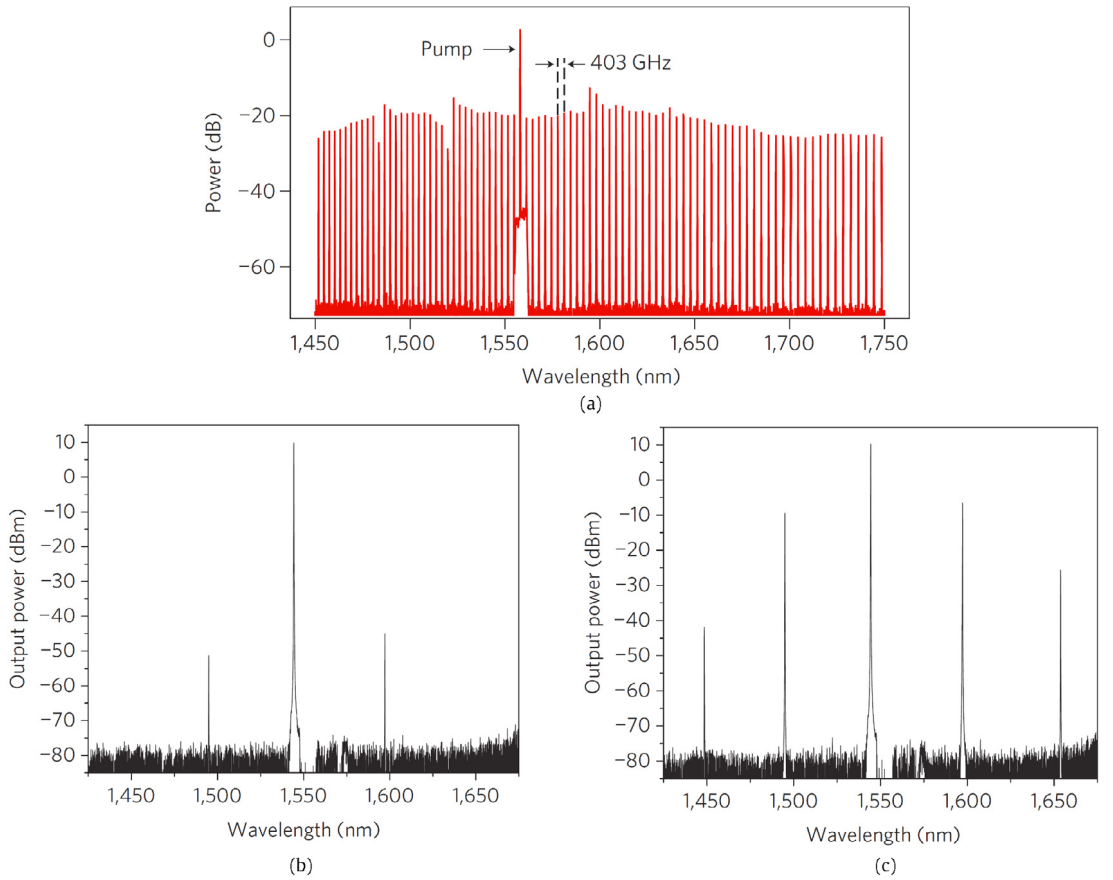

Fig. 14. Summary of the first comb observations in integrated resonators (a) OPO in a two-port silicon nitride (Si_3N_4) micro-ring resonator. The measured resonator had a radius of 58 μm, a Q-factor of 500,000, an FSR of 403 GHz and anomalous group velocity dispersion (GVD) for $\lambda < \lambda_0 = 1610$ nm. Broad spectrum operation, with lines spaced by 1 FSR, for a pump power of 310 mW at 1557.8 nm. After Ref. [11] (b–c) Four-port Hydex micro-ring resonator (radius: 135 μm, FSR: 200 GHz, Q: 1.2×10^6). Output spectra (measured at the output of the drop port) for a pump injected in the input port and tuned to a ring resonance at 1544.15 nm (pump power: (b) 50.8 mW, (c) 53.8 mW). The spectrum is generated with lines spaced by 32 FSR. After Ref. [12].

4.3. Temporal features of micro-combs

The previous set of experiments clearly showed the extremely high potential of micro-combs as broadband, efficient sources. Although several spectral observations were carried out by different groups, these measurements could not give any physical insight into the temporal properties of the micro-comb radiation. Since micro-combs are generated via parametric oscillation, in which the phases of different comb lines are mutually related, some sort of correlation between the generated lines was expected. However, it was not straightforward to conclude whether the comb lines could maintain a stable phase relationship, raising the question of whether or not they could be made coherent.

The first characterisation of the coherence of micro-combs appeared in 2011 when Ferdous et al. [10] presented a careful line-by-line characterisation of micro-combs generated from a silicon nitride resonator. The experimental set-up is shown in Fig. 15. In this study, the authors controlled and adjusted the relative phase of the comb lines via a spatial light modulator in a pulse shaper [167]. Autocorrelation measurements were then performed to determine if the micro-combs could be compressed to form transform-limited pulses. The ability to fully compress the pulses to become transform limited indicated a high coherence of the comb lines and vice versa. Two different comb behaviours were found in their experiments, which were referred to as Type I and Type II combs.

Type I combs are a cascade of sidebands, as shown in Fig. 16(a), which are usually formed with single FSR spacing as the pump laser is tuned into the resonance. Combs spaced by multiple FSRs and with no fill-in lines show similar characteristics to Type I combs (see Fig. 17(a)). These Type I comb features can also be found in [12,166,168], as commented in Figs. 13 and 14. Different phase distributions were found in these experiments, depending on the specific experimental configuration, with the aim of achieving transform-limited optical pulses (see Fig. 16(b) and (c)).

This demonstrated, for the first time, that a coherent optical pulse could be obtained via parametric oscillation, meaning that micro-combs could feature a stable spectral phase distribution, resulting in temporally invariant pulses. Fig. 16(d)

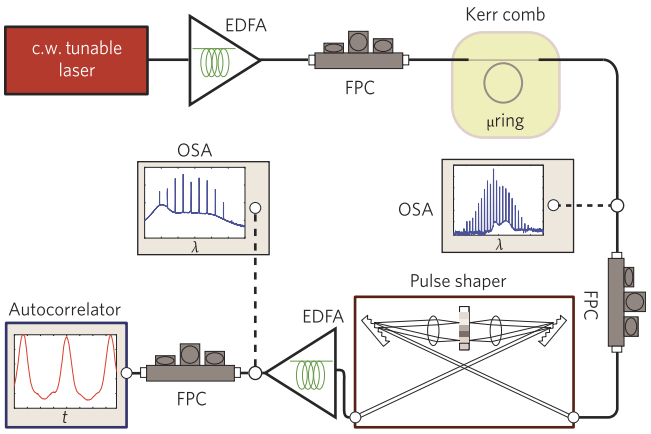

Fig. 15. Spectral line-by-line shaping of micro-combs. EDFA: Erbium-doped fibre amplifier; FPC: fibre polarisation controller; micro-ring: silicon nitride micro-ring; OSA: optical spectrum analyser. The phase applied to each comb line is adjusted iteratively via the pulse shaper to maximise the second harmonic generation (SHG) signal at the autocorrelator. (After Ref. [10].)

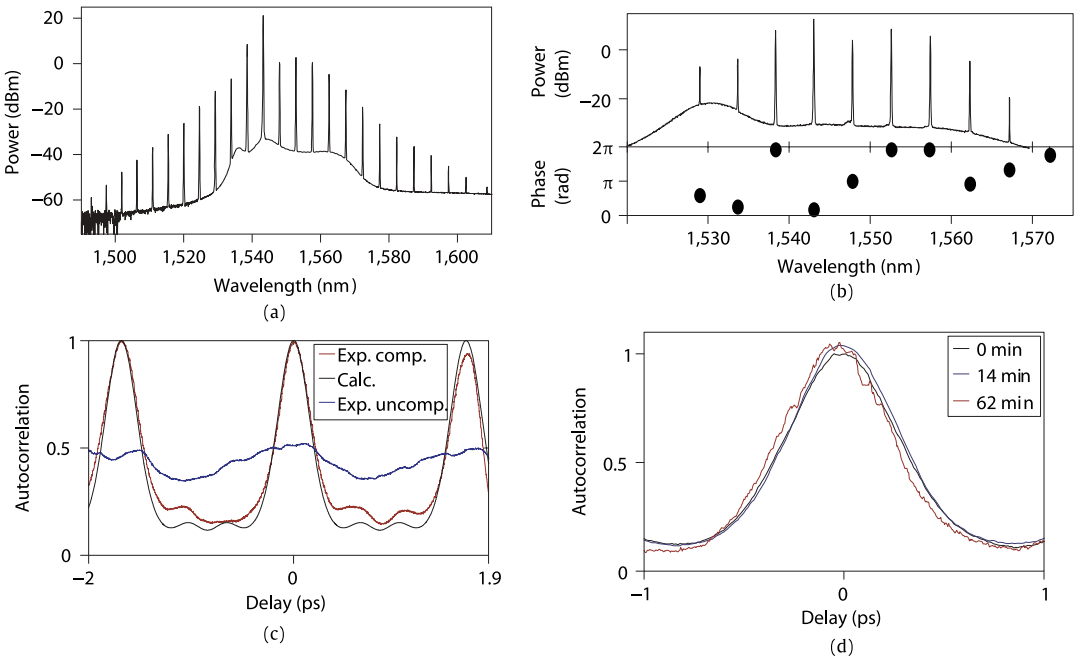

Fig. 16. Compressed pulses of Type I combs. (a) Spectrum after the micro-ring. The pump wavelength, on-chip pump power and ring radius are 1543.07 nm, 0.45 W and 40 μm, respectively (b) Spectrum after the pulse shaper, together with the phase applied to each comb line for optimum SHG (c) Autocorrelation traces. Red line, compressed pulse; blue line, uncompressed pulse; black line, calculated by taking the spectrum shown in (b) and assuming a flat spectral phase (d) Autocorrelation traces for compressed pulses, measured at 0, 14 and 62 min, respectively, after spectral phase compensation. (After Ref. [10].)

shows the stability of the compressed pulse after line-by-line shaping over a long observation time. The high stability also provided information and confirmation of the strict equidistance of the comb lines, which is a question worth considering for micro-combs since the cavity dispersion leads to non-equidistant cold cavity modes. Suppose δf_n denotes small fixed shifts of the individual comb lines from their ideal equidistant positions: these frequency shifts would give rise to phase errors $\delta\phi_n = 2\pi\delta f_n t$ that grow in time. In order to avoid significant waveform changes, the phase errors should (conservatively) satisfy $|\delta\phi_n| < 0.7\pi$. With an observation time of 3600 s as shown in Fig. 16(d), the estimated δf_n are conservatively of the order of 1×10^{-4} Hz or below. This result is consistent with measurements performed on micro-combs generated from silica micro-toroids, indicating uniformity in the comb spacing at least at the 1×10^{-3} Hz level [8].

Note, however, that, in these early experiments, the dispersion of the fibre connecting the micro-ring to the measurement apparatus was neither characterised nor compensated. Therefore, the actual spectral phase functions in the as-generated

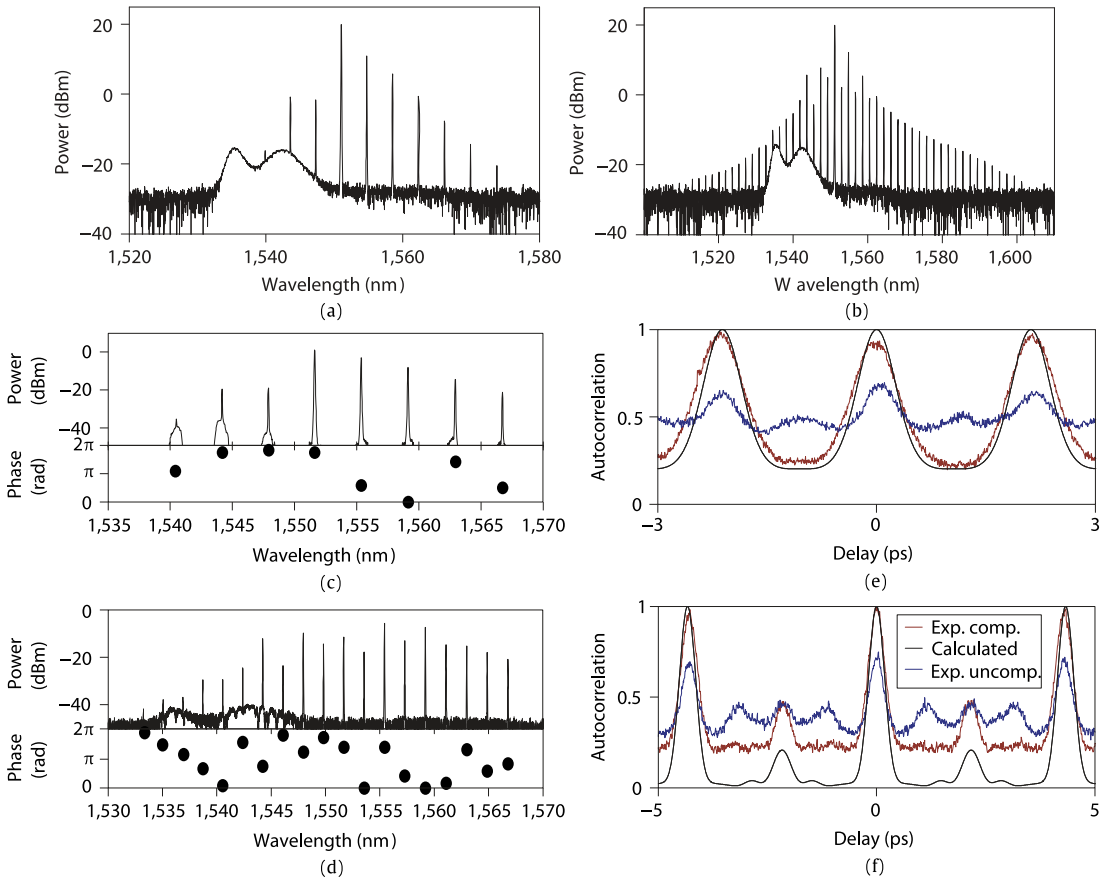

Fig. 17. Compressed pulses of Type II combs. (a), (b) Spectra after the micro-ring. The ring radius is 100 μm. The pump power is 1.4 W. The pump wavelengths are: (a) 1551.67 nm; (b) 1551.74 nm; (c), (d) Spectra after the pulse shaper (corresponding to (a), (b), respectively), together with the phase applied to each comb line for optimum SHG signals; (e), (f) Autocorrelation traces. Red lines, compressed pulse; blue lines, uncompressed pulse; black lines, calculated by taking the spectra shown in (c), (d) and assuming a flat spectral phase. (After Ref. [10].)

combs were not determined. To measure the optical time-domain waveform inside the micro-resonator, the fibre dispersion after the micro-resonator needs to be compensated [51,169].

Type II combs are generated first with multi-FSR spaced lines (primary combs) and subsequently followed by fill-in lines (secondary combs) as the pump laser is tuned into the resonance. It is generally impossible to find a phase distribution of the pulse shaper for Type II combs that could be compressed into transform-limited pulses, which indicates a reduced coherence in comparison to Type I combs. Fig. 17 shows an example of Type II combs. Comb lines spaced at 2 FSR were first generated (Fig. 17(a)). The coherence at this stage was good (Fig. 17(c) and (e)) and similar to Type I combs. When the pump laser was further tuned into the resonance, fill-in lines appeared, resulting in a 1-FSR-spaced comb (Fig. 17(b)). The coherence at this stage was degraded, which can be concluded from the limited contrast ratio of the autocorrelation trace after line-by-line pulse compression (Fig. 17(f)). The generation of fill-in lines involved multiple four-wave mixing processes that were driven by the individual primary lines generating the subgroups of frequency combs [13,144]. These sub-combs may have different offset frequencies, which were responsible for the reduced coherence of the Type II combs.

A similar behaviour was also observed in fused quartz high-Q-resonators [168]. It is worth noting that, by carefully controlling the pump laser power and de-tuning, Type II combs have the potential to be translated into highly coherent mode-locked states, via injection locking or soliton formation [13,50,51,55], which will be discussed in the following sections.

5. Modelling of optical micro-combs: temporal dynamics and the Lugiato–Lefever equation

The coupled-mode formalism was the first approach to be used in the modelling of micro-comb temporal dynamics. Whilst physically accurate, coupled-mode formalisms do not easily allow the derivation of analytic or semi-analytic results which may describe combs that enclose more than just a few modes. Thus, obtaining general guidelines to comb formation characteristics was difficult, especially for a full understanding of the complex temporal dynamics and the coherent régimes of the combs.

These drawbacks can be alleviated by deriving a mean-field equation for the comb formation. As already outlined in Section 1, the most widely used mean-field model for describing comb temporal dynamics is the Lugiato–Lefever equation (LLE), which allows for a number of *semi-analytical* considerations. These include the analysis of modulation instability (MI) and the definition of temporal cavity solitons. Such considerations are capable of facilitating a deeper understanding of the intricate formation of the comb's characteristics that have been in evidence from the first set of experimental investigations summarised in the previous section. Originally, the LLE was derived for describing spatial dissipative structures in diffractive cavities [33] and was later derived for modelling the temporal dynamics of nonlinear fibre-ring resonators in the presence of dispersion [37–39]. The LLE model works well for describing closed-fibre loop cavities, as well as single-mode waveguide ring-resonators.

The derivation of the LLE starts from the infinite-dimensional map that involves the nonlinear Schrödinger (NLS) equation, used to model the propagation of a slowly-varying electric-field envelope within a single spatial mode of a waveguide and the appropriate boundary conditions. These take into account the coherent coupling with the injected pump field and relate the intra-cavity fields between successive round-trips. The LLE is then obtained by simply averaging the field over the path of the resonator. Notably, the LLE can also be readily extended to take into account the presence of higher-order propagation effects that become important as the comb bandwidth grows larger [46,47], analogous with extensions of the NLS equation for treating supercontinuum generation [170]. From the LLE modelling point of view, the most notable difference between a micro-resonator and a coherently driven passive fibre-loop cavity is that, in the former, the temporal waveforms have a time duration which is comparable with the cavity round-trip time. This means that the LLE for describing a micro-resonator should be strictly solved as a periodic problem [47,48]; whereas, in the case of fibre cavities, the LLE may be solved, approximately but safely, as an infinite line problem [46].

It is also worth pointing out that there may be specific situations, in particular when the intra-cavity power is very high (which does not necessarily require a very high input pump power), when the LLE mean-field approach is no longer a valid approximation. In these situations, which may occur both for the fibre cavity [171] and in the micro-resonator case [172], the original (i.e. without cavity averaging) Ikeda map should be used to describe both temporal dynamics and comb generation. In fact, the map predicts several interesting and significant physical effects (such as period-doubling MIs and super-cavity solitons) which are beyond the reach of the mean-field description.

More recently, it has also been shown that the time-domain description provided by the LLE may also be obtained by a proper reduction of the coupled-mode theory [47]: hence the LLE approach also applies well to more complex resonators' geometries. It must be noted that the modal expansion is derived by starting from the vector wave equation for the electric field, c.f. Eq. (15). It is, therefore, somewhat more general than the infinite dimensional cavity map approach, since it can also take into account imperfect mode overlap, see Ref. [47]. The two formalisms are, however, completely equivalent, both formally and, from the point of view of computational complexity [173], in the mean-field limit when the modes are assumed to be degenerate.

The full modal expansion and the average LLE are thus useful in different and complementary ways. On the one hand, the modal expansion is useful to determine threshold phenomena or to investigate the dynamics of the comb generation process when a small number of modes are involved and it is suitable to understand the spectral properties of the comb. On the other hand, the generalised LLE provides a deeper insight when the number of interacting modes is large. It allows for deriving approximate analytical solutions and it is also more intuitive from a temporal standpoint. The situation is fully equivalent to the study of parametric instabilities and amplification in the frequency domain by means of a coupled-wave approach and, in the temporal domain, by means of the MI analysis of the NLS equation [174].

In the sub-sections below, we will briefly outline the derivation of the LLE, starting either from the infinite-dimensional cavity map approach or from the modal expansion approach. We will then use the LLE to further analyse the comb formation.

5.1. Infinite-dimensional cavity map

The infinite-dimensional cavity map (or Ikeda map) approach considers the evolution of the slowly-varying envelope of the electric field over consecutive round-trips in the resonator. The full dynamics can then be described in two steps. In the beginning of each round-trip, the intra-cavity light is subject to cavity boundary conditions that manifest themselves by losses due to the input coupler and by the coherent addition of the continuous-wave (CW) driving field E_{in}, expressed in $[\sqrt{W}]$. The field then evolves over a single round-trip under the influence of linear loss, chromatic dispersion and Kerr nonlinearity. Assuming single spatial mode and monochromatic driving, field propagation is described mathematically by the following infinite-dimensional map:

$$E^{(m+1)}(0,\tau) = \sqrt{\theta}\,E_{\mathrm{in}} + \sqrt{1-\theta}\,E^{(m)}(L,\tau)e^{i\phi_0}, \tag{48}$$

$$\frac{\partial E(z,\tau)}{\partial z} = -\frac{\alpha_{\mathrm{i}}}{2}E + i\sum_{k\geq 2}\frac{\beta_k}{k!}\left(i\frac{\partial}{\partial\tau}\right)^k E + i\gamma|E|^2E\,. \tag{49}$$

Here $E^{(m)}(z,\tau)$ is the intra-cavity field during the mth round-trip, z is the longitudinal coordinate along the resonator and τ is time expressed in a reference frame moving with the group velocity of light at the driving frequency ω_0. The variable θ is the power transmission coefficient of the input/output coupler, L is the round-trip length of the resonator and ϕ_0 is

the linear phase accumulated by the intra-cavity field with respect to the driving field over one round-trip. α_i is the linear absorption coefficient of the resonator and the β_ks are the Taylor series expansion coefficients of the resonator propagation constant $\beta(\omega)$ about the driving angular frequency ω_0: $\beta_k = \mathrm{d}^k\beta/\mathrm{d}\omega^k|_{\omega_0}$. Note that $\phi_0 = \beta_0 L$. Finally, $\gamma = n_2\omega_0/(cA_{\mathrm{eff}})$ is the resonator nonlinear coefficient, n_2 being the nonlinear refractive index, c the speed of light in vacuum and A_{eff} the effective mode area.

Maps similar to those described by Eqs. (48) and (49) have been widely used to analyse nonlinear spatial cavities, as well as macroscopic optical fibre resonators [31,32,37,171,175–178]. Moreover, Eq. (49) can be identified as a form of generalised NLS equation that is often encountered in nonlinear fibre optics [170,174,179].

In the context of micro-combs, a time-domain infinite-dimensional map was first used in 2009 by Agha et al. to numerically simulate comb formation in silica micro-spheres [180]. However, the critical role of the cavity phase de-tuning, described by the parameter ϕ_0, was not fully recognised at the time. Its role was not elaborated until 2013 when the full map, given by Eqs. (48) and (49), was discussed in the context of micro-combs [46].

5.2. Mean-field theory: the Lugiato–Lefever equation

In low-loss structures, where the field exhibits negligible evolution over a single round-trip, the map described by Eqs. (48) and (49) can be averaged into a single, externally-driven and damped NLS equation [37]:

$$t_{\mathrm{R}}\frac{\partial E(t,\tau)}{\partial t} = \left[-\alpha - i\delta_0 + iL\sum_{k\geq 2}\frac{\beta_k}{k!}\left(i\frac{\partial}{\partial\tau}\right)^k + i\gamma L|E|^2\right]E + \sqrt{\theta}\,E_{\mathrm{in}}. \tag{50}$$

Here t_{R} is the round-trip time, $\alpha = (\alpha_i L + \theta)/2$ describes the total cavity losses and $\delta_0 = 2\pi l - \phi_0$ is the phase de-tuning of the driving field with respect to the closest linear resonance (with order l). The continuous variable t measures the *slow time* of the cavity and it can be linked to the round-trip index as $E(t = mt_R, \tau) = E^{(m)}(z = 0, \tau)$. Hence, the field varies with t for timescales longer than the round-trip time t_{R}.

If dispersion coefficients beyond the second-order are neglected ($\beta_k = 0$ for $k \geq 3$), then Eq. (50) is formally identical to the LLE that was derived to describe either the generation of dissipative spatial structures in spatially diffractive cavities [33,181,182] or temporal structures in dispersive nonlinear Kerr cavities [37], respectively. However, in the case of micro-resonators, it should be borne in mind that the derivation of Eq. (50) from the map Eqs. (48) and (49) requires that its solution is defined over a finite temporal window $\tau \in [-t_{\mathrm{R}}/2, t_{\mathrm{R}}/2]$, equal to the cavity round-trip time t_{R} [48].

In the context of micro-combs, an equation equivalent to the LLE was first discussed in 2009 by Matsko et al. [183]. They showed that the truncated three-wave analysis of the LLE can be used to describe the onset of comb generation; see also Ref. [48], which reports analytical solutions and the stability analysis for combs represented by three-mode truncations. Ref. [183] also suggested that pulse-like solutions of the LLE could be used to represent mode-locked comb states. In 2011, Matsko et al. examined pulse-like solutions of the LLE in more detail, in the limit case of vanishing loss ($\alpha = 0$) where LLE exhibits exact analytic solutions [22]. Whilst these solutions were earlier derived by Barashenkov and Smirnov [184], the significance of Ref. [22] was to highlight their potential relevance to micro-combs. Possibly due to the fact that loss is a key ingredient for the correct physical description of dissipative structures in optical cavities, these initial LLE-based results did not immediately attract wide interest in the micro-comb community.

It was not until 2013 that the LLE approach gained in popularity, driven by several independent studies [46–48]. These works established that the generalised LLE [Eq. (50)] allows for broadband combs with thousands of modes to be realistically and efficiently modelled [46] and that this framework is fully congruent with the previously established coupled-mode approaches [47,48] as far as the numerical complexity is concerned [173]. The generalised LLE has subsequently been used extensively to numerically simulate Kerr comb dynamics.

The derivation of the generalised LLE assumes a relatively small change of the field over a single round-trip. Accordingly, the equation only holds in the limit of high-finesse cavities $\mathcal{F} \gg 1$. This condition is routinely satisfied for typical high-Q-resonators whose finesse $\mathcal{F}$ falls in the range $\mathcal{F} \sim 10^2 - 10^5$. In addition, in order to be consistent with the assumption of slow evolution, both the accumulated linear and nonlinear phase shifts must remain small over one round-trip. Mathematically, these conditions can be written respectively as $\sum_{k\geq 2}\beta_k L\Delta\omega^k/k! \lesssim \pi$, where $\Delta\omega$ is the (angular) spectral width of the generated comb and $\gamma L|E|^2 \lesssim \pi$. Note that these conditions must be verified a posteriori. Note also that the previous conditions do not necessarily mean that the dispersive and nonlinear phase shifts remain small within the cavity round-trip, as it occurs, for example, in the case of dispersion-managed fibre cavities [185]. It is also worth mentioning that, for specific resonator architectures and pumping régimes, it may be necessary to include additional higher-order terms in the generalised LLE to ensure accuracy. These include dispersion of the nonlinearity [186,187], noise in the driving CW laser [188], as well as stimulated Raman scattering, multi-photon absorption and free carrier effects [186,189,190].

The (generalised) LLE can be numerically integrated by using techniques commonly used to simulate the NLS equation, its generalised forms and supercontinuum generation — namely, the well-known split-step Fourier method and its variants [174,191]. Also, its steady-state solutions ($\partial E/\partial t = 0$) can be obtained by directly looking for the roots of the right-hand side of Eq. (50) [46]. As shown below, the analysis of the LLE steady-state solutions and their bifurcations provides significant insight to comb characteristics [28]. In all cases, the temporal simulation window is set equal to the round-trip time t_{R}. The periodic boundary conditions inherent to the split-step Fourier method then ensure that the increment in the corresponding frequency-grid equals the cavity FSR (around the pump frequency), which coincides with the fundamental comb spacing.

5.3. Connection to the coupled-mode formalism

The modal expansion and the infinite-dimensional cavity map formalisms are strongly connected [22,46,47,173] and they are exactly equivalent in the limit of the mean-field approximation [47]. This can be shown by expanding the slowly-varying intra-cavity field envelope at a particular position in the resonator as a modal sum

$$E(t,\vartheta) = \sum_l \mathcal{E}_l(t)\, e^{il\vartheta}\,, \tag{51}$$

where $\vartheta \in [-\pi,\pi]$ is the azimuthal angle along the circumference of the cavity. The partial derivatives of $E(t,\vartheta)$ can be evaluated as

$$\frac{\partial E}{\partial t} = \sum_l \frac{d\mathcal{E}_l}{dt}\, e^{il\vartheta}, \tag{52}$$

$$i^n \frac{\partial^n E}{\partial \vartheta^n} = \sum_l \mathcal{E}_l\,(-l)^n\, e^{il\vartheta}\,. \tag{53}$$

Using the modal evolution Eq. (38) and, subsequently, Eq. (53) in Eq. (52), it follows that, in the approximation of quasi-degeneracy for losses, frequencies and spatial profiles, the total field obeys the equation

$$\begin{aligned} t_\mathrm{R}\frac{\partial E}{\partial t} = &\left[-\frac{1}{2}\Delta\omega_\mathrm{t}\, t_\mathrm{R} + i\, t_\mathrm{R}\,\sigma + iL\sum_{n=2}^{N}(i\Omega_\mathrm{R})^n \frac{\beta_n}{n!}\,\frac{\partial^n}{\partial\vartheta^n}\right] E \\ &+ iL\gamma|E|^2E + \sqrt{t_\mathrm{R}\,\Delta\omega_\mathrm{e}}\,E_\mathrm{in}\,. \end{aligned} \tag{54}$$

The previous equation coincides with the LLE introduced above (50). Indeed, it is easy to show that the loaded linewidth $\Delta\omega_\mathrm{t} = 2\alpha/t_\mathrm{R}$, the extrinsic linewidth $\Delta\omega_\mathrm{e} = \vartheta/t_\mathrm{R}$ and the laser frequency de-tuning $\sigma = -\delta_0/t_\mathrm{R}$. Finally, the azimuthal angle ϑ is related to fast time in Eq. (50) through $\vartheta = 2\pi\cdot\tau/t_\mathrm{R} = \Omega_\mathrm{R}\tau$. With these substitutions, Eq. (50) is identically recovered, affirming the equivalence of the two frameworks.

Since Eq. (51) is, in fact, just an ordinary Fourier transform, it can be easily seen that the two formalisms give complementary perspectives for describing the same physical situation. The infinite-dimensional cavity map can be interpreted as a time-domain formalism that describes the slow evolution of the temporal (or azimuthal) field profile; while the modal expansion can be interpreted as a frequency-domain formalism that describes the slow evolution of each resonant mode, i.e. each comb line. Outside the limit of the mean-field approximation there is, however, a small discrepancy between the two formalisms that stems from the two different ways that the respective evolution equations are derived allowing, for example, the modal expansion approach to model imperfect mode overlap, while the cavity map has the ability to model high-power multi-stable states.

The LLE, hence, can be written either using a two-timescale approach where the field evolves on a slow evolution timescale and the temporal profile is described using the ordinary (fast) time (see Eq. (50)) or, alternatively, it can be expressed using a slow evolution time and the azimuthal angle, as in Eq. (54). The azimuthal angle has the advantage that it naturally takes into account the periodicity of the field inside the resonator, while the time variable has the advantage of being the natural conjugate variable of frequency.

In addition, the same type of split-step Fourier methods can be used to simulate either the coupled-mode equations or the mean-field LLE. Indeed, since the two approaches are fundamentally equivalent, they can both be numerically simulated with equal efficiency, as has recently been shown by Hansson et al. [173]. The original implementations of numerical methods for coupled-mode approaches were unnecessarily associated with heavy computational complexity, which prevented the simulation of broadband combs having thousands of modes. The actual simulation speed and the scaling dependence on the number of modes in the simulation is, indeed, dictated by the choice of algorithm in the method of implementation. Octave-spanning frequency combs consisting of several thousand modes can be readily simulated using fast Fourier transform methods, also with the coupled-mode theory, in a matter of minutes on a standard computer. The contribution from the nonlinear Kerr term is most easily calculated in the time-domain, while the dispersion should preferably be calculated in the Fourier domain. The choice of which method to use for simulations should, therefore, depend on the convenience afforded by each method for a particular problem.

5.4. Normalised Lugiato–Lefever equation

The generalised LLE possesses a number of steady-state solutions that are directly relevant to micro-combs. As we shall see below, the analysis of these solutions and their bifurcations provides significant insights into comb characteristics and formation dynamics [28,192]. It is useful in this context to consider a dimensionless form of Eq. (50). This is obtained through the following change of variables [28,45]:

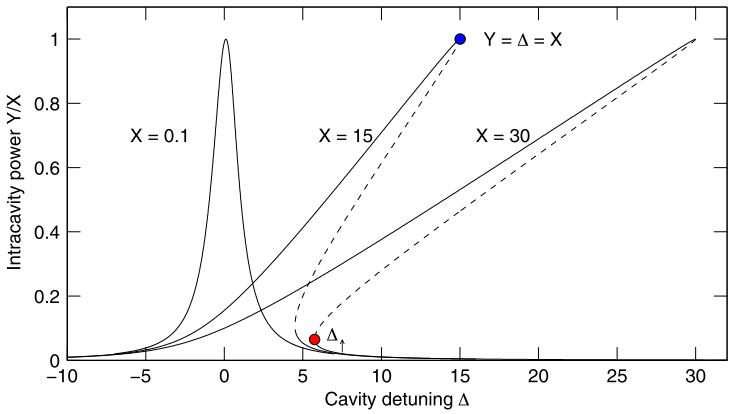

Fig. 18. Intra-cavity powers Y normalised to pump power X as a function of cavity de-tuning Δ for three different normalised pump values: $X = 0.1$, $X = 15$ and $X = 30$. The red solid circle indicates the up-switching point $\Delta_\uparrow$ for $X = 30$ and the blue solid circle highlights that, due to Kerr nonlinearity, the resonance is shifted to $\Delta = X$ (where it also happens that the intra-cavity power satisfies the relation $Y = X$).

$$t' = \alpha \frac{t}{t_R}, \quad \tau' = \tau \sqrt{\frac{2\alpha}{|\beta_2|L}}, \quad E' = E\sqrt{\frac{\gamma L}{\alpha}},$$
$$\Delta = \frac{\delta_0}{\alpha}, \quad d_k = \frac{L\beta_k}{\alpha k!}\left(\sqrt{\frac{2\alpha}{|\beta_2|L}}\right)^k, \quad S = E_{in}\sqrt{\frac{\gamma L\theta}{\alpha^3}}.$$

The LLE (50) then becomes

$$\frac{\partial E'(t', \tau')}{\partial t'} = \left[-1 + i(|E'|^2 - \Delta) + i\sum_{k\geq 2} d_k \left(i\frac{\partial}{\partial \tau'}\right)^k\right] E' + S, \tag{55}$$

with the additional periodicity condition $E'(t', \tau') = E'(t', \tau' + t'_R)$, where t'_R is the normalised cavity round-trip time. For a given t'_R and dispersion, the solutions and dynamics of Eq. (55) are fully governed by only two parameters: the normalised pump strength S and cavity de-tuning Δ.

The simplest solutions of Eq. (57) are CW ($\partial E'/\partial \tau' = 0$) and, therefore, independent of dispersion. They describe the nonlinear resonances of the cavity and satisfy the cubic polynomial:

$$X = Y^3 - 2\Delta Y^2 + (\Delta^2 + 1)Y, \tag{56}$$

where $X = |S|^2$ and $Y = |E'|^2$ are, respectively, the normalised pump and intra-cavity powers. At a constant pump power, Eq. (56) describes the nonlinear Kerr tilt of the cavity resonance. This is shown in Fig. 18, where we plot the intra-cavity powers Y (normalised to the pump power X) that solve Eq. (56) for a range of normalised pump powers X. It is apparent that, as X increases, the peak of the cavity resonance is displaced, giving rise to an overall tilt towards positive de-tunings. In particular, in the normalisation adopted here, the peak of the resonance shifts to $\Delta = X$. It is also worth noting that, to the first order, $\Delta = 1/(FSR \cdot \alpha)[\omega_p - \omega_0]$, where ω_p is the angular frequency of the cold cavity resonance (unloaded) that is closest to the driving laser. Therefore, it is clear that if $\Delta > 0$, then the resonance is de-tuned towards longer wavelengths.

As X becomes sufficiently large, the cavity response $[Y(\Delta)]$ becomes multivalued for de-tunings lying in between the up-switching point $\Delta_\uparrow$ and X (see Fig. 18). This simply reflects the bi-stable nature of the system [37]. Note that, for $X \gg 1$, the up-switching $\Delta_\uparrow \simeq 3(X/4)^{1/3}$ [28]. Finally, we remark that, although there are three CW solutions, we speak of two stable states and not three because the intermediate branch (indicated as a dotted black line in Fig. 18) is always homogeneously unstable [28].

5.5. Comb dynamics in the anomalous dispersion régime

The vast majority of experimentally-observed micro-combs have been generated in a régime where the resonator exhibits anomalous dispersion ($\beta_2 < 0$). Although this is not strictly required and comb generation has been predicted and also observed with normal dispersion [38,48,51,192–195], comb formation is much easier to attain in the anomalous dispersion régime. Furthermore, a wealth of interesting nonlinear physics involving the formation of temporal cavity solitons in the anomalous dispersion régime has been reported. Therefore, we focus here on comb dynamics and characteristics obtained when pumping the micro-resonator in the anomalous dispersion régime. For simplicity, we first consider a resonator with negligible higher-order dispersion ($\beta_k = 0$ for $k \geq 3$). This approximation will be relaxed in Section 5.6 where the pertinent

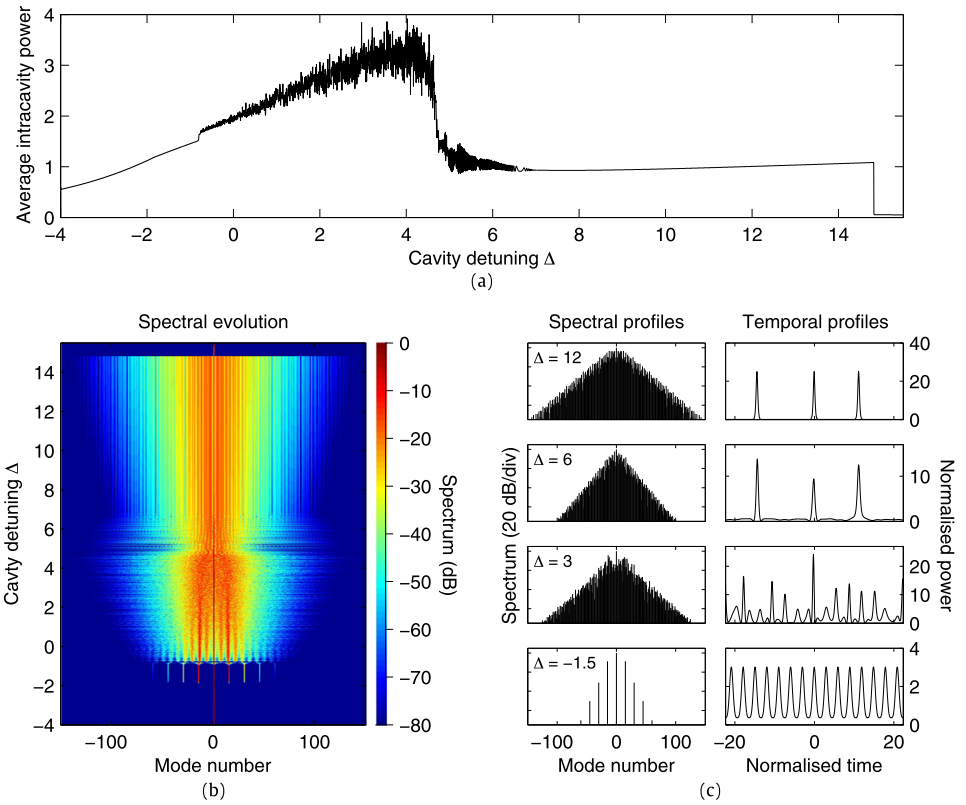

Fig. 19. LLE-simulated micro-comb dynamics when scanning a laser over a resonance. (a) Average intra-cavity power and (b) instantaneous spectrum when the cavity de-tuning Δ is continuously varied from $\Delta = -4$ to $\Delta = 15.5$. (c) Spectral and temporal profiles for selected de-tunings.

contributions will be specifically discussed. With these assumptions, the normalised LLE reduces to:

$$\frac{\partial E'(t',\tau')}{\partial t'} = \left[-1 + i(|E'|^2 - \Delta) + i\frac{\partial^2}{\partial \tau'^2}\right]E' + S. \tag{57}$$

We first present results from numerical simulations that illustrate typical micro-comb dynamics. We numerically integrate the normalised LLE using the split-step method, with an initial condition of vacuum fluctuations. For the sake of discussion, we adopt a set of experimental parameters describing a 35.2 GHz MgF_2 resonator [50], driven with $P_{in} \approx$ 9.3 mW, so that the normalised pump power is $X = 12$. This is a typical value in the micro-comb context. In order to reveal the full comb dynamics and all régimes of operation, we adiabatically ramp the de-tuning Δ along the tilted cavity response [50,186,196]. This models the experimental procedure of tuning the laser frequency into resonance from high frequencies.

Fig. 19(a) shows the average intra-cavity power as the de-tuning is varied, while the false colour plot in Fig. 19(a) shows the corresponding comb spectrum. The intra-cavity field follows the CW cavity response up until the de-tuning $\Delta \approx -2$, at which point comb formation initiates through the generation of primary sidebands separated from the pump by multiple FSRs. A further increase in the de-tuning beyond $\Delta \approx -0.7$ results in the intermediate cavity modes becoming populated and the comb losing its stability. Two further bifurcations can be observed at $\Delta = 4.7$ and $\Delta = 6.9$, before the comb finally decays back to a CW at $\Delta = 14.8$. Similar transitions and comb formation dynamics have been observed in several experiments [13,50].

It is apparent that four different régimes of comb dynamics appear in Fig. 19(b): their distinctive spectral and temporal features are illustrated in more detail in Fig. 19(c). These régimes are not unique to this particular simulation and they are found to manifest themselves over a comparatively wide range of parameters. It is, however, important to emphasise that the LLE exhibits a very rich dynamical behaviour and not all parameter configurations give rise to typical behaviour (see Section 5.5.4).

Each of the four characteristic régimes seen in Fig. 19 can be understood in terms of a manifestation of a particular type of a solution of the LLE [28,196]. For increasing values of cavity de-tuning, they are: (i) MI-induced stable dissipative structures (ii) MI-induced chaotic dissipative structures (iii) interacting (unstable) cavity solitons (CSs) and (iv) phase-locked (stable) cavity solitons. When the de-tuning is scanned, the comb successively transitions from one régime to the other, as dictated by the

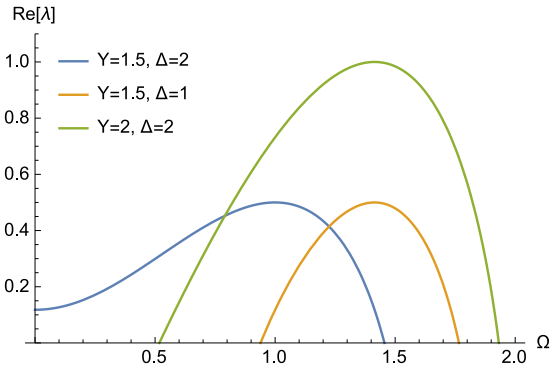

Fig. 20. Modulational instability gain spectrum for different values of intra-cavity power and de-tuning. Note that the gain does not start from zero frequency, as in the case of the NLS equation.

existence and stability of the underlying solutions. In what follows, we consider the characteristics and inter-relationships of these solutions, which allows us to deconstruct the dynamics of micro-comb formation under quite general conditions [28].

5.5.1. Modulation instability

The first two comb régimes are linked to MI. Specifically, whilst the upper and lower branches of the cavity response are homogeneously stable, they can both exhibit instability to time-periodic modulations. In the mean-field framework, MI can be analysed through a linear stability analysis of the CW solutions [37,38,48]. It is found that, in the anomalous dispersion régime, the upper branch of the cavity response is modulationally unstable when the normalised intra-cavity power satisfies the relation $Y > 1$ or, equivalently, for de-tunings $\Delta > \Delta_{\mathrm{MI}} = 1-\sqrt{X-1}$. We can accordingly identify $X = 1$ as an absolute MI threshold: the minimum driving power required for the instability to manifest itself. Fig. 20 shows typical MI gain spectra for several parameter values. Note that the linear stability analysis in the LLE framework represents a three-wave coupled-mode description and, therefore, it can be directly linked to the usual description of (hyper)parametric four-wave mixing, as discussed in Ref. [48] and in Section 3.5. In this context, however, we note that some early works on micro-combs neglected the role of the cavity de-tuning (and assumed $\Delta = 0$), which led to the MI threshold (or hyperparametric threshold) to be derived as $X = 2$.

Fig. 21 shows the CW response for the parameters above, with the solutions exhibiting MI highlighted in red. Here MI can be observed for de-tunings larger than $\Delta_{\mathrm{MI}} = -2.3$, which agrees with the de-tuning at which comb formation initiates. MI then leads to the amplification of those frequency components that experience largest parametric gain. At the threshold ($\Delta = \Delta_{\mathrm{MI}}$), these components are separated from the pump by

$$\Omega_{\mathrm{MI}} = \left[1+\sqrt{X-1}\right]^{1/2}. \tag{58}$$

Cascaded FWM, between the MI sidebands and the pump, subsequently leads to the generation of a comb with spacing close to Ω_{MI}. Typically $\Omega_{\mathrm{MI}}/(2\pi) >$ FSR and the onset of MI can, therefore, be associated with the primary combs that have been shown to underlie the initial stages of comb formation [144].

In the time-domain, MI leads to the formation of *dissipative structures* or periodic temporal patterns, as seen in Fig. 19(c) and in Fig. 21. This phenomenon was first predicted in the context of transverse or spatial effects by Lugiato and Lefever [33] and has subsequently been numerically and experimentally observed in numerous studies. It is worth emphasising that the periodic (spatial or temporal) patterns, also referred to as Turing patterns or Turing rolls [192,197], are *steady-state* solutions of the LLE; they do not exhibit the periodic recurrence in space (or slow time) as is characteristic for MI in single-pass fibre configurations [198–202]. These solutions can be found by looking for the roots of the right-hand side of Eq. (57), with an initial guess that contains the periodicity of the sought solution. Fig. 21 shows the peak power for a range of such solutions, with $X = 12$ as above (magenta). The solutions were obtained using a multidimensional Newton–Raphson solver and a continuation method [46] with the MI frequency set to Ω_{MI}, the most unstable frequency at threshold.

The MI branch is seen to connect to the CW branch at Δ_{MI} and to become unstable (dotted line) for large Δ. In the unstable régime, the components of the comb are separated by a single FSR and their amplitudes evolve chaotically, exhibiting fluctuations over timescales of the order of a photon lifetime [196,203]. This régime resembles deterministic chaos and it has also been linked to the generation of optical rogue waves [204,205]. Significantly, the régime observed in Fig. 19 for de-tunings $\Delta \in [-0.7,\ 4.7]$ displays these very characteristics. It is interesting to note that, in split-step simulations [Fig. 19], transition into this régime occurs at $\Delta \approx -0.7$, whilst the MI solution plotted in Fig. 21 already becomes unstable at $\Delta = -1.3$. However, this is simply due to the fact that, for low de-tunings, the instability of the patterned solutions occurs across timescales much longer than those over which the de-tuning is varied in Fig. 19. Indeed, split-step simulations performed at fixed de-tunings $\Delta > -1.3$ reveal extremely slow instabilities that are not captured in Fig. 19.

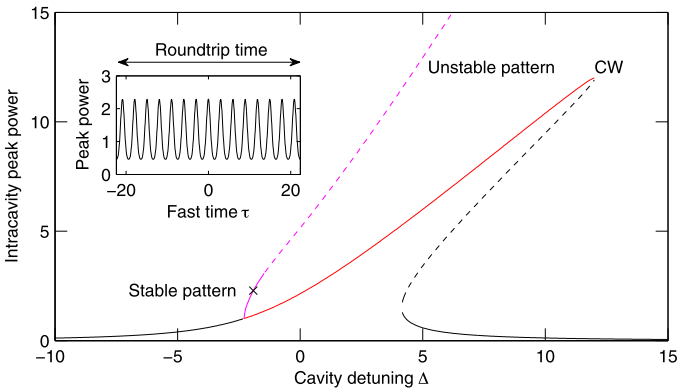

Fig. 21. Characteristics of patterned MI solutions. Black line shows the CW response and red line highlights the solutions exhibiting modulation instability. The magenta curve indicates the peak power of the patterned MI solutions. A particular solution (de-tuning indicated by a cross) is shown in more detail in the inset. Solid and dashed lines indicate stable and unstable solutions, respectively.

The initial stages of the comb dynamics shown in Fig. 19 can be readily put into the context of MI. The intra-cavity CW power increases until the de-tuning exceeds the threshold for MI, which then gives rise to a steady-state pattern (region 1). This solution eventually becomes unstable, which results in a chaotic pattern that fluctuates over several round-trips (region 2). However, as the de-tuning is further increased, the comb loses its Turing pattern characteristics (regions 3, 4); temporal structures become progressively localised in time, instead of periodically or quasi-periodically filling the entire cavity. This is because, for sufficiently large de-tunings, the nature of the solution describing the comb changes from Turing patterns into *temporal cavity solitons*.

5.5.2. Temporal cavity solitons

Temporal cavity solitons (CS) are localised structures that arise under the condition that MI coexists with a stable CW solution and they can be considered intermediate between the two states [182]. Specifically, CSs coincide with a single period of the MI pattern in some finite region and, elsewhere, with the CW solution. Accordingly, temporal CSs correspond to pulses of light that sit on top of a CW background, perpetually circulating the resonator. Just like the patterned solutions, they correspond with steady-state solutions of the LLE.

Physically, CSs arise from a double balance: their dispersive spreading is counteracted by the self-focusing Kerr nonlinearity, while all the energy they lose owing to cavity loss is replenished by coherent driving from the CW driving field. They exhibit massive multistability in the sense that, for the exact same system parameters (including the CW driving power), the resonator can support zero, one or several independently-circulating CSs. However, aside from the trivial temporal shifts, they would all be identical. This is because, for fixed pump–resonator values, only a single set of CS characteristics (peak power, duration, relative phase with respect to the CW) is permitted. Because of the (almost) instantaneous character of the Kerr nonlinearity that underpins their self-localisation and energy balance, CSs can be individually addressed: appropriate perturbations allow new CSs to be created (or old ones destroyed) without any impact on other simultaneously existing CSs. This feature distinguishes temporal CSs from pulses in typical mode-locked lasers, whose slow-gain recovery dynamics prevent their individual addressability [206,207]. Both CSs and mode-locked laser pulses belong to the broader class of structures known as dissipative solitons [208,209].

Cavity solitons have a lively history and they have been extensively investigated since the early 1980s [31,210–212]. The vast majority of these studies have, however, revolved around two-dimensional transverse nonlinear optics [182,213], where the solitons manifest themselves as self-localised beams persisting in spatially diffractive cavities [214]. While Wabnitz discussed the concept in the time-domain as early as 1993 [39], the first experimental observation of temporal CSs was not reported until 2010 by Leo et al. [45].

The experiments by Leo et al. were performed in a fibre ring-resonator with macroscopic dimensions, with many other studies subsequently using similar configurations to explore in detail the dynamics and characteristics of temporal CSs [215–221]. In the context of micro-cavities, it was already suggested in 2010 by Leo et al. that similar coherent temporal structures could underpin micro-resonator frequency combs [45]. Later theoretical studies provided further support for this proposition [22,46,47], particularly by showing that the LLE is applicable for the modelling of micro-comb formation. Experimentally, stable train formation was observed in 2012, both in MgF_2 and silicon nitride micro-resonators [49,50]. These pulses were first identified as temporal CSs by Herr et al., as discussed in the next section, who showed that the characteristics of the measured pulses agreed with those expected for cavity solitons, as predicted by the LLE [50]. Following these pioneering experiments, signatures of CSs have been observed in many micro-comb experiments [222–226].

It is worth emphasising that, despite their significant difference in physical size, passive fibre ring-resonators [45,215–218,220,221] are analogous to Kerr micro-resonators. Indeed, the temporal and spectral dynamics of both systems are

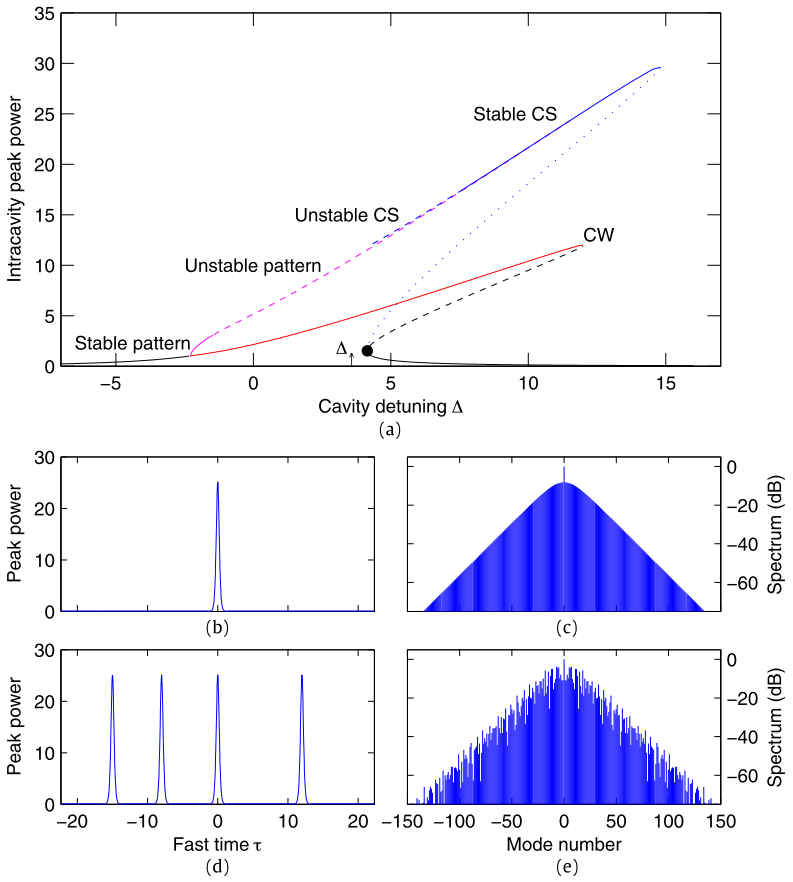

Fig. 22. Characteristics of CS solutions. (a) Peak powers of the CW (black), MI (magenta) and CS (blue) branches. Dashed lines indicate unstable solutions. (b, c) Example temporal (b) and spectral (c) profiles of a single CS for $\Delta = 12$. (d, e) Temporal (d) and (e) spectral profiles for a four-soliton solution at the same $\Delta = 12$. The time axis in (b) and (d) spans a single round-trip.

dominated, on the one hand, by the interplay of group-velocity dispersion and Kerr nonlinearity and, on the other hand, by the balance between cavity loss and coherent driving by the pump. Temporal dissipative structure generation in both fibre laser and micro-resonator systems is described (to first order) by the same model equations (e.g. the LLE, plus periodic boundary conditions in time).

Of course, the analogy should not be pushed beyond its reach, as the different physical footprints also bring about differences. For example, micro-cavities typically exhibit strong thermal nonlinearities that do not play a role in fibre ring-resonators. In addition, while in passive fibre ring-resonators CSs can be controllably created (and erased) by launching localised perturbations into the resonator [45,219], similar methods are not applicable in the micro-cavity context due to their large free spectral range (FSR). Instead, altogether new techniques for CS excitation and erasure have been developed in the micro-cavity context [50,224,225].

Moreover, in fibre cavities the temporal duration of the CS is negligible when compared to the cavity recirculation time (which can thus be considered as virtually infinite). Whereas in micro-resonators, temporal dissipative structures, such as periodic Turing patterns, may have a temporal duration equal to that of the cavity round-trip time.

Despite these differences, the close analogy between passive fibre ring-resonators and Kerr micro-cavities (and, to a lesser extent, spatially diffractive cavities) is nevertheless valuable, as it allows knowledge gained from one context to be transferred to gain insights in the other. For example, the small FSR of fibre resonators permits direct measurements of the round-trip-by-round-trip cavity dynamics, which cannot easily be achieved in micro-cavity experiments. On the other hand, the novel method of spontaneous CS excitation, first demonstrated in a micro-resonator by Herr et al. [50], has subsequently also been successfully implemented in fibre-cavity experiments [220,221].

Because CSs require the coexistence of MI and a stable CW solution, they only exist for values of the de-tuning above the up-switching point. The de-tuning at which they exist also has an upper limit of approximately $\pi^2 X/8$ [184]. Between these limits, the steady-state CS solutions can be found by looking for the roots of the right-hand side of Eq. (57) using an appropriate temporally localised initial guess. Fig. 22(a) shows the CS peak power as a function of Δ for $X = 12$, superimposed with the CW and MI branches shown in Fig. 21. Examples of the temporal and spectral profiles of a stable

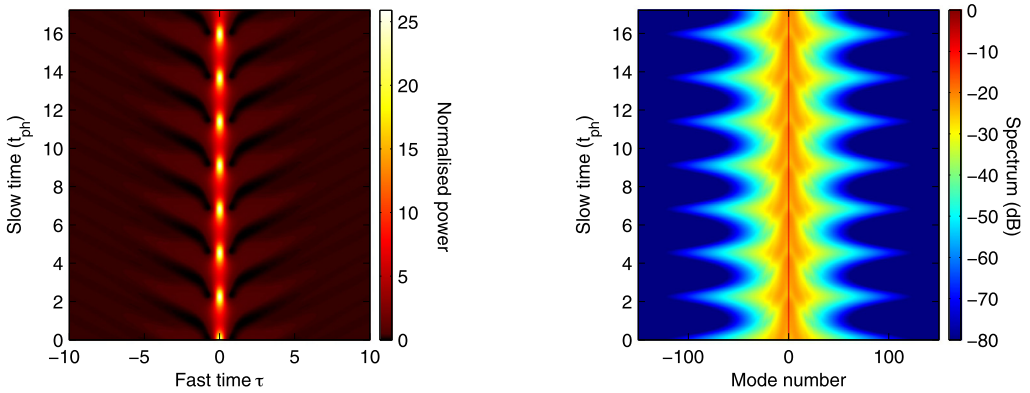

(a) Temporal evolution. (b) Spectral evolution.

Fig. 23. Dynamics of breathing CSs in the (a) temporal and (b) spectral domains.

CS solution are shown in Fig. 22(b) and (c), respectively. For this example, there is only a single CS in the cavity and so the comb spacing coincides with the FSR. However, it should be emphasised that multiple CSs can simultaneously coexist, which will naturally impact the spectral characteristics through spectral interference. To illustrate this point, Fig. 22(d) and (e) show temporal and spectral characteristics for a stable steady-state solution now with four CSs in the cavity. We use the same parameters as above, hence the temporal profiles of all the CSs are identical to those in Fig. 22(b) and (c). However, the spectrum can be seen to exhibit considerable fine features arising from the spectral interference of all the CSs. Indeed, closely-spaced CSs are known to interact through evanescent tail overlap: being dissipative structures, a soliton collision may result in annihilation of one soliton of the pair [39]. By adjusting the driving CW amplitude, it is possible to control and suppress soliton–soliton interactions and arrive at a stable pattern of phase-locked non-interacting CSs [39,227].

For lower values of the de-tuning, the soliton branch becomes unstable through a Hopf bifurcation. In this régime, solitons are oscillating (breathing) over several round-trips [28,196,228]. These dynamics are illustrated in Fig. 23(a) and (b) where we show the spectral and temporal evolution of breathing CSs over 17 photon lifetimes.

Cavity solitons complete the description of comb dynamics shown in Fig. 19. Specifically, as the de-tuning increases beyond the up-switching point ($\Delta_\uparrow = 4.15$), cycles of the MI pattern begin to reshape into oscillating CSs (region 3). These oscillations cease once the de-tuning is sufficiently large to support stable CSs (region 4). The comb then remains stable until the de-tuning exceeds the limit of CS existence. For the parameters in Fig. 19, this limit is given by $\Delta \sim \pi^2 X/8 \sim 14.8$, in agreement with the observed decay to CW.

5.5.3. Analytic approximations

No exact closed-form solution is known for cavity solitons of the LLE. However, by using NLS soliton perturbation theory, an approximate solution can be derived in the limit $X,\ \Delta \gg 1$, which is relevant to most micro-comb configurations [28,39]. Neglecting the weak CW background, this approximation reads:

$$E_{\mathrm{CS}} = \sqrt{2\Delta}\ \mathrm{sech}\left(\sqrt{\Delta}\tau\right). \tag{59}$$

Interestingly, E_{CS} *is* a solution of the LLE for a synchronous pump $S = E_{\mathrm{CS}}$ [229] and, in the appropriate limit, it also coincides with the localised part of the solution for zero losses derived by Barashenkov and Smirnov [22,184].

The CS approximation above can be used to obtain an estimate for the bandwidth of the corresponding frequency comb [28]. Specifically, by assuming on-resonance pumping ($\Delta = X$) and critical coupling ($\alpha = \theta$), the 3-dB comb bandwidth can be estimated (in dimensional units) from:

$$\Delta f_{3\mathrm{dB}} = \frac{0.315}{1.763}\sqrt{\frac{2\gamma P_{\mathrm{in}} Q \lambda_{\mathrm{p}} \mathrm{FSR}}{\pi c |\beta_2|}} = \frac{0.315}{1.763}\sqrt{\frac{2\gamma P_{\mathrm{in}} \mathcal{F}}{\pi |\beta_2|}}, \tag{60}$$

where $P_{in} = |E_{in}|^2$ is the power of the driving field at the resonator input.

Eq. (60) underpins the relevance of various pump–resonator parameters and it has been shown to be in reasonable agreement with experimentally-reported micro-combs [28]. However, it must be emphasised that its derivation neglects all higher-order effects. Accordingly, the estimate (60) becomes inaccurate for broadband combs whose dynamics can no longer be captured by the elementary LLE. The dominant deviation arises from higher-order dispersion [28,187], as outlined in more detail in Section 5.6. Finally, in addition to obtaining an estimate for the 3 dB bandwidth, Eq. (59) was also recently used to estimate the full nonlinear comb conversion efficiency [230].

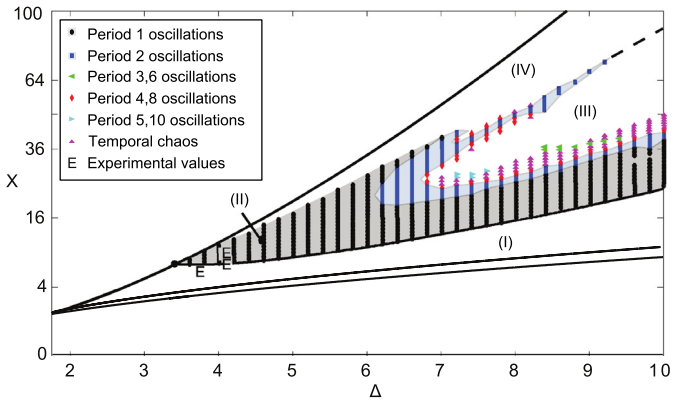

Fig. 24. Bifurcation characteristics of CSs of the LLE over a wide zone in the (Δ, X) plane. Stable CSs exist in region (I), while they are unstable (oscillating) in region (II). Transient chaos occurs in region (III) and the entire system destabilises in region (IV), exhibiting full spatio-temporal chaos.
Source: Adapted from Ref. [216].

5.5.4. Beyond the quintessential

The above analysis shows that the comb transitions in Fig. 19 can be understood as the bifurcation sequence: stable MI-induced patterns → unstable MI-induced patterns → unstable CSs → stable CSs. Similar dynamics manifest themselves for a range of pump parameters X, yet it is important to emphasise that, even in a pure LLE system, régimes where deviations arise also exist. In-depth analyses of the characteristics of LLE solutions have been reported by a number of groups [184,192,216] and Fig. 24 illustrates a bifurcation map over a wide parameter zone in the (Δ, X) plane [216]. It is clear that, for some X, the LLE admits no (breathing) CS solutions, whilst more complex chaotic régimes can emerge for others [216]. Accordingly, not all parameters permit adiabatic ramping into the soliton régime; the unstable MI régime can instead decay directly into the lower branch of the CW response. It must also be emphasised that perturbations to the elementary LLE can considerably modify the range of existence of various solutions. For example, higher-order dispersion has been shown to promote combs associated with single CSs, allowing them to exist even in régimes where they are forbidden in the elementary LLE [231].

In addition to the pump parameter X, the cavity round-trip time t_R can also have a profound influence on the nature of the comb solutions. Specifically, it is found that only stable combs emerge when the round-trip time is sufficiently small so that only a single period of MI can fit inside the resonator [10,188]. These combs have been referred to as Type I (see previous section) combs so as to distinguish them from Type II configurations, where the MI period is much smaller than the round-trip length [10]. The stability of Type I combs has been verified in experiments utilising spectral line-by-line pulse shaping [10], as discussed in Section 4.3.

Finally, it should be emphasised that, as comb formation is triggered from random vacuum fluctuations, the precise comb dynamics will vary from realisation to realisation. This is particularly reflected in the soliton régime and it is found that the number of emerging solitons can vary significantly depending on the initial noise seed [50].

5.6. Effect of higher-order dispersion

The analysis above considered the elementary LLE which assumes the resonator group velocity dispersion to be constant. While this approximation is valid for narrowband combs, in general the group velocity dispersion (GVD) can exhibit a significant variation over the comb bandwidth. Accordingly, for broadband combs it is necessary to consider the effect of higher-order dispersion terms.

5.6.1. Dispersive wave generation

One of the most important effects of higher-order dispersion is that it causes the patterned MI peaks and CSs to emit linear radiation. This occurs because higher-order dispersion allows linear radiation to be phase-matched with the driving field and it gives rise to spectral peaks that are vividly displaced from the pumped mode. Analogous dispersive wave (DW) generation has been extensively studied in fibre optics since the 1980s [232–234] but the process was not linked to micro-combs until 2012, when it was described in terms of cascaded FWM [235]. Indeed, subsequent mean-field numerical modelling revealed that MI patterns and temporal CSs could emit DWs [46,186,196] and that this could explain previously unidentified spectral features observed in the experiments [25]. A conclusive experimental observation of DW emission by CSs was recently reported by Jang et al. using a microscopic fibre resonator [217].

Fig. 25(a) shows a dispersion profile approximating a 226 GHz silicon nitride resonator. The GVD is seen to vary considerably and to switch from anomalous to normal dispersion at approximately 1765 nm. Fig. 25(b) and (c) shows two ensemble-averaged comb spectra obtained from numerical simulations that include the full dispersion profile in Fig. 25(a). Other parameters are approximated from the experiments in Ref. [25]: the resonator has a finesse of 350 and it is driven

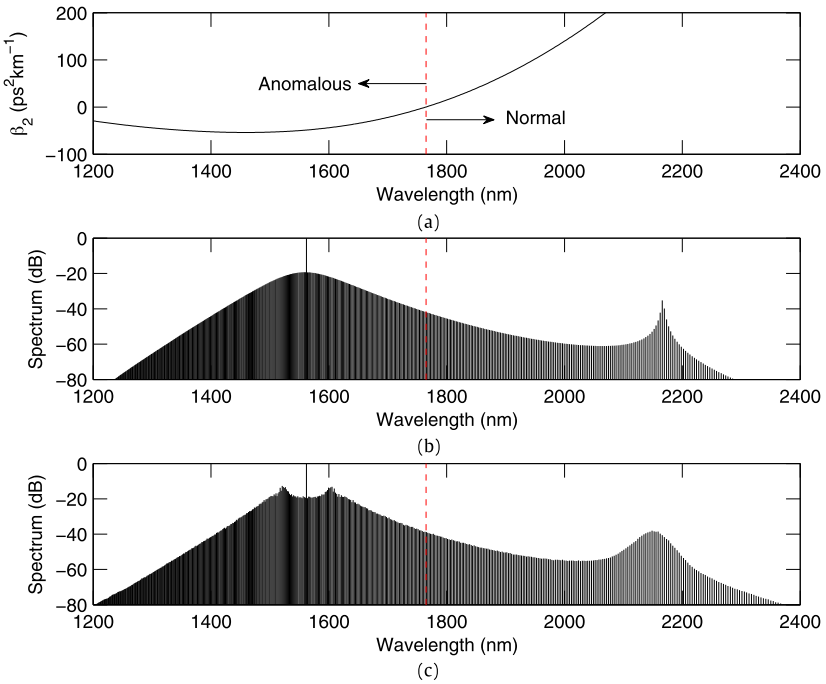

Fig. 25. Mean spectra of simulated micro-combs generated in a 226 GHz silicon nitride resonator for two different values of cavity de-tuning. In (a) the de-tuning is $\Delta = 6$ and the comb corresponds to a stable CS comb, while in (b) $\Delta = 3$ and the comb corresponds to unstable MI. Both spectra show a typical dispersive wave peak centred at 2166 nm.

with 760 mW of pump power (normalised pump strength $X = 6$). The comb in Fig. 25(b) corresponds to a stable soliton comb ($\Delta = 6$) with a single CS populating the cavity, whilst the comb in Fig. 25(b) is operating in the unstable MI-induced pattern régime ($\Delta = 3$). The CS spectrum displays a very clear and sharp DW peak at approximately 2166 nm. In the MI régime, the same peak appears considerably broader and smoother, owing to the significant fluctuations exhibited by the temporal structures in this régime [196].

Fig. 26 shows temporal characteristics corresponding to the CS spectrum in Fig. 25(b). Specifically, Fig. 26(a) illustrates the field evolution over several photon lifetimes, while (b) and (c) depict a snapshot over a particular round-trip (indicated with white dashed line in (a)). Two observations can be made. Firstly, the CS is seen to exhibit a constant time-domain drift. This can be understood to arise from a spectral recoiling effect: conservation of energy implies that the soliton must spectrally shift in the direction opposite the emitted radiation. Accordingly, the group velocity of the soliton will be different to that of light at the pumped mode. Hence, at each round-trip the soliton experiences a temporal drift V relative to the group velocity at the pump wavelength. Typically, this drift is very small - for the particular simulation in Fig. 26 we have $V \approx -71$ attoseconds. The second observation that can be made is that the DW corresponds in the time-domain to an oscillating radiation tail that is attached to the soliton [236], as clearly seen in Fig. 26(c) which shows a zoom-in of the leading tail of the CS.

For typical micro-comb conditions, the DW frequency shift $\Delta\Omega_{\mathrm{DW}}$ can be approximated using a resonance equation [217, 236]:

$$\sum_{k\geq 2} \frac{\beta_k}{k!} \Delta\Omega_{\mathrm{DW}}^k L - V\Delta\Omega_{\mathrm{DW}} + [2\gamma L P_0 - \delta_0] = 0. \tag{61}$$

For the parameters in Fig. 25, this equation predicts the DW to manifest itself at 2167 nm, in agreement with the simulation result. Finally, we note that Eq. (61) is an accurate approximation for typical micro-comb parameters but a more complete prediction has also been derived by Milian et al. [236]. This prediction is applicable to arbitrary resonator configurations and also captures the damping oscillations at the CS edge [217].

5.6.2. Bandwidth shaping

Higher-order dispersion may have a significant impact on the micro-comb spectrum [28,187,237,238]. In particular, when the GVD exhibits significant relative variation over the comb bandwidth, Eq. (60) loses its validity and must be phenomenologically corrected.

A first-order correction can be estimated from the dispersive wave emission mechanism. Specifically, since the DWs are linear, significant spectral broadening is not expected beyond their spectral shift. Therefore, the comb bandwidth is expected

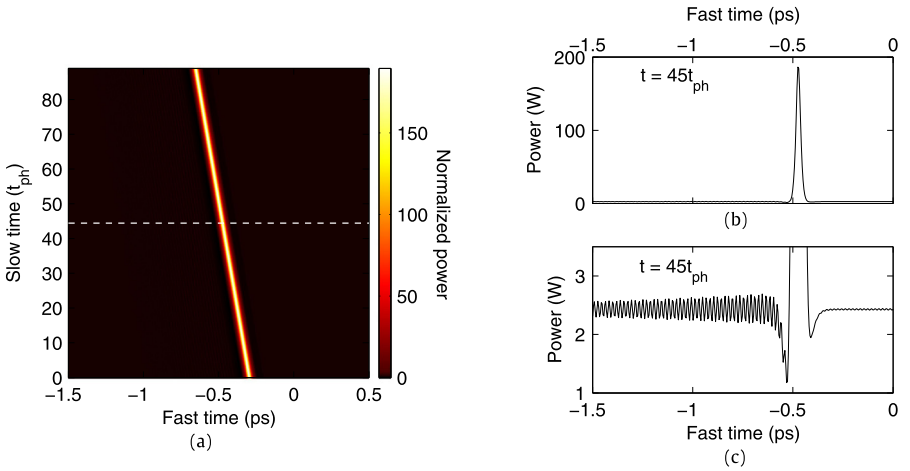

Fig. 26. Time-domain characteristics of a CS perturbed by higher-order dispersion. (a) Temporal evolution showing how the CS exhibits a time-domain drift. (b) Temporal CS profile at $t = 45t_{\mathrm{ph}}$, indicated by the dashed line in (a). A zoom on the leading tail of the CS is shown in (c).

to possess an upper limit of $2|\Omega_{\mathrm{DW}}/(2\pi)|$. Combined with the general prediction of Eq. (60), this implies that, for a broadband comb, it is beneficial to have a low and flat GVD [28,187,237,239].

The impact of higher-order dispersion further suggests the possibility of tailoring the comb spectrum to specific applications via dispersion engineering [187]. Indeed, specific dispersion landscapes have been suggested and demonstrated that optimise selected comb characteristics, such as power-per-mode [187], bandwidth [187] or flatness [237]. The DW emission process also offers interesting opportunities to concentrate the comb spectral density within a narrow spectral region of interest by suitably designing the dispersion topology [238].

6. Generation of coherent micro-combs

Section 5 summarised the relevant features of the Lugiato–Lefever equation (LLE) that is at the basis of the theoretical description of optical parametric generation in micro-resonators. This analysis clarified that coherent optical states can be produced by exciting the cavity with a resonant continuous-wave (CW) pump. This is consistent with the first experimental observations by Ferdous et al. [10] reported in Section 4.3.

In this section, we review the experimental observations of coherent optical combs, together with progress made towards gaining control of the micro-comb generation, including detailed studies of the micro-comb phase profile characteristics. Several challenges were faced by these studies, mostly related to the proper control of the key parameters necessary to achieve coherent states.

Together with the experimental observations of temporal cavity solitons (CSs) and the detailed study of the properties of optical parametric oscillation in the standard pumping configuration – e.g. with an external CW optical pump injected into one of the resonances – some alternative approaches to the generation of micro-combs have been demonstrated, including parametric seeding, self-injection locking and filter-driven four-wave mixing (FWM). These efforts have paved the way for the applications discussed in Section 7.

6.1. Experimental observation of temporal cavity solitons and nonlinear dynamics

Parametric generation, or oscillation, in CW-pumped nonlinear micro-resonators is mainly governed by two parameters of the optical pump: its power and its relative frequency shift with respect to the cavity resonance, i.e. the de-tuning. This was discussed theoretically in Section 5.5.2 and is summarised in Figs. 22 and 24, highlighting the range where these parameters allow for coherent states, such as temporal CSs. The ultimate performance and behaviour of micro-combs is, however, strongly dependent on the excitation conditions and so it has been critical to find a proper experimental approach to enable one to excite the CS on the CW background. The continuous scanning of the pump de-tuning from blue de-tuned to red de-tuned values has proved to be a winning strategy for this purpose.

It was first proposed theoretically by Matsko et al. [203] and is shown in Fig. 19 (Section 5.5) [28,186]. When the comb enters into a state that is in a parameter region where stable CSs are allowed, the intra-cavity power experiences a sudden drop and CSs are formed. This behaviour is at the basis of the first experimental demonstration of temporal CS-based micro-combs [50]. Stable pulsed operation of a silicon nitride (Si_3N_4) micro-resonator, in the form of femtosecond pulse trains associated with frequency combs, was reported in 2013 by Saha and co-workers [49]. The clear identification of CSs in micro-resonators was first verified experimentally by Herr et al. [50] in 2014, when they overcame an important experimental challenge in getting access to the CS region of parameters.

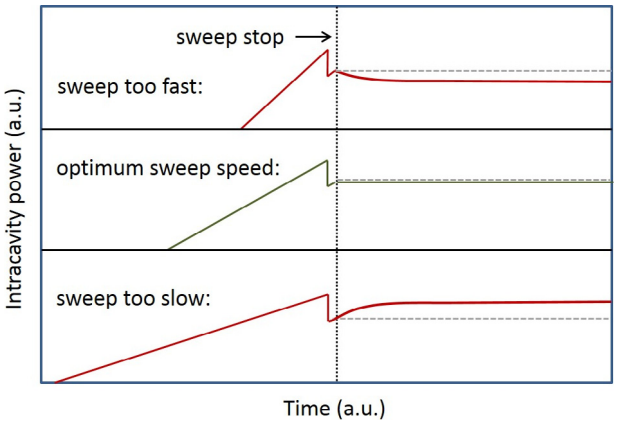

Fig. 27. Scheme for achieving a stable phase-locked state in a micro-resonator with thermal nonlinearity. In order to generate a phase-locked comb state, the pump laser frequency is swept into a micro-resonator resonance. Increasing intra-cavity power leads to heating of the resonator and, typically, a red-shift in the resonance. The transition into a phase-locked state leads to a sudden decrease in intra-cavity power as a result of loss in coupling efficiency. In the case of a fast laser sweep (upper panel), the resonator still heats up after stopping the sweep, increasing the (absolute) de-tuning of the pump laser frequency from the resonator mode which, in turn, leads to a decreasing intra-cavity power. This can lead to a loss of the phase-locked state that requires a power level as shown by the horizontal dashed line. Sweeping the laser too slow into the resonance leads to an increasing intra-cavity power after stopping the sweep (lower panel). This is a result of the sudden reduction of intra-cavity power after transitioning into the phase-locked state and a subsequent slow temperature decrease of the resonator which, in turn, leads to a decreased (absolute) de-tuning of the pump laser frequency from the resonator mode. The optimal laser sweep speed is shown in the middle panel. Here, the temperature decrease, due to the transition into the phase-locked state, is exactly compensated for by the residual heating after stopping the laser sweep.

Thermal effects have proved to be an important challenge in implementing such adiabatic cavity de-tuning procedures for exciting CSs. A thermo-optical nonlinearity (described in Section 3.6.1 and references therein) induces a refractive index change that is proportional to the intensity of the optical field. This effect is governed by the thermal capacitance and resistance of the resonator and so is typically very slow, in contrast to the nonlinear response arising from the ultra-fast Kerr effect that underpins the mechanism for the generation of the comb modes.

While thermo-optical effects do not contribute to any energy exchange between pump and comb modes, nonetheless they effectively modify the steady-state behaviour of the intra-cavity pump by creating a slow dependence of the cavity de-tuning with pump power. Thermal stability has traditionally only been reached in resonators where heating leads to a linear decrease in intra-cavity power. In this class of micro-resonators a thermal-locking régime can be reached. However, the thermal bi-stability will influence the final amount of optically-coupled power.

The transition from a chaotic comb régime to a phase-locked state leads to an abrupt change in circulating intra-cavity power [50], (Fig. 19(a)), where the transition is evident for a normalised cavity de-tuning (Δ) greater than five. It is very important to stress that, after the soliton state is formed, the coupled power into the resonator needs to be maintained constant, otherwise the solitary state can be lost. This level of change in power induces an effective variation in the de-tuning for thermal bi-stability that needs to be accounted for in order to reach a stable comb state associated with a temporal solitary pulse.

This thermal de-tuning induced by the sudden intra-cavity power change can be compensated for by adjusting the rate at which the power in the cavity is increased. The experimental challenge has been to find the right sweep rate at which the residual resonator heating, which occurs after the sweep is stopped, is compensated for by the temperature decrease induced by the sudden loss of intra-cavity power after the transition into the phase-locked state (see also supplementary material in [50]).

Fig. 27 shows theoretical examples of tuning into a micro-resonator resonance with a transition into a phase-locked state at different laser sweep speeds. The panel in the middle shows the optimum speed rate that allows the coupled power to be maintained constant after the phase-locked state is achieved.

This approach has been the key to obtaining stable phase-locked states in most micro-resonator materials that have positive thermal nonlinearities. However, it has been suggested very recently [240] that a negative thermo-optic coefficient (as in CaF_2, where thermal locking cannot usually be reached) could also lead to CS states.

Fig. 28 shows an optical spectrum and time-domain trace of a single soliton state generated in a MgF_2 micro-resonator with a mode spacing of 35 GHz. The spectrum of the soliton state follows a regular hyperbolic secant profile. The inset shows the radio-frequency beat-note - its narrow bandwidth reflects the coherence of the soliton state.

In a single soliton state, the phase amongst the comb modes is nearly flat, as first reported by Herr and co-workers [50]. A flat phase results in a transform-limited optical pulse and this can be readily observed via a frequency-resolved optical gating (FROG) spectrogram (Fig. 28(b)).

As noted in Section 5.5.4, however, the precise dynamical nature of the comb can vary from case to case and can show a nontrivial behaviour of the phase of the comb lines. This dependence was already evident in the early work of Ferdous

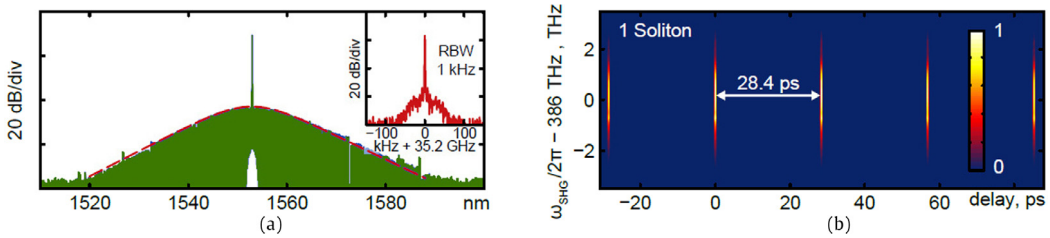

Fig. 28. Soliton generation in a MgF_2 micro-resonator. (a) Shows the optical spectrum of the generated soliton with a characteristic hyperbolic secant shape. The inset is a microwave spectrum of the 35-GHz-repetition-rate, at which the solitons are emitted. (b) Shows a time-domain measurement of the soliton using frequency-resolved optical gating (FROG).
Source: Data from T. Herr and T.J. Kippenberg and co-workers.

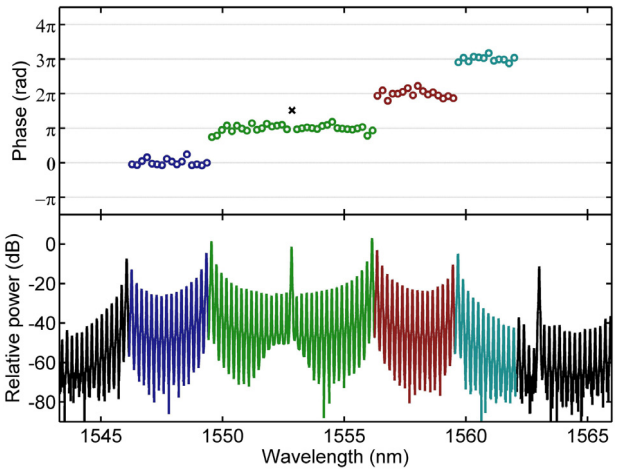

Fig. 29. Phase steps in the optical spectrum of a micro-resonator-based frequency comb. The phase of the comb modes of different sections of the micro-comb show steps of multiples of π.
Source: From Ref. [241].

et al. (see also Section 4.3) but, in that work, detailed experimental evidence of the different nonlinear régimes was missing. Subsequently, a focused study of the phase properties of several nonlinear comb configurations was carried out by Del'Haye et al. [241] where, in addition to soliton states, micro-comb states with more peculiar spectral envelopes were also observed where steps in the relative phase of the different micro-comb sections occurred. This is in contrast to single soliton states, where all the phase differences between neighbouring combs are almost constant. Fig. 29 shows an optical spectrum and the measured phases of a micro-comb generated in a fused silica micro-rod with a 25 GHz mode spacing. The phases were measured by adjusting all of the individual phases of the comb modes until the shortest possible pulse was generated. In this state, the phase difference between all neighbouring comb modes was constant. Subtracting the applied phases to the comb modes revealed their initial phases.

Fig. 30 shows additional comb spectra with corresponding phases measured in a fused silica micro-disc with a 16.4 GHz mode spacing. Most phases show distinct steps of π between different spectral regions of the comb, although some comb states exhibited rather smooth transitions of the phase (Fig. 30(b)). The state in Fig. 30(a) is different, in the sense that the phase is asymmetric around the pump laser wavelength at 1557 nm. Multi-soliton states were also observed in silica discs by Yi et al. [222].

6.1.1. Chaotic régimes in micro-combs

In Section 5.5.2 we saw how the existence of CSs is dependent on the de-tuning Δ of the pump laser frequency with respect to the micro-cavity resonance. This parameter also regulates the nature of the different chaotic régimes that are often encountered in micro-comb generation.

Chaotic micro-combs have been experimentally and theoretically analysed by Matsko et al., Coillet et al. and Webb et al. [203,242,243]. In particular, different routes to chaos have been observed for regions of de-tuning and power parameters where the CS are permitted, as opposed to regions where they are not. A detailed study of this was reported by Coillet and Chembo [242] who analysed the bifurcation diagram for several dissipative structures permitted by the LLE for different values of de-tuning Δ. We note that CSs only occur beyond a threshold in Δ, as seen in Fig. 24, where CSs cannot

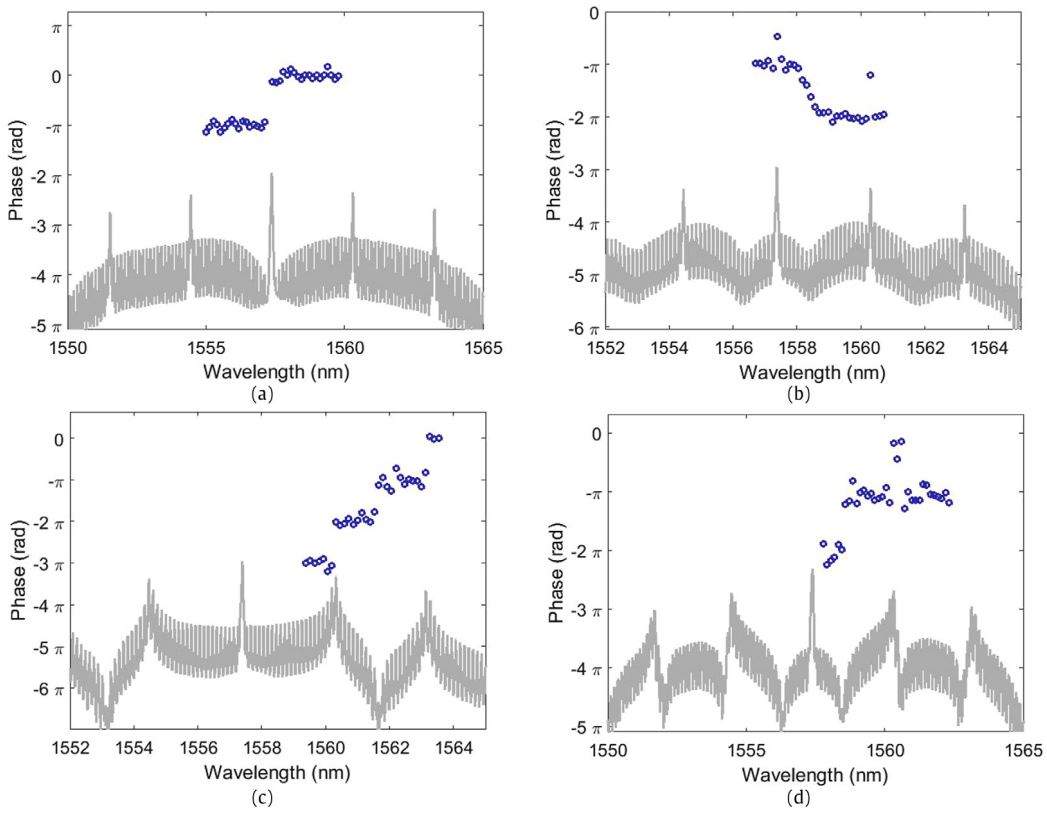

Fig. 30. Phase steps in micro-combs. Panels (a)–(d) show different types of micro-combs with phase steps of multiples of π between sections of the comb. The corresponding optical spectra are shown as grey trace in the background, with arbitrary power units in log scale. All spectra have been recorded with the same pump mode at a wavelength of 1557 nm in a fused silica disc with 16 GHz mode spacing. Panel (a) shows a comb with antisymmetric phases around the pump laser. Panel (b) shows a comb without steps but with a smooth transition between regions of different phases.
Source: Adapted from Ref. [241].

be excited for $\Delta < 1.8$ regardless of the input pump power X. Hence $\Delta = 1.8$ represents a boundary threshold between the two different operating régimes.

The route to chaos for these régimes, therefore, possesses different bifurcation diagrams, which translate into different average spectral features as represented in Fig. 31. For $\Delta = 0.3$, CSs cannot be excited for any pump power and chaos arises from the destabilisation of modulation instability (MI)-seeded combs through the dynamic transition from Type I to Type II combs. These primary and secondary combs evolve by populating nearby modes until every mode is filled. Conversely, for $\Delta = 2.7$, chaos originates from the destabilisation of a single cavity soliton, as also described in Section 5.5.4 (Fig. 24).

6.2. Mode interaction-aided comb generation

Most resonators possess multiple transverse eigenmode families with different polarisations, e.g. TE and TM, and different numbers of maxima and minima in the two orthogonal directions, as described in B.2. Modes in different families are typically only weakly coupled to each other but, in certain cases, when the resonance frequencies nearly coincide, they may experience strong interactions. Modal interaction can strongly affect the comb spectrum and can be conveniently exploited, for example, for comb generation in normal dispersion resonators.

6.2.1. Mode crossing

Accidental-mode degeneracy has a high chance of being frequently observed in multi-mode micro-resonators, especially when the micro-resonator has an increased geometry size. Different mode families usually have different group velocities, corresponding to different free spectral ranges (FSRs) of their resonant frequencies. Therefore, mode crossing regions can exist periodically along the frequency axis. Since the different modes have very close resonant frequencies at the mode degeneracy points, even a weak coupling can lead to significant energy exchange between them, thus changing their properties compared to the case without coupling. Mode crossing (also termed level crossing) is a widely-observed and intensely-studied phenomenon in multiple areas of physics, including quantum mechanics, microwave systems, optical waveguides and cavities. For historic reviews and summaries, see the review articles [244–247]. In optical micro-resonators,

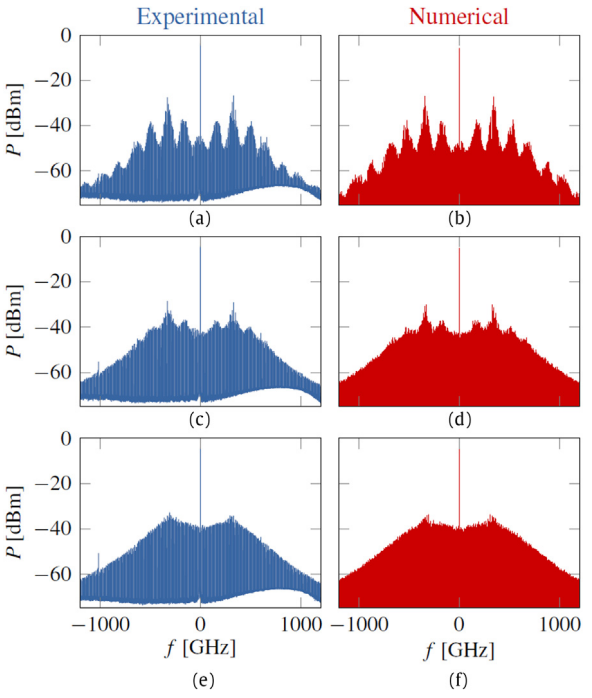

Fig. 31. Experimental observation of chaotic comb states in an 11-mm-diameter MgF_2 resonator with a mode spacing of 6 GHz. Panels (a), (c), (e) show measurements of chaotic micro-comb spectra, with the corresponding simulated comb states in panels (b), (d), (f). Δ is 0.3,1.8 and 2.7 for (b), (d), (f), respectively. Different values for Δ correspond to different de-tunings between the pump laser frequency and the micro-resonator resonance frequency. After Ref. [242].

their geometry is one key parameter to induce mode coupling [248,249]. Even for micro-resonator designs which, ideally, have no mode coupling, the real device can show strong coupling due to fabrication non-idealities, such as scattering, geometry deformation and refractive index inhomogeneity [250–252]. The fundamental consequence of mode coupling is that the eigenvalues of the coupled modes become different compared to those without coupling.

$$\Omega_{\pm} = \frac{\Omega_1 + \Omega_2}{2} \pm \frac{1}{2}\sqrt{(\Omega_1 - \Omega_2)^2 + 4\kappa_{12}\kappa_{21}}. \tag{62}$$

Here $\Omega_{1,2} = \omega_{1,2} + i\alpha_{1,2}$ are eigenvalues of the two original uncoupled modes; the real parts $\omega_{1,2}$ are their angular frequencies and the imaginary parts $\alpha_{1,2}$ are their decay rates (i.e. cavity losses). If the loss mechanisms of the two original modes are independent, we have $\kappa_{12} = \kappa_{21}^* = \kappa$. In the special case when the two uncoupled modes have identical frequencies and losses ($\Omega_1 = \Omega_2 = \Omega$), the eigenvalues of the coupled-mode system are given by $\Omega_{\pm} = \Omega \pm |\kappa|$. The new eigenvalues correspond to two super-modes whose frequencies are separated by $2|\kappa|$. This behaviour is generally named mode coupling-induced-avoided-crossing (anti-crossing). In general, both the frequencies and decay rates of the super-modes change with respect to the values that they would have without mode coupling. Both effects can affect the comb dynamics. The frequency shift affects the phase-matching condition for four-wave mixing (FWM) and has, so far, been found more critical. The effect can be regarded as a change of the local group velocity dispersion which sometimes is large enough to change its sign compared to the global dispersion.

Fig. 32 shows a typical example of a local change in group velocity dispersion due to mode interactions. Fig. 32(a) depicts the FSR versus the optical wavelength for a Si_3N_4 micro-ring containing two transverse modes. Both modes show an overall normal dispersion, which corresponds roughly to a linear increase in FSR with wavelength. However, this typical FSR trend may drastically change in some wavelength ranges where avoided mode-crossings happen, due to mode interaction-induced resonance shifts. In the absence of mode coupling, the two lines would intersect, but here it is clear that the modes distinctly avoid any intersection in the resonance frequencies.

The zoomed-in FSR spectrum is shown in Fig. 32(c) and in the local group velocity dispersion in Fig. 32(d), which is extracted from the local slope of the FSR spectrum. The local dispersion of one mode (Mode 1, red line) is clearly anomalous ($D > 0$) for the range of wavelengths close to a mode-crossing point, whereas it is normal, $D \sim -156$ ps/nm/km, away from mode-crossing regions.

Mode interactions in micro-resonators with anomalous dispersion have been studied by Grudinin et al. [239], where local variations in the FWM efficiency in MgF_2 whispering-gallery mode (WGM) resonators were observed. These were attributed to a change in phase-matching conditions for the FWM process that resulted from local variations in dispersion induced by the avoided mode crossing.

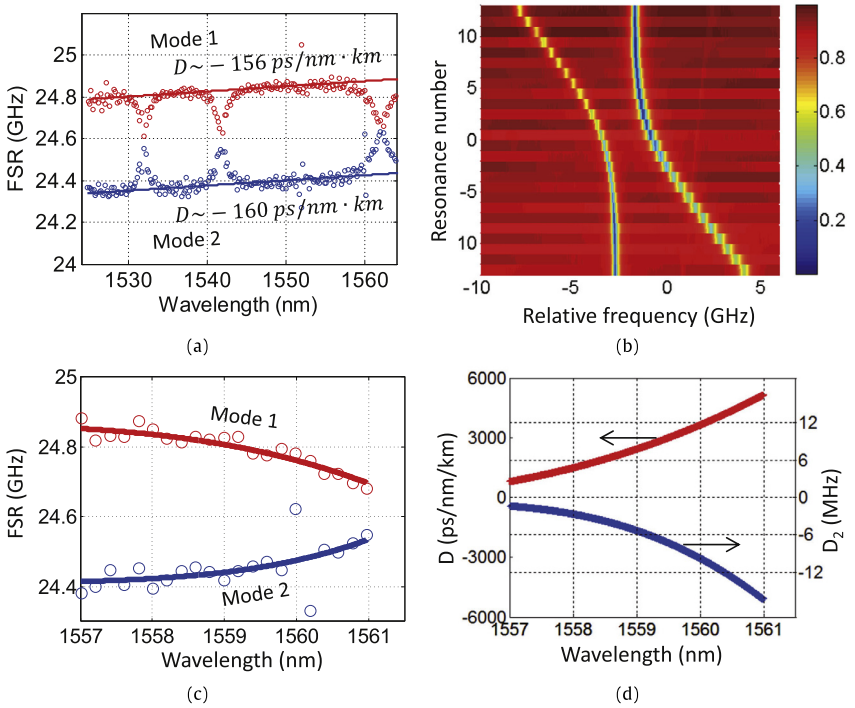

Fig. 32. Mode interactions in a Si_3N_4 micro-ring. (a) Measured FSR versus optical wavelength for two TE modes plotted in red circles and blue triangles and fitted with $D \sim -156$ ps/nm/km and $D \sim -160$ ps/nm/km, respectively. (b) Aligned resonances with fixed increment showing an absence of mode crossing, in the region around 1542 nm. (c) Zoomed-in view and fitted FSR spectrum in the mode-crossing region around 1561 nm. (d) Calculated local dispersion of the two modes plotted in red and blue, respectively. (After Ref. [137].)

Polarisation mode crossings have been observed in Si_3N_4 ring-resonators [253]. Strong polarisation mode coupling between the fundamental TE and TM modes may lead to a splitting of the resonances in the transmission spectrum and may manifest itself as a reduction of the mode intensity when a frequency comb is generated, as in the experiments of Ramelow and co-workers [253].

The influence of mode interactions on the formation of CSs was also studied by Herr et al. [254]. They reported experimental and numerical investigations of the influence of higher-order dispersion and mode coupling in crystalline micro-resonators. Such resonators showed complex mode structures featuring multiple mode families, exhibiting both normal and anomalous group velocity dispersion. It was found that only certain mode families supported soliton formation. Furthermore, it was observed that avoided mode crossings could prevent soliton formation when the mode-crossing point was too close in frequency to the pump mode.

Very interestingly, mode interactions have been recognised as key to enabling frequency comb generation in micro-resonators with normal group velocity dispersion. The importance of mode interactions was first pointed out by Savchenkov et al. [255] who noted that they were responsible for generating most frequency combs in WGM resonators that had normal dispersion. The mode interactions were shown to have a large influence on the group velocity dispersion of the resonator, thus either increasing or decreasing the parametric oscillation threshold. It was pointed out that, since mode crossings locally modify the effective dispersion, they can be beneficial in allowing the generation of frequency combs for mode families that are otherwise characterised as having normal dispersion. The dynamics of comb formation in the presence of mode coupling has been modelled by various extensions of either the LLE or modal expansion methods [51,254]. However, the scalar LLE described in Section 5 generally does not account for more than a single mode family.

Liu et al. further investigated [137] mode coupling in few-moded, normal GVD Si_3N_4 micro-resonators. A signature for comb generation that occurs via mode coupling was found to be that one of the initial sideband frequencies was pinned at the mode-crossing frequency (see Fig. 33(a)). This allowed combs with different FSRs to be generated by changing the frequency of the pump laser and can provide a route for the generation of coherent Type I frequency combs (with native single FSR mode spacing), enabled by the large effective anomalous dispersion induced by mode coupling. Mode coupling may further lead to an asymmetry in the comb spectrum, by limiting the growth of the comb bandwidth on the pinned side. Fig. 33(b) shows the spectrum of a Type I comb. The intra-cavity waveform was found to contain pulses close to being transform-limited pulses (Fig. 33(c)). The comb also showed very low-intensity noise (Fig. 33(d)), which is a preliminary signature of a coherent mode-locked micro-comb.

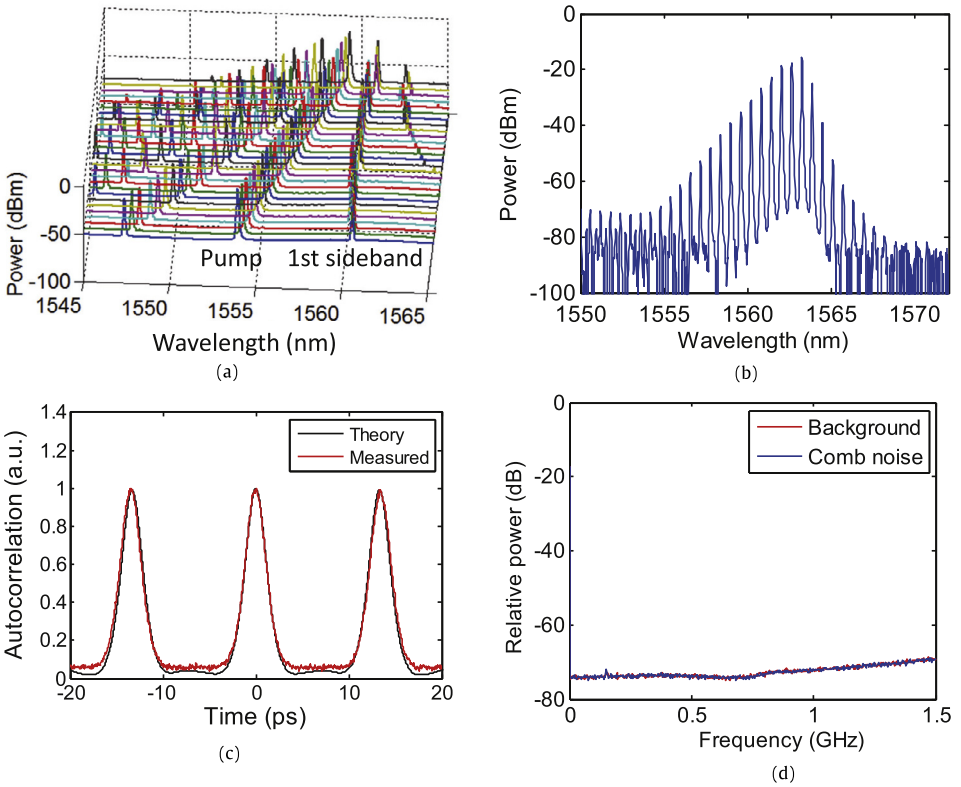

Fig. 33. Mode interaction-aided comb generation in a Si_3N_4 micro-ring (the same ring as in Fig. 32). (a) Primary comb pinning. The laser pumps different resonances. One of the first comb sidebands keeps an approximately constant location around 1560 nm. (b) Type I comb spaced by 1 FSR. (c) Autocorrelation trace of the comb in (b), measured at the drop-port. The intra-cavity waveform is almost a transform-limited pulse. (d) Intensity noise of the comb in (b), which is below the sensitivity of the measuring electrical spectrum analyser. (After Ref. [137].)

6.2.2. *Dark mode-locked pulses*

In the case of micro-resonators with global normal dispersion, mode-locked dark pulses may also be excited by the mode interaction [51], so that the comb transitions to a mode-locked state with a much broader spectrum. Fig. 34(a) shows the spectra of such a comb, generated from a normal-dispersion Si_3N_4 micro-ring. The frequency de-tuning between the pump laser and the micro-ring resonance is gradually adjusted from stages I to III, thus bringing the pump closer into resonance. Fig. 34(b) shows the comb intensity noise at each stage. A spectrally-broad mode-locked comb with low-intensity noise is obtained at stage III. Its zoomed-in spectrum and phase profile are shown in Fig. 34(c). The phase profile is retrieved by using the method of line-by-line pulse shaping. It has been reported that bright soliton combs in the anomalous dispersion region have a nearly uniform phase profile, corresponding to an ultra-short bright pulse in the cavity [50] (in the single soliton case). In comparison, the phase profile of dark pulse combs is generally far from flat. Fig. 34(d) shows the time-domain waveform reconstructed with the amplitude and phase information in Fig. 34(c). A complex chirp structure can be observed. Note that such dark pulses in micro-resonators differ from the topological dark solitons found in normal dispersion single-mode fibres [256,257]. The fibre dark solitons have a π-phase shift between the background levels which is incompatible with the periodic boundary conditions imposed by the cavity.

By contrast, the formation of dark pulses in cavities is related to interactions between switching waves that connect the two bi-stable CW solutions of the intra-cavity field [258,259]. It is worth noting that mode interactions are not necessary to maintain the stable dark pulses but, essentially, only provide an excitation pathway. However, the presence of mode interactions may cause distortions of the dark pulse. The duty cycle of the dark pulse can also be affected by mode interactions, so that the waveform in the cavity appears to be a bright pulse (which is termed 'platicon' in Ref. [260]). Mode interactions and dark pulse formation provide a solution for broadband frequency comb generation in wavelength ranges (e.g. in the visible) where normal material dispersion is likely to dominate.

6.2.3. *Programmable mode interaction control with coupled micro-resonators*

As discussed in Section 6.2.1, mode interactions are very useful for comb generation in the normal dispersion region. However, in a single micro-resonator mode interactions generally rely on accidental degeneracies of the modes and are, therefore, very difficult to control. This drawback can be overcome by using a dual-coupled micro-resonator structure,

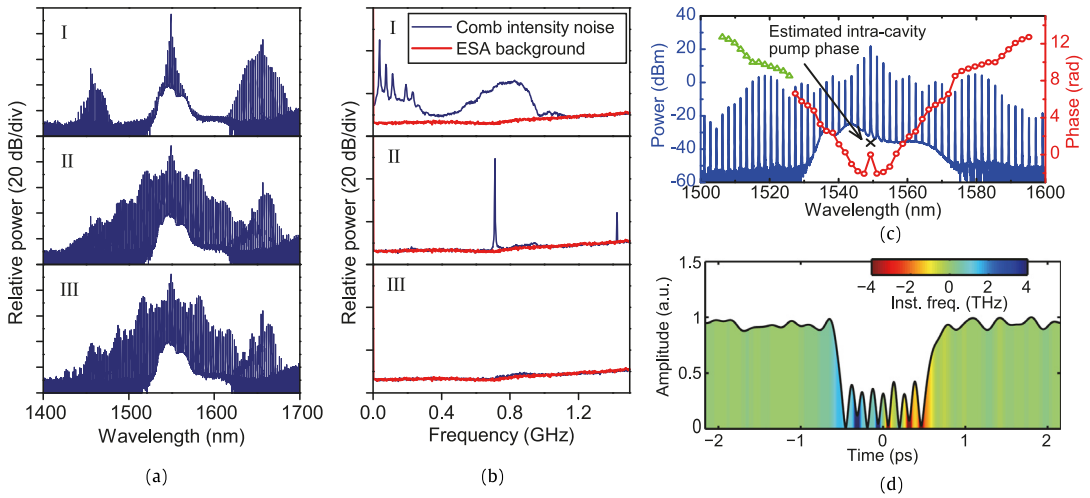

Fig. 34. Comb generation related to dark pulse formation. (a) Comb spectra. The frequency de-tuning between the pump laser and the micro-ring is gradually adjusted from stages I to III. (b) Comb intensity noise at each stage. The background noise of the electrical spectrum analyser (ESA) is also shown. (c) Zoomed-in spectrum and phase profile for the comb at stage III. The phase profile marked in red is retrieved through line-by-line shaping. The green part is out of the pulse shaper passband and is estimated based on spectral symmetry. The comb is measured at the through-port and is thus superimposed on the pump field from the input waveguide. The intra-cavity pump amplitude and phase are estimated based on the cavity-coupling condition and the nonlinear loss induced by comb generation. (d) Reconstructed intra-cavity waveform. (Inst. freq.: instantaneous frequency) (After Ref. [51]).

as proposed in Ref. [261]. Similar structures have been demonstrated previously for high-efficiency on-chip four-wave mixing [262]. Fig. 35(a) shows an image of the dual-coupled Si_3N_4 micro-rings used in Ref. [261]. The cross-section dimension of the micro-ring waveguide was carefully designed to achieve a single transverse mode per polarisation in order to avoid uncontrollable interactions between different transverse modes in each individual ring. The two rings (main and auxiliary) had slightly different radii corresponding to different FSRs. Their resonances thus crossed each other at certain frequencies (see the transmission spectra in Fig. 35(b)). Mode coupling then happens between the two rings. By thermally tuning the auxiliary ring with a micro-heater, the mode-crossing frequency can be controlled. Fig. 35(c) shows the zoomed-in transmission spectra of one resonance for the main ring. As the heater power was varied, tuneable mode splitting could be clearly observed.

As discussed in Section 6.2.1, one of the primary comb sidebands always arises at the mode-crossing frequency. This phenomenon can be used for comb repetition-rate selection. Fig. 35(d) shows the comb spectra with the repetition-rate tuned from 1-FSR to 6-FSR. The pump laser drives one resonance of the main ring and is fixed in frequency after it is tuned into the resonance. Comb generation with different repetition-rates can then be achieved by thermally tuning the auxiliary ring with the micro-heater. Mode-locked combs could also be obtained by optimising the heater voltage. Fig. 35(e) shows an example in which the comb can be compressed to transform-limited pulses via line-by-line pulse shaping. The dual-coupled micro-resonator scheme has also been employed for comb generation in the anomalous dispersion region, with the goal of adjusting the pump coupling conditions to improve the efficiency of pump-to-comb power conversion [263].

6.3. Schemes for the control of micro-combs

6.3.1. Two-colour pumping, electro-optical control and self-injection locking

In parallel with the first observation of CW-seeded micro-combs, some early investigations were reported on how to control comb generation by acting on the injected pump. In 2009 Strekalov and Yu proposed a comb generation technique based on the use of two optical pumps in a magnesium fluorite resonator in order to achieve better efficiency for the comb generation process [264]. (Fig. 36(a).) As lately also pointed out by Hansson and Wabnitz [265], such a configuration is thresholdless since it does not rely on the optical parametric generation or cavity MI discussed in Sections 3 and 5, but on the cascaded FWM process. Note that similar schemes for the control and generation of background-free ultra-high repetition-rate trains of CSs in Kerr fibre-ring cavities were already proposed by Haelterman et al. in the 1990s [229].

It is notable that, even though bi-chromatically-pumped systems are background free, it is still possible to find CS solutions for such configurations (Fig. 36(b)). Instead of sitting on a constant background, the solitons are found to be superimposed on top of the thresholdless low-intensity pattern that is generated through FWM of the two pump modes. The position of the solitons is restricted by the stationary pattern, which effectively suppresses timing jitter and interactions between different solitons [227]. Two-colour pumping presents some advantages since, in this case, the generated pulses are background free. It can also be used for the generation of bimodal phase states with potential for all-optical random number generation [266].

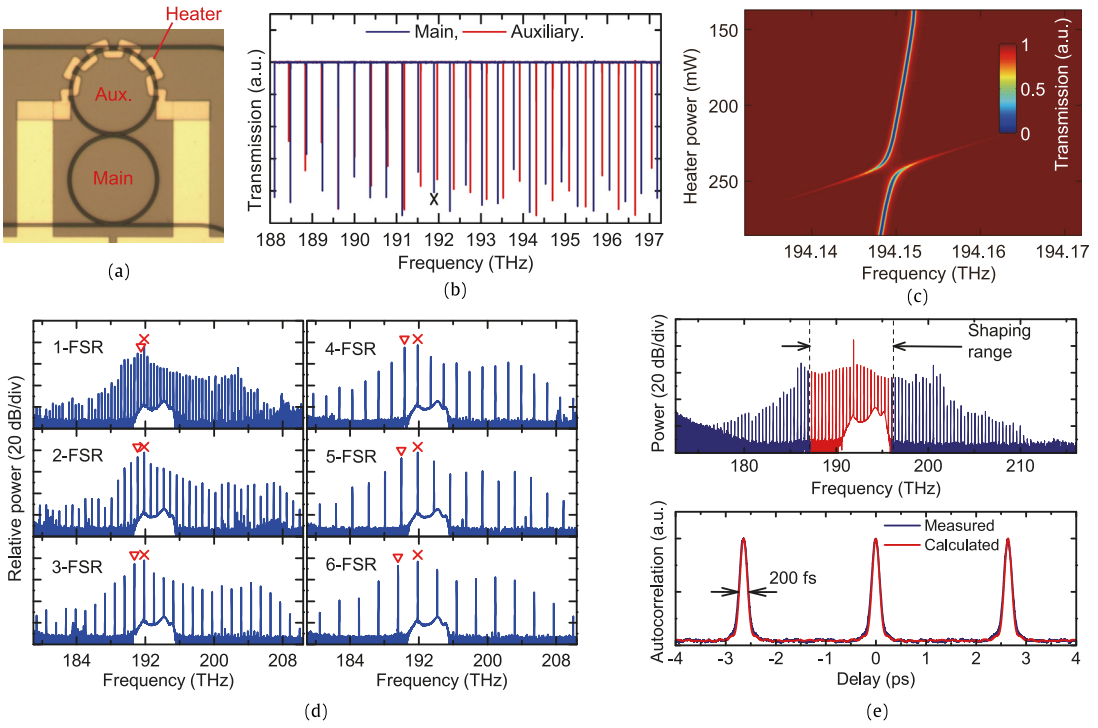

Fig. 35. Comb generation with dual-coupled micro-resonators. (a) Microscope image of dual-coupled SiN micro-rings (main and auxiliary). A micro-heater is fabricated on top of the auxiliary ring for thermal tuning. (b) Transmission spectra of the two rings. The resonance marked with a cross is pumped for comb generation in (d) and (e). (c) Zoomed-in transmission spectra of the main ring when the heater power is changed, showing tuneable mode splitting. (d) Repetition-rate selectable comb. The line marked with a cross is the pump. The line marked with a triangle is where mode crossing happens. (e) Mode-locked comb. Upper: spectrum; lower: autocorrelation trace after line-by-line pulse shaping. The calculated autocorrelation of the ideal transform-limited pulse is also shown for comparison. After Ref. [261].

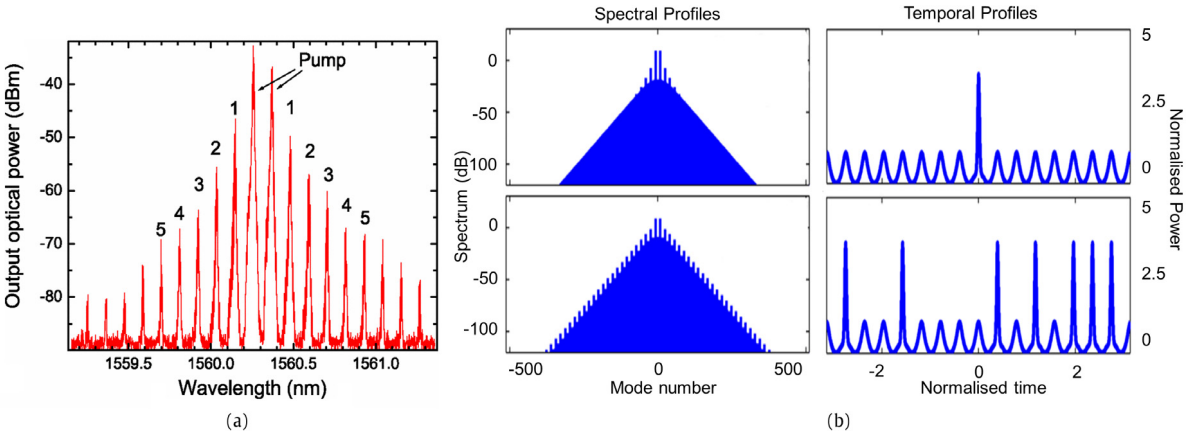

Fig. 36. Micro-comb generation from bi-chromatic seeding: (a) Early experiments from [264], the two highest peaks correspond to the two laser pumps, (respectively, with input power 2.9 mW). After Ref. [264]. (b) Numerical simulation of the bi-chromatically-pumped Lugiato–Lefever equation showing coexistence of cavity solitons on top of a thresholdless stationary pattern of low-intensity pulses. After Ref. [265].

In a similar spirit, parametric electro-optic seeding was introduced by Papp, Del'Haye and Diddams [53] in order to avoid a break-up of the micro-resonator comb into various sub-combs under certain coupling conditions [13]. They experimentally investigated the properties of these kinds of micro-comb [53] and also showed that the micro-comb spacing locks to the spacing of the electro-optically modulated pump sidebands when the modulation frequency is close enough to the intrinsic micro-resonator mode spacing [54]. Fig. 37 shows experimental measurements of the injection-locking process while parametrically seeding a micro-comb [54].

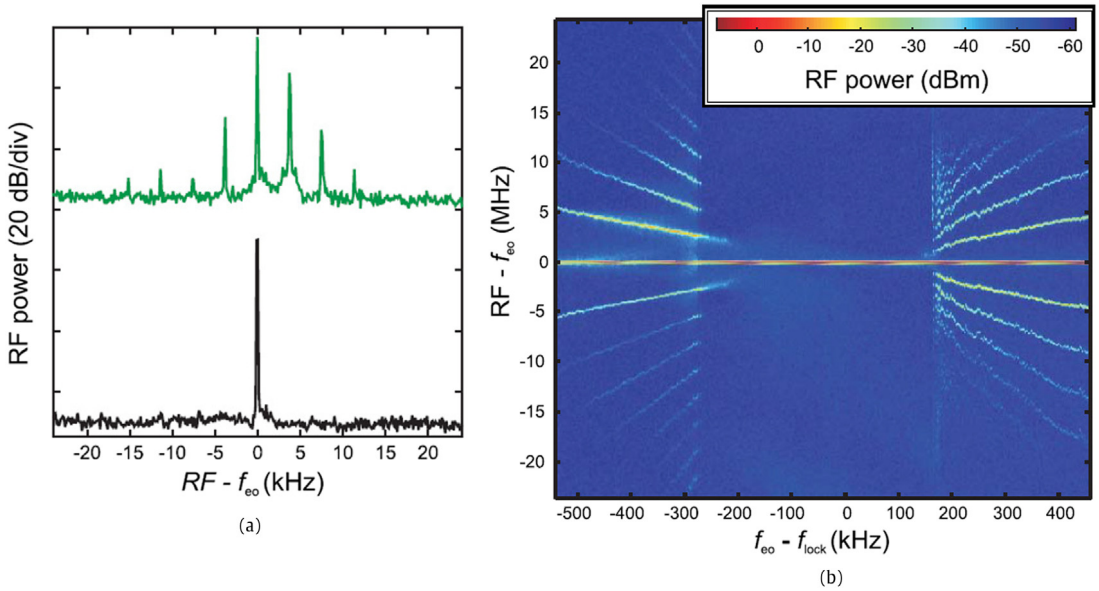

Fig. 37. Parametric seeding and injection locking of a micro-comb by Papp and co-workers. Panel (a) presents two radio-frequency mode spacing beat-note spectra of a micro-comb. The upper part of panel (a) shows several beat-notes, which indicate frequency offsets between different parts of the comb spectrum. When the seeding frequency is close enough to the natural mode spacing of the micro-comb, the radio-frequency beat-notes collapse into a single beat-note (lower part of panel (a)). Panel (b) shows a colour-coded plot of the mode spacing beat-note spectrum at different seeding frequencies (horizontal axis). The comb is injection-locked to the seed frequency in the central part in a range of approximately 300 kHz (more details by Papp et al. in Ref. [54]).

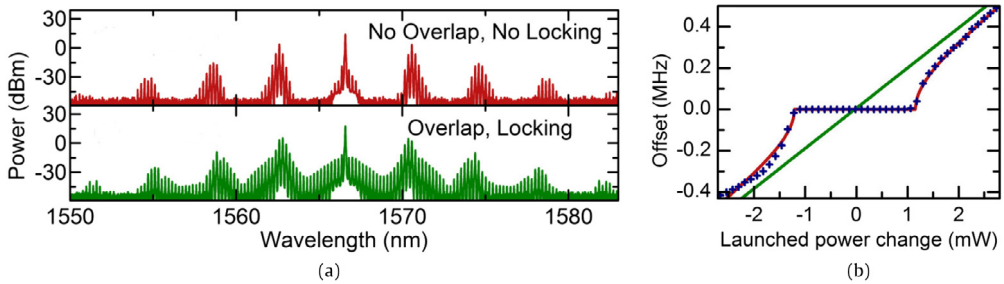

Fig. 38. Self-injection locking in a fused silica micro-rod resonator with 25 GHz FSR by Del'Haye and co-workers. Panel (a) depicts two micro-comb spectra consisting of sub-combs. In case the sub-combs overlap, the resulting sub-comb can be self-injection locked (zero offset between sub-combs) by changing the launched power, as shown in panel (b).

An additional approach to prevent micro-combs from splitting up into sub-combs with mutual offsets utilises an intrinsic self-injection locking of micro-combs. Here, the seed power for comb generation can be adjusted in a way that the offset between sub-combs is reduced. When the offset is small enough, the comb self-injection locks into a continuous optical frequency comb, as demonstrated by Del'Haye et al. [55]. Fig. 38 shows a measurement of self-injection locking of a micro-comb with several sub-combs by varying the launched power into the micro-resonator.

Electro-optic control of the optical comb has also been exploited in order to address the active stabilisation of the lines, which is particularly important for high repetition-rate combs that cannot be measured directly by standard electronic means. In 2012 Diddams and co-workers [52] demonstrated the measurement and stabilisation of the mode spacing of a 140-GHz-micro-comb by bridging the gap between comb modes via electro-optic sidebands.

6.3.2. Self-locking schemes of the pump frequency in a resonator line

As discussed in Section 6.1, an important problem in micro-comb generation is the strong thermo-optical dependence of the refractive index of the resonator. The field enhancement of the micro-resonator not only lowers the energy threshold for the observation of the ultra-fast Kerr nonlinearity, but also enhances the thermo-optical dependence of the refractive index which, in turn, translates into a slow dependence of the comb on the optical intensity. This implies that the resonant frequencies of the micro-cavity will fluctuate with the pump energy. Although a thermal-locking phenomenon occurs for small fluctuations of the pump energy [159], this often translates into a decoupling and, hence, shutting down of the comb if

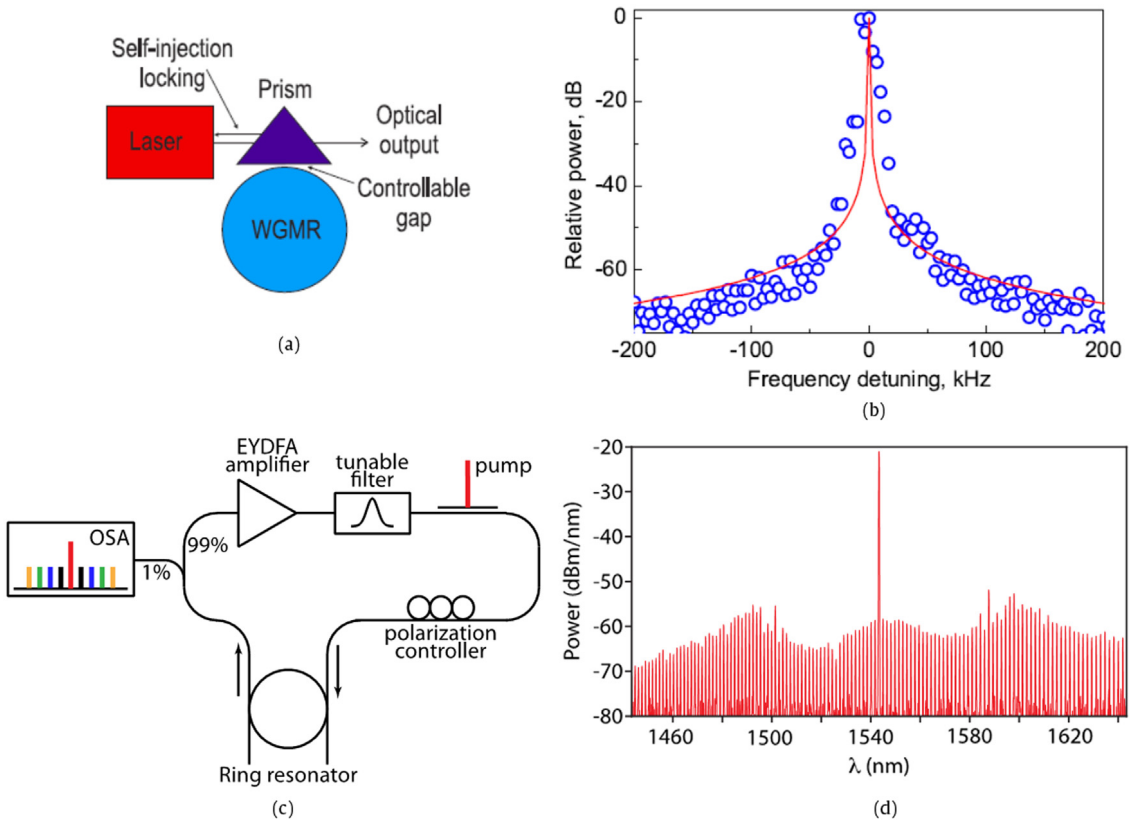

Fig. 39. (a–b) Self-injection technique. (a), (c) Set-up. After Ref. [267]. (b) Narrow line laser oscillation thanks to self-injection coupling. (c–d) Self-locked OPO. (c) A four-port micro-resonator is embedded in an outer fibre-loop cavity with a lasing gain medium: a filter in the lasing cavity allows only one of the micro-resonator resonances to lase. (d) Output optical spectrum: OPO is excited in the micro-resonator by the oscillating laser pump. After Ref. [57].

a stabilising active loop is not in place [9,21]. Moreover, as detailed in Section 3, thermal locking takes place only for materials with a proper sign of the thermal expansion coefficient. For this reason, some approaches to link the pump frequency to the resonator line have been proposed, based on different feedback mechanisms.

For prism-coupled WGM resonators, an efficient approach to link the pump laser to a micro-cavity resonance is the so-called self-injection locking. This passive feedback mechanism was initially proposed by Liang and co-workers to narrow the line of a distributed feedback laser (DFB) with a WGM resonator [267]. Resonant Rayleigh scattering of the micro-cavity is the enabling mechanism of this approach. A WGM resonator is used to filter a DFB laser and some scattered light from the resonator then reflects back into the laser. The linewidth of the laser then collapses due to self-injection locking, keeping light within the WGM resonance. This approach has been widely used to create extremely narrowband CW lasers (Fig. 39(a), (b) see Ref. [268] and references therein) and for controlling parametric oscillation [56]: the frequency of the laser can still be controlled within the WGM resonance.

Another self-locked system was proposed by Pasquazi et al. in 2012 [57,269] (Fig. 39(c), (d)) that employed the insertion of a four-port micro-resonator into a laser-cavity loop in order to induce oscillation of the pump. This scheme is termed filter-driven FWM and is discussed in detail in Section 6.4. It involves embedding the micro-resonator in an outer fibre-loop cavity that contains optical gain. Here, only a single resonance of the micro-cavity lines up with a resonance of the outer loop and experiences amplification. This radiation is then passively linked to the resonator line and it is used as a pump for the optical parametric oscillation in the micro-cavity. Although, in the first experiments the oscillating laser pump displayed a low frequency modulation induced by super-mode/Q-switching instabilities, this scheme proved to be a viable way to self lock the oscillation in sub-threshold pump oscillation for quantum-correlated photon state generation [270,271], see also Section 8. This approach has also been explored for two-port micro-resonators by Johnson and co-workers [272].

6.3.3. Active stabilisation and thermal tuning of continuous-wave-pumped lines

Most techniques for achieving coherent frequency comb generation in micro-resonator require sweeping the pump laser frequency. However, this has a number of drawbacks since the quality of the comb – particularly its phase characteristics – is governed by the linewidth and amplitude noise of the pump. Tuneable lasers are relatively noisy and have a broader linewidth (typically 100 kHz) than fixed-wavelength lasers. Such devices are typically based on a monolithic cavity that has

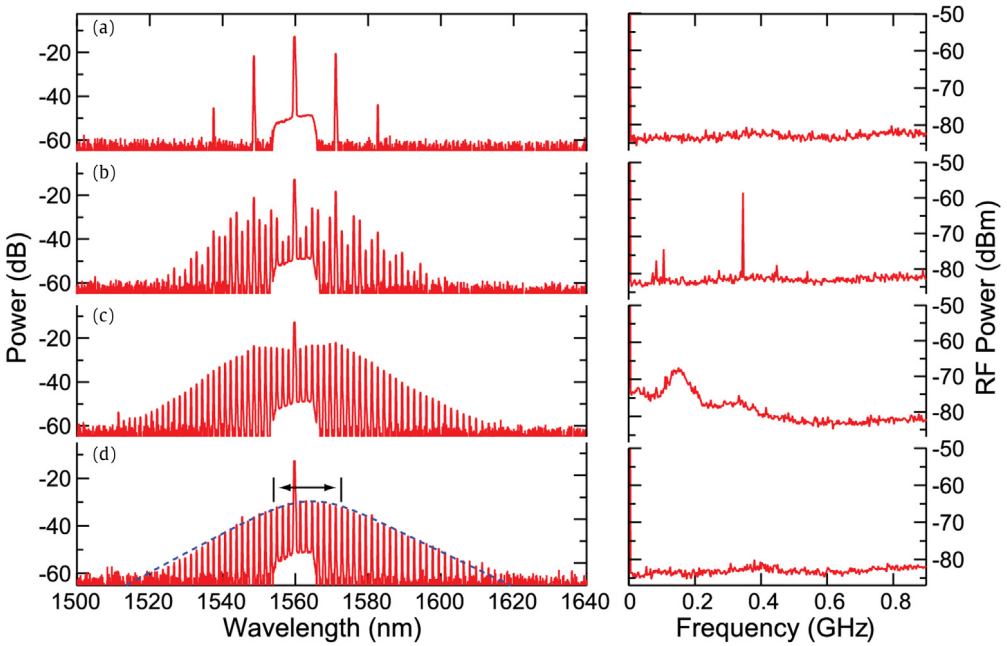

Fig. 40. Generated frequency comb spectra for different cavity resonance de-tunings produced by terminating the heater current scan at different values. The 3 dB bandwidth of the soliton was 20 nm. After Ref. [225].

no moving or mechanical components and, consequently, these lasers have achieved record linewidths of $<$40 mHz [273] and can significantly reduce the noise on the comb lines.

To generate combs with a fixed wavelength laser, resonance-tuning techniques are required to control the de-tuning between the laser and the resonator. Integrated heaters were employed by Xue et al. [51] to implement rapid thermal tuning of the resonator to achieve coherent comb generation in the normal-dispersion region. A similar method was also used recently by Joshi et al. [225] to achieve repeatable and systematic generation of soliton combs in the anomalous-dispersion region. These types of integrated heaters, allow very fast thermal tuning of the resonance on timescales less than $<$100 μs - much shorter than thermal relaxation times. Soliton pulses have been excited following the technique described in Section 6.1, inducing a progressive resonance de-tuning from negative to positive values via thermal de-tuning. In agreement with the work of Herr et al. [50], the authors found that the scanning speed is critical in order to achieve consistent and reliable generation. The fast response time of the heaters allowed them to achieve the proper control of the scanning time. The different micro-comb stages achieved during the scanning (from Type I comb to Type II comb to chaotic interaction up to soliton formation) are shown in Fig. 40.

Another important point relates to the ability of maintaining the soliton state against thermal drifting which, over long timescales, can destroy it or cause a loss of coherence. Recently, an active control approach to maintain the soliton state against thermal drifting was also reported by Yi and co-workers [222,223]. They used a complex simultaneous dynamic control of the pump laser frequency and power, within a feedback loop monitoring the average soliton output power, where it was observed that the speed of the pump frequency scan affected the reproducibility of the soliton states. For a fixed cavity loading, the relative de-tuning determines the soliton power and, consequently, the pulse width. The authors noted a one-to-one relationship between de-tuning and several soliton properties and used it to provide long-term locking of the laser de-tuning [222,223]. One and two soliton states are shown in Fig. 41. Using this servo mechanism, these states were stably maintained for long times.

6.4. Filter-driven four-wave mixing laser

The filter-driven FWM (FD-FWM) laser, introduced by Peccianti et al. [58], is an alternative approach for coherent micro-comb generation that is based on passive laser mode-locking, instead of optical parametric generation. For this reason, its modelling and dynamics are not described by the LLE discussed in Section 5. We briefly describe its approach and modelling.

The optical set-up of a FD-FWM laser is shown in Fig. 42(a): a four-port ring micro-resonator is embedded in an active laser loop. The fibre cavity loop contains an optical amplifier to provide gain, a Faraday isolator, a polarisation controller and a free-space delay line. In addition, a passband filter, is inserted in the fibre-loop in order to control the central oscillating wavelength. Similar to the self-locked approach in Fig. 39, this scheme directly embeds the pump in the micro-cavity and is resilient to thermally-induced decoupling.

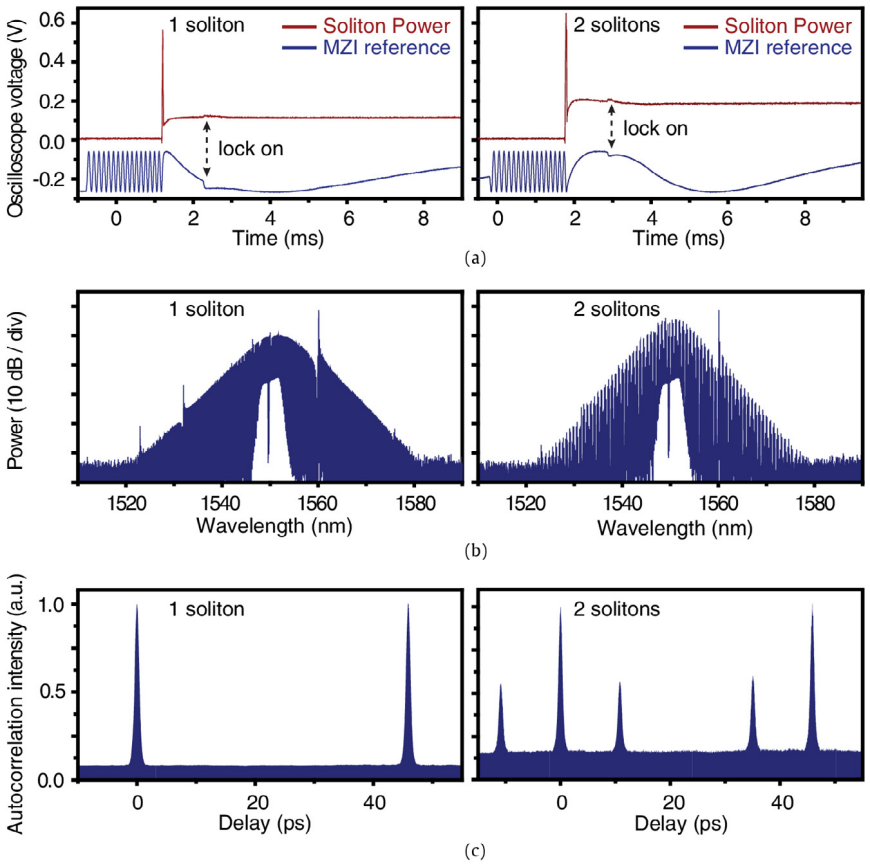

Fig. 41. Excitation of a single (left) and two-soliton (right) state, controlled by monitoring the output average power of the soliton. (a) Soliton average power and servo-locking control signal in time (b) Soliton spectra (c) Soliton autocorrelation. After Ref. [223].

To describe the working mechanism of this configuration, it is useful to recall the operating principle of passively mode-locked lasers, which requires the interplay of gain, nonlinearity and dispersion [209]. Specifically, we are interested in the multiple pulse, or harmonically mode-locked régimes, which have largely been explored in fibre-loop lasers in order to increase their repetition-rates [209]. The first experimental evidence of the generation of a train of solitary pulses per round-trip was reported in 1995, where Franco et al. introduced the so-called modulational instability laser [274]. Some success in controlling the properties of these lasers was achieved in 1997 by Yoshida et al. [275], who inserted a Fabry–Perot (FP) filter in the laser cavity loop to force the oscillation at a repetition-rate equal to the FSR of the FP, thus effectively filtering the main cavity modes (also known as super-modes). In 2002 Sylvestre and co-workers [276] demonstrated that the operation of these lasers could be understood on the basis of a mode-locking principle introduced in 1998 by Quiroga-Teixeiro and termed *dissipative four-wave mixing* (DFWM) [277]. Since these pioneering works, the generation of high repetition-rate pulse trains has been demonstrated by several groups using different approaches [278–280].

Compared with an ultra-short cavity pulsed-laser, DFWM has the advantage of maintaining the narrow linewidths of long cavity fibre lasers (showing a reduced Schawlow–Townes [209] noise), while exploiting the large FSR of short cavities. Practically speaking, however, this advantage was never realised as this configuration suffers from strong super-mode instability [279]. Achieving the necessary gain and nonlinearity requires that these lasers employ long fibre lengths - typically exceeding 50 - 100 m, which correspond to an FSR of the main cavity of the order of only a few MHz. For high repetition-rates, each FP resonance, therefore, encloses a significant number of main cavity super-modes, allowing all of them to oscillate and mix randomly. Consequently, the stream of high repetition-rate pulses is strongly deteriorated by the low-frequency noise arising from the beating of these (randomly-phased) super-modes.

The FD-FWM laser approach is related to the DFWM laser concept but with the critical difference that nonlinear frequency mixing, which is responsible for the mode-locking, occurs entirely within the high-Q micro-ring resonator cavity [58,59]. This is in stark contrast to classic DFWM, where the nonlinear interactions occur in the fibre and the field is separately filtered by a FP resonator. The FD-FWM approach increases the effective nonlinearity by orders of magnitude, owing to the field enhancement in the high-Q cavity. This nonlinear mechanism is filter driven, meaning that it inherently suppresses any natural shifting of the spectral content of the modes outside the filter bandwidth which, in turn, reduces the nonlinear losses.

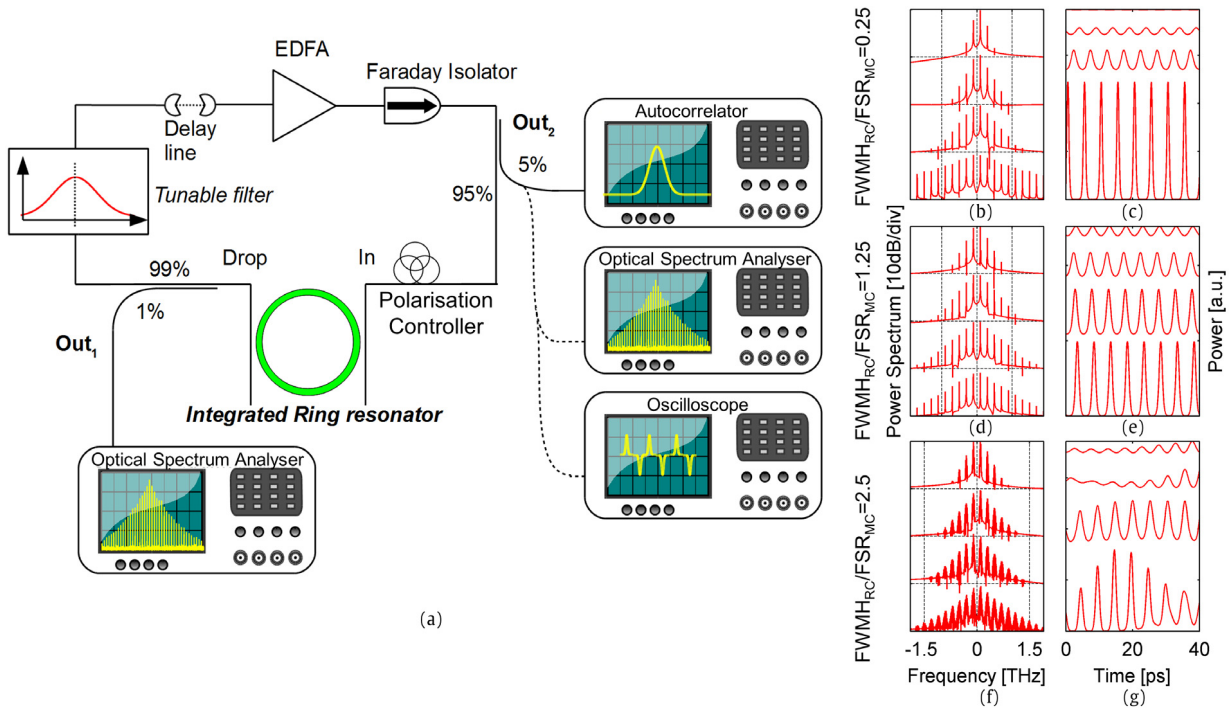

Fig. 42. Filter-Driven Four-Wave Mixing Laser scheme. (a) A four-port micro-resonator is embedded in an outer fibre-loop cavity with a lasing gain medium. (b–g) Numerical simulations for different ratios of the ring lines FWHM over the main cavity FSR, $\mathrm{FWHM_{RC}/FSR_{MC}}$ = 0.25(b, c), 1.25(d, e) and 2.5(f, g). The top–bottom curve for each panel is for growing cavity saturation powers. Power spectral densities (b, d, f) and the temporal evolution (c, e, g) of the intensity are reported.

This increases the efficiency of the FWM process, while sustaining the spectral comb lines, thereby reducing the operating pump threshold and the need for long main-cavity loops as no fibre-based (external) nonlinearities are required.

6.4.1. Numerical model

The numerical modelling of the FD-FWM laser involves the coupled equations of the field evolution $f(z,t)$ in the amplifying fibre and the field $a(z,t)$ evolving in the nonlinear ring [58]

$$\begin{cases} \dfrac{\partial f}{\partial z} + \dfrac{1}{v_F}\dfrac{\partial f}{\partial t} + i v_F^2 \dfrac{\beta_F}{2}\dfrac{\partial^2 f}{\partial z^2} = g(f)\left[1 + \dfrac{1}{v_F^2 \Delta\omega_G^2}\dfrac{\partial^2}{\partial z^2}\right] f - \alpha f, \\ \dfrac{\partial a}{\partial z} + \dfrac{1}{v_R}\dfrac{\partial a}{\partial t} + i v_R^2 \dfrac{\beta_R}{2}\dfrac{\partial^2 a}{\partial z^2} + i\gamma |a|^2 a = 0, \end{cases} \tag{63}$$

where v_F v_R and β_F and β_R are the group velocities and second-order dispersion in the fibre and in the ring, respectively, γ is the nonlinear coefficient in the ring, α is the absorption and $g(f)$ is the saturable gain in the fibre expressed as

$$g(f) = G_0 \exp\left[-\int \frac{|f(z,t)|^2}{P_0 L_F} dz\right], \tag{64}$$

with G_0 and P_0 being the gain and saturation power, respectively. The spatial frequency $\Delta\omega_G$ regulates the gain bandwidth. The variables L_F and L_R are the lengths of the fibre and ring cavities, respectively. The equations represent the standard evolution of a pulse in a waveguide and are solved in time. These equations are coupled at the ring ports via the relations:

$$\begin{cases} a\,(z=0,t) \;=\; T\, e^{i\phi_{RC}}\, a\,(z=L_R,t) + R\, e^{i\phi_{MC}} f\,(z=L_F,t) \\ f\,(z=0,t) \;=\; -R\, e^{i\phi_{RC}}\, a\left(z=\dfrac{L_R}{2},t\right), \end{cases} \tag{65}$$

where T and R are the (real) transmission and reflection coefficients, with $T^2+R^2 = 1$. These coefficients regulate the micro-cavity resonance bandwidth. The parameter controlling the phase of the main cavity modes is ϕ_{MC}, which also determines the spectral position of the main cavity modes with respect to the resonances associated with the ring-resonator. Finally,

ϕ_{RC} regulates the position of the ring resonances with respect to the centre of the gain bandwidth. Eq. (65) is used for each port of the ring.

The simulations in Fig. 42(b) show that the super-mode instability could be either induced or suppressed by optimising the main cavity length. The cavity energy (relative to the gain saturation power) may also affect the laser stability, since it regulates the number of super-modes that oscillate; higher powers support more lines, hence the laser stability will be reduced. The stability for the case of high-power configurations can be improved by decreasing the ratio of the micro-ring linewidth versus the main cavity FSR. The numerical analysis shows that the laser stability also depends on the relative phase of the main cavity modes. In particular, it depends on the precise alignment of the central two or three cavity modes relative to the ring-resonator mode, which has a critical effect on how many super-modes will oscillate.

6.4.2. Experiments: stable, unstable and dual-line oscillation

Peccianti, Pasquazi et al. [58,59] observed three main operating régimes of the FD-FWM laser: unstable, stable and dual-mode, depending on the phase of the main cavity relative to the micro-cavity resonance, controlled with a delay line.

Fig. 43(a, d, g, j) shows the optical and radio-frequency results for the unstable pulsation of the laser in the first column. The data was obtained with the set-up described in Fig. 42(a) by driving an erbium-doped fibre amplifier (EDFA) at the maximum available current, corresponding to approximately 16 mW at the input of the micro-ring. The main cavity FSR was 64 MHz. Panel (a) shows the second-harmonic non-collinear autocorrelation, where a periodic modulation at 200 GHz is visible with an extremely poor contrast. Panel (g) shows a comb-like spectrum spaced by the FSR of the micro-ring (200 GHz), indicating that a fast modulation of the laser output is present. The expected autocorrelation, calculated from the optical spectrum under the assumption of fully-coherent pulses, is also presented in (a) (dashed lines), showing the high background of the measured traces, reflecting unstable oscillation. The envelope signal recorded with a photodetector is reported in panels (d) and (j) in time and frequency, respectively. From this measurement, it is evident that only few main cavity modes were oscillating. A slow temporal modulation of the order of 6 μs, due to an unstable Q-switching régime, was also observed.

A stable régime of operation was obtained by adjusting the delay line. This completely eliminated any main cavity super-mode beating and, consequently, gave rise to an extremely stable output, as reflected in both the temporal output and radio-frequency spectrum, reported in Fig. 43(b, e, h, k), together with the optical spectra and autocorrelation traces. In this case, the autocorrelation calculated from the optical spectrum under the assumption of fully-coherent pulses fully matched the experimental traces, indicating the coherence of the train. The radio-frequency signal exhibited a dominant DC component with a bandwidth < 0.25 Hz (the resolution of the measurement system), as well as an out-of-band noise that was 55 dB lower than the DC peak. The ratio between the power of the DC component and spectral noise (within the 200 MHz bandwidth) was estimated to be larger than 41 dB, again limited by the measurement sensitivity which, in that case, was affected by the detection and sampling noise.

Another interesting laser operation régime, with properties similar to the stable case, is depicted in Fig. 43(c, f, i, l). Also, in this case, the expected autocorrelation, calculated from the optical spectrum under the assumption of fully-coherent pulses, was consistent with the measured autocorrelation trace, showing that the pulses were stable. Conversely, the radio-frequency spectrum showed a highly coherent beating at 65 MHz. Such a frequency was consistent with the FSR of the main cavity, indicating that two distinct modes of the main cavity were oscillating per micro-ring resonator line. Such mode doublets were present in all the excited resonances of the micro-resonator: this was verified by filtering out the different micro-resonator lines and measuring their radio-frequency spectra independently. These results showed that the system produced two replicas of the 200 GHz comb spaced by 65 MHz. Hence, the 65 MHz beating was related to the instantaneous frequency difference between the two-comb replicas. The radio-frequency spectrum around 65 MHz was an accurate reflection of the dynamics of the line-to-line spacing of the main cavity modes. This confirmed the instantaneous frequency locking between the lines of the main cavity modes.

7. Applications of micro-combs

7.1. Metrology

7.1.1. Towards miniature atomic clocks

Optical frequency combs have enabled major breakthroughs in metrology, most notably in the development of optical atomic clocks [281] that offer unprecedented stabilities of up to 10^{-18} [1–5]. As with any clock, an atomic clock is comprised of an oscillator and a clockwork: the oscillator provides the reference source for the clock, while the clockwork converts the clock frequency to a range that is experimentally accessible. For optical atomic clocks, the reference source is an atomic transition driven by a laser of extremely narrow linewidth, while the clockwork consists of an optical frequency comb. The comb itself consists of a regular array of equally-spaced frequencies, with a spacing given by the pulse repetition-rate frequency Δf in the temporal domain. A measurement of the pulse train intensity, e.g. with a photodiode, provides a radio-frequency signal that can be easily transferred to electronic devices. Such a radio-frequency signal has the frequency Δf of the train of pulses that, under proper conditions, possesses the same high fractional stability of the optical reference frequency. Hence, an optical frequency comb transfers the high fractional stability of the optical reference to a radio-frequency signal.

Optical frequency combs are defined by two independent parameters: the absolute offset of the comb, typically referred to as the carrier envelope offset (CEO) frequency (or simply *offset frequency*), and the repetition-rate, given by the frequency

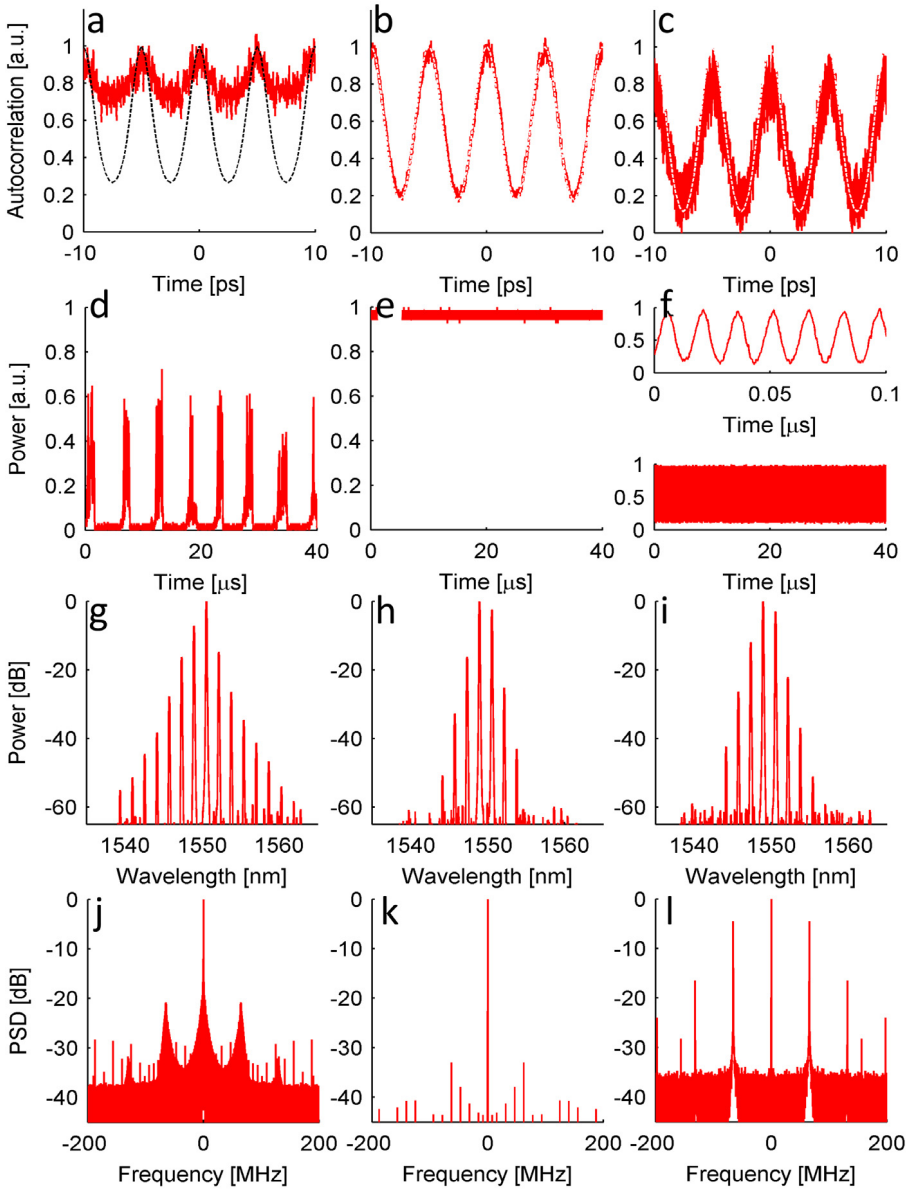

Fig. 43. Filter-Driven Four-Wave Mixing Laser Output. Unstable (a, d, g, j), stable (b, e, h, k) and dual-line (c, f, i, l) oscillations. Autocorrelations (a–c), radio-frequency signal of the laser output in time (d–f) (inset in (f)). Optical spectrum (g–i) and radio-frequency spectrum (j–l). After Refs. [58,59].

spacing between consecutive comb teeth. To stabilise a comb, a reference is generally needed for each independent parameter and an optical frequency comb can consequently be fully stabilised using two reference laser frequencies. The fractional stability of the comb, however, is a function of the frequency span between the two atomic references and so, if the two references are very close together, the fractional stability of the resulting radio-frequency signal is highly deteriorated.

In order to address this challenge, the research groups of Theodor Hänsch and John Hall introduced a powerful self-referencing method which can be applied to optical frequency combs that have a wide spectrum — covering at least one octave [1–4,4,5,282]. A self-referenced optical frequency comb requires only a single reference, e.g. an atomic line, for full stabilisation. The fractional stability obtained with this approach is dependent only on the linewidth of the atomic reference, which is directly transferred to the microwave (i.e. repetition-rate) frequency. The second required reference is directly obtained by the comb itself, with the self-referencing approach described in Fig. 44. When a frequency comb spans more than one octave, a frequency line near the low-frequency limit is doubled via second harmonic generation (SHG) and then beaten together with the line in the comb near the second harmonic wavelength. The beat frequency is identically equal to the offset frequency and is typically in the microwave or radio-frequency régime and can, therefore, be measured electronically and used to stabilise the comb. This, therefore, enables one to accurately determine the absolute frequency of every comb line.

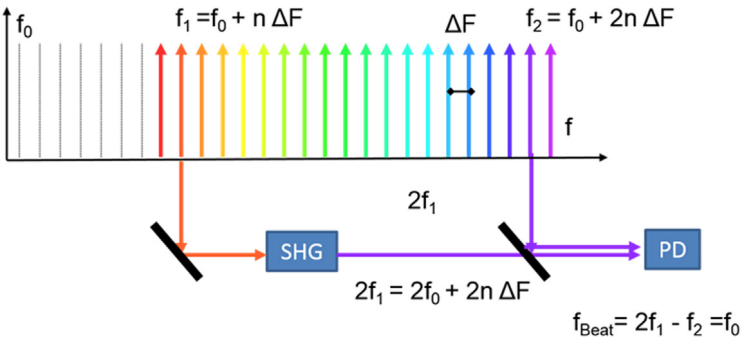

Fig. 44. Schematic of the f–2f stabilisation in an optical frequency comb.

In order to measure an unknown optical frequency, a radio-frequency beat-note can be generated between the unknown optical frequency and the nearest frequency comb mode. Since the position of the comb mode is absolutely known, such radio-frequency beating allows one to determine the optical frequency of the unknown signal. Hence, a fully-stable optical frequency comb produces a direct link to the microwave régime because it allows the measurement of optical frequencies solely by measuring radio-frequencies. This represented a revolution in metrology [1–5,282].

The importance of micro-combs to ultimately provide miniature optical atomic clocks has been recognised from the very first observation of the large optical spectrum [8,283] generated by a continuous-wave (CW)-pumped micro-resonator. The challenge with micro-combs is that the ability to control the coherence of the comb, by using the methods outlined in the previous sections, is absolutely instrumental for the application of these combs to metrology.

The first stabilisation of a coherent micro-comb to an atomic transition was achieved by Savchenkov et al. [56], with the compact implementation shown in Fig. 45. The micro-comb was excited with a self-injection mechanism in a WGM resonator in calcium fluoride to keep the optical pump locked to one of the resonator lines, as discussed in Section 6. The optical pump used was eventually locked to the ^{87}Rb transition by thermally modulating the resonator. This work highlighted an important feature in CW-pumped combs — that the central frequency and the repetition-rate of micro-combs are both affected by any thermal modulation and so their drift in time is correlated. For this reason, in Ref. [56] only a single parameter could be stabilised.

The full stabilisation of a micro-comb was recently accomplished [54] (see Fig. 46) by using an alternative approach to micro-comb generation that independently allowed the control of the repetition-rate and central frequency. A comb was obtained by electro-optical modulation of a CW laser followed by FWM interaction in a highly nonlinear fibre (HNLF), as described in Section 6 by Papp et al. [54]. The comb was then injected and spectrally broadened in a micro-resonator. The generated micro-comb was further spectrally broadened using additional amplification, followed by a nonlinear (HNLF) stage. The output large bandwidth comb was finally stabilised by referencing it to two rubidium spectral lines. The control parameters used here were the central frequency of the pump laser and the frequency of the electro-optical modulator. This demonstration represents an alternative route for independently controlling the two degrees of freedom of a micro-comb - the resulting microwave output is a precise integer subdivision of the Rb reference.

Notably, electro-optic modulation has also been successfully used to create an f–2f stabilised Kerr comb with a similar scheme, without the use of a micro-resonator but only using HNLF as a nonlinear medium to spectrally broaden the comb [284]. The first direct f–2f carrier envelope offset frequency measurement of a micro-comb was demonstrated using a fused silica micro-disc with an externally-broadened spectrum in a nonlinear fibre [285]. This result was achieved with a micro-comb with a 16 GHz repetition-rate. Both carrier envelope offset frequency and repetition-rate have been simultaneously and phase-coherently stabilised to a hydrogen-maser-based reference clock.

The offset frequency of a coherent optical comb in a micro-resonator generating temporal CSs has been recently measured in the microwave domain by Jost et al. [286]. A coherent micro-comb was obtained by exciting a CS in a magnesium fluoride cavity, following the method described in Section 6 [50]. The micro-comb spectrum was then broadened by up to 2/3 of an octave in an additional nonlinear stage using a HNLF fibre and then followed by a 2f–3f interferometric scheme in order to measure the offset frequency of the micro-comb in the microwave régime. More recently, a coherent micro-comb state, spanning more than 2/3 of an octave, was obtained in a silicon nitride (Si_3N_4) resonator by Brasch et al. [224]. They engineered the resonator in order to obtain an efficient dispersive wave (or Cherenkov radiation, see also Section 5.6 and references therein) emitted by a cavity soliton. In this way, they obtained a large bandwidth coherent comb that could be phasestabilised with the help of a frequency comb and a common radio-frequency reference. These results are promising for self-referenced stabilisation, as the achieved coherent two-thirds of an octave can be self-referenced with the 2f–3f interferometric scheme. The effect of multiple-mode families on Cherenkov radiation was also recently studied by Matsko et al. [287].

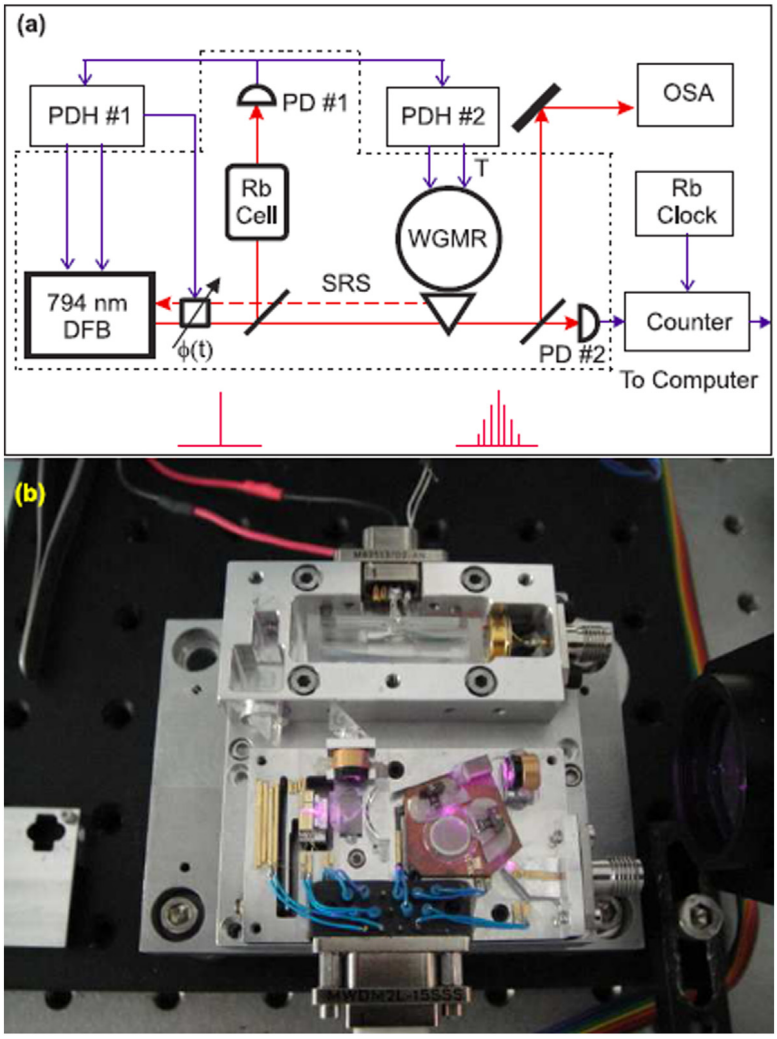

Fig. 45. (a) Schematic and (b) photograph of a compact clock linking a WGM crystalline resonator to a rubidium reference. Only a single parameter could be controlled in this scheme. After Ref. [56].

7.1.2. Spectroscopy and mid-infrared generation

Optical frequency comb science has brought about a revolution to many fields but surely one of the major contributions has been to the area of spectroscopy and, in particular, molecular spectroscopy [288–291]. Indeed, an optical frequency comb source can illuminate a sample with a ruler of sharp laser lines having very high precision. Each line can be easily detected using low-cost detector array technology. This approach can achieve a degree of accuracy that a conventional spectrometer cannot reach, even with optical path lengths of tens of metres. In this way, very small changes in the spectrum, due to processes such as molecular vibrational overtones, can be detected. Such changes are usually not visible using standard techniques that employ white light. Even better performance can be obtained with comb sources operating in the MIR region, where the signature of molecular vibrations is stronger. MIR optical frequency combs have demonstrated the ability to detect gas concentrations at very low levels of parts-per-billion [291].

Micro-combs have been demonstrated in many different frequency ranges, spanning from the visible to the mid-infrared (MIR). MIR generation was first demonstrated at 2.5 μm based on crystalline micro-resonators by Wang et al. [27] and, more recently, on a silicon chip by Griffith et al., based on a ring-resonator with a Q-factor of 590,000, as shown in Fig. 47(a) and (b), respectively. This achievement was accomplished by using several strategies to reduce both the linear and nonlinear losses that are characteristic of silicon and which have, thus far, prevented the achievement of parametric oscillation in silicon micro-resonators. Very high-Q-factors were obtained by employing a novel thermal oxidation-based etchless fabrication process in order to achieve ultra-low-loss waveguides. Interestingly, it was originally expected that by operating the device beyond 2.0 μm, where two-photon absorption vanishes in silicon, would be enough to eliminate both nonlinear absorption and the subsequent effects of free carriers. In the end, however, it transpired that even the effects of three-photon absorption

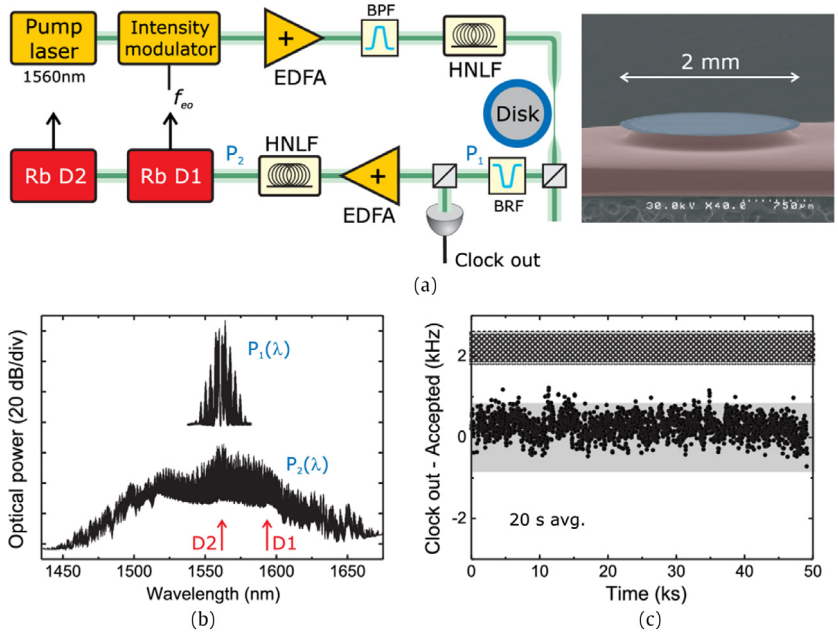

Fig. 46. (a) Schematic, (b) comb spectrum and (c) clock output obtained linking a WGM glass resonator to a rubidium reference. Full stabilisation was achieved with this scheme and the help of additional nonlinear stages. After Ref. [54].

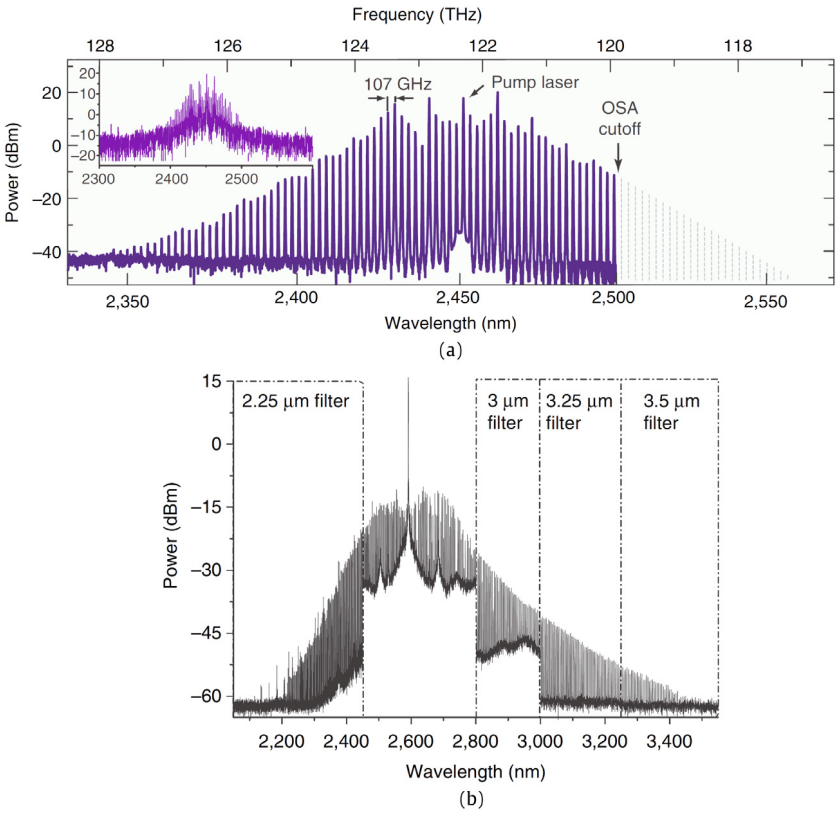

Fig. 47. Mid-infrared micro-comb generation (a) in magnesium fluoride resonators, after Ref. [27] and (b) in an integrated silicon resonator, after Ref. [133].

were large enough to require the use of a p–i–n junction to sweep the free carriers originating from such a nonlinear absorption in silicon. This comb source was subsequently used to measure the absorption spectrum of acetylene gas near 3.0 μm. More recently, the dual-comb spectroscopy approach was implemented completely on-chip using two micro-combs, showing all the potential of these devices for spectroscopy [292].

7.2. Radio-frequency photonics

Radio-frequency photonics deals with applications in the microwave range through the use of photonic technologies. High-frequency analogue signal transmission, control of phased arrays, analogue-to-digital conversion, spectral filtering and signal processing of microwaves have been implemented by using this approach, typically relying on the modulation of an optical frequency with the radio-frequency signal to be processed. The optical signal can then be manipulated with low-loss photonic approaches and converted back to the microwave régime. Due to their stability and large number of lines, optical frequency combs are seen as an important tool in this context [293]. Another promising application of optical frequency combs is spectrally-pure microwave signal generation which can be achieved by detecting the beat-note of a stabilised optical frequency comb. Here, micro-combs offer a powerful way to achieve compact microwave signal generators with ultra-low phase noise.

7.2.1. Radio-frequency filters

A basic application of radio-frequency photonics is the synthesis of radio-frequency filters - devices capable of processing electrical radio-frequency signals with opto-electric devices [294,295]. Photonic radio-frequency filters can offer several advantages over their electrical counterparts, including programmable filter shapes, fast tuneability and compatibility with fibre-based remote interrogation. The most popular scheme uses optical dispersive delay lines to realise tapped delay-line filters, essentially equivalent to the digital filters known in digital signal processing but implemented in photonic hardware.

Discrete frequency samples of the optical signal containing the radio-frequency modulation are time delayed, weight tailored, summed together and, at the end, detected by a photo-detector to generate the radio-frequency output. This type of filter requires a large number of equidistant wavelengths and optical frequency combs have recently demonstrated a great potential in this direction [296].

High-quality, large spectral-range multi-wavelength sources for radio-frequency photonic filtering applications have typically been based on mode-locked fibre lasers [297] and electro-optically-generated combs [293,296]. Recent demonstrations have also shown the significant potential of micro-combs towards high-performance transversal filtering for radio-frequency signal processing.

Xue et al. reported the first demonstration of micro-comb-based photonic RF filters [63]. The experimental scheme is illustrated in Fig. 48(a). A Si_3N_4 micro-ring was pumped with a power of 1.43 W, generating a frequency comb with a spacing of 231.3 GHz, spanning over 200 nm above the sensitivity of the spectrum analyser (Fig. 48(b)). The comb was then spectrally shaped and passed through the complex-tap filtering structure that was proposed in [298,299]. The ultra-broad spectrum of micro-combs can increase the quality factor and time-bandwidth product of photonic radio-frequency filtering (which is roughly equal to the number of comb lines). Fig. 48(c) shows the comb spectrum which was shaped into a smooth Hamming window after passing through a pulse shaper [167,300]. The spectral-range covers the whole lightwave C band, limited only by the passband of the pulse shaper.

The outstanding feature of micro-combs is that they can achieve a large line spacing compared to general mode-locked fibre lasers and electro-optic combs. For the comb-based photonic radio-frequency filters, the maximum radio-frequency that can be handled is limited to half of the comb spacing (called Nyquist zone) [298]. The large spacing of micro-combs gives rise to a large Nyquist zone which, in Fig. 48, is 115.6 GHz. Furthermore, the large comb spacing also makes it possible to suppress unwanted radio-frequency passbands by combining programmable optical filtering and electrical-domain filtering. Fig. 48(d) shows the single-passband radio-frequency transfer functions, which were programmed to a flat-top shape and tuned in a range only limited by the cut-off frequencies of the modulator and the photo-detector.

Nguyen et al. [64] reported a quadrature Hilbert transform filter using an integrated micro-comb, achieving filters with up to 20 taps. A radio-frequency quadrature coupler was demonstrated with more than a 5-octave 3 dB bandwidth and with a near-constant relative phase over the passband.

An ideal Hilbert transformer exhibits a constant amplitude frequency response and a $\pm 90^\circ$ frequency independent phase shift centred around the main (central) frequency. The impulse response of an ideal Hilbert transformer is a continuous hyperbolic function $1/(\pi t)$ that extends to infinity in time. In order to realise this impulse response using transversal filtering, the hyperbolic function is truncated and sampled in time by discrete taps [301]. The theoretical radio-frequency transfer function of the filter is the Fourier transform of the impulse response. In previous demonstrations of a Hilbert transformer using photonic transversal filtering, discrete filter taps were realised by employing an array of discrete CW laser sources. However, this approach limits the number of filter taps to only four, resulting in less than a 3-octave bandwidth. Conversely, the wide spectral width and large frequency spacing of the integrated micro-comb allowed for a large number of high-quality filter taps, without any increase in the system complexity, thus achieving a much wider radio-frequency bandwidth than is typically obtained with standard microwave circuits.

Fig. 49(d) shows the measured radio-frequency amplitude frequency response for 12, 16 and 20 taps, respectively, which all exhibit the expected behaviour. All three filters have the same null frequency at 16.9 GHz, corresponding to the tap

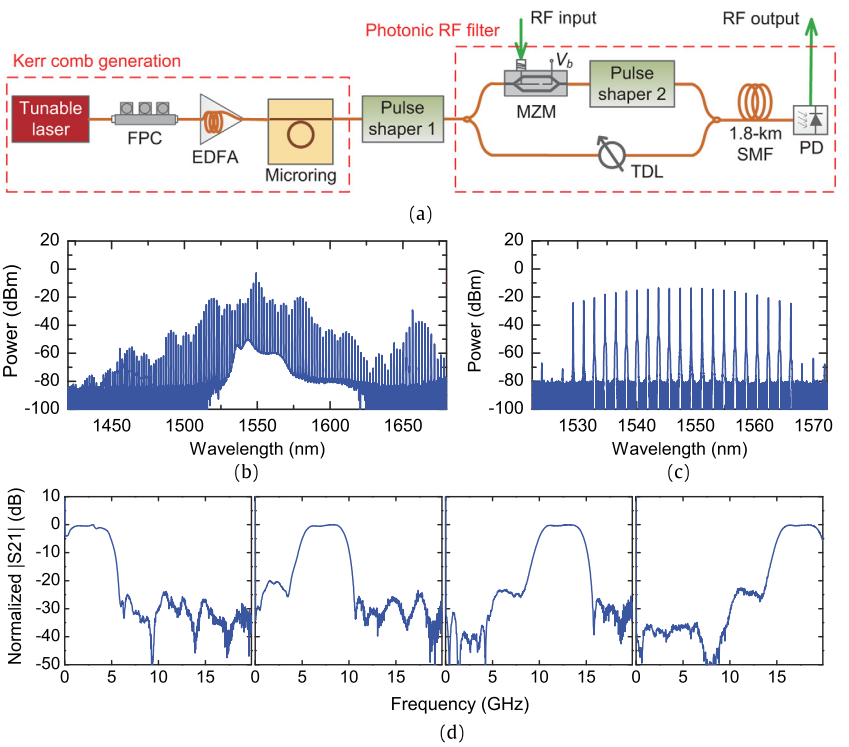

Fig. 48. Micro-comb-based photonic radio-frequency filter. (a) Experimental set-up. FPC: fibre polarisation controller; EDFA: erbium-doped fibre amplifier; MZM: Mach–Zehnder modulator; TDL: tuneable delay-line; SMF: single-mode fibre; PD: photo-detector. (b) Comb spectrum after the micro-ring. (c) Shaped comb spectrum after pulse shaper 1. (d) Single-passband radio-frequency transfer function that was configured into a flat-top shape by programming pulse shaper 2. The centre frequency was tuned between 0 and 20 GHz. After Ref. [63].

spacing of $\Delta t = 1/f_c = 59$ ps given by the difference in delay between the comb lines, equal to the ring FSR $= 1.6$ nm, produced by propagation through a 2.122 km long single-mode fibre with a dispersion parameter $D = 17.4$ ps/(nm km). All filters show a <3 dB amplitude ripple. Increasing the number of filter taps increases the filter bandwidth. For a 20-tap filter, the filter had a 3 dB bandwidth extending from 16.4 GHz down to 0.3 GHz, corresponding to more than five octaves. It is possible to increase this bandwidth further by using more comb lines in the filter. In this experiment only a small portion of the generated comb spectrum was actually used, due to the limited bandwidth of the commercial pulse shaper and of the gain of the optical amplifier. Fig. 49(e) presents the measured phase response of filters with different numbers of taps, showing very similar responses. Each shows a relatively constant phase of near $-90°$ within the passband.

7.2.2. Low phase-noise photonic microwave oscillators

Low phase-noise microwave oscillators are key elements in many applications, such as wireless communications, radar detection, metrology and radio astronomy. Photonic microwave oscillators have been demonstrated to generate microwave signals with ultra-low phase-noise [302–304]. The outstanding performance of photonic microwave oscillators becomes more prominent as the microwave frequency increases (e.g. tens to hundreds of GHz) because the phase-noise of traditional electronic oscillators also becomes higher with increasing frequency. Indeed, a state-of-the-art approach to microwave signal generation is obtained by using optical frequency division [303] - a technique based on optical frequency combs. However, a drawback of photonic microwave oscillators is that they are generally bulky and complex, which significantly limits their use outside the laboratory.

The high potential of micro-combs in implementing compact photonic microwave oscillators has been recognised since the beginning of their development [21,168,305]. Stable and spectrally-pure microwave signals can be obtained by using a fast photodiode to detect the beat-note of a phase-locked micro-comb. Some early experiments have shown that the phase-noise of the microwave signal generated with a free-running micro-comb is comparable to an open-loop, high-performance electronic microwave oscillator [305]. Detailed investigations of the sources of phase-noise were performed by Liang et al. [62,306–308]. It was found that the phase-noise of the micro-comb beat-note is affected by several parameters, including the pump laser relative-intensity noise, the shot noise, the micro-resonator Q-factor, the thermal fluctuations, the pump-resonance de-tuning and the comb mode-locking mechanism.

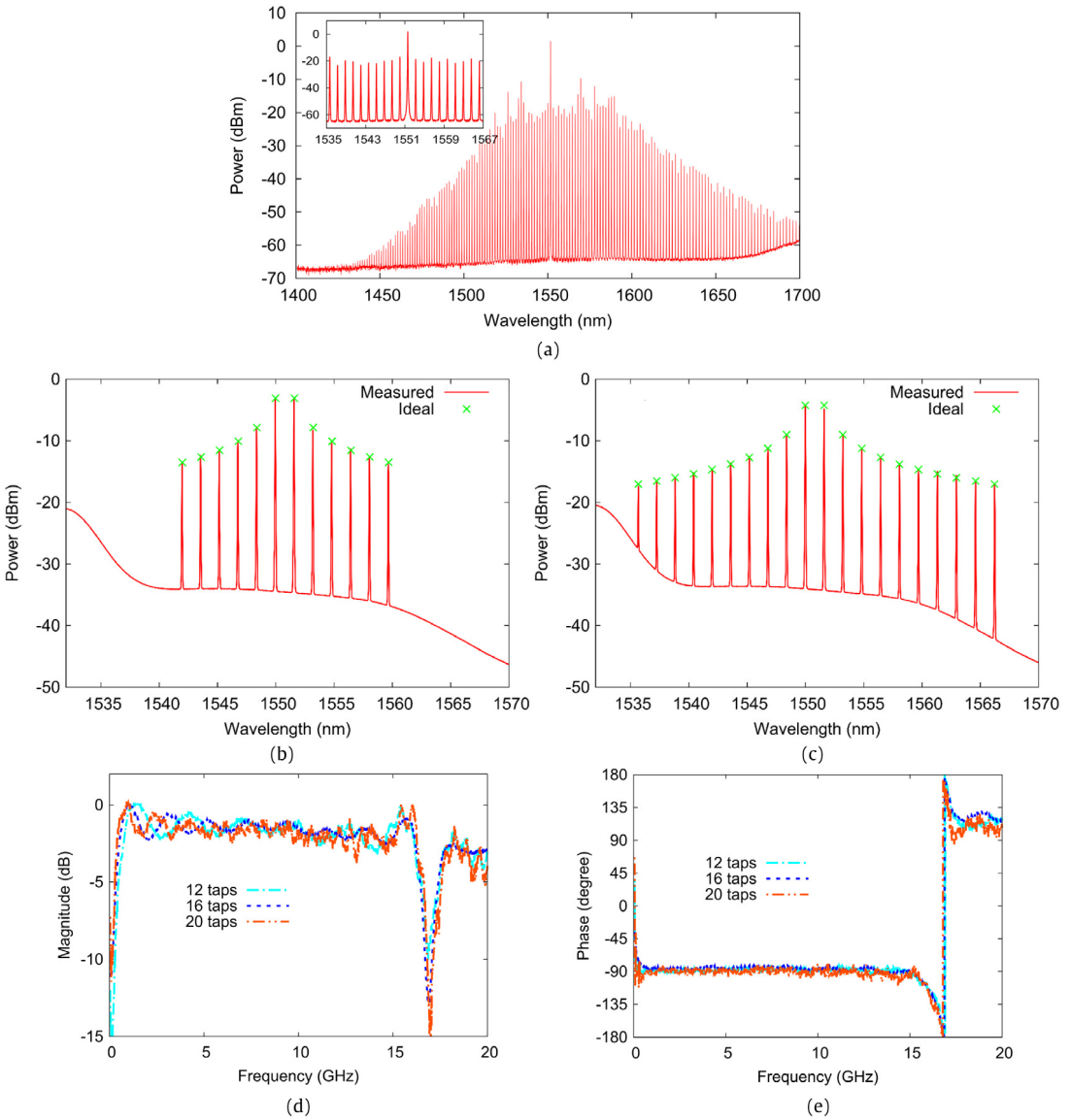

Fig. 49. Micro-comb-based Hilbert transform filter (a) Spectrum of the comb generated from the micro-ring, measured by an OSA with a resolution of 0.5 nm. Inset: Zoom-in of the spectrum around the pump wavelength. EDFA2 output showing the weight of each tap for: (b) 12-tap filter, and (c) 20-tap filter. Measured system radio-frequency response: (d) amplitude; and (e) phase response. After Ref. [64].

A broader comb spectrum with more phase-locked lines generally produces microwave signals with lower close-in noise and a higher noise floor. Fig. 50(a) shows the radio-frequency spectrum of a 9.9-GHz microwave signal generated by a phase-locked broadband comb (optical spectrum shown in Fig. 50(b)) from a high-Q MgF_2 WGM resonator (intrinsic Q $\sim 5 \times 10^9$) [62]. The pump laser was a semiconductor DFB laser, which was frequency locked to a selected resonator mode through self-injection locking [268]. The temperature of the resonator was stabilised to milli-Kelvin (mK) levels. A drop-port [169] was used to retrieve the comb for microwave generation. By using the drop-port, the noisy time-independent background from the pump laser was suppressed due to the resonator's filtering action. The measured single-sideband power-spectral density of the microwave phase-noise is −60 dBc/Hz at 10 Hz and −90 dBc/Hz at 100 Hz (Fig. 50(c)).

The frequency stability was measured as the Allan deviation approached 10^{-10}, at integration times of 1–100 s. The performance is superior to chip-scale laser-based radio-frequency photonic oscillators. The phase-noise at small offset frequencies below 1 kHz is limited by fluctuations of the resonator frequency. The noise floor above 10 MHz is limited by shot noise and can be further reduced by inserting a narrow-band radio-frequency filter after the photo-detector.At intermediate

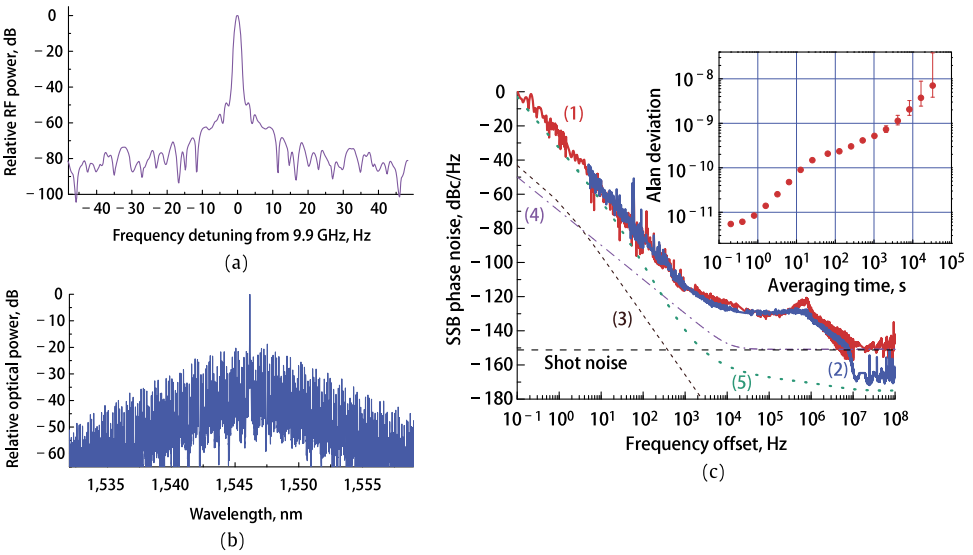

Fig. 50. Microwave signal generation with a micro-comb. (a) Spectrum of the microwave signal measured with 9 Hz resolution bandwidth. (b) Spectrum of the frequency comb generating the microwave signal. (c) Single-sideband phase-noise of the microwave signal without (red line, (1)) and with (blue line, (2)) a narrow-band radio-frequency filter placed after the photo-detector. The measured noise at offset-frequencies below 1 kHz and above 10 MHz is within 3 dB of the noise floor of the microwave phase-noise measurement system used. The other curves are: (3) theoretical thermo-refractive noise (4) quantum noise (5) sensitivity of the phase-noise measurement system. The inset shows Allan deviation of the microwave signal. After Ref. [62].

frequencies between 1 kHz and 10 MHz, the phase-noise is due to a transfer of the laser relative-intensity noise to the microwave phase modulation through comb dynamics. In Fig. 50(c), the theoretical limits resulting from quantum vacuum fluctuations and thermodynamic fluctuations of the resonator temperature and volume are also shown. We note that there is still room to further improve the spectral purity by reducing the laser relative-intensity noise and employing better thermal and mechanical stabilisation of the system.

7.3. High-speed optical communications

In order to increase the transmission capacity of optical fibres, wavelength-division multiplexing (WDM) has long been used, where data is transmitted simultaneously over multiple optical wavelengths. The use of this approach has evolved to ever shorter distance scales, from large-scale long-haul communications to metro networks and is now entering the domain of data centres and, eventually, board-to-board and even on-chip optical interconnects for super computers. In all cases, micro-combs have great potential as ultra-compact WDM sources. Early attempts of micro-comb-based communications used simple on–off keying (OOK) modulation [61,309], where information is carried by the optical intensity. In this case, low comb intensity noise is essential for achieving high performance. Error-free transmission for each individual line of a low-noise micro-comb, transmitted over tens of kilometres of single-mode fibre, has been demonstrated with a power penalty of less than 0.5 dB (see Fig. 51) [61]. Although highly coherent schemes seem not to be required for on–off keying, the coherence and intensity noise are generally correlated. For micro-combs, low-intensity noise generally corresponds to high coherence and vice versa [309], so the methods of generating coherent micro-combs discussed in Section 6 are generally required to achieve a low-intensity noise.

Coherent data transmission, which typically poses stringent requirements on the spectral purity of the optical carrier, has also been demonstrated with phase-locked micro-combs. In the first work reported by Pfeifle et al. in 2014 [60], a data stream of 392 Gbit s^{-1} was encoded on six lines of a micro-comb using quadrature phase-shift-keying (QPSK) and 16-state quadrature amplitude modulation (16QAM). The optical spectrum after modulation is shown in Fig. 52(a). The constellation diagrams are presented in Fig. 52(b) in which no excess phase-noise is observed. A second experiment demonstrated the feedback stabilisation of the comb and transmission of a 1.44 Tbit s^{-1} data stream over up to 300 km with twenty comb lines. These results showed that micro-combs can indeed meet the highly demanding requirements of coherent communications and, thus, offer an attractive route towards chip-scale terabit/s transceivers. The régime of Turing rolls, which corresponds in the spectral domain to the so-called primary combs, has been shown to display exceptional coherence and phase-locking properties [310]. This type of comb was, therefore, used for coherent optical communications, which allowed for data transmission at the record rate of 144 Gb/s per carrier [311].

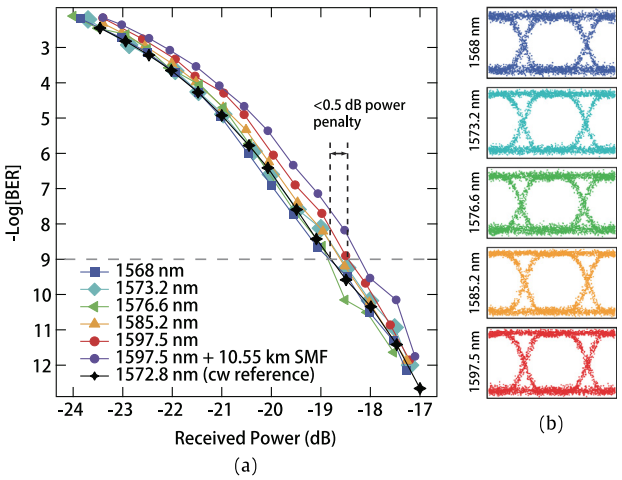

Fig. 51. Data transmission based on a micro-comb. After Ref. [61]: demonstration of on–off keying modulation of a micro-comb source (a) power penalty (b) eye diagram.

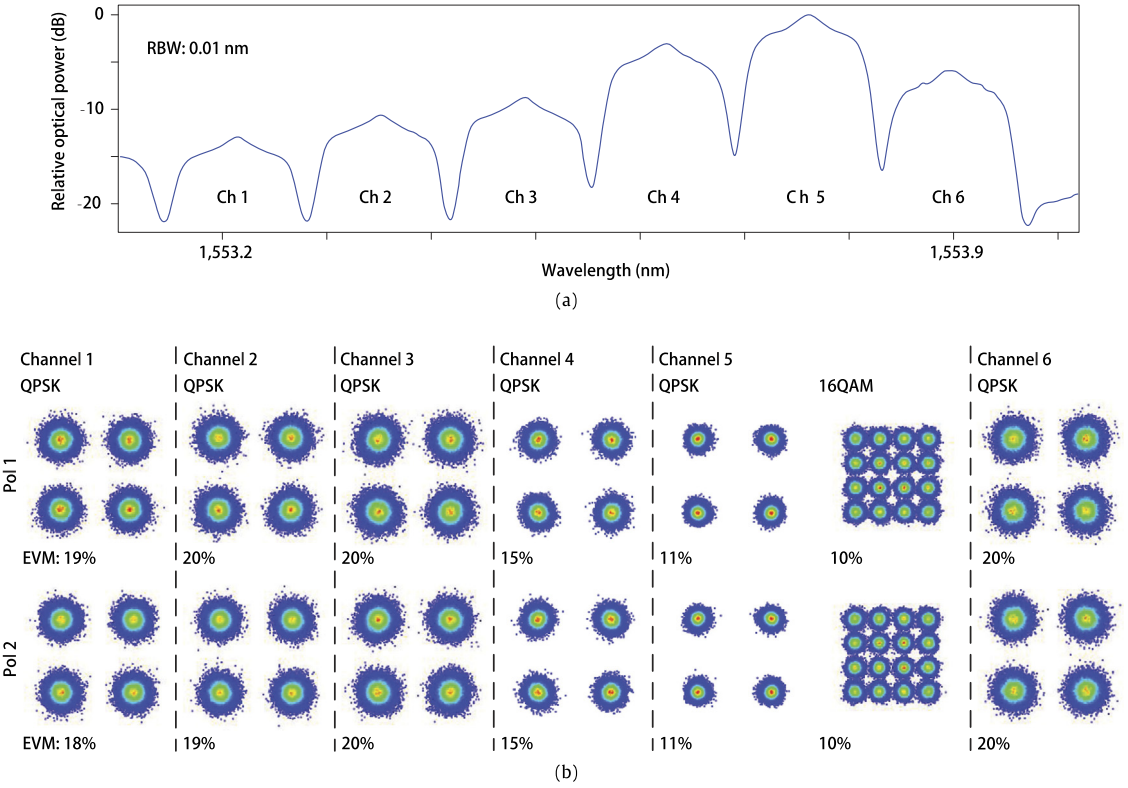

Fig. 52. Coherent data transmission using a Kerr micro-resonator frequency comb. (a) Spectrum of modulated carriers for all six data channels. (b) Constellation diagrams for each channel and for both polarisations, as well as the corresponding error vector magnitude (EVM). The constellation diagrams show no sign of an excessive phase-noise, which would result in constellation points that are elongated along the azimuthal direction. For QPSK, the BER of all channels is below 4.5×10^{-3}, which corresponds to an EVM of 38%; for channels 4 and 5, the BER is even smaller than 1×10^{-9} (EVM, 16.7%). The good quality of channel 5 enables transmission of a 16QAM signal with a measured BER of 7.5×10^{-4}. After Ref. [60].

8. Micro-combs for applications to quantum optics

While interest in optical frequency combs, to date, has predominantly been for classical applications, substantial activity is growing in exploring their applications in quantum optics. As discussed in Section 4, Kerr optical frequency combs result

from a cascade of photonic interactions of the kind

$$\hbar\omega_m + \hbar\omega_{\mathrm{p}} \rightarrow \hbar\omega_n + \hbar\omega_q, \tag{66}$$

where two input photons, m and p, interact coherently via the Kerr nonlinearity to yield two output photons, n and q. Without any further analysis, this interpretation already suggests that purely quantum phenomena, based on the non-classical nature of light, can play a significant role in these combs.

Furthermore, micro-comb-based multi-chromatic non-classical light sources are attracting great interest in quantum information science and can bring important advances, such as the realisation of compact sources for quantum communication [270,312–315] and the generation of entangled states for, e.g. quantum computation [316,317] and topological quantum error correction [318]. The development of (heralded) single photon [319] or entangled photon-pair sources [320] has already bridged the gap from academic research to consumer use, with quantum communication systems [321] (including quantum key distribution, QKD) already realised as commercial products.

Motivated by a growing market for quantum technology, integrated designs for quantum applications are attracting great interest [322]. Recent breakthroughs in on-chip quantum devices include the realisation of integrated sources of heralded single photons [128,312] and entangled photons [323–326], as well as the demonstration of quantum algorithms on-chip [327,328].

However, several challenges in these realisations still need to be resolved. For example, most integrated quantum sources demonstrated to date only operate at single frequencies and with low efficiency, therefore having limited applications. Indeed, frequency multiplexing could drastically improve the speed-bottleneck of current quantum communication systems, which is why multi-channel sources are being investigated. In addition, while proof-of-concept devices towards optical quantum computation have been demonstrated [316,317], up until now there have only been very few reports of sources for the scalable generation of non-classical light [329].

Exploiting the quantum properties of integrated optical frequency combs may offer the chance to overcome several of these limitations. First, frequency combs operate intrinsically at multiple frequencies and, therefore, can provide the desired multiplexed photon-pair generation. Furthermore, the small physical footprint and intrinsic compatibility with monolithic integration provide very high stability and phase coherence. By combining these attributes, integrated quantum frequency combs could provide highly-desired and powerful sources of non-classical light for both multiplexed quantum communications, as well as for quantum computation [322].

This section summarises some of the recent results in this framework: we will present the theoretical ideas needed for the quantum analysis of Kerr combs where the resonators are pumped below and above threshold, thereby allowing for understanding phenomena such as entanglement, spontaneous four-wave mixing or two-mode squeezing [330] and we will summarise the very first experimental results in these régimes.

8.1. Theoretical modelling: Quantum Langevin equations for Kerr combs

The dynamical behaviour of Kerr combs at the quantum level can be determined by defining a Hamiltonian operator for the system. This approach has the advantage of underlying the conservation rules that are closely related to commutators involving the Hamiltonian. This formalism can, in fact, also be used in the deterministic semi-classical limit [193].

Let us consider a Kerr comb with $2K + 1$ modes labelled as $l = -K, \ldots, K$, with $l = 0$ being the central (or pumped) mode. The quantum state of each mode l can be described by the annihilation and creation operators $\hat{\mathrm{a}}_l$ and $\hat{\mathrm{a}}_l^\dagger$, respectively, which obey the boson commutation rules

$$\begin{aligned} &[\hat{\mathrm{a}}_l\,, \hat{\mathrm{a}}_{l'}^\dagger] = \delta_{l,l'} \\ &[\hat{\mathrm{a}}_l, \hat{\mathrm{a}}_{l'}] = [\hat{\mathrm{a}}_l^\dagger, \hat{\mathrm{a}}_{l'}^\dagger] = 0. \end{aligned} \tag{67}$$

The semi-classical photon number $N_l = |\mathcal{A}_l|^2 = \mathcal{A}_l^* \mathcal{A}_l$ is now replaced by its quantum counterpart, which is the photon number operator $\hat{\mathrm{n}}_l = \hat{\mathrm{a}}_l^\dagger \hat{\mathrm{a}}_l$.

In order to avoid a violation of the Heisenberg uncertainty principle, vacuum fluctuation operators $\hat{\mathrm{V}}_{\mathrm{s},l}$ have to be associated with every loss mechanism for each mode l, where s can stand either for the intrinsic losses, for the coupling losses at the through-port or, eventually, for the coupling losses at the drop-port (in the add-drop configuration). These operators have a zero expectation value and obey the commutation rules

$$[\hat{\mathrm{V}}_{\mathrm{s},l}(t), \hat{\mathrm{V}}_{s',l'}^\dagger(t')] = \delta_{\mathrm{s},s'}\, \delta_{l,l'}\, \delta(t - t'). \tag{68}$$

The Hamiltonian of the system is explicitly defined as

$$\hat{\mathrm{H}}_{\mathrm{tot}} = \hat{\mathrm{H}}_{\mathrm{free}} + \hat{\mathrm{H}}_{\mathrm{pump}} + \hat{\mathrm{H}}_{\mathrm{Kerr}} \qquad \text{with}$$

$$\hat{\mathrm{H}}_{\mathrm{free}} = \hbar \sum_l \left[\sigma - \frac{1}{2}\zeta_2 l^2\right] \hat{\mathrm{a}}_l^\dagger \hat{\mathrm{a}}_l \qquad \text{and}$$

$$\hat{\mathrm{H}}_{\mathrm{pump}} = i\hbar\sqrt{\Delta\omega_{\mathrm{e}}}A_{\mathrm{in}}\left(\hat{\mathrm{a}}_0^{\dagger} - \hat{\mathrm{a}}_0\right) \qquad \text{and}$$

$$\hat{\mathrm{H}}_{\mathrm{Kerr}} = -\frac{1}{2}\hbar g_0 \sum_{m,n,p,q} \delta(m-n+p-q)\,\hat{\mathrm{a}}_n^{\dagger}\hat{\mathrm{a}}_q^{\dagger}\hat{\mathrm{a}}_m\hat{\mathrm{a}}_{\mathrm{p}}. \tag{69}$$

The Hamiltonian $\hat{\mathrm{H}}_{\mathrm{free}}$ corresponds to the propagation of the fields, where $\sigma = \omega_L - \omega_l$ is the laser de-tuning and ζ_2 is the second-order group velocity of the eigenmodes. The variable $\hat{\mathrm{H}}_{\mathrm{pump}}$ stands for the external pump excitation (with $A_{\mathrm{in}} = \sqrt{P/\hbar\omega_0}$ being the pump field, i.e. the input photon flux, expressed in s^{-1} and $\Delta\omega_{\mathrm{e}}$ representing coupling losses) and $\hat{\mathrm{H}}_{\mathrm{Kerr}}$ corresponds to the nonlinear interactions related to the Kerr nonlinearity. This Hamiltonian enables us to obtain an explicit quantum Langevin equation for the annihilation operators $\hat{\mathrm{a}}_l$ following [330]

$$\begin{aligned}\dot{\hat{\mathrm{a}}}_l &= -\frac{1}{2}\Delta\omega_{\mathrm{t}}\,\hat{\mathrm{a}}_l + \frac{1}{i\hbar}[\hat{\mathrm{a}}_l, \hat{\mathrm{H}}_{\mathrm{tot}}] + \sum_{\mathrm{s}}\sqrt{\Delta\omega_{\mathrm{e,s}}}\,\hat{\mathrm{V}}_{\mathrm{s},l} \\ &= -\frac{1}{2}\Delta\omega_{\mathrm{t}}\,\hat{\mathrm{a}}_l - i\left[\sigma - \frac{1}{2}\zeta_2 l^2\right]\hat{\mathrm{a}}_l + \delta(l-l_0)\sqrt{\Delta\omega_{\mathrm{e}}}\,A_{\mathrm{in}} \\ &\quad + ig_0\sum_{m,n,p}\delta(m-n+p-l)\,\hat{\mathrm{a}}_n^{\dagger}\hat{\mathrm{a}}_m\hat{\mathrm{a}}_{\mathrm{p}} + \sum_{\mathrm{s}}\sqrt{\Delta\omega_{\mathrm{e,s}}}\,\hat{\mathrm{V}}_{\mathrm{s},l}\,,\end{aligned} \tag{70}$$

where the index s runs across the various loss terms corresponding to the configuration under study and l_0 represents the mode of the external laser pump.

8.1.1. System below threshold: spontaneous four-wave mixing

In the case of a resonator pumped below threshold, the classical viewpoint assumes that the pump field is the unique oscillating mode inside the resonator, while all the side-modes have zero power (in other words, we have $\mathcal{A}_0 \neq 0$ and $\mathcal{A}_l \equiv 0$ for $l \neq 0$).

From a quantum point of view, the pump field actually triggers *spontaneous four-wave mixing* where two pump photons are symmetrically up- and down-converted in the Fourier domain, thereby leading to the simultaneous and spontaneous generation of *signal* and *idler* photons, respectively. This phenomenology corresponds to the photonic interaction

$$2\hbar\omega_{\mathrm{p}} \rightarrow \hbar\omega_{\mathrm{s}} + \hbar\omega_{\mathrm{i}}, \tag{71}$$

where $\omega_{\mathrm{p}} \equiv \omega_0$, $\omega_{\mathrm{s}} \equiv \omega_L$ and $\omega_{\mathrm{i}} \equiv \omega_{-L}$ are the pump, signal and idler angular frequencies, respectively (with $L > 0$).

The phenomenon of spontaneous FWM is of a purely quantum nature, since it is a result of the coupling between the intra-cavity pump photons and the vacuum fluctuations of the various side-modes.

The spectral density of the output photon flux generated by spontaneous FWM in the side-modes $\pm l$ can be explicitly calculated as

$$S_{\mathrm{sp},l}(\omega) = \rho\,\frac{\Delta\omega_{\mathrm{t}}^2 g_0^2|\mathcal{A}_0|^4}{[(\Delta\omega_{\mathrm{t}}/2)^2 - g_0^2|\mathcal{A}_0|^4 + \xi_l^2 - \omega^2]^2 + \Delta\omega_{\mathrm{t}}^2\omega^2}\,, \tag{72}$$

where $\xi_l = \sigma - \frac{1}{2}\zeta_2 l^2 + 2g_0|\mathcal{A}_0|^2$ is the overall de-tuning induced by laser de-tuning, group velocity dispersion and self-phase modulation for a given mode l; while the parameter $\rho \in [0, 1]$ is the ratio between out-coupling and total losses or, equivalently, the ratio between the number of detected photons versus the total number of annihilated photons [330].

The best performance for spontaneous FWM is achieved for $\rho \rightarrow 1$, which corresponds to strong over coupling in the detection port. Therefore, it appears that ultra-low-loss resonators are the most suitable devices for the purpose of spontaneous FWM, as ρ always increases with the intrinsic Q-factor. It can also be shown that the side-modes $\pm l$ are entangled and that their spectra are correlated [330].

8.1.2. System above threshold: two-mode squeezing

When the system is pumped above threshold, the photonic interaction (71) becomes stimulated instead of spontaneous (for the typical case of modulation instability).

In a Kerr comb, the out-coupled photon flux is exactly the same as for the side-modes $\pm l$ in the semi-classical limit, so that the difference

$$N_{\mathrm{out},\Delta} = N_{\mathrm{out},l} - N_{\mathrm{out},-l} \tag{73}$$

is expected to be strictly null. Experimentally, this signal corresponds to the difference of optical powers that are photo-detected for the modes $+l$ and $-l$. From a quantum perspective, it can be shown that the operator

$$\hat{\mathrm{N}}_{\mathrm{out},\Delta} = \hat{\mathrm{N}}_{\mathrm{out},l} - \hat{\mathrm{N}}_{\mathrm{out},-l} \tag{74}$$

for the photon number difference operator is not null but, instead, yields fluctuations that are sometimes referred to as the standard quantum noise limit (which, in this case, is the shot noise). However, when optimal conditions are met, the

power spectrum of the quantum noise can be decreased below the shot noise level and this phenomenon corresponds to two-mode squeezing [331]. In Ref. [332], Lugiato and Castelli have pioneered investigations on the quantum properties of the optical systems governed by the LLE. They have demonstrated that the intensity difference exhibits fluctuations below the quantum noise floor and this theoretical result has been experimentally confirmed in the research work reported in Ref. [333], summarised below. This squeezing is intrinsically linked to the fact that, in the limit of a minimal three-mode comb (pump, signal and idler), the operator $\hat{N}_{\mathrm{out},\Delta}$ commutes with the Hamiltonian $\hat{H}_{\mathrm{tot}}$, meaning that the photon number difference is a conserved quantity.

A quantum analysis shows that the squeezed spectrum can be rewritten under the normalised form

$$S_{\mathrm{sq}}(\omega) = 1 - \rho \frac{\Delta\omega_{\mathrm{t}}^2}{\omega^2 + \Delta\omega_{\mathrm{t}}^2}, \tag{75}$$

where the asymptotic value 1 corresponds to the shot noise level [330,332]. The spectrum described by $S_{\mathrm{sq}}(\omega)$ is an inverted Lorentzian which qualitatively displays a dip below the shot noise level close to the zero frequency with $S_{\mathrm{sq}}(0) = 1 - \rho$ and converges to the shot noise level as $S_{\mathrm{sq}}(\omega) \to 1$ when $\omega = \pm\infty$. The parameter ρ is, therefore, a direct indicator of the squeezing efficiency, as $\rho \to 1$ leads to quasi-perfect squeezing at zero frequency. In Kerr comb generation, efficient squeezing ($\rho \to 1$) is achieved with strong over coupling. Hence, exactly as for spontaneous FWM, ultra-low-loss resonators are ideal since they systematically maximise ρ.

It can be shown that this two-mode squeezing is observed not only for roll patterns close to threshold within a three-modes approximation but also for any type of stationary Kerr comb, regardless of the number of modes involved and the dispersion régime, even far above threshold.

8.2. Experiments: photon-pair generation, entanglement and squeezing

Spontaneous FWM has been used to generate photon-pairs in several frameworks [322], including micro-resonators that are compatible with integrated silicon technology. In general, the requirements of an ideal source would include: long-term operational stability and insensitivity to environmental changes; compatibility with quantum memories; operation at telecom wavelengths (near 1550 nm) over several channels and the possibility of using large-scale electronic chip fabrication processes (CMOS). In addition, further benefits of frequency multiplexing include the ability to allow high-dimensional multi-user operation, as well as polarisation diversity for polarisation-dependent applications [334].

Photon-pair generation based on SFWM has been demonstrated in silicon ring-resonators by Clemmen et al. in 2009 [128] and by Azzini et al. [335] in 2012. Azzini et al. reached a coincidence-to-accidental ratio (CAR) of 250 for pump powers below 1 mW. Improved performance has subsequently been obtained by Engin et al. [312] with a reverse-biased design to lower the nonlinear losses of silicon micro-resonators, reaching a maximum CAR ratio of 602 ± 37. The generation of photon-pairs over multiple channels was later obtained on a silicon chip by Kumar et al. [313] by using a coupled micro-ring resonator pumped at a single wavelength. In this work the authors demonstrated photon-pair generation and the capability of tuning the wavelength of the generated pairs via electric current. Heralded single photon emission was demonstrated on a chip in 2014 by Reimer et al. [270] in doped silica micro-ring resonators, with a Q-factor exceeding one million. The pump field was obtained using the self-locked OPO configuration described in Section 6 [57,58,269], where the micro-resonator was pumped below threshold in order to operate in the quantum régime. In this approach, a micro-ring resonator is embedded in an external active cavity, where an additional filter allows the active oscillation of the pump laser only in a single resonance of the micro-cavity. Here, any thermal fluctuations are passively locked and the excitation scheme allows for long-term stability – up to several weeks with less than 5% fluctuation – with no need for external, active feedback. Five independent multiplexed channels of heralded photons were realised (centred at standard telecom channels, separated by 200 GHz) with CARs in a range from 10 to 14 and a linewidth of 110 MHz (limited by the set up), thus achieving compatibility with quantum memories that are usually based on atomic transitions with typical linewidths in the order of 100 MHz. The source achieved nearly single-mode operation with a clear, heralded signal-idler dip ($g^{(2)}(0) < 0.144$) seen in the measurements, as expected for a source operating in the single photon régime. Heralded single photon emission over two multiplexed channels was obtained by Jiang et al. [314] in a fibre-coupled monolithic micro-disc resonator with Q-factor of half a million, achieving a CAR of up to 1386 ± 278.

However, we note that, in order to produce complex quantum states [334], polarisation-diverse photons are highly desired. Reimer et al. recently introduced a SFWM configuration employing two orthogonally-polarised excitation fields [271] (see the experimental set-up in Fig. 53). This configuration exploited the fundamental transverse electric (TE) and transverse magnetic (TM) modes of a high-Q micro-resonator, which had slightly different dispersions for the two polarisations, resulting in a frequency offset of 70 GHz between the two sets of modes. The FSR of both modes was almost identical (in this experiment 200.39 and 200.51 GHz, respectively). When two orthogonally-polarised excitation fields are coupled into two close resonances, stimulated FWM between the fields is suppressed because the idlers are generated out of resonance due to the frequency offset. Conversely, if the TE and TM mode dispersions are similar, so that the difference in FSR between the two modes (120 MHz in the experiment) is smaller than the bandwidth of the resonances, spontaneous FWM processes can take place, generating orthogonally-polarised photon-pairs resonant with the micro-cavity modes. This approach allowed the observation of Type II spontaneous FWM, in analogy to Type II spontaneous down-conversion in second-order media.

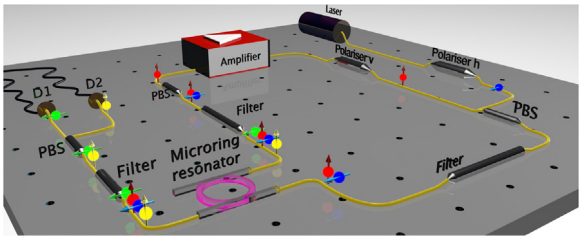

Fig. 53. Experimental set-up of the hybrid self-locked and external pumping scheme. The TE polarisation was pumped in a self-locked scheme, while the TM excitation field (actively locked to the resonance) was added and extracted by two polarisation beam splitters (PBSs) placed before and after the micro-ring resonator. The amplified spontaneous emission of the amplifier was transmitted through the bandpass filter before the resonator, thus selecting the desired pump resonance. The output of the resonator was then fed back into the amplifier and acted as a seed to initiate lasing on the TE resonance. The photon-pairs were extracted at the through-port of the resonator and detected, after filtering out the pump fields, and directed to detectors D1 and D2. The arrow on top of the amplifier represents the propagation direction of the light inside the cavity. The coloured spheres with arrows illustrate the frequency and polarisation of the involved fields: red and blue are the TE and TM pumps, respectively, while yellow and green are the TE and TM photons, respectively, generated through Type II spontaneous FWM. After Ref. [271].

With this approach, the authors could obtain the direct generation of orthogonally-polarised photon-pairs on a chip (see Fig. 54) [271].

In particular, the source was operated in a hybrid self-locked pump configuration, where one polarisation was excited in a self-locked way, while the other was excited with an external laser. This configuration allowed for stable long-term operation, as well as precise control, over both pump powers. When operated below the OPO threshold, the device directly generated orthogonally-polarised photon-pairs with a CAR up to twelve, limited by loss, dark counts and quantum efficiency of the detectors, as well as by the photons generated through Type-0 SFWM of the individual excitation fields. For orthogonally-polarised photon-pairs, the coincidence counts (C) are expected to scale with the product of both pump powers [336]. No coincidences (within the noise) were measured when the ring was either not pumped, or pumped with the TE field alone, where the non-zero clicks are attributed to the dark counts of the detector. A linear-scaling behaviour is visible (Fig. 54) with increasing TM pump power and constant TE power, while a quadratic-scaling (without linear contribution) is observed with increasing, balanced pump powers. A coincidence rate of around 4 Hz was measured at 5 mW balanced pump power at the input of the chip (5 mW is the highest achievable pump power featured by a CAR above 10). Accounting for detection and propagation losses, this corresponded to a pair production rate of 40 kHz and a pair production probability of 1.48×10^{-12}.

The heralded autocorrelation function $g_h^{(2)}$ shows a clear dip of $g_h^{(2)}(0) \approx 0.26 \pm 0.11 < 0.50$, demonstrating that the source operated in a non-classical single-photon régime, while the idler–idler autocorrelation showed a clear peak with a maximum of 2.01 ± 0.03, corresponding to $N = 0.99 \pm 0.03 \approx 1$ effective modes, highlighting the high purity of the source. Finally, the production of cross-polarised photon-pairs is limited not only to the adjacent resonances but also the generation of frequency-multiplexed cross-polarised photon-pairs is possible. Indeed, cross-polarised photon-pairs over 12, number limited by the available filters, resonant pairs were measured, each with pair production rates above 20 kHz at 5 mW balanced pump power.

One of the more practical approaches to achieving quantum correlation of photon-pairs is time–energy entanglement, since it can be readily achieved via photonic-integrated circuits [337] and is particularly robust to transmission over long distances in optical fibres [338,339]. This latter property makes it particularly suitable for quantum key distribution and, indeed, time–energy entangled photon-pairs have been shown to produce higher quantum key generation rates compared to entangled photon-pairs in lower-dimensional Hilbert spaces [340]. Micro-resonators also offer a very attractive platform on which to achieve the generation of correlated photon-pairs in the form of entanglement [325,326,341–346]. Recently, an efficient source of time–energy entangled photon-pairs based on a silicon-on-insulator micro-ring resonator was demonstrated by Grassani et al. [326]. As with classical frequency combs, the large field-enhancement provided by the micro-resonator [92,128,347,348], combined with the large intrinsic effective nonlinearity in the silicon nanowires, yielded a substantial improvement in performance with respect to silicon waveguide sources, including much better spectral properties, pair production rates and linewidths of the emitted pairs, as well as a dramatic reduction in device footprint.

Fig. 55 shows the device including the transmission spectrum, along with the pump, signal and idler wavelengths. With continuous-wave (CW) pumping, the emission time of the photon-pairs is determined to be within the coherence time of the pump laser, leading to the possibility of the pairs being time–energy entangled [349]. In [326], a double interferometer [349,350], unbalanced by $\Delta T \gg \tau$ (where τ is the coherence time of the signal and idler photons, to avoid first-order interference, $\Delta T \approx 0.67$ ns while $\tau \approx 10$ ps), was used to measure the entanglement. With the interferometer arms fixed [351], the histogram of the arrival time of idler photons relative to signal photons showed three peaks — the early and late peaks corresponding to the signal and idler photons taking opposite paths and the middle peak corresponding to them taking the same (either long or short) paths. The coincidence rate for the central peak is:

$$C(\phi) = 2C_0(1 + \cos(\phi + \theta)), \tag{76}$$

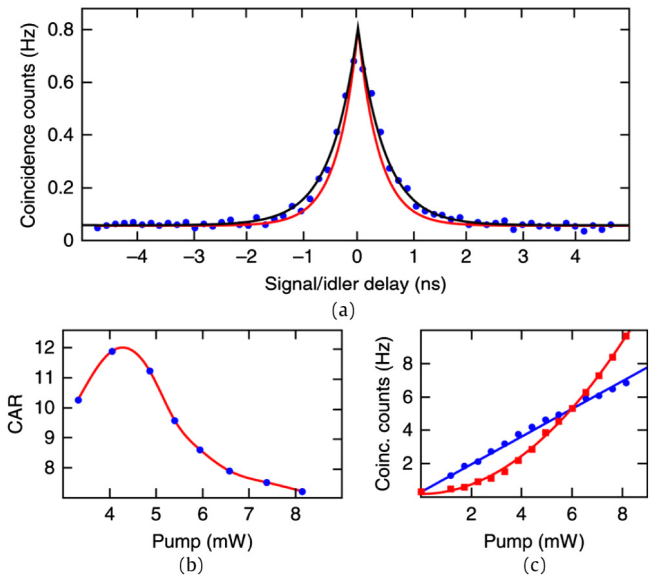

Fig. 54. Coincidence counts, coincidence-to-accidental ratio (CAR) and power scaling. (a) Measured photon coincidence peak, showing the raw measured coincidences (C) in Hz. The black curve corresponds to the optimum fit, resulting in a measured photon bandwidth of 320 MHz, while the red curve corresponds to the fit with the expected photon bandwidth of 410 MHz. (b) CAR as a function of balanced pump power (the line connecting the points is plotted for visual purposes), showing a CAR above 10 for balanced pump powers between 3 and 5 mW. (c) Measured photon coincidence counts (sum of all coincidence counts measured within the FWHM of the coincidence peak) for balanced and unbalanced pump powers. In the unbalanced configuration (blue circles), the TE pump power is kept constant at 6 mW and the TM pump power is increased, showing a linear-scaling behaviour. In the balanced configuration (red squares), TE and TM pump powers are identically increased, demonstrating a clear quadratic scaling behaviour without any linear contribution. After Ref. [271].

where C_0 is the detected coincidence rate measured by blocking one arm in each interferometer, ϕ is the sum of the phases acquired by the photons passing through the long arms, relative to the short ones, $\phi = \phi_S + \phi_I$ and θ is a constant phase-term dependent on the unknown (actual) lengths of the interferometer arms. The side peaks (corresponding to distinguishable events) are independent of variations in ϕ (Fig. 56 (a–d) showing the histograms for different ϕ), while the central peak oscillates from near-zero coincidence counts to nearly four times the height of the side peaks, following the sinusoidal relationship of Eq. (76). The resulting visibility $V = 89.3\% \pm 2.6\%$ ($>1/\sqrt{2}$) proves the violation of Bell's inequality and, thus, the presence of entanglement by 7.1 standard deviations [352].

This micro-resonator-based source of entangled photons yielded unprecedented performance, such as a high purity of the emitted two-photon states and a spectral brightness per coupled pump photon of 6×10^7, $\mathrm{nm}^{-1}\,\mathrm{mW}^{-2}\,\mathrm{s}^{-1}$ - more than four orders of magnitude larger than in long silicon waveguides [128,325,353]. The small footprint of the device would allow scaleability, as well as integration of other components, such as pump filters and signal/idler de-multiplexers on a single chip, since the required delays of centimetres are achievable on-chip.

Progress has also recently been made [333] in exploiting integrated micro-resonators to generate non-classical states of light above the OPO threshold. Squeezed states of light, based on continuous rather than discrete variables, have recently been explored by Dutt et al. in micro-resonators, which are particularly attractive because of their large resonant field-enhancement. In squeezing, the signal and idler beams contain strong quantum intensity correlations that lead to noise in their intensity difference, which is less than the standard quantum limit. In micro-resonators there is a trade-off between high field-enhancement, hence increased squeezing efficiency with increasing Q and the corresponding decrease in bandwidth. For applications such as entanglement-based quantum key distribution in the continuous-variable régime [354], a large squeezing bandwidth is needed for high data rates. In [333], the CMOS compatibility and high degree of optical confinement in a micron-sized silicon nitride oscillator [11] enabled efficient squeezing with GHz cavity linewidths.

When carefully designed to engineer dispersion correctly, OPO based on FWM in a Si_3N_4 micro-ring resonator has the potential to generate a very large number of beams spanning more than an octave [25], as previously described in Sections 2 and 4. Squeezing was achieved (Fig. 57) by using a CW-tuneable laser pumping the OPO just above threshold, when only two modes oscillated. The output from the ring was collected with a high-NA objective lens and directed into a diffraction grating to spatially separate the pump, signal and idler beams. The signal and idler beams were then detected with balanced detectors, followed by a low-noise trans-impedance amplifier to enhance the difference in photo-currents between the detectors. An electronic spectrum analyser was used to measure the variance in the intensity-difference noise between the two balanced detectors. Fig. 58 shows the results of the squeezing measurements, where more than 30% sub-shot noise quantum intensity correlations between the twin beams was generated when the pump laser was tuned to an on-chip resonance at 1549.6 nm. The solid line is the signal-idler intensity correlation measurement that is below the shot noise level,

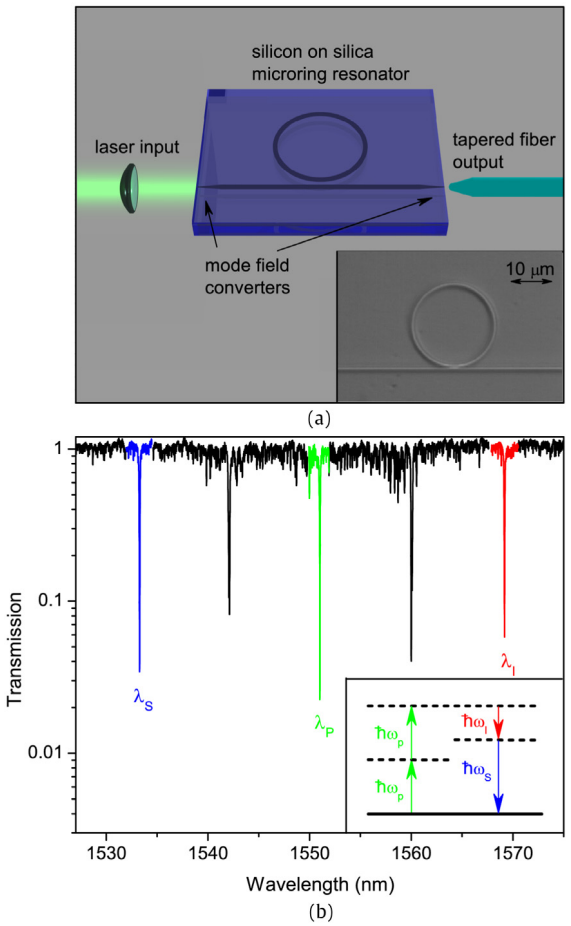

Fig. 55. Ring-resonator device schematic (top) and transmission spectrum (bottom). The 2-port ring-resonator had a radius of 10 μm, a FSR of 9 nm and a Q-factor of 15,000. The nanowire waveguides had transverse dimensions of 500 nm (width) and 220 nm (height) on SOI. The pump resonance is highlighted in green and the signal and idler resonances employed in the experiment are indicated in blue and red, respectively. After Ref. [326].

demonstrating clear intensity-difference squeezing. Squeezing was not observed at very low frequencies due to technical noise in the pump laser. The on-chip OPOs used in [333] can, in principle, generate large squeezing factors over broad bandwidths due to their highly overcoupled design. The squeezing factor degraded linearly with increasing attenuation and the intensity-difference noise approached the shot noise level for high attenuation, as is typical of squeezed states (Fig. 58(b)). Higher intrinsic Q-factors [143] would help in lowering the oscillation threshold, possibly reaching much stronger noise reductions in this platform. Note that the squeezing in [333] was achieved in the MHz range only because of limitations in bandwidth of the low dark-noise detectors.

9. Conclusions

Micro-combs, namely optical frequency combs in micro-resonators, have been shown to be an exceptionally active field of research, with many conceptual advances in nonlinear physics and technological breakthroughs demonstrated only in the past few years. These developments have capitalised on the great scientific effort that brought optical micro-cavity technologies to maturity two decades ago, both for the case of bulk resonators and for CMOS-compatible integrated resonators. These devices have already made their way to commercialisation as sensors or filters. Moreover, the fundamental dynamics of micro-comb sources are based on the interplay of Kerr nonlinearity and optical dispersion — physical effects that are common to many micro-cavity platforms. This underlying background, as reviewed in Sections 2 and 3, has provided an excellent motivation for investigating micro-resonator-based sources, to bring a new generation of practical, cheap and low-power consumption sources to the photonics community. The potential of these multiple wavelength oscillators to realise compact and high-performance optical frequency comb generators for metrology and telecom applications was already evident in the first experimental demonstration of large bandwidth optical parametric oscillators, which we summarised in detail in Section 4. These sources were generally obtained by resonantly pumping micro-resonators and

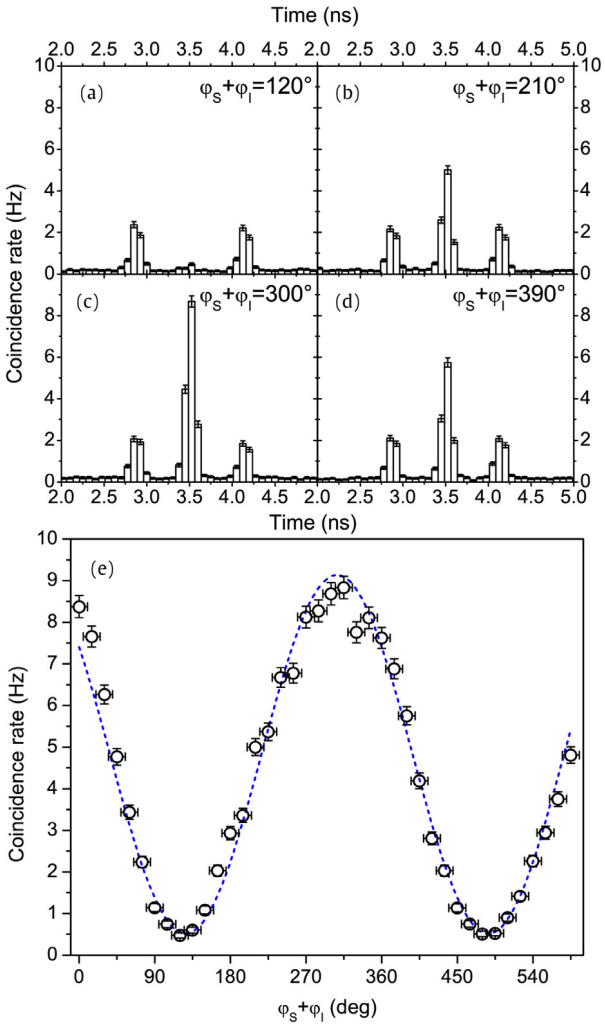

Fig. 56. Entanglement between signal and idler photons. (a–d) Histograms of the coincidence rate for four different phase settings. (e) Two-photon interference of the double interferometer configuration: the coincidence count rate of the central peak is plotted as a function of the phase $\phi_s + \phi_i$. The integration time is 120 s for each point and the pump power is 1.5 mW. The dotted black curve is a best fit of the experimental data. After Ref. [326].

inducing four-wave mixing optical parametric generation. The extremely large bandwidths of the parametric gain, which in compact micro-cavities could be obtained at pump power levels in the order of only 100 mW, have raised the hope of the scientific community that micro-resonators could provide a means of achieving coherent octave-spanning combs in a compact footprint to be used for the f–2f interferometry scheme developed by Theodore Hänsch and John Hall with their respective groups [1–5,282]. Recent progress in the stabilisation of these sources has raised the possibility of many interesting scientific and technological applications. The complex issue of the coherence of the micro-combs has motivated substantial and important theoretical developments, as discussed in Section 5. The Lugiato–Lefever equation has proved to be an effective tool for micro-comb modelling which has pushed the experimental field towards the demonstration of temporal cavity solitons. The control of the coherent generation and stabilisation of the solitary solutions has generated a set of important developments, starting from the generation of dark pulses to the demonstration of alternative techniques for micro-comb generation, such as parametrical seeding and filter-driven four-wave mixing, discussed in Section 6. It is very important to underline that a different portfolio of technologies has proved to be effective for comb generation, with a particular focus on crystal and glass bulk resonators that possess the best Q-factors demonstrated thus far, as well as silicon nitride and oxinitride technologies for their potential as on-chip optical sources. At the same time, silicon, incapable of supporting parametric oscillation in the telecom band because of two-photon absorption and free-carrier effects, has opened up new possibilities in the mid-IR at frequency ranges where the two-photon absorption vanishes. These developments have paved the way for the demonstration of many advances in metrology, starting from the first realisation of a reference-stabilised clock to the recent demonstration of a 2/3 octave-spanning coherent comb, as well as a number of other interesting

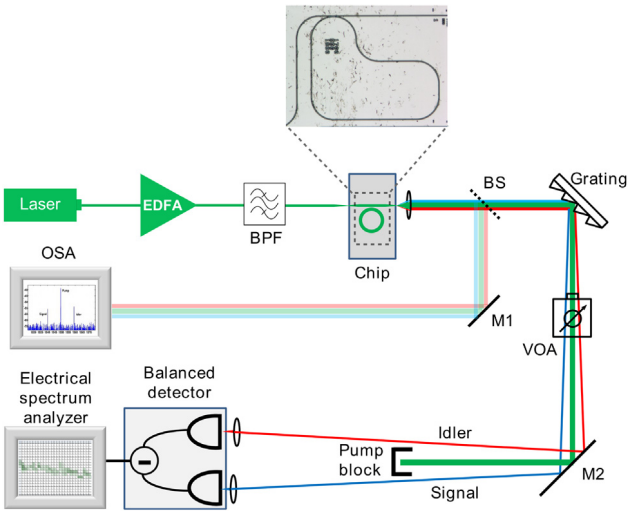

Fig. 57. Experimental set-up for squeezed state generation. The on-chip micro-ring resonator was pumped by a CW laser followed by an EDFA and a bandpass filter (BPF). To ensure efficient coupling in and out of the chip, inverse tapers, together with a lensed fibre, were used. The output of the waveguide was collected with a high-NA objective lens. The diffraction grating spatially separated the pump and the twin beams. After blocking the pump, the beams were focused onto a balanced detector. The RF output of the balanced detector was sent to an RF spectrum analyser. A small fraction of the beams was sent to an OSA to monitor the onset of parametric oscillation. The inset shows a microscope image of the ring-resonator coupled to the bus waveguide. The shape of the fabricated ring is noncircular to fit the resonator within one field of the electron-beam lithography tool, thus avoiding stitching errors. VOA: Variable optical attenuator. M1, M2: Mirrors. BS: Beam splitter. After Ref. [333].

achievements in the fields of radio-frequency photonics and optical telecommunications. Finally, a new and exciting chapter is opening for these devices in terms of quantum optical micro-combs. New applications, such as the recent demonstration of a source of multiple-entangled photons, have appeared in the literature. Clearly, the results summarised in Section 8, as indeed in all of this review, will prove to be just the beginning of this new and exciting field.

Acknowledgements

A.P. and M.P. acknowledge the support of the U.K. Quantum Technology Hub for Sensors and Metrology, EPSRC, under Grant EP/M013294/1, of the Marie Curie Action MC-CIG and IIF REA grant 630833 and 327627.

L.R. is grateful for financial support from the Natural Sciences and Engineering Research Council (NSERC) of Canada.

D.M. acknowledges support from Australian Research Council Discovery Projects scheme (DP150104327).

M.E. acknowledges support from the Marsden Fund and the Rutherford Discovery Fellowships of the Royal Society of New Zealand.

Y. K. C. would like to acknowledge funding from the European Research Council (ERC) through the projects NextPhase (StG 278616) & Versyt (PoC 632108), from the *Centre National d'Etudes Spatiales* (CNES) through the project SHYRO and from the Labex ACTION. T.H. and S.W. acknowledge support from Ministero dell'Istruzione, dell'Università e della Ricerca (MIUR) (PRIN-2015KEZNYM).

X.X. and A.M.W. acknowledge funding from National Science Foundation under grant ECCS-1509578, by the Air Force Office of Scientific Research under grant FA9550-15-1-0211 and by the DARPA PULSE program through grant W31P40-13-1-0018 from AMRDEC. X.X. is also supported by the National Natural Science Foundation of China under grant 6169190011, 6169190012, 61420106003 and the Beijing Natural Science Foundation under grant 4172029.

R.M. acknowledges support by the Natural Sciences and Engineering Research Council of Canada (NSERC) through the Steacie (411724-2011), Strategic (STPGP 478876-15), Discovery (RGPIN-2014-06093) and Acceleration (462548-2014) Grants Schemes, by the MESI PSR-SIIRI Initiative (PSR-SIIRI-952) in Quebec and by the Canada Research Chair Program (950-23138). Furthermore, he is grateful for additional support from the Government of the Russian Federation through the ITMO Fellowship and Professorship Program (grant 074-U 01) and from the 1000 Talents Sichuan Program in China.

Appendix A. Derivation of reciprocity theorem in terms of the resonator eigenmodes

The reciprocity theorem is obtained from the requirement that the individual modes and the full field be simultaneous solutions of Maxwell's equations. This can be found in many electromagnetic textbooks. For the benefit of the readers, here we report the derivation within the formalism of Section 3, explicitly expressing it in terms of the resonator eigenmodes $\mathbf{E}_\ell, \mathbf{H}_\ell$. From the vector identity $\nabla \cdot (\mathbf{A} \times \mathbf{B}) = (\nabla \times \mathbf{A}) \cdot \mathbf{B} - (\nabla \times \mathbf{B}) \cdot \mathbf{A}$ it follows that

$$\nabla \cdot (\mathbf{H} \times \mathbf{E}_\ell^*) = (\nabla \times \mathbf{H}) \cdot \mathbf{E}_\ell^* - (\nabla \times \mathbf{E}_\ell^*) \cdot \mathbf{H}, \tag{77}$$

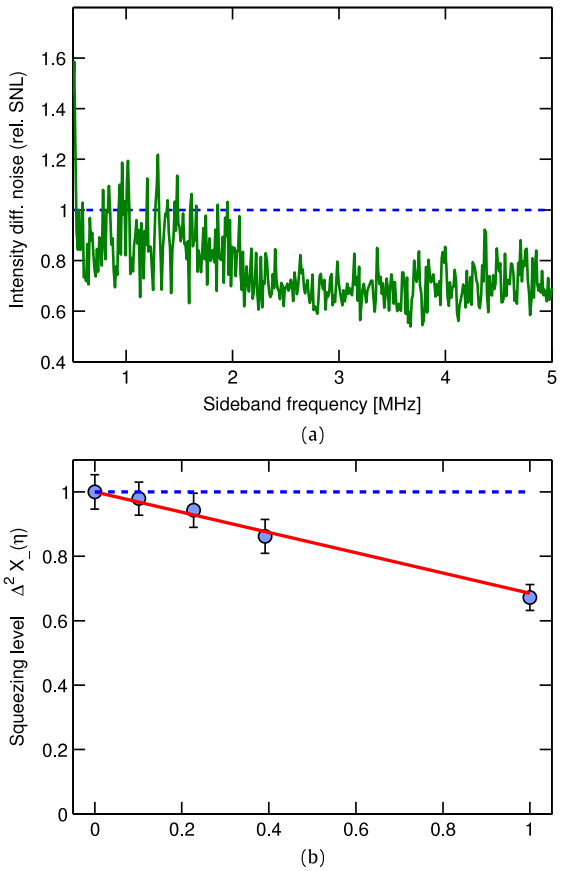

Fig. 58. Intensity-difference squeezing. (a) The variance of the signal and idler photo-current difference normalised to the shot noise level (SNL) on a linear scale. The dashed line at 1 represents the SNL and the solid line represents the intensity difference fluctuations. The dark-noise clearance is 16 dB at 0.5 MHz and decreases to 5 dB at 5 MHz. The data was taken with a pump power of 93 mW. The power in the signal and idler beams was 45 μW. (b) Variation of squeezing with attenuation at a sideband frequency of 3 MHz. The *x* axis is the transmittivity of the variable optical attenuator. The *y* axis is the intensity-difference noise in shot noise units, that is, the variance of the signal and idler photo-current difference compared to the shot noise level. Error bars are determined from the standard deviation of the measured data points. After Ref. [333].

$$\nabla \cdot (\mathbf{E} \times \mathbf{H}_\ell^*) = (\nabla \times \mathbf{E}) \cdot \mathbf{H}_\ell^* - (\nabla \times \mathbf{H}_\ell^*) \cdot \mathbf{E}, \tag{78}$$

and subtracting these two relations while integrating over the volume gives

$$\begin{aligned} &\int_V \left[\left((\nabla \times \mathbf{H}) \cdot \mathbf{E}_\ell^* - (\nabla \times \mathbf{E}_\ell^*) \cdot \mathbf{H} \right) - \left((\nabla \times \mathbf{E}) \cdot \mathbf{H}_\ell^* - (\nabla \times \mathbf{H}_\ell^*) \cdot \mathbf{E} \right) \right] dV \\ &= \int_V \left[\nabla \cdot (\mathbf{H} \times \mathbf{E}_\ell^*) - \nabla \cdot (\mathbf{E} \times \mathbf{H}_\ell^*) \right] dV = \oint_S \left(\mathbf{H} \times \mathbf{E}_\ell^* - \mathbf{E} \times \mathbf{H}_\ell^* \right) \cdot ds \approx 0, \end{aligned} \tag{79}$$

where we have used the divergence theorem in the penultimate step to pass to a surface integral. The last integral may be neglected since it represents a cross-flux of power in the outer surface and is zero for confined resonator modes. The reciprocity theorem Eq. (14), expressed in terms of the micro-cavity eigenmodes, is now obtained by substituting the curl operators in the first integral for the RHS of Eqs. (1), (5):

$$\begin{aligned} &\int_V \left[\frac{\partial \mathbf{D}}{\partial t} \cdot \mathbf{E}_\ell^* + i\omega_\ell \varepsilon_0 \epsilon(\mathbf{r}, \omega_\ell) \mathbf{E} \cdot \mathbf{E}_\ell^* \right] dV + \mu_0 \int_V \left[\frac{\partial \mathbf{H}}{\partial t} \cdot \mathbf{H}_\ell^* + i\omega_\ell \mathbf{H} \cdot \mathbf{H}_\ell^* \right] dV \\ &= - \int_V \frac{\partial \mathbf{P}^{\Delta}}{\partial t} \cdot \mathbf{E}_\ell^* dV. \end{aligned} \tag{80}$$

Appendix B. Eigenmodes and eigenfrequencies: the case of the spherical resonator

The spatial problem aims to determine the eigenmodes and the eigenfrequencies of the resonator cavity. As an instructive example, the simplest WGM resonator is undoubtedly the sphere, about which many studies have been performed in the

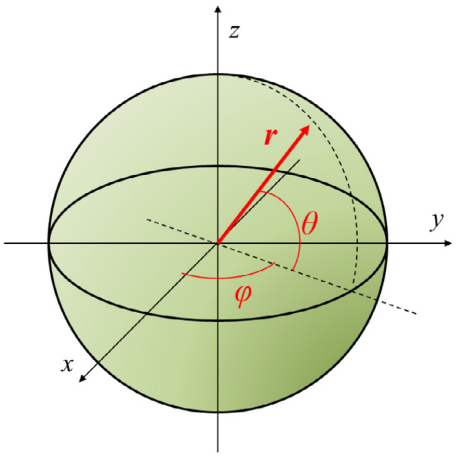

Fig. 59. Diagram of a spherical resonator with the associated Cartesian and polar axis with respect to the equatorial plane.

last few decades. This textbook case provides a brief overview of the modal structure in WGM resonators and allows for a deep understanding of the phenomena of interest.

B.1. Spherical resonator

Here, we consider a situation where the resonator is a sphere of radius a, made of a material with refractive index n_0. We start from the eigenmode Eq. (6), with $\epsilon(r) = n_0^2$ for $r \leq a$ and 1 for $r > a$. This equation can be solved exactly in spherical coordinates, r, θ, ϕ, where the angles θ and ϕ stand for the co-latitude and for the longitude, respectively, and $\hat{\mathbf{e}}_r, \hat{\mathbf{e}}_\theta, \hat{\mathbf{e}}_\phi$ are the spherical unit vectors (see Fig. 59).

In the following, we use l, m, n as separate indices of the mode numbers. The eigenmode solutions are also distinct in two polarisations, TE or TM. For a spherical resonator, TE/TM modes do not possess any significant electric (magnetic) component along the radial direction $\hat{\mathbf{e}}_r$. Each mode set has an associated eigenvalue k_{lnp}, where p stands for either TE or TM. The resonant wavelength in vacuum of each mode is $2\pi/k_{lnp}$ and the frequency is $\omega_{lnp} = k_{lnp}c$. Note that the eigenfrequencies depend only on two mode numbers (l, n) for each polarisation in this specific problem. For the two polarisations, the modes are found to be [355]

$$\mathbf{e}_{\ell mn,TE}(\mathbf{r}) = \frac{e^{im\phi}}{k_{\ell np} r} S_{\ell np}(r)\mathbf{X}_{\ell m}(\theta), \tag{81}$$

$$\mathbf{e}_{\ell mn,TM}(\mathbf{r}) = \frac{e^{im\phi}}{k_{\ell np}^2 n_0^2}\left\{\frac{1}{r}\frac{d}{dr}S_{\ell np}(r)\mathbf{Y}_{\ell m}(\theta) + \frac{1}{r^2}S_{\ell np}(r)\mathbf{Z}_{\ell m}(\theta)\right\}. \tag{82}$$

The spherical vectors are defined in terms of Legendre polynomials [356]

$$\begin{aligned}
\mathbf{X}_{\ell m}(\theta) &= i\frac{m}{\sin\theta}\mathrm{P}_\ell^m(\cos\theta)\,\hat{\mathbf{e}}_\theta - \frac{\partial}{\partial\theta}\mathrm{P}_\ell^m(\cos\theta)\,\hat{\mathbf{e}}_\phi \\
\mathbf{Y}_{\ell m}(\theta) &= \frac{\partial}{\partial\theta}\mathrm{P}_\ell^m(\cos\theta)\,\hat{\mathbf{e}}_\theta - i\frac{m}{\sin\theta}\mathrm{P}_\ell^m(\cos\theta)\,\hat{\mathbf{e}}_\phi, \\
\mathbf{Z}_{\ell m}(\theta) &= \ell(\ell+1)\mathrm{P}_\ell^m(\cos\theta)\,\hat{\mathbf{e}}_r\,.
\end{aligned} \tag{83}$$

The functions $\mathrm{P}_\ell^m(\cos\theta)$ are the associated Legendre polynomials, the mode indices m and ℓ need to fulfil $-\ell \leq m \leq \ell$. The function $S_{\ell np}$ is the radial Debye potential, which is such that $S_{\ell np}(r) = \psi_\ell(n_0 k_{\ell np} r)$ when $r \leq a$.

The eigenvalue $k_{\ell np}$ can now be found as the nth solution of the algebraic equation

$$\frac{\chi_\ell'(k_{\ell np}a)}{\chi_\ell(k_{\ell np}a)} = p\frac{\psi_\ell'(k_{\ell np}a)}{\psi_\ell(k_{\ell np}a)} \quad \text{with} \quad p = \begin{cases} n_0 & \text{for TE modes} \\ 1/n_0 & \text{for TM modes,} \end{cases} \tag{84}$$

while ψ_ℓ and χ_ℓ are the ℓ-th order Riccati–Bessel functions. For all practical purposes, it can be considered that $S_{\ell np}(r)$ decays exponentially outside the resonator, with a characteristic length that is of the order of the wavelength $2\pi/k_{\ell np}$. Note that here we are in the régime of strong index contrast.

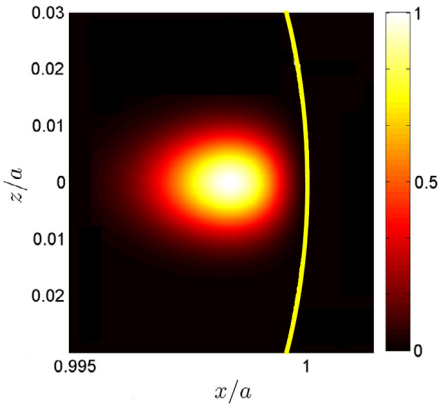

Fig. 60. Eigenmode distribution of the fundamental TE WGM, with mode number $l = 14\,350$ at 1.5605 μm in a spherical CaF_2 resonator with radius $a = 2.5$ mm. The mode has equal polar and azimuthal eigenvalues and is localised in a narrow region near the equator of the sphere. The right bar shows the magnitude of the intensity.

B.2. Eigenmode families: polarisation and spatial profile

Most resonators will, depending on geometry, support multiple mode families. Mode families can be separated according to polarisation, such as TE/TM modes, and in terms of fundamental versus higher-order modes. The most familiar and important mode families are provided by the (quasi) TE/TM modes. As also seen for the case of a spherical resonator in the previous sub-section, their names refer to the fact that either the electric or magnetic field is (mostly) contained in the plane that is perpendicular to a specific direction (e.g. the radial vector of the sphere in a spherical resonator). The TE and TM modes usually have different effective refractive indices and different dispersion properties due the geometric contribution to the effective index. They can also experience different confinement and loss. When designing micro-resonators, it is important to consider which mode polarisation one wants to work with and optimise coupling and dispersion properties for that family. TE/TM modes also have cut-off frequencies, below which no resonances are present: these can be important to consider in order to suppress coupling to higher order modes within the same family. Modes with different polarisations are orthogonal, provided that their frequencies are nondegenerate but can still interact with each other due to scattering interactions, such as the Raman effect.

Depending on the eigennumbers ℓ, m and n, the eigenmodes can have very different spatial distributions. The most important family in a spherical cavity corresponds to the cavity modes for which the electric field is strongly confined in a narrow torus near the equatorial circle and is quasi-null everywhere else. Mathematically, this configuration corresponds to the fundamental radial mode $n = 1$ with large, but equal, polar and azimuthal eigenvalues ($m \equiv \ell \gg 1$). It can be shown from Eqs. (83) that the TE mode becomes asymptotically parallel to $\hat{\mathbf{e}}_\theta$, while the TM mode becomes parallel to $\hat{\mathbf{e}}_r$. Therefore, the eigenmodes only depend on two parameters: the angular eigenvalue ℓ, which is a degenerate scalar parameter, and the vectorial polarisation p, standing for TE or TM modes.

In the fundamental family ($n = 1$), the solutions $\mathbf{e}_{\ell p}(\mathbf{r})$ of Eq. (6) are simply expressed as the normalised TE/TM fields following

$$\bar{\mathbf{e}}_{\ell,TE}(\mathbf{r}) = \frac{\mathbf{e}_{\ell\ell 1,TE}}{N_{\ell,TE}} \quad \text{and} \quad \bar{\mathbf{e}}_{\ell,TM}(\mathbf{r}) = \frac{\mathbf{e}_{\ell\ell 1,TM}}{N_{\ell,TM}}\,, \tag{85}$$

where the normalisation constants $N_{\ell p}$ are obtained from the condition

$$\int_V \bar{\mathbf{e}}^*_{\ell p}(\mathbf{r}) \cdot \bar{\mathbf{e}}_{\ell' p'}(\mathbf{r})\, dV = \delta_{\ell,\ell'}\delta_{p,p'} V_{\ell p}\,. \tag{86}$$

The spatial profiles (see Fig. 60) allow for the calculation of important parameters, such as the modal volume.

B.3. Eigenfrequencies and modal dispersion

The eigenfrequencies of a WGM resonator are generally not equidistant. This non-equidistance arises from dispersion, which has two main contributions. The first one is generally referred to as the geometrical dispersion, which originates from the geometrical shape of the resonator itself. For example, in the case of a sphere, the eigenfrequencies in the fundamental family of modes can be approximated as [357]

$$\begin{aligned}\omega_{\ell p} &= k_{\ell 1 p} \cdot c \\ &= \frac{c}{n_0\, a}\left\{\left[\ell + \frac{1}{2}\right] + \xi_1\left[\frac{\ell + \frac{1}{2}}{2}\right]^{1/3} - \frac{p}{\sqrt{n_0^2 - 1}} + \frac{3}{20}\xi_1^2\left[\frac{\ell + \frac{1}{2}}{2}\right]^{-1/3} + \mathcal{O}\left[\ell + \frac{1}{2}\right]^{-2/3}\right\},\end{aligned} \tag{87}$$

where p is polarisation dependent, as explicitly defined in Eq. (84), while ξ_n is the nth root of the Airy function $\mathrm{Ai}(-z)$ and corresponds to the nth radial order ($\xi_1 = 2.338$ for $n = 1$).

The second contribution arises from the chromatic dispersion of the bulk material of the resonator. This contribution can be accurately evaluated by using the dependence of the refractive index from the frequency, e.g. a Sellmeier expansion, whenever it is tabulated.

References

[1] R. Holzwarth, T. Udem, T. Hänsch, J. Knight, W. Wadsworth, P. Russell, Optical frequency synthesizer for precision spectroscopy, Phys. Rev. Lett. 85 (2000) 2264–2267.
[2] D.J. Jones, S.A. Diddams, J.K. Ranka, Carrier-envelope phase control of femtosecond mode-locked lasers and direct optical frequency synthesis, Science 288 (2000) 635–639.
[3] T. Udem, R. Holzwarth, T.W. Hänsch, Optical frequency metrology, Nature 416 (2002) 233–237.
[4] S.T. Cundiff, J. Ye, Colloquium: Femtosecond optical frequency combs, Rev. Modern Phys. 75 (2003) 325–342.
[5] T.W. Hänsch, Passion for Precision, Nobel Lecture, 2005.
[6] K.J. Vahala, Optical microcavities, Nature 424 (2003) 839–846.
[7] S. Spillane, T. Kippenberg, K. Vahala, Ultralow-threshold Raman laser using a spherical dielectric microcavity, Nature 415 (2002) 621–623.
[8] P. Del'Haye, A. Schliesser, O. Arcizet, T. Wilken, R. Holzwarth, T.J. Kippenberg, Optical frequency comb generation from a monolithic microresonator, Nature 450 (2007) 1214–1217.
[9] P. Del'Haye, O. Arcizet, A. Schliesser, R. Holzwarth, T.J. Kippenberg, Full stabilization of a microresonator-based optical frequency bomb, Phys. Rev. Lett. 101 (2008) 053903.
[10] F. Ferdous, H. Miao, D.E. Leaird, K. Srinivasan, J. Wang, L. Chen, L.T. Varghese, A.M. Weiner, Spectral line-by-line pulse shaping of on-chip microresonator frequency combs, Nature Photon. 5 (2011) 770–776.
[11] J. Levy, A. Gondarenko, M. Foster, A. Turner-Foster, A. Gaeta, M. Lipson, CMOS-compatible multiple-wavelength oscillator for on-chip optical interconnects, Nature Photon. 4 (2010) 37–40.
[12] L. Razzari, D. Duchesne, M. Ferrera, R. Morandotti, S. Chu, B. Little, D. Moss, CMOS-compatible integrated optical hyper-parametric oscillator, Nature Photon. 4 (2010) 41–45.
[13] T. Herr, K. Hartinger, J. Riemensberger, Universal formation dynamics and noise of Kerr-frequency combs in microresonators, Nature Photon. 6 (2012) 480–487.
[14] Q. Xu, B. Schmidt, S. Pradhan, M. Lipson, Micrometre-scale silicon electro-optic modulator, Nature 435 (2005) 325–327.
[15] M. Asghari, A. Krishnamoorthy, Silicon photonics: Energy-efficient communication, Nature Photon. 5 (2011) 268–270.
[16] H.J. Caulfield, S. Dolev, Why future supercomputing requires optics, Nature Photon. 4 (2010) 261–263.
[17] X. Chen, C. Li, H.K. Tsang, Device engineering for silicon photonics, NPG Asia Mater. 3 (2011) 34–40.
[18] Z. Jiang, C.-B. Huang, D.E. Leaird, A.M. Weiner, Optical arbitrary waveform processing of more than 100 spectral comb lines, Nature Photon. 1 (2007) 463–467.
[19] S.T. Cundiff, A.M. Weiner, Optical arbitrary waveform generation, Nature Photon. 4 (2010) 760–766.
[20] T. Kippenberg, S. Spillane, K. Vahala, Kerr-nonlinearity optical parametric oscillation in an ultrahigh-Q toroid microcavity, Phys. Rev. Lett. 93 (2004) 083904.
[21] A. Savchenkov, A. Matsko, D. Strekalov, M. Mohageg, V. Ilchenko, L. Maleki, Low threshold optical oscillations in a whispering gallery mode CaF 2 resonator, Phys. Rev. Lett. 93 (2004) 243905.
[22] A.B. Matsko, A.A. Savchenkov, W. Liang, V.S. Ilchenko, D. Seidel, L. Maleki, Mode-locked Kerr frequency combs, Opt. Lett. 36 (2011) 2845–2847.
[23] Y. Chembo, D. Strekalov, N. Yu, Spectrum and dynamics of optical frequency combs generated with monolithic whispering gallery mode resonators, Phys. Rev. Lett. 104 (2010) 103902.
[24] P. Del'Haye, T. Herr, E. Gavartin, M. Gorodetsky, R. Holzwarth, T. Kippenberg, Octave spanning tunable frequency comb from a microresonator, Phys. Rev. Lett. 107 (2011) 063901.
[25] Y. Okawachi, K. Saha, J.S. Levy, Y.H. Wen, M. Lipson, A.L. Gaeta, Octave-spanning frequency comb generation in a silicon nitride chip, Opt. Lett. 36 (2011) 3398–3400.
[26] A. Savchenkov, A. Matsko, W. Liang, V. Ilchenko, D. Seidel, L. Maleki, Kerr combs with selectable central frequency, Nature Photon. 5 (2011) 293–296.
[27] C.Y. Wang, T. Herr, P. Del'Haye, A. Schliesser, J. Hofer, R. Holzwarth, T.W. Hänsch, N. Picqu, T.J. Kippenberg, Mid-infrared optical frequency combs at 2.5 μm based on crystalline microresonators, Nature Commun. 4 (2013) 1345.
[28] S. Coen, M. Erkintalo, Universal scaling laws of Kerr frequency combs, Opt. Lett. 38 (2013) 1790–1792.
[29] K. Ikeda, Multiple-valued stationary state and its instability of the transmitted light by a ring cavity system, Opt. Commun. 30 (1979) 257–261.
[30] K. Ikeda, H. Daido, O. Akimoto, Optical turbulence: chaotic behavior of transmitted light from a ring cavity, Phys. Rev. Lett. 45 (1980) 709–712.
[31] D.W. Mc Laughlin, J.V. Moloney, A.C. Newell, Solitary waves as fixed points of infinite-dimensional maps in an optical bistable ring cavity, Phys. Rev. Lett. 51 (1983) 75.
[32] D.W. McLaughlin, J.V. Moloney, A.C. Newell, New class of instabilities in passive optical cavities, Phys. Rev. Lett. 54 (1985) 681.
[33] L.A. Lugiato, R. Lefever, Spatial dissipative structures in passive optical systems, Phys. Rev. Lett. 58 (1987) 2209–2211.
[34] D.J. Kaup, A.C. Newell, Theory of nonlinear oscillating dipolar excitations in one-dimensional condensates, Phys. Rev. B 18 (10) (1978) 5162.
[35] K. Nozaki, N. Bekki, Chaos in a perturbed nonlinear Schrödinger equation, Phys. Rev. Lett. 50 (1983) 1226.
[36] K. Nozaki, N. Bekki, Low dimensional chaos in a driven damped nonlinear Schrödinger equation, Physica D 21 (1986) 381–393.
[37] M. Haelterman, S. Trillo, S. Wabnitz, Dissipative modulation instability in a nonlinear dispersive ring cavity, Opt. Commun. 91 (1992) 401–407.
[38] M. Haelterman, S. Trillo, S. Wabnitz, Additive-modulation-instability ring laser in the normal dispersion regime of a fiber, Opt. Lett. 17 (1992) 745–747.
[39] S. Wabnitz, Suppression of interactions in a phase-locked soliton optical memory, Opt. Lett. 18 (1993) 601–603.
[40] F. Arecchi, Optical morphogenesis: pattern formation and competition in nonlinear optics, Physica D 86 (1995) 297–322.
[41] E. Pampaloni, S. Residori, S. Soria, F.T. Arecchi, Phase locking in nonlinear optical patterns, Phys. Rev. Lett. 78 (1997) 1042–1045.
[42] A. Schreiber, B. Thring, M. Kreuzer, T. Tschudi, Experimental investigation of solitary structures in a nonlinear optical feedback system, Opt. Commun. 136 (1997) 415–418.
[43] S. Barland, J.R. Tredicce, M. Brambilla, L.A. Lugiato, S. Balle, M. Giudici, T. Maggipinto, L. Spinelli, G. Tissoni, T. Knödl, M. Miller, R. Jäger, Cavity solitons as pixels in semiconductor microcavities, Nature 419 (2002) 699–702.
[44] L. Lugiato, F. Prati, M. Brambilla, Nonlinear Optical Systems, Cambridge University Press, 2015.
[45] F. Leo, S. Coen, P. Kockaert, S.-P. Gorza, P. Emplit, M. Haelterman, Temporal cavity solitons in one-dimensional Kerr media as bits in an all-optical buffer, Nature Photon. 4 (2010) 471–476.

[46] S. Coen, H.G. Randle, T. Sylvestre, M. Erkintalo, Modeling of octave-spanning Kerr frequency combs using a generalized mean-field Lugiato-Lefever model, Opt. Lett. 38 (2013) 37–39.
[47] Y.K. Chembo, C.R. Menyuk, Spatiotemporal Lugiato-Lefever formalism for Kerr-comb generation in whispering-gallery-mode resonators, Phys. Rev. A 87 (2013) 053852.
[48] T. Hansson, D. Modotto, S. Wabnitz, Dynamics of the modulational instability in microresonator frequency combs, Phys. Rev. A 88 (2013) 023819.
[49] K. Saha, Y. Okawachi, B. Shim, J.S. Levy, R. Salem, A.R. Johnson, M.A. Foster, M.R.E. Lamont, M. Lipson, A.L. Gaeta, Modelocking and femtosecond pulse generation in chip-based frequency combs, Opt. Express 21 (2013) 1335–1343.
[50] T. Herr, V. Brasch, J.D. Jost, C.Y. Wang, N.M. Kondratiev, M.L. Gorodetsky, T.J. Kippenberg, Temporal solitons in optical microresonators, Nature Photon. 8 (2014) 145–152.
[51] X. Xue, Y. Xuan, Y. Liu, P.-H. Wang, S. Chen, J. Wang, D.E. Leaird, M. Qi, A.M. Weiner, Mode-locked dark pulse Kerr combs in normal-dispersion microresonators, Nature Photon. 9 (2015) 594–600.
[52] P. Del'Haye, S.B. Papp, S.A. Diddams, Hybrid electro-optically modulated microcombs, Phys. Rev. Lett. 109 (2012) 263901.
[53] S.B. Papp, P. Del'Haye, S.A. Diddams, Parametric seeding of a microresonator optical frequency comb, Opt. Express 21 (2013) 17615–17624.
[54] S.B. Papp, K. Beha, P. Del'Haye, H. Quinlan, F. Lee, K.J. Vahala, S.A. Diddams, Microresonator frequency comb optical clock, Optica 1 (2014) 10–14.
[55] P. Del'Haye, K. Beha, S.B. Papp, S.A. Diddams, Self-injection locking and phase-locked states in microresonator-based optical frequency combs, Phys. Rev. Lett. 112 (2014) 043905.
[56] A. Savchenkov, D. Eliyahu, W. Liang, V. Ilchenko, J. Byrd, A. Matsko, D. Seidel, L. Maleki, Stabilization of a Kerr frequency comb oscillator, Opt. Lett. 38 (2013) 2636–2639.
[57] A. Pasquazi, L. Caspani, M. Peccianti, M. Clerici, M. Ferrera, L. Razzari, D. Duchesne, B.E. Little, S.T. Chu, D.J. Moss, R. Morandotti, Self-locked optical parametric oscillation in a CMOS compatible microring resonator: a route to robust optical frequency comb generation on a chip, Opt. Express 21 (2013) 13333–13341.
[58] M. Peccianti, A. Pasquazi, Y. Park, B. Little, S. Chu, D. Moss, R. Morandotti, Demonstration of a stable ultrafast laser based on a nonlinear microcavity, Nature Commun. 3 (2012) 765.
[59] A. Pasquazi, M. Peccianti, B. Little, S. Chu, D. Moss, R. Morandotti, Stable, dual mode, high repetition rate modelocked laser based on a microring resonator, Opt. Express 20 (2012) 27355–27362.
[60] J. Pfeifle, V. Brasch, M. Lauermann, Y. Yu, D. Wegner, T. Herr, K. Hartinger, P. Schindler, J. Li, D. Hillerkuss, R. Schmogrow, C. Weimann, R. Holzwarth, W. Freude, J. Leuthold, T.J. Kippenberg, C. Koos, Coherent terabit communications with microresonator Kerr frequency combs, Nature Photon. 8 (2014) 375–380.
[61] J.S. Levy, K. Saha, Y. Okawachi, M. Foster, A. Gaeta, M. Lipson, High-performance silicon-nitride-based multiple-wavelength source, IEEE Photon. Technol. Lett. 24 (2012) 1375–1377.
[62] W. Liang, D. Eliyahu, V. Ilchenko, A. Savchenkov, A. Matsko, D. Seidel, L. Maleki, High spectral purity Kerr frequency comb radio frequency photonic oscillator, Nature Commun. 6 (2015) 7957.
[63] X. Xue, Y. Xuan, H.-J. Kim, J. Wang, D.E. Leaird, M. Qi, A.M. Weiner, Programmable single-bandpass photonic RF filter based on Kerr comb from a microring, J. Lightw. Technol. 4 (2014) 3557–3565.
[64] T.G. Nguyen, M. Shoeiby, S.T. Chu, B.E. Little, R. Morandotti, A. Mitchell, D.J. Moss, Integrated frequency comb source based Hilbert transformer for wideband microwave photonic phase analysis, Opt. Express 23 (2015) 22087.
[65] V. Lefèver-Seguin, S. Haroche, Towards cavity-QED experiments with silica microspheres, Mater. Sci. Eng. B-Solid 48 (1997) 53–58.
[66] V. Ilchenko, A. Matsko, Optical resonators with whispering-gallery modes - Part II: Applications, IEEE J. Sel. Top. Quantum Electron. 12 (2006) 15–32.
[67] S. Feng, T. Lei, H. Chen, H. Cai, X. Luo, A. Poon, Silicon photonics: from a microresonator perspective, Laser Photonics Rev. 6 (2012) 145–177.
[68] A.B. Matsko, V.S. Ilchenko, Optical resonators with whispering-gallery modes-part I: basics, IEEE J. Sel. Top. Quantum Electron. 12 (2006) 3–14.
[69] Y. Yomomoto, R. Slusher, Optical processes in microcavities, Phys. Today 46 (1993) 66–73.
[70] H. Haus, Waves and Fields in Optoelectronics, in: Prentice-Hall Series in Solid State Physical Electronics, 1984.
[71] B. Little, S. Chu, H. Haus, J. Foresi, J.-P. Laine, Microring resonator channel dropping filters, J. Lightw. Technol. 15 (1997) 998–1005.
[72] C. Doerr, L. Stulz, M. Cappuzzo, E. Laskowski, A. Paunescu, L. Gomez, J. Gates, S. Shunk, A. White, 40-Wavelength add-drop filter, IEEE Photon. Technol. Lett. 11 (1999) 1437–1439.
[73] K. Djordjev, S.-J. Choi, S.-J. Choi, P. Dapkus, Microdisk tunable resonant filters and switches, IEEE Photon. Technol. Lett. 14 (2002) 828–830.
[74] H. Nishihara, M. Haruna, T. Suhara, Optical Integrated Circuits, in: McGraw-Hill Optical and Electro-Optical Engineering Series, McGraw-Hill, 1989.
[75] Y. Hibino, Passive optical devices for photonic networks, IEICE Trans. Commun. E83-B (2000) 2178–2190.
[76] B. Offrein, R. Germann, F. Horst, H. Salemink, R. Beyeler, G. Bona, Resonant coupler-based tunable add-after-drop filter in silicon-oxynitride technology for WDM networks, IEEE J. Sel. Top. Quantum Electron. 5 (1999) 1400–1406.
[77] A. Serpengüzel, Amorphous silicon nitride microcavities, J. Opt. Soc. Amer. B 18 (2001) 989–993.
[78] B. Little, S. Chu, P. Absil, J. Hryniewicz, F. Johnson, F. Seiferth, D. Gill, V. Van, O. King, M. Trakalo, Very high-order microring resonator filters for WDM applications, IEEE Photon. Technol. Lett. 16 (2004) 2263–2265.
[79] M. Shaw, J. Guo, G. Vawter, S. Habermehl, C. Sullivan, Fabrication techniques for low-loss silicon nitride waveguides, Proc. SPIE 5720 (2005) 109–118.
[80] A. Campillo, J. Eversole, H. Lin, Cavity quantum electrodynamic enhancement of stimulated emission in microdroplets, Phys. Rev. Lett. 67 (1991) 437–440.
[81] F. Vollmer, D. Braun, A. Libchaber, M. Khoshsima, I. Teraoka, S. Arnold, Protein detection by optical shift of a resonant microcavity, Appl. Phys. Lett. 80 (2002) 4057–4059.
[82] S. Arnold, M. Khoshsima, I. Teraoka, S. Holler, F. Vollmer, Shift of whispering-gallery modes in microspheres by protein adsorption, Opt. Lett. 28 (2003) 272–274.
[83] V.B. Braginsky, M.L. Gorodetsky, V.S. Ilchenko, Quality-factor and nonlinear properties of optical whispering-gallery modes, Phys. Lett. A 137 (1989) 393–397.
[84] A.A. Savchenkov, A.B. Matsko, V.S. Ilchenko, L. Maleki, Optical resonators with ten million finesse, Opt. Express 15 (2007) 6768–6773.
[85] M.L. Gorodetsky, A.A. Savchenkov, V.S. Ilchenko, Ultimate Q of optical microsphere resonators, Opt. Lett. 21 (1996) 453–455.
[86] D. Armani, T. Kippenberg, S. Spillane, K. Vahala, Ultra-high-Q toroid microcavity on a chip, Nature 421 (2003) 925–928.
[87] A.M. Armani, Single molecule detection using optical microcavities, in: I. Chremmos, O. Schwelb, N. Uzunoglu (Eds.), Photonic Microresonator Research and Applications, in: Springer Series in Optical Science, vol. 156, Springer US, Boston, MA, 2010, pp. 253–273.
[88] V. Ilchenko, A. Savchenkov, A. Matsko, L. Maleki, Nonlinear optics and crystalline whispering gallery mode cavities, Phys. Rev. Lett. 92 (2004) 439031–439034.
[89] L. Maleki, A. Matsko, Lithium niobate whispering gallery resonators: applications and fundamental studies, in: P. Ferraro, S. Grilli, P. De Natale (Eds.), Ferroelectric Crystals for Photonic Applications, in: Springer Series in Materials Science, vol. 91, Springer, Berlin Heidelberg, 2009, pp. 337–383.
[90] B. Little, H. Haus, J. Foresi, L. Kimerling, E. Ippen, D. Ripin, Wavelength switching and routing using absorption and resonance, IEEE Photon. Technol. Lett. 10 (1998) 816–818.

[91] P. Dong, W. Qian, H. Liang, R. Shafiiha, D. Feng, G. Li, J.E. Cunningham, A.V. Krishnamoorthy, M. Asghari, Thermally tunable silicon racetrack resonators with ultralow tuning power, Opt. Express 18 (2010) 20298–20304.
[92] V. Almeida, C. Barrios, R. Panepucci, M. Lipson, All-optical control of light on a silicon chip, Nature 431 (2004) 1081–1084.
[93] A. Turner, M. Foster, A. Gaeta, M. Lipson, Ultra-low power parametric frequency conversion in a silicon microring resonator, Opt. Express 16 (2008) 4881–4887.
[94] M. Ferrera, L. Razzari, D. Duchesne, R. Morandotti, Z. Yang, M. Liscidini, J.E. Sipe, S. Chu, B.E. Little, D.J. Moss, Low-power continuous-wave nonlinear optics in doped silica glass integrated waveguide structures, Nature Photon. 2 (2008) 737–740.
[95] A.J. Maker, A.M. Armani, Fabrication of silica ultra high quality factor microresonators, J. Vis. Exp. 65 (2012) 4164.
[96] J.P. Laine, C. Tapalian, B. Little, H. Haus, Acceleration sensor based on high-Q optical microsphere resonator and pedestal antiresonant reflecting waveguide coupler, Sens. Actuat. A-Phys. 93 (2001) 1–7.
[97] V. Sandoghdar, F. Treussart, J. Hare, V. Lefèver-Seguin, J.-M. Raimond, S. Haroche, Very low threshold whispering-gallery-mode microsphere laser, Phys. Rev. A 54 (1996) R1777–R1780.
[98] M. Cai, O. Painter, K. Vahala, P. Sercel, Fiber-coupled microsphere laser, Opt. Lett. 25 (2000) 1430–1432.
[99] D.W. Vernooy, A. Furusawa, N.P. Georgiades, V.S. Ilchenko, H.J. Kimble, Cavity QED with high-Q whispering gallery modes, Phys. Rev. A 57 (1998) R2293–R2296.
[100] A. Serpengüzel, S. Arnold, G. Griffel, Excitation of resonances of microspheres on an optical fiber, Opt. Lett. 20 (1995) 654–656.
[101] M. Cai, O. Painter, K.J. Vahala, Observation of critical coupling in a fiber taper to a silica-microsphere whispering-gallery mode system, Phys. Rev. Lett. 85 (2000) 74–77.
[102] J.C. Knight, G. Cheung, F. Jacques, T.A. Birks, Phase-matched excitation of whispering-gallery-mode resonances by a fiber taper, Opt. Lett. 22 (1997) 1129–1131.
[103] V.S. Ilchenko, X.S. Yao, L. Maleki, Pigtailing the high-Q microsphere cavity: A simple fiber coupler for optical whispering-gallery modes, Opt. Lett. 24 (1999) 723–725.
[104] F. Treussart, N. Dubreuil, J.C. Knight, V. Sandoghdar, J. Hare, V. Lefèver-Seguin, J.-M. Raimond, S. Haroche, Microlasers based on silica microspheres, Ann. Telecommun. 52 (1997) 557–568.
[105] F. Treussart, V.S. Ilchenko, J.-F. Roch, J. Hare, V. Lefèver-Seguin, J.-M. Raimond, S. Haroche, Evidence for intrinsic Kerr bistability of high-Q microsphere resonators in superfluid helium, Eur. Phys. J. D 1 (1998) 235–238.
[106] A. Chiasera, Y. Dumeige, P. Feron, M. Ferrari, Y. Jestin, G. Nunzi Conti, S. Pelli, S. Soria, G.C. Righini, Spherical whispering-gallery-mode microresonators, Laser Photonics Rev. 4 (2010) 457–482.
[107] T.J. Kippenberg, S.M. Spillane, K.J. Vahala, Demonstration of ultra-high-Q small mode volume toroid microcavities on a chip, Appl. Phys. Lett. 85 (2004) 6113–6115.
[108] X. Zhang, H.S. Choi, A.M. Armani, Ultimate quality factor of silica microtoroid resonant cavities, Appl. Phys. Lett. 96 (2010) 153304.
[109] S.B. Papp, P. Del'Haye, S.A. Diddams, Mechanical control of a microrod-resonator optical frequency comb, Phys. Rev. X 3 (2013) 031003.
[110] A. Coillet, R. Henriet, K. Phan Huy, M. Jacquot, L. Furfaro, I. Balakireva, L. Larger, Y.K. Chembo, Microwave photonics systems based on whispering-gallery-mode resonators, J. Vis. Exp. 78 (2013) 50423.
[111] H. Tavernier, P. Salzenstein, K. Volyanskiy, Y.K. Chembo, L. Larger, Magnesium fluoride whispering gallery mode disk-resonators for microwave photonics applications, IEEE Photon. Technol. Lett. 22 (2010) 1629–1631.
[112] G. Lin, S. Diallo, R. Henriet, M. Jacquot, Y.K. Chembo, Barium fluoride whispering-gallery-mode disk-resonator with one billion quality-factor, Opt. Lett. 39 (2014) 6009–6012.
[113] R. Henriet, G. Lin, A. Coillet, M. Jacquot, L. Furfaro, L. Larger, Y.K. Chembo, Kerr optical frequency comb generation in strontium fluoride whispering-gallery mode resonators with billion quality factor, Opt. Lett. 40 (2015) 1567–1570.
[114] S. Diallo, G. Lin, R. Martineghi, L. Furfaro, M. Jacquot, Y.K. Chembo, Brillouin lasing in ultra-high Q lithium fluoride disk-resonators, IEEE Photon. Technol. Lett. 28 (2016) 955–958.
[115] K. Ikeda, R.E. Saperstein, N. Alic, Y. Fainman, Thermal and Kerr nonlinear properties of plasma-deposited silicon nitride/silicon dioxide waveguides, Opt. Express 16 (2008) 12987–12994.
[116] R. Won, M. Paniccia, Integrating silicon photonics, Nature Photon. 4 (2010) 498–499.
[117] T. Baehr-Jones, T. Pinguet, P. L. Guo-Qiang, S. Danziger, D. Prather, M. Hochberg, Myths and rumours of silicon photonics, Nature Photon. 6 (2012) 206–208.
[118] J. Leuthold, C. Koos, W. Freude, Nonlinear silicon photonics, Nature Photon. 4 (2010) 535–544.
[119] H. Rong, A. Liu, R. Jones, O. Cohen, D. Hak, R. Nicolaescu, A. Fang, M. Paniccia, An all-silicon Raman laser, Nature 433 (2005) 292–294.
[120] M.A. Foster, R. Salem, D.F. Geraghty, A.C. Turner-Foster, M. Lipson, A.L. Gaeta, Silicon-chip-based ultrafast optical oscilloscope, Nature 456 (2008) 81–84.
[121] C. Monat, B. Corcoran, D. Pudo, M. Ebnali-Heidari, C. Grillet, M.D. Pelusi, D.J. Moss, B.J. Eggleton, T.P. White, L. O'Faolain, T.F. Krauss, Slow light enhanced nonlinear optics in silicon photonic crystal waveguides, IEEE J. Sel. Top. Quantum Electron. 16 (2010) 344–356.
[122] R. Salem, M.A. Foster, A.C. Turner, D.F. Geraghty, M. Lipson, A.L. Gaeta, Signal regeneration using low-power four-wave mixing on silicon chip, Nature Photon. 2 (2008) 35–38.
[123] M.A. Foster, A.C. Turner, J.E. Sharping, B.S. Schmidt, M. Lipson, A.L. Gaeta, Broad-band optical parametric gain on a silicon photonic chip, Nature 441 (2006) 960–963.
[124] B. Kuyken, X. Liu, G. Roelkens, R. Baets, R.M. Osgood, W.M.J. Green, 50 dB parametric on-chip gain in silicon photonic wires, Opt. Lett. 36 (2011) 4401–4403.
[125] S. Zlatanovic, J.S. Park, S. Moro, J.M.C. Boggio, I.B. Divliansky, N. Alic, S. Mookherjea, S. Radic, Mid-infrared wavelength conversion in silicon waveguides using ultracompact telecom-band-derived pump source, Nature Photon. 4 (2010) 561–564.
[126] X. Liu, R.M. Osgood, Y.A. Vlasov, W.M. Green, Mid-infrared optical parametric amplifier using silicon nanophotonic waveguides, Nature Photon. 4 (2010) 557–560.
[127] N. Singh, D.D. Hudson, Y. Yu, C. Grillet, S.D. Jackson, A. Casas-Bedoya, A. Read, P. Atanackovic, S.G. Duvall, S. Palomba, B. Luther-Davies, S. Madden, D.J. Moss, B.J. Eggleton, Midinfrared supercontinuum generation from 2 to 6 μm in a silicon nanowire, Optica 2 (9) (2015) 797–802.
[128] S. Clemmen, K.P. Huy, W. Bogaerts, R.G. Baets, P. Emplit, S. Massar, Continuous wave photon pair generation in silicon-on-insulator waveguides and ring resonators, Opt. Express 17 (2009) 16558–16570.
[129] A. Liu, H. Rong, M. Paniccia, O. Cohen, D. Hak, Net optical gain in a low loss silicon-on-insulator waveguide by stimulated Raman scattering, Opt. Express 12 (2004) 4261–4268.
[130] F. Gholami, S. Zlatanovic, A. Simic, L. Liu, D. Borlaug, N. Alic, M.P. Nezhad, Y. Fainman, S. Radic, Third-order nonlinearity in silicon beyond 2350 nm, Appl. Phys. Lett. 99 (2011) 081102.
[131] Q. Lin, J. Zhang, G. Piredda, R.W. Boyd, P.M. Fauchet, G.P. Agrawal, Dispersion of silicon nonlinearities in the near infrared region, Appl. Phys. Lett. 91 (2007) 021111.
[132] M. Dinu, F. Quochi, H. Garcia, Third-order nonlinearities in silicon at telecom wavelengths, Appl. Phys. Lett. 82 (2003) 2954–2956.

[133] A.G. Griffith, R.K. Lau, J. Cardenas, Y. Okawachi, A. Mohanty, R. Fain, Y.H.D. Lee, M. Yu, C.T. Phare, C.B. Poitras, A.L. Gaeta, M. Lipson, Silicon-chip mid-infrared frequency comb generation, Nature Commun. 6 (2015) 6299.
[134] D.J. Moss, R. Morandotti, A.L. Gaeta, M. Lipson, New CMOS-compatible platforms based on silicon nitride and Hydex for nonlinear optics, Nature Photon. 7 (2013) 597–607.
[135] C.H. Henry, R.F. Kazarinov, H.J. Lee, K.J. Orlowsky, L.E. Katz, Low loss Si_3N_4 - SiO_2 optical waveguides on Si, Appl. Opt. 26 (1987) 2621–2624.
[136] D. Duchesne, M. Ferrera, L. Razzari, R. Morandotti, B.E. Little, S.T. Chu, D.J. Moss, Efficient self-phase modulation in low loss, high index doped silica glass integrated waveguides, Opt. Express 17 (2009) 1865–1870.
[137] Y. Liu, Y. Xuan, X. Xue, P.-H. Wang, S. Chen, A.J. Metcalf, J. Wang, D.E. Leaird, M. Qi, A.M. Weiner, Investigation of mode coupling in normal-dispersion silicon nitride microresonators for Kerr frequency comb generation, Optica 1 (2014) 137–144.
[138] A.R. Johnson, Y. Okawachi, J.S. Levy, J. Cardenas, K. Saha, M. Lipson, A.L. Gaeta, Chip-based frequency combs with sub-100 GHz repetition rates, Opt. Lett. 37 (2012) 875–877.
[139] J.S. Levy, M.A. Foster, A.L. Gaeta, M. Lipson, Harmonic generation in silicon nitride ring resonators, Opt. Express 19 (2011) 11415–11421.
[140] R. Pafchek, R. Tummidi, J. Li, M.A. Webster, E. Chen, T.L. Koch, Low-loss silicon-on-insulator shallow-ridge TE and TM waveguides formed using thermal oxidation, Appl. Opt. 48 (2009) 958–963.
[141] H.J. Lee, C.H. Henry, R.F. Kazarinov, K.J. Orlowsky, Low loss Bragg reflectors on $SiO_2 - Si_3N_4 - SiO_2$ rib waveguides, Appl. Opt. 26 (1987) 2618–2620.
[142] A. Yariv, Quantum Electronics, third ed., Wiley, 1989.
[143] K. Luke, A. Dutt, C.B. Poitras, M. Lipson, Overcoming Si_3N_4 film stress limitations for high quality factor ring resonators, Opt. Express 21 (2013) 22829–22833.
[144] Y.K. Chembo, N. Yu, Modal expansion approach to optical-frequency-comb generation with monolithic whispering-gallery-mode resonators, Phys. Rev. A 82 (2010) 033801.
[145] C.R. Lourés, D. Faccio, F. Biancalana, Nonlinear cavity and frequency comb radiations induced by negative frequency field effects, Phys. Rev. Lett. 115 (2015) 193904.
[146] A. Taflove, S.C. Hagness, Computational Electrodynamics: the Finite-Difference Time-Domain Method, Artech House, 2005.
[147] A. Yariv, Universal relations for coupling of optical power between microresonators and dielectric waveguides, Electron. Lett. 36 (2000) 321–322.
[148] A.N. Oraevsky, Whispering-gallery waves, Quantum Electron. 32 (2002) 377–400.
[149] D.M. Pozar, Microwave Engineering, fourth ed., Wiley, 2009.
[150] M. Oxborrow, Traceable 2-D finite-element simulation of the whispering-gallery modes of axisymmetric electromagnetic resonators, IEEE Trans. Microw. Theory Tech. 55 (2007) 1209–1218.
[151] I.S. Grudinin, N. Yu, Finite-element modeling of coupled optical microdisk resonators for displacement sensing, J. Opt. Soc. Amer. B 29 (2012) 3010–3014.
[152] I.S. Grudinin, A.B. Matsko, L. Maleki, On the fundamental limits of Q factor of crystalline dielectric resonators, Opt. Express 15 (2007) 3390–3395.
[153] P.P. Absil, J.V. Hryniewicz, B.E. Little, P.S. Cho, R.A. Wilson, L.G. Joneckis, P.T. Ho, Wavelength conversion in GaAs micro-ring resonators, Opt. Lett. 25 (2000) 554–556.
[154] T. Hansson, D. Modotto, S. Wabnitz, Analytical approach to the design of microring resonators for nonlinear four-wave mixing applications, J. Opt. Soc. Amer. B 31 (2014) 1109–1117.
[155] R.W. Boyd, Nonlinear Optics, second ed., Academic Press, 2003.
[156] S. Diallo, G. Lin, Y.K. Chembo, Giant thermo-optical relaxation oscillations in mm-size whispering gallery mode disk-resonators, Opt. Lett. 40 (2015) 3834–3837.
[157] A.B. Matsko, A.A. Savchenkov, N. Yu, L. Maleki, Whispering-gallery-mode resonators as frequency references. I. Fundamental limitations, J. Opt. Soc. Amer. B 24 (2007) 1324–1335.
[158] A.A. Savchenkov, A.B. Matsko, V.S. Ilchenko, N. Yu, L. Maleki, Whispering-gallery-mode resonators as frequency references. II. Stabilization, J. Opt. Soc. Amer. B 24 (2007) 2988–2997.
[159] T. Carmon, L. Yang, K.J. Vahala, Dynamical thermal behavior and thermal self-stability of microcavities, Opt. Express 12 (2004) 4742–4750.
[160] A.E. Fomin, M.L. Gorodetsky, I.S. Grudinin, V.S. Ilchenko, Nonstationary nonlinear effects in optical microspheres, J. Opt. Soc. Amer. B 22 (2005) 459–465.
[161] L. He, Y.-F. Xiao, J. Zhu, S.K. Ozdemir, L. Yang, Oscillatory thermal dynamics in high-Q PDMS-coated silica toroidal microresonators, Opt. Express 17 (2009) 9571–9581.
[162] Y. Deng, R. Flores-Flores, R.K. Jain, M. Hossein-Zadeh, Thermo-optomechanical oscillations in high-Q ZBLAN microspheres, Opt. Lett. 38 (2013) 4413–4416.
[163] Y. Deng, F. Liu, Z.C. Leseman, M. Hossein-Zadeh, Thermo-optomechanical oscillator for sensing applications, Opt. Express 21 (2013) 4653–4664.
[164] A.B. Matsko, A.A. Savchenkov, D. Strekalov, V.S. Ilchenko, L. Maleki, Optical hyperparametric oscillations in a whispering-gallery-mode resonator: Threshold and phase diffusion, Phys. Rev. A 71 (2005) 033804.
[165] I.H. Agha, Y. Okawachi, M.A. Foster, J.E. Sharping, A.L. Gaeta, Four-wave-mixing parametric oscillations in dispersion-compensated high-Q silica microspheres, Phys. Rev. A 76 (2007) 043837.
[166] I.S. Grudinin, N. Yu, L. Maleki, Generation of optical frequency combs with a CaF_2 resonator, Opt. Lett. 34 (2009) 878–880.
[167] A.M. Weiner, Femtosecond pulse shaping using spatial light modulators, Rev. Sci. Instrum. 71 (2000) 1929–1960.
[168] S.B. Papp, S.A. Diddams, Spectral and temporal characterization of a fused-quartz-microresonator optical frequency comb, Phys. Rev. A 84 (2011) 053833.
[169] P.-H. Wang, Y. Xuan, L. Fan, L.T. Varghese, J. Wang, Y. Liu, X. Xue, D.E. Leaird, M. Qi, A.M. Weiner, Drop-port study of microresonator frequency combs: power transfer, spectra and time-domain characterization, Opt. Express 21 (2013) 22441–22452.
[170] J.M. Dudley, G. Genty, S. Coen, Supercontinuum generation in photonic crystal fiber, Rev. Modern Phys. 78 (2006) 1135–1184.
[171] S. Coen, M. Haelterman, Modulational instability induced by cavity boundary conditions in a normally dispersive optical fiber, Phys. Rev. Lett. 79 (1997) 4139–4142.
[172] T. Hansson, S. Wabnitz, Frequency comb generation beyond the Lugiato-Lefever equation: multi-stability and super cavity solitons, J. Opt. Soc. Amer. B 32 (2015) 1259–1266.
[173] T. Hansson, D. Modotto, S. Wabnitz, On the numerical simulation of Kerr frequency combs using coupled mode equations, Opt. Commun. 312 (2014) 134–136.
[174] G.P. Agrawal, Nonlinear Fiber Optics, fourth ed., Academic Press, 2007.
[175] A. Aceves, H. Adachihara, C. Jones, J.C. Lerman, D.W. McLaughlin, J.V. Moloney, A.C. Newell, Chaos and coherent structures in partial differential equations, Physica D 18 (1986) 85–112.
[176] R. Vallé, Role of the group velocity dispersion in the onset of instabilities in a nonlinear ring cavity, Opt. Commun. 93 (1992) 389–399.
[177] G. Steinmeyer, A. Buchholz, M. Hänsel, M. Heuer, A. Schwache, F. Mitschke, Dynamical pulse shaping in a nonlinear resonator, Phys. Rev. A 52 (1995) 830–838.

[178] S. Coen, M. Haelterman, P. Emplit, L. Delage, L.M. Simohamed, F. Reynaud, Experimental investigation of the dynamics of a stabilized nonlinear fiber ring resonator, J. Opt. Soc. Amer. B 15 (1998) 2283–2293.
[179] K.J. Blow, D. Wood, Theoretical description of transient stimulated Raman scattering in optical fibers, IEEE J. Quantum Electron. 25 (1989) 2665–2673.
[180] I.H. Agha, Y. Okawachi, A.L. Gaeta, Theoretical and experimental investigation of broadband cascaded four-wave mixing in high-Q microspheres, Opt. Express 17 (2009) 16209–16215.
[181] A.J. Scroggie, W.J. Firth, G.S. McDonald, M. Tlidi, R. Lefèver, L.A. Lugiato, Pattern formation in a passive Kerr cavity, Chaos Solitons Fractals 4 (1994) 1323–1354. Special Issue: Nonlinear Optical Structures, Patterns, Chaos.
[182] L.A. Lugiato, Introduction to the feature section on cavity solitons: An overview, IEEE J. Quantum Electron. 39 (2003) 193–196.
[183] A.B. Matsko, A.A. Savchenkov, W. Liang, V.S. Ilchenko, D. Seidel, L. Maleki, Whispering gallery mode oscillators and optical comb generators, in: Proc. of 7th Symp. Frequency Standards and Metrology, World Scientific, 2009, pp. 539–558.
[184] I.V. Barashenkov, Y.S. Smirnov, Existence and stability chart for the ac-driven, damped nonlinear Schrödinger solitons, Phys. Rev. E 54 (1996) 5707–5725.
[185] M. Conforti, A. Mussot, A. Kudlinski, S. Trillo, Modulational instability in dispersion oscillating fiber ring cavities, Opt. Lett. 39 (2014) 4200–4203.
[186] M.R.E. Lamont, Y. Okawachi, A.L. Gaeta, Route to stabilized ultrabroadband microresonator-based frequency combs, Opt. Lett. 38 (2013) 3478–3481.
[187] Y. Okawachi, M.R.E. Lamont, K. Luke, D.O. Carvalho, M. Yu, M. Lipson, A.L. Gaeta, Bandwidth shaping of microresonator-based frequency combs via dispersion engineering, Opt. Lett. 39 (2014) 3535–3538.
[188] V. Torres-Company, D. Castelló-Lurbe, E. Silvestre, Comparative analysis of spectral coherence in microresonator frequency combs, Opt. Express 22 (2014) 4678–4691.
[189] T. Hansson, D. Modotto, S. Wabnitz, Mid-infrared soliton and Raman frequency comb generation in silicon microrings, Opt. Lett. 39 (2014) 6747.
[190] Y.K. Chembo, I.S. Grudinin, N. Yu, Spatiotemporal dynamics of Kerr-Raman optical frequency combs, Phys. Rev. A 92 (2015) 043818.
[191] J.M. Dudley, J. Taylor, Supercontinuum Generation in Optical Fibers, Cambridge University Press, 2001.
[192] C. Godey, I.V. Balakireva, A. Coillet, Y.K. Chembo, Stability analysis of the spatiotemporal Lugiato-Lefèver model for Kerr optical frequency combs in the anomalous and normal dispersion regimes, Phys. Rev. A 89 (2014) 063814.
[193] A.B. Matsko, A.A. Savchenkov, L. Maleki, Normal group-velocity dispersion Kerr frequency comb, Opt. Lett. 37 (2012) 43–45.
[194] W. Liang, A.A. Savchenkov, V.S. Ilchenko, D. Eliyahu, D. Seidel, A.B. Matsko, L. Maleki, Generation of a coherent near-infrared Kerr frequency comb in a monolithic microresonator with normal GVD, Opt. Lett. 39 (2014) 2920–2923.
[195] S.-W. Huang, H. Zhou, J. Yang, J.F. McMillan, A. Matsko, M. Yu, D.-L. Kwong, L. Maleki, C.W. Wong, Mode-locked ultrashort pulse generation from on-chip normal dispersion microresonators, Phys. Rev. Lett. 114 (2015) 053901.
[196] M. Erkintalo, S. Coen, Coherence properties of Kerr frequency combs, Opt. Lett. 39 (2014) 283–286.
[197] A. Coillet, I. Balakireva, R. Henriet, K. Saleh, L. Larger, J. Dudley, C. Menyuk, Y. Chembo, Azimuthal Turing patterns, bright and dark cavity solitons in Kerr combs generated with whispering-gallery-mode resonators, IEEE Photon. J. 5 (2013) 6100409.
[198] E. Infeld, Quantitive theory of the Fermi-Pasta-Ulam recurrence in the nonlinear Schrödinger equation, Phys. Rev. Lett. 47 (1981) 717–718.
[199] S. Trillo, S. Wabnitz, Dynamics of the nonlinear modulational instability in optical fibers, Opt. Lett. 16 (1991) 986–988.
[200] G. Van Simaeys, P. Emplit, M. Haelterman, Experimental demonstration of the Fermi-Pasta-Ulam recurrence in a modulationally unstable optical wave, Phys. Rev. Lett. 87 (2001) 033902.
[201] N.N. Akhmediev, Nonlinear physics: Déjà vu in optics, Nature 413 (2001) 267–268.
[202] A. Mussot, A. Kudlinski, M. Droques, P. Szriftgiser, N. Akhmediev, Fermi-Pasta-Ulam recurrence in nonlinear fiber optics: the role of reversible and irreversible losses, Phys. Rev. X 4 (2014) 011054.
[203] A.B. Matsko, W. Liang, A.A. Savchenkov, L. Maleki, Chaotic dynamics of frequency combs generated with continuously pumped nonlinear microresonators, Opt. Lett. 38 (2013) 525–527.
[204] A. Coillet, J. Dudley, G. Genty, L. Larger, Y.K. Chembo, Optical rogue waves in whispering-gallery-mode resonators, Phys. Rev. A 89 (2014) 013835.
[205] J.M. Dudley, F. Dias, M. Erkintalo, G. Genty, Instabilities, breathers and rogue waves in optics, Nature Photon. 8 (2014) 755–764.
[206] W.J. Firth, Temporal cavity solitons: Buffering optical data, Nature Photon. 4 (2010) 415–417.
[207] M. Marconi, J. Javaloyes, S. Balle, M. Giudici, How lasing localized structures evolve out of passive mode locking, Phys. Rev. Lett. 112 (2014) 223901.
[208] N. Akhmediev, A. Ankiewicz, Dissipative Solitons: From Optics to Biology and Medicine, Springer, Berlin, Heidelberg, 2008.
[209] P. Grelu, N. Akhmediev, Dissipative solitons for mode-locked lasers, Nature Photon. 6 (2012) 84–92.
[210] G.S. McDonald, W.J. Firth, Spatial solitary-wave optical memory, J. Opt. Soc. Amer. B 7 (1990) 1328–1335.
[211] N.N. Rosanov, G.V. Khodova, Diffractive autosolitons in nonlinear interferometers, J. Opt. Soc. Amer. B 7 (1990) 1057–1065.
[212] M. Tlidi, P. Mandel, R. Lefèver, Localized structures and localized patterns in optical bistability, Phys. Rev. Lett. 73 (1994) 640–643.
[213] W.J. Firth, C.O. Weiss, Cavity and feedback solitons, Opt. Photonics News 13 (2002) 54–58.
[214] S. Barland, J.R. Tredicce, M. Brambilla, L.A. Lugiato, S. Balle, M. Giudici, T. Maggipinto, L. Spinelli, G. Tissoni, T. Knödl, M. Miller, R. Jäger, Cavity solitons as pixels in semiconductor microcavities, Nature 419 (2002) 699–702.
[215] J.K. Jang, M. Erkintalo, S.G. Murdoch, S. Coen, Ultraweak long-range interactions of solitons observed over astronomical distances, Nature Photon. 7 (2013) 657–663.
[216] F. Leo, L. Gelens, P. Emplit, M. Haelterman, S. Coen, Dynamics of one-dimensional Kerr cavity solitons, Opt. Express 21 (2013) 9180–9191.
[217] J.K. Jang, M. Erkintalo, S.G. Murdoch, S. Coen, Observation of dispersive wave emission by temporal cavity solitons, Opt. Lett. 39 (2014) 5503–5506.
[218] J.K. Jang, M. Erkintalo, S. Coen, S.G. Murdoch, Temporal tweezing of light through the trapping and manipulation of temporal cavity solitons, Nature Commun. 6 (2015) 7370.
[219] J.K. Jang, M. Erkintalo, S.G. Murdoch, S. Coen, Writing and erasing of temporal cavity solitons by direct phase modulation of the cavity driving field, Opt. Lett. 40 (2015) 4755–4758.
[220] K. Luo, J.K. Jang, S. Coen, S.G. Murdoch, M. Erkintalo, Spontaneous creation and annihilation of temporal cavity solitons in a coherently driven passive fiber resonator, Opt. Lett. 40 (2015) 3735.
[221] M. Anderson, F. Leo, S. Coen, M. Erkintalo, S.G. Murdoch, Observations of spatiotemporal instabilities of temporal cavity solitons, Optica 3 (2016) 1071.
[222] X. Yi, Q.-F. Yang, K.Y. Yang, M.-G. Suh, K. Vahala, Soliton frequency comb at microwave rates in a high-Q silica microresonator, Optica 41 (2) (2015) 1078–1085.
[223] X. Yi, Q.-F. Yang, K.Y. Yang, K. Vahala, Active capture and stabilization of temporal solitons in microresonators, Opt. Lett. 41 (9) (2016) 2037–2040.
[224] V. Brasch, M. Geiselmann, T. Herr, G. Lihachev, M.H.P. Pfeiffer, M.L. Gorodetsky, T.J. Kippenberg, Photonic chip–based optical frequency comb using soliton Cherenkov radiation, Science 351 (2016) 357–360.
[225] C. Joshi, J.K. Jang, K. Luke, X. Ji, S.A. Miller, A. Klenner, Y. Okawachi, M. Lipson, A.L. Gaeta, Thermally controlled comb generation and soliton modelocking in microresonators, Opt. Lett. 41 (2016) 2565–2568.
[226] K.E. Webb, M. Erkintalo, S. Coen, S.G. Murdoch, Experimental observation of coherent cavity soliton frequency combs in silica microspheres, Opt. Lett. 41 (2016) 1539–4794.
[227] S. Wabnitz, Control of soliton train transmission, storage, and clock recovery by cw light injection, J. Opt. Soc. Amer. B 13 (1996) 2739–2749.

[228] A.B. Matsko, A.A. Savchenkov, L. Maleki, On excitation of breather solitons in an optical microresonator, Opt. Lett. 37 (2012) 4856–4858.
[229] M. Haelterman, S. Trillo, S. Wabnitz, Generation of ultrahigh repetition rate soliton trains in fibre ring, Electron. Lett. 29 (1993) 119.
[230] C. Bao, Z. Lin, A. Matsko, Y. Yan, Z. Zhao, G. Xie, A.M. Agarwal, L.C. Kimerling, J. Michel, L. Maleki, A.E. Willner, Nonlinear conversion efficiency in Kerr frequency comb generation, Opt. Lett. 39 (2014) 6126–6129.
[231] P. Parra-Rivas, D. Gomila, F. Leo, S. Coen, L. Gelens, Third-order chromatic dispersion stabilizes Kerr frequency combs, Opt. Lett. 39 (2014) 2971–2974.
[232] P.K.A. Wai, C.R. Menyuk, Y.C. Lee, H.H. Chen, Nonlinear pulse propagation in the neighborhood of the zero-dispersion wavelength of monomode optical fibers, Opt. Lett. 11 (1986) 464–466.
[233] N. Akhmediev, M. Karlsson, Cherenkov radiation emitted by solitons in optical fibers, Phys. Rev. A 51 (1995) 2602–2607.
[234] D.V. Skryabin, A.V. Gorbach, Colloquium: Looking at a soliton through the prism of optical supercontinuum, Rev. Modern Phys. 82 (2010) 1287–1299.
[235] M. Erkintalo, Y.Q. Xu, S.G. Murdoch, J.M. Dudley, G. Genty, Cascaded phase matching and nonlinear symmetry breaking in fiber frequency combs, Phys. Rev. Lett. 109 (2012) 223904.
[236] C. Milin, D. Skryabin, Soliton families and resonant radiation in a micro-ring resonator near zero group-velocity dispersion, Opt. Express 22 (2014) 3732.
[237] L. Zhang, C. Bao, V. Singh, J. Mu, C. Yang, A.M. Agarwal, L.C. Kimerling, J. Michel, Generation of two-cycle pulses and octave-spanning frequency combs in a dispersion-flattened micro-resonator, Opt. Lett. 38 (2013) 5122.
[238] S. Wang, H. Guo, X. Bai, X. Zeng, Broadband Kerr frequency combs and intracavity soliton dynamics influenced by high-order cavity dispersion, Opt. Lett. 39 (2014) 2880–2883.
[239] I.S. Grudinin, L. Baumgartel, N. Yu, Impact of cavity spectrum on span in microresonator frequency combs, Opt. Express 21 (2013) 26929–26935.
[240] T. Kobatake, T. Kato, H. Itobe, Y. Nakagawa, T. Tanabe, Thermal effects on Kerr comb generation in a CaF_2 whispering-gallery mode microcavity, IEEE Photon. J. 8 (2016) 7430257.
[241] P. Del'Haye, A. Coillet, W. Loh, K. Beha, S.B. Papp, S.A. Diddams, Phase steps and resonator detuning measurements in microresonator frequency combs, Nature Commun. 6 (2015) 5668.
[242] A. Coillet, Y.K. Chembo, Routes to spatiotemporal chaos in Kerr optical frequency combs, Chaos 24 (2014) 013113.
[243] K.E. Webb, J.K. Jang, J. Anthony, S. Coen, M. Erkintalo, S.G. Murdoch, Measurement of microresonator frequency comb coherence by spectral interferometry, Opt. Lett. 41 (2016) 277–280.
[244] H.A. Haus, W. Huang, Coupled-mode theory, Proc. IEEE 79 (1991) 1505–1518.
[245] W. Huang, Coupled-mode theory for optical waveguides: an overview, J. Opt. Soc. Am. A 1 (1994) 963–983.
[246] H. Cao, J. Wiersig, Dielectric microcavities: Model systems for wave chaos and non-Hermitian physics, Rev. Modern Phys. 87 (2015) 61–111.
[247] D.V. Strekalov, C. Marquardt, A.B. Matsko, H.G. Schwefel, G. Leuchs, Nonlinear and quantum optics with whispering gallery resonators, J. Optics-UK 18 (2016) 123002.
[248] J. Wiersig, Formation of long-lived, scarlike modes near avoided resonance crossings in optical microcavities, Phys. Rev. Lett. 97 (2006) 253901.
[249] T. Carmon, H.G.L. Schwefel, L. Yang, M. Oxborrow, A.D. Stone, K.J. Vahala, Static envelope patterns in composite resonances generated by level crossing in optical toroidal microcavities, Phys. Rev. Lett. 100 (2008) 103905.
[250] T. Klaassen, J. de Jong, M. van Exter, J.P. Woerdman, Transverse mode coupling in an optical resonator, Opt. Lett. 30 (2005) 1959–1961.
[251] J. Zhu, Ş.K. Özdemir, L. He, L. Yang, Controlled manipulation of mode splitting in an optical microcavity by two Rayleigh scatters, Opt. Express 18 (2010) 23535–23543.
[252] S.T. Attar, V. Shuvayev, L. Deych, L.L. Martin, T. Carmon, Level-crossing and modal structure in microdroplet resonators, Opt. Express 24 (2016) 13134–13141.
[253] S. Ramelow, A. Farsi, S. Clemmen, J.S. Levy, A.R. Johnson, Y. Okawachi, M.R.E. Lamont, M. Lipson, A.L. Gaeta, Strong polarization mode coupling in microresonators, Opt. Lett. 39 (2014) 5134.
[254] T. Herr, V. Brasch, J.D. Jost, I. Mirgorodskiy, G. Lihachev, M.L. Gorodetsky, T.J. Kippenberg, Mode spectrum and temporal soliton formation in optical microresonators, Phys. Rev. Lett. 113 (2014) 123901.
[255] A.A. Savchenkov, A.B. Matsko, W. Liang, V.S. Ilchenko, D. Seidel, L. Maleki, Kerr frequency comb generation in overmoded resonators, Opt. Express 20 (2012) 27290–27298.
[256] A.M. Weiner, J.P. Heritage, R.J. Hawkins, R.N. Thurston, E.M. Kirschner, D.E. Leaird, W.J. Tomlinson, Experimental observation of the fundamental dark soliton in optical fibers, Phys. Rev. Lett. 61 (1988) 2445–2448.
[257] A. Hasegawa, M. Matsumoto, Optical Solitons in Fibers, Springer-Verlag, Berlin, Heidelberg, 2003.
[258] N.N. Rosanov, Spatial Hysteresis and Optical Patterns, Springer, San Diego, USA, 2002.
[259] S. Coen, M. Tlidi, P. Emplit, M. Haelterman, Convection versus dispersion in optical bistability, Phys. Rev. Lett. 83 (1999) 2328–2331.
[260] V.E. Lobanov, G. Lihachev, T.J. Kippenberg, M.L. Gorodetsky, Frequency combs and platicons in optical microresonators with normal GVD, Opt. Express 23 (2015) 7713–7721.
[261] X. Xue, Y. Xuan, P.-H. Wang, Y. Liu, D.E. Leaird, M. Qi, A.M. Weiner, Normal-dispersion microcombs enabled by controllable mode interactions, Laser Photonics Rev. 9 (2015) L23–L28.
[262] C.M. Gentry, X. Zeng, M.A. Popović, Tunable coupled-mode dispersion compensation and its application to on-chip resonant four-wave mixing, Opt. Lett. 39 (2014) 5689–5692.
[263] S.A. Miller, Y. Okawachi, S. Ramelow, K. Luke, A. Dutt, A. Farsi, A.L. Gaeta, M. Lipson, Tunable coupled-mode dispersion compensation and its application to on-chip resonant four-wave mixing, Opt. Express 23 (2015) 21527–21540.
[264] D. Strekalov, N. Yu, Generation of optical combs in a whispering gallery mode resonator from a bichromatic pump, Phys. Rev. A 79 (2009) 041805(R).
[265] T. Hansson, S. Wabnitz, Bichromatically pumped microresonator frequency combs, Phys. Rev. A 90 (2014) 013811.
[266] Y. Okawachi, M. Yu, K. Luke, D.O. Carvalho, S. Ramelow, A. Farsi, M. Lipson, A.L. Gaeta, Dual-pumped degenerate Kerr oscillator in a silicon nitride microresonator, Opt. Lett. 40 (2015) 5267–5270.
[267] W. Liang, V. Ilchenko, A. Savchenkov, A. Matsko, D. Seidel, L. Maleki, Whispering-gallery-mode-resonator-based ultranarrow linewidth external-cavity semiconductor laser, Opt. Lett. 35 (2010) 2822–2824.
[268] W. Liang, V. Ilchenko, D. Eliyahu, A. Savchenkov, A. Matsko, D. Seidel, L. Maleki, Ultralow noise miniature external cavity semiconductor laser, Nature Commun. 6 (2015) 7371.
[269] L. Caspani, C. Reimer, A. Pasquazi, M. Peccianti, M. Clerici, M. Ferrera, L. Razzari, D. Duchesne, B.E. Little, S.T. Chu, D.J. Moss, R. Morandotti, A novel integrated laser source without a laser, SPIE Newsroom (2013). http://dx.doi.org/10.1117/2.1201312.005240.
[270] C. Reimer, L. Caspani, M. Clerici, M. Ferrera, M. Kues, M. Peccianti, A. Pasquazi, L. Razzari, B.E. Little, S.T. Chu, D.J. Moss, R. Morandotti, Integrated frequency comb source of heralded single photons, Opt. Express 22 (2014) 6535–6546.
[271] C. Reimer, M. Kues, L. Caspani, B. Wetzel, P. Roztocki, M. Clerici, Y. Jestin, M. Ferrera, M. Peccianti, A. Pasquazi, B.E. Little, S.T. Chu, D.J. Moss, R. Morandotti, Cross-polarized photon-pair generation and bi-chromatically pumped optical parametric oscillation on a chip, Nature Commun. 6 (2015) 8236.
[272] A.R. Johnson, Y. Okawachi, M.R.E. Lamont, J.S. Levy, M. Lipson, A.L. Gaeta, Microresonator-based comb generation without an external laser source, Opt. Express 22 (2014) 1394–1401.

[273] T. Kessler, C. Hagemann, C. Grebing, T. Legero, U. Sterr, F. Riehle, M.J. Martin, L. Chen, J. Ye, A sub-40-mHz-linewidth laser based on a silicon single-crystal optical cavity, Nature Photon. 6 (2012) 687–692.
[274] P. Franco, F. Fontana, I. Cristiani, M. Midrio, M. Romagnoli, Self-induced modulational-instability laser, Opt. Lett. 20 (1995) 2009–2011.
[275] E. Yoshida, M. Nakazawa, Low-threshold 115-GHz continuous-wave modulational-instability erbium-doped fiber laser, Opt. Lett. 22 (1997) 1409–1411.
[276] T. Sylvestre, S. Coen, P. Emplit, M. Haelterman, Self-induced modulational instability laser revisited: normal dispersion and dark-pulse train generation, Opt. Lett. 27 (2002) 482–484.
[277] M. Quiroga-Teixeiro, C. Balslev Clausen, M. Sørensen, P. Christiansen, P. Andrekson, Passive mode locking by dissipative four-wave mixing, J. Opt. Soc. Amer. B 15 (1998) 1315–1321.
[278] S. Zhang, F. Lu, X. Dong, P. Shum, X. Yang, X. Zhou, Y. Gong, C. Lu, Passive mode locking at harmonics of the free spectral range of the intracavity filter in a fiber ring laser, Opt. Lett. 30 (2005) 2852–2854.
[279] J. Schröder, D. Alasia, T. Sylvestre, S. Coen, Dynamics of an ultrahigh-repetition-rate passively mode-locked Raman fiber laser, J. Opt. Soc. Amer. B 25 (2008) 1178–1186.
[280] J. Schröder, T. Vo, B. Eggleton, Repetition-rate-selective, wavelength-tunable mode-locked laser at up to 640 GHz, Opt. Lett. 34 (2009) 3902–3904.
[281] S. Diddams, T. Udem, J. Bergquist, E. Curtis, R. Drullinger, L. Hollberg, W. Itano, W. Lee, C. Oates, K. Vogel, D. Wineland, An optical clock based on a single trapped $^{199}Hg^{+}$ ion, Science 293 (2001) 825–828.
[282] S. Diddams, D. Jones, J. Ye, S. Cundiff, J. Hall, J. Ranka, R. Windeler, R. Holzwarth, T. Udem, T. Hänsch, Direct link between microwave and optical frequencies with a 300 THz femtosecond laser comb, Phys. Rev. Lett. 84 (2000) 5102–5105.
[283] S.T. Cundiff, Metrology: new generation of combs, Nature 450 (2007) 1175–1176.
[284] K. Beha, D. Cole, P. Del'Haye, A. Coillet, S. Diddams, S. Papp, Self-referencing a CW laser with efficient nonlinear optics, 2015. arXiv:1507.06344, 1507.06344.
[285] P. Del'Haye, A. Coillet, T. Fortier, K. Beha, D.C. Cole, K.Y. Yang, H. Lee, K.J. Vahala, S.B. Papp, S.A. Diddams, Phase coherent link of an atomic clock to a self-referenced microresonator frequency comb, Nature Photon. 10 (2016) 516–520.
[286] V. Brasch, M. Geiselmann, T. Herr, G. Lihachev, M. Pfeiffer, M. Gorodetsky, T. Kippenberg, Photonic chip-based optical frequency comb using soliton Cherenkov radiation, Science 351 (2016) 357–360.
[287] A.B. Matsko, W. Liang, A.A. Savchenkov, D. Eliyahu, L. Maleki, Optical Cherenkov radiation in overmoded microresonators, Opt. Lett. 41 (2016) 2907–2910.
[288] S. Diddams, L. Hollberg, V. Mbele, Molecular fingerprinting with the resolved modes of a femtosecond laser frequency comb, Nature 445 (2007) 627–630.
[289] M. Thorpe, K. Moll, J. Jones, B. Safdi, J. Ye, Broadband cavity ringdown spectroscopy for sensitive and rapid molecular defection, Science 311 (2006) 1595–1599.
[290] K.-K. Ni, S. Ospelkaus, M.H.G. de Miranda, A. Pe'er, B. Neyenhuis, J.J. Zirbel, S. Kotochigova, P.S. Julienne, D.S. Jin, J. Ye, A high phase-space-density gas of polar molecules, Science 322 (2008) 231–235.
[291] A. Foltynowicz, P. Masowski, T. Ban, F. Adler, K.C. Cossel, T.C. Briles, J. Ye, Optical frequency comb spectroscopy, Farad. Discuss. 150 (2011) 23–31.
[292] M.-G. Suh, Q.-F. Yang, K.Y. Yang, X. Yi, K.J. Vahala, Microresonator soliton dual-comb spectroscopy, Science 354 (2016) 600–603.
[293] V. Torres-Company, A.M. Weiner, Optical frequency comb technology for ultra-broadband radio-frequency photonics, Laser Photonics Rev. 8 (2014) 368–393, and references therein.
[294] J. Capmany, B. Ortega, D. Pastor, A tutorial on microwave photonic filters, J. Lightw. Technol. 24 (2006) 201–229.
[295] J. Capmany, J. Mora, I. Gasulla, J. Sancho, Microwave photonic signal processing, J. Lightw. Technol. 31 (2013) 571–586.
[296] V.R. Supradeepa, C.M. Long, R. Wu, F. Ferdous, E. Hamidi, D.E. Leaird, A.M. Weiner, Comb-based radiofrequency photonic filters with rapid tunability and high selectivity, Nature Photon. 6 (2012) 186–194.
[297] A. Ortigosa-Blanch, J. Mora, J. Capmany, B. Ortega, D. Pastor, Tunable radio-frequency photonic filter based on an actively mode-locked fiber laser, Opt. Lett. 31 (2006) 709–711.
[298] E. Hamidi, D.E. Leaird, A.M. Weiner, Tunable programmable microwave photonic filters based on an optical frequency comb, IEEE Trans. Microw. Theory Tech. 58 (2010) 3269–3278.
[299] M. Song, C.M. Long, R. Wu, D. Seo, D.E. Leaird, A.M. Weiner, Reconfigurable and tunable flat-top microwave photonic filters utilizing optical frequency combs, IEEE Photon. Technol. Lett. 23 (2011) 1618–1620.
[300] A.M. Weiner, Ultrafast Optics, Wiley, 2009.
[301] H. Emami, N. Sarkhosh, L.A. Bui, A. Mitchell, Wideband RF photonic in-phase and quadrature-phase generation, Opt. Lett. 33 (2008) 98–100.
[302] L. Maleki, Sources: The optoelectronic oscillator, Nature Photon. 5 (2011) 728–730.
[303] T.M. Fortier, M.S. Kirchner, F. Quinlan, J. Taylor, J.C. Bergquist, T. Rosenband, N. Lemke, A. Ludlow, Y. Jiang, C. Oates, S.A. Diddams, Generation of ultrastable microwaves via optical frequency division, Nature Photon. 5 (2011) 425–429.
[304] J. Li, X. Yi, H. Lee, S.A. Diddams, K.J. Vahala, Electro-optical frequency division and stable microwave synthesis, Science 345 (2014) 309–313.
[305] J. Li, H. Lee, T. Chen, K.J. Vahala, Low-pump-power, low-phase-noise, and microwave to millimeter-wave repetition rate operation in microcombs, Phys. Rev. Lett. 109 (2012) 233901.
[306] A. Savchenkov, E. Rubiola, A. Matsko, V. Ilchenko, L. Maleki, Phase noise of whispering gallery photonic hyper-parametric microwave oscillators, Opt. Express 16 (2008) 4130–4144.
[307] A.B. Matsko, L. Maleki, On timing jitter of mode locked Kerr frequency combs, Opt. Express 21 (2013) 28862–28876.
[308] A.B. Matsko, L. Maleki, Noise conversion in Kerr comb RF photonic oscillators, J. Opt. Soc. Amer. B 32 (2015) 232–240.
[309] P.-H. Wang, F. Ferdous, H. Miao, J. Wang, D.E. Leaird, K. Srinivasan, L. Chen, V. Aksyuk, A.M. Weiner, Observation of correlation between route to formation, coherence, noise, and communication performance of Kerr combs, Opt. Express 20 (2012) 29284–29295.
[310] A. Coillet, Y.K. Chembo, On the robustness of phase-locking in Kerr optical frequency combs, Opt. Lett. 39 (2014) 1529–1533.
[311] J. Pfeifle, A. Coillet, R. Henriet, K. Saleh, P. Schindler, C. Weimann, W. Freude, I.V. Balakireva, L. Larger, C. Koos, Y.K. Chembo, Optimally coherent Kerr combs generated with crystalline whispering gallery mode resonators for ultrahigh capacity fiber communications, Phys. Rev. Lett. 114 (2015) 093902.
[312] E. Engin, D. Bonneau, C.M. Natarajan, A.S. Clark, M.G. Tanner, R.H. Hadfield, S.N. Dorenbos, V. Zwiller, K. Ohira, N. Suzuki, H. Yoshida, N. Iizuka, M. Ezaki, J.L. O'Brien, M.G. Thompson, Photon pair generation in a silicon micro-ring resonator with reverse bias enhancement, Opt. Express 21 (2013) 27826–27834.
[313] R. Kumar, J.R. Ong, J. Recchio, K. Srinivasan, S. Mookherjea, Spectrally multiplexed and tunable wavelength photon pairs at 1.55 μm from a silicon coupled-resonator optical waveguide, Opt. Lett. 38 (2013) 2969–2971.
[314] W. Jiang, X. Lu, J. Zhang, O. Painter, Q. Lin, A silicon-chip source of bright photon-pairs, Opt. Express 23 (2015) 20884–20904.
[315] F. Monteiro, A. Martin, B. Sanguinetti, H. Zbinden, R.T. Thew, Narrowband photon pair source for quantum networks, Opt. Express 22 (2014) 4371–4378.
[316] R. Raussendorf, H.J. Briegel, A one-way quantum computer, Phys. Rev. Lett. 86 (2001) 5188–5191.

[317] P. Walther, K.J. Resch, T. Rudolph, E. Schenck, H. Weinfurter, V. Vedral, M. Aspelmeyer, A. Zeilinger, Experimental one-way quantum computing, Nature 434 (2005) 169–176.
[318] R. Raussendorf, J. Harrington, K. Goyal, Topological fault-tolerance in cluster state quantum computation, New J. Phys. 9 (2007) 199.
[319] C. Kurtsiefer, S. Mayer, P. Zarda, H. Weinfurter, Stable solid-state source of single photons, Phys. Rev. Lett. 85 (2000) 290–293.
[320] P.G. Kwiat, K. Mattle, H. Weinfurter, A. Zeilinger, A.V. Sergienko, Y. Shih, New high-intensity source of polarization-entangled photon pairs, Phys. Rev. Lett. 75 (1995) 4337–4341.
[321] N. Gisin, G. Ribordy, W. Tittel, H. Zbinden, Quantum cryptography, Rev. Modern Phys. 74 (2002) 145–195.
[322] J.L. O'Brien, A. Furusawa, J. Vuckovic, Photonic quantum technologies, Nature Photon. 3 (2009) 687–695, and references therein.
[323] H. Takesue, Y. Tokura, H. Fukuda, T. Tsuchizawa, T. Watanabe, K. Yamada, S.-I. Itabashi, Entanglement generation using silicon wire waveguide, Appl. Phys. Lett. 91 (2007) 201108.
[324] L. Olislager, J. Safioui, S. Clemmen, K.P. Huy, W. Bogaerts, R. Baets, P. Emplit, S. Massar, Silicon-on-insulator integrated source of polarization-entangled photons, Opt. Lett. 38 (2013) 1960–1962.
[325] N. Matsuda, H. Le Jeannic, H. Fukuda, T. Tsuchizawa, W.J. Munro, K. Shimizu, K. Yamada, Y. Tokura, H. Takesue, A monolithically integrated polarization entangled photon pair source on a silicon chip, Sci. Rep. 2 (2012) 817.
[326] D. Grassani, S. Azzini, M. Liscidini, M. Galli, M.J. Strain, M. Sorel, J.E. Sipe, D. Bajoni, Micrometer-scale integrated silicon source of time-energy entangled photons, Optica 2 (2015) 88–94.
[327] A. Politi, M.J. Cryan, J.G. Rarity, S. Yu, J.L. O'Brien, Silica-on-silicon waveguide quantum circuits, Science 320 (2008) 646–649.
[328] A. Politi, J.C.F. Matthews, J.L. O'Brien, Shor's quantum factoring algorithm on a photonic chip, Science 325 (2009) 1221–1224.
[329] S. Yokoyama, R. Ukai, S.C. Armstrong, C. Sornphiphatphong, T. Kaji, S. Suzuki, J. Yoshikawa, H. Yonezawa, N.C. Menicucci, A. Furusawa, Ultra-large-scale continuous-variable cluster states multiplexed in the time domain, Nature Photon. 7 (2013) 982–986.
[330] Y.K. Chembo, Quantum dynamics of Kerr optical frequency combs below and above threshold: spontaneous four-wave-mixing, entanglement and squeezed states of light, Phys. Rev. A 93 (2016) 033820.
[331] C. Fabre, Squeezed states of light, Phys. Rep. 219 (1992) 215–225.
[332] L.A. Lugiato, F. Castelli, Quantum noise reduction in a spatial dissipative structure, Phys. Rev. Lett. 68 (1992) 3284–3286.
[333] A. Dutt, K. Luke, S. Manipatruni, A.L. Gaeta, P. Nussenzveig, M. Lipson, On-chip optical squeezing, Phys. Rev. Appl. 3 (2015) 044005.
[334] Q. Lin, G.P. Agrawal, Vector theory of four-wave mixing: polarization effects in fiber-optic parametric amplifiers, J. Opt. Soc. Amer. B 21 (2004) 1216–1224.
[335] S. Azzini, D. Grassani, M.J. Strain, M. Sorel, L.G. Helt, J.E. Sipe, M. Liscidini, M. Galli, D. Bajoni, Ultra-low power generation of twin photons in a compact silicon ring resonator, Opt. Express 20 (2012) 23100–23107.
[336] G.P.A.Q. Lin, F. Yaman, Photon-pair generation in optical fibers through four-wave mixing: Role of Raman scattering and pump polarization, Phys. Rev. A 75 (2007) 023803.
[337] P.J. Shadbolt, M.R. Verde, A. Peruzzo, A. Politi, A. Laing, M. Lobino, J.C.F. Matthews, M.G. Thompson, J.L. O'Brien, Generating, manipulating and measuring entanglement and mixture with a reconfigurable photonic circuit, Nature Photon. 6 (2012) 45–49.
[338] W. Tittel, J. Brendel, H. Zbinden, N. Gisin, Quantum cryptography using entangled photons in energy-time Bell states, Phys. Rev. Lett. 84 (2000) 4737–4740.
[339] I. Marcikic, H. de Riedmatten, W. Tittel, H. Zbinden, M. Legré, N. Gisin, Distribution of time-bin entangled qubits over 50 km of optical fiber, Phys. Rev. Lett. 93 (2004) 180502.
[340] J. Mower, Z. Zhang, P. Desjardins, C. Lee, J.H. Shapiro, D. Englund, High-dimensional quantum key distribution using dispersive optics, Phys. Rev. A 87 (2013) 062322.
[341] J.E. Sharping, K.F. Lee, M.A. Foster, A.C. Turner, B.S. Schmidt, M. Lipson, A.L. Gaeta, P. Kumar, Generation of correlated photons in nanoscale silicon waveguides, Opt. Express 14 (2006) 12388–12393.
[342] L.G. Helt, Z. Yang, M. Liscidini, J.E. Sipe, Spontaneous four-wave mixing in microring resonators, Opt. Lett. 35 (2010) 3006–3008.
[343] J. Chen, Z.H. Levine, J. Fan, A.L. Migdall, Frequency-bin entangled comb of photon pairs from a silicon-on-insulator micro-resonator, Opt. Express 19 (2011) 1470–1483.
[344] L.G. Helt, M. Liscidini, J.E. Sipe, How does it scale? Comparing quantum and classical nonlinear optical processes in integrated devices, J. Opt. Soc. Amer. B 29 (2012) 2199–2212.
[345] R.M. Camacho, Entangled photon generation using four-wave mixing in azimuthally symmetric microresonators, Opt. Express 20 (2012) 21977–21991.
[346] Z. Vernon, J.E. Sipe, Spontaneous four-wave mixing in lossy microring resonators, Phys. Rev. A 91 (2015) 053802.
[347] M. Davanco, J.R. Ong, A.B. Shehata, A. Tosi, I. Agha, S. Assefa, F. Xia, W.M.J. Green, S. Mookherjea, K. Srinivasan, Telecommunications-band heralded single photons from a silicon nanophotonic chip, Appl. Phys. Lett. 100 (2012) 261104.
[348] S. Azzini, D. Grassani, M. Galli, D. Gerace, M. Patrini, M. Liscidini, P. Velha, D. Bajoni, Stimulated and spontaneous four-wave mixing in silicon-on-insulator coupled photonic wire nano-cavities, Appl. Phys. Lett. 103 (2013) 031117.
[349] J.D. Franson, Bell inequality for position and time, Phys. Rev. Lett. 62 (1989) 2205–2208.
[350] J.D. Franson, Two-photon interferometry over large distances, Phys. Rev. A 44 (1991) 4552–4555.
[351] D. Grassani, M. Galli, D. Bajoni, Active stabilization of a Michelson interferometer at an arbitrary phase with subnanometer resolution, Opt. Lett. 39 (2014) 2530–2533.
[352] P.G. Kwiat, A.M. Steinberg, R.Y. Chiao, High-visibility interference in a Bell-inequality experiment for energy and time, Phys. Rev. A 47 (1993) R2472–R2475.
[353] K. Harada, H. Takesue, H. Fukuda, T. Tsuchizawa, T. Watanabe, K. Yamada, Y. Tokura, S. Itabashi, Generation of high-purity entangled photon pairs using silicon wirewaveguide, Opt. Express 16 (2008) 20368–20373.
[354] C. Silberhorn, N. Korolkova, G. Leuchs, Quantum key distribution with bright entangled beams, Phys. Rev. Lett. 88 (2002) 167902.
[355] B.R. Johnson, Theory of morphology-dependent resonances: shape resonances and width formulas, J. Opt. Soc. Am. A 10 (1993) 343–352.
[356] M. Abramowitz, I. Stegun, Handbook of Mathematical Functions: with Formulas, Graphs, and Mathematical Tables, in: Applied Mathematics Series, Dover Publications, 1964.
[357] S. Schiller, Asymptotic expansion of morphological resonance frequencies in Mie scattering, Appl. Opt. 32 (1993) 2181–2185.